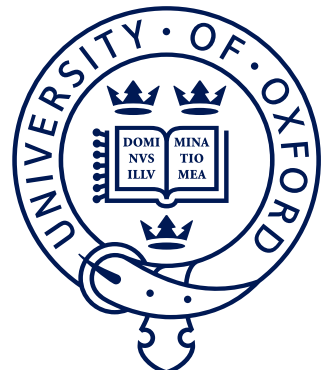


¹ **CP violation in $B^\pm \rightarrow Dh^\pm$ decays**
² **where $D \rightarrow K_S^0 h'^+ h'^-$**

³ *A measurement of the CKM angle γ at LHCb and understanding
⁴ the impact of neutral kaon CP violation*



⁶ Mikkel Bjørn
⁷ St. Anne's College
⁸ University of Oxford

⁹ A thesis submitted for the degree of
¹⁰ *Doctor of Philosophy*
¹¹ Trinity 2020

¹²

Acknowledgements

¹³ suitable thank you's

Abstract

14

¹⁵ World's best measurement of γ . Details to be added.

Contents

16

17	Preface	vii
18	1 Theoretical background	1
19	1.1 The C, P and T symmetries and their violation	1
20	1.2 CP violation in the Standard Model	3
21	1.2.1 The CKM matrix and the Unitarity Triangle	4
22	1.2.2 Measuring γ in tree level decays	7
23	1.3 Measuring γ using multi-body D final states	11
24	1.3.1 Dalitz plots and the phase space of multi-body decays	11
25	1.3.2 The GGSZ method to measure γ	13
26	1.3.3 A model-independent approach	15
27	1.3.4 Measuring strong-phase inputs at charm factories	17
28	1.3.5 Global CP asymmetry and the relation to GLW and ADS measurements	21
29	1.4 Strategy for the LHCb measurement	25
31	2 The LHCb experiment	28
32	2.1 The LHCb subdetectors	30
33	2.1.1 The VELO	31
34	2.1.2 Magnet and tracking stations	33
35	2.1.3 The RICH detectors	35
36	2.1.4 Calorimeters	37
37	2.1.5 Muon detectors	39
38	2.2 Reconstruction	39
39	2.2.1 Track reconstruction	40
40	2.2.2 Particle identification	41
41	2.3 The LHCb trigger system	43
42	2.3.1 The level-0 hardware trigger	44
43	2.3.2 High-level triggers	45
44	2.3.3 Offline data filtering: the LHCb stripping	46
45	2.4 Simulation	47

46	3 Neutral kaon CP violation and material	48
47	interaction in BPGGSZ measurements	
48	3.1 CP violation and material interaction of neutral kaons	48
49	3.1.1 A first look at the impact on γ measurements	52
50	3.2 Impact on BPGGSZ measurements of γ :	
51	principles	54
52	3.2.1 Modified symmetry relations	54
53	3.2.2 Relationship between the K_S^0 and K_L^0 amplitudes	55
54	3.2.3 Modification of the BPGGSZ yield equations	56
55	3.3 Impact on BPGGSZ measurements of γ :	
56	LHCb and Belle II measurements	59
57	3.3.1 Detector geometries	60
58	3.3.2 Kaon momentum distributions	61
59	3.3.3 Experimental time acceptance	62
60	3.3.4 Detector material budget	63
61	3.3.5 Calculation procedure	65
62	3.3.6 Results	66
63	3.3.7 Coupled $B^\pm \rightarrow DK^\pm$ and $B^\pm \rightarrow D\pi^\pm$ measurements	68
64	3.4 Concluding remarks	69
65	4 A BPGGSZ measurement of γ with $B^\pm \rightarrow Dh^\pm$ decays	71
66	4.1 Candidate reconstruction and selection	71
67	4.1.1 Initial requirements	72
68	4.1.2 Boosted decision tree	74
69	4.1.3 Particle-identification requirements	80
70	4.1.4 Final requirements	81
71	4.1.5 Selected candidates	81
72	4.2 Signal selection efficiencies	82
73	4.2.1 Efficiency of the PID requirements	85
74	4.2.2 Efficiency profile over the Dalitz plot	86
75	4.3 Background studies	88
76	4.3.1 Charmless decays	90
77	4.3.2 Background from four-body D decays	91
78	4.3.3 Semi-leptonic backgrounds	92
79	4.3.4 Cross-feed from other $D \rightarrow K_S^0 h^+ h^-$ decays	100
80	4.3.5 Swapped-track backgrounds	100
81	4.4 Signal and background mass shapes	101
82	4.4.1 Signal decays	103
83	4.4.2 Cross-feed between $B^\pm \rightarrow Dh^\pm$ channels	104

84	4.4.3	Partially reconstructed backgrounds	106
85	4.4.4	Combinatorial background	112
86	4.4.5	Fit results	112
87	4.5	Measurement of the CP-violation observables	115
88	4.5.1	Fit setup	116
89	4.5.2	Main results	124
90	4.5.3	Cross checks	125
91	4.6	Systematic uncertainties	132
92	4.6.1	Strong phase uncertainties	134
93	4.6.2	Efficiency-profile-related systematic uncertainties	134
94	4.6.3	Mass shapes	138
95	4.6.4	CP violation and material interaction of the K_S^0	145
96	4.6.5	Impact of D mixing	145
97	4.6.6	PID efficiencies	146
98	4.6.7	Dalitz-coordinate resolution	146
99	4.6.8	The fixed yield fractions	147
100	4.6.9	Systematic uncertainty due to backgrounds that are not modelled in fit	148
101	4.6.10	Bias correction	150
102	4.6.11	Charmless backgrounds	150
103	4.6.12	Summary of systematic uncertainties	151
104	4.7	Obtained constraints on γ	152
105	4.7.1	Statistical approach	153
106	4.7.2	Interpretation results	155
107	4.7.3	Compatibility with other measurements	158

109 Appendices

110	A Projections of main fit to data	162
111	Bibliography	163

Preface

112

113 The work presented in this thesis has been resulted in two papers, either under
114 review or published in the Journal of High Energy Physics. These are

115 [1] *Measurement of the CKM angle γ using $B^\pm \rightarrow [K_S^0 h^+ h^-]_D h^\pm$ decays*,
116 submitted to JHEP.

117 This paper describes a measurement of the CKM angle γ using pp collision
118 data taken with the LHCb experiment during the Run 1 of the LHC, in 2011
119 and 2012, and during the full Run 2, in 2015–2018. The measurement uses the
120 decay channels $B^\pm \rightarrow D h^\pm$ where $D \rightarrow K_S^0 h'^+ h'^-$, in which h and h' denotes
121 pions or kaons. It obtains a value of $\gamma = (69 \pm 5)^\circ$, which constitutes the
122 world’s best single-measurement determination of γ . The work is the main
123 focus of this thesis and described in detail in Chapter 4.

124 [2] *CP violation and material interaction of neutral kaons in measurements*
125 *of the CKM angle γ using $B^\pm \rightarrow D K^\pm$ decays where $D \rightarrow K_S^0 \pi^+ \pi^-$* , JHEP
126 19 (2020) 106.

127 This paper describes a phenomenological study of the impact of neutral
128 kaon CP violation and material interaction on measurements of γ . With the
129 increased measurement precision to come in the near future, an understanding
130 of these effects is crucial, especially in the context of $B \rightarrow D\pi$ decays; however
131 no detailed study had been published at the start of this thesis. The study is
132 the subject of Chapter 3. Some text excerpts and figures from the paper have
133 been reproduced in the thesis.

134 All of the work described in this thesis is my own, except where clearly referenced
135 to others. Furthermore, I contributed significantly to an analysis of $B^\pm \rightarrow D K^\pm$
136 decays with LHCb data taken in 2015 and 2016, now published in

137 [3] *Measurement of the CKM angle γ using $B^\pm \rightarrow D K^\pm$ with $D \rightarrow K_S^0 \pi^+ \pi^-$*
138 *$K_S^0 K^+ K^-$ decays*, JHEP 08 (2018) 176.

139 I was responsible for the analysis of the signal channel, systematic studies, and
140 the interpretation. The measurement is superseded by that of Ref. [1] and is not
141 described in detail in the thesis.

1

142

143

Theoretical background

144 This chapter lays out the theoretical framework of the thesis. Section 1.1 introduces
145 charge and parity symmetry violation in general, while Section 1.2 covers the
146 description in the Standard Model and the general theory behind charge-parity
147 symmetry violation measurements in charged B decays. Section 1.3 focuses on
148 the theory of measurements using $B^\pm \rightarrow Dh^\pm$ decays with multi-body D final
149 states, after which the specific analysis strategy for the measurement described
150 in the thesis is outlined out in Section 1.4.

151 1.1 The C, P and T symmetries and their vio- 152 lation

153 The concept of symmetry play a fundamental role in modern physics. By Noether's
154 theorem [4], the simple assumption of invariance of our physical laws under universal
155 temporal and spatial translations leads to the very non-trivial prediction of conserved
156 energy and momentum; within the field of particle physics, the interactions and
157 dynamics of the Standard Model (SM) follow completely simply from requiring
158 the fundamental particle fields to satisfy a local $U(1) \times SU(2) \times SU(3)$ gauge
159 symmetry [5]; and one of the short-comings of the SM, is that it fails to explain
160 the apparent *lack* of symmetry in our matter-dominated universe [6]. Indeed, it is
161 important to experimentally establish the symmetries of our world at a fundamental
162 level, and the degree to which they are broken.

163 Three discrete symmetries of importance are the symmetries under

I'll
adjust
this para-
graph
when
I've
written
the intro-
duction.

- 164 1. The charge operator C , which conjugates all internal quantum numbers of a
 165 quantum state and thus converts particles into their anti-particle counter parts.
 166 For example, C transforms the electric charge of a particle state $Q \rightarrow -Q$.
- 167 2. The parity operator P , which inverts the spatial dimensions of space time:
 168 $\vec{x} \rightarrow -\vec{x}$. As such, it transforms left-handed particle fields into right-handed
 169 particle fields and vice versa.
- 170 3. The time-inversion operator T , which inverts the temporal dimension of space
 171 time: $t \rightarrow -t$.

172 These are fundamentally related by the *CPT* theorem [7] , which states that any
 173 Lorentz-invariant Quantum Field Theory (QFT) must be symmetric under the
 174 simultaneous application of *all* three operators. However, any one of the symmetries
 175 can be broken individually, and experiments have shown the physical laws of our
 176 world to violate each of the C , P , and T symmetries.

177 Such a symmetry-breaking effect was established for the first time in 1956, when
 178 Chien-Shiung Wu observed parity violation in weak decays of Co-60 nuclei [8], after
 179 carrying out an experiment that was proposed by Yang Chen-Ning and Tsung-Dao
 180 Lee [9]. While this experiment established the breaking of P symmetry, it left open
 181 the possibility that the physical laws are invariant under a combination of a charge-
 182 and parity inversion; that they are *CP* symmetric. However, this was disproved in
 183 1964 when Kronin and Fitch observed that long-lived kaons, which predominantly
 184 decay to the *CP*-odd 3π state, could also decay to the *CP*-even $\pi\pi$ states [10].

185 Since then *CP* violation has been found in the B^0 system by the BaBar and Belle
 186 collaborations [11,12] during the early 2000's; the B factories, along with CDF, also
 187 saw evidence for *CP* violation in B^\pm decays [13–18] later confirmed by LHCb [19],
 188 and *CP* violation was measured for the B_s^0 meson by LHCb in 2013 [20]; within the
 189 last year and a half, the first observation of *CP*-violation in D^0 decays has also been
 190 made by the LHCb collaboration [21], and most recently evidence for *CP*-violation in
 191 the neutrino sector has been reported by the T2K collaboration [22]. The observed
 192 effects can be divided into distinct classes. The conceptually simplest case is

- 193 1. *CP-violation in decay*, where $|A/\bar{A}| \neq 1$ for some decay amplitude A , and the
 194 amplitude \bar{A} of the *CP*-conjugate decay. The result is different decay rates in
 195 two *CP*-conjugate decays

$$\Gamma(M \rightarrow f) \neq \Gamma(\bar{M} \rightarrow \bar{f}). \quad (1.1)$$

This type of CP violation was not seen until the late 1980ies [23, 24], more than 20 years after the first observation of CP violation, and only finally established around the year 2000 [25, 26]. Also this discovery was made in $K \rightarrow \pi\pi$ decays.

CP -violation in decay is the only type possible for charged initial states, and it is thus the main focus of the thesis. Two additional CP -violating effect are possible for neutral initial states (a situation that will be the main focus of Chapter 3). These effects are

2. CP -violation in mixing, which denotes the case where the mixing rates between the M^0 and \bar{M}^0 states differ

$$\Gamma(M^0 \rightarrow \bar{M}^0) \neq \Gamma(\bar{M}^0 \rightarrow M^0). \quad (1.2)$$

The CP violation first observed by Kronin and Fitch in the neutral kaon sector [10] is (dominantly) of this type.

3. CP -violation in interference between mixing and decay, which can be present for a neutral initial states M^0 decaying into a final state f common to both M^0 and \bar{M}^0 . The decay rate includes an interference term between two amplitudes: the amplitude for a direct $M^0 \rightarrow f$ decay and the amplitude for a decay after mixing: $M^0 \rightarrow \bar{M}^0 \rightarrow f$. Even in the absence of the two aforementioned effects, the rates $\Gamma(M^0 \rightarrow f)$ and $\Gamma(\bar{M}^0 \rightarrow \bar{f})$ can differ due to the interference term. Such CP asymmetries have been measured in eg. $B^0 \rightarrow J/\psi K$ by LHCb and the B factories, and in $B_s^0 \rightarrow J/\psi \phi$ decays by the LHC and Tevatron experiments [27].

CP violation measurements thus have a long, rich, and still-developing history.

1.2 CP violation in the Standard Model

All existing measurements of CP violation in the quark sector are naturally explained in the SM; indeed, the need to explain the observation CP violation in neutral kaons was a driving force in the development of the model in the first place, when it lead Kobayashi and Maskawa to predict the existence of then-unknown particles in 1973 [28] (now known to be the third generation quarks).

1.2.1 The CKM matrix and the Unitarity Triangle

The SM contains three generations of quarks, each consisting of an up-type quark (u , c , and t) and a down-type quark (d , s , and b). The charged weak interaction of the W^\pm boson couples up and down-type quarks. The quark states that couple to the W are not (a priori) identical to the mass eigenstates, and can be denoted $(u', c', \text{ and } t')$ and $(d', s', \text{ and } b')$. A basis for the quark states can be chosen such that the weakly coupling up-quark states are identical to the propagating quark states, $u = u'$, but then the down-type quark state are different: $d' \neq d$. The two bases of the down-type quarks are related via the Cabibbo-Kobayashi-Maskawa (CKM) matrix [28, 29]¹

$$\begin{pmatrix} d' \\ s' \\ t' \end{pmatrix} = V \begin{pmatrix} d \\ s \\ t \end{pmatrix} = \begin{pmatrix} V_{ud} & V_{us} & V_{ub} \\ V_{cd} & V_{cs} & V_{cb} \\ V_{td} & V_{ts} & V_{tb} \end{pmatrix} \begin{pmatrix} d \\ s \\ t \end{pmatrix}. \quad (1.3)$$

Thus the Lagrangian terms representing the coupling of a W^\pm boson with a u - and a d -type quark is

$$\mathcal{L}_{W^+} = -\frac{g}{\sqrt{2}} V_{ud} (\bar{u} \gamma^\mu W_\mu^+ d) \quad \mathcal{L}_{W^-} = -\frac{g}{\sqrt{2}} V_{ud}^* (\bar{d} \gamma^\mu W_\mu^- u) \quad (1.4)$$

where g is the weak coupling constant, γ_u are the Dirac matrices, and u and d represent the left-handed components of the physical quark states.

The CKM matrix is a unitary complex 3×3 matrix, and hence has $3^2 = 9$ independent, real parameters. However, 5 of these can be absorbed into non-physical phases of the quark states (both mass and weak eigenstates) and hence the matrix has 4 real, physical parameters: 3 mixing angles and a single phase. Chau and Keung [30] proposed the parameterisation

$$V = \begin{pmatrix} 1 & 0 & 0 \\ 0 & c_{23} & s_{23} \\ 0 & -s_{23} & c_{23} \end{pmatrix} \begin{pmatrix} c_{13} & 0 & s_{13}e^{-i\delta_{CP}} \\ 0 & 1 & 0 \\ -s_{13}e^{-i\delta_{CP}} & 0 & c_{13} \end{pmatrix} \begin{pmatrix} c_{12} & s_{12} & 0 \\ -s_{12} & c_{12} & 1 \\ 0 & 0 & 1 \end{pmatrix} \\ = \begin{pmatrix} c_{12}c_{13} & s_{12}c_{13} & s_{13}e^{-i\delta_{CP}} \\ -s_{12}c_{23} - c_{12}s_{23}s_{13}e^{i\delta_{CP}} & c_{12}c_{23} - s_{12}s_{23}s_{13}e^{i\delta_{CP}} & s_{23}c_{13} \\ s_{12}s_{23} - c_{12}c_{23}s_{13}e^{i\delta_{CP}} & -c_{12}s_{23} - s_{12}s_{23}s_{13}e^{i\delta_{CP}} & c_{23}c_{13} \end{pmatrix} \quad (1.5)$$

which is the preferred standard by the PDG [31]. Here, $s_{ij} \equiv \sin \theta_{ij}$ and $c_{ij} \equiv \cos \theta_{ij}$ denote the sine and cosine of three rotation angles in quark space; $\theta_{12} = \theta_C$ being the usual Cabibbo angle [29].

¹ A basis for the quarks can of course be chosen, such that neither the up-quarks or the down-quarks are expressed in their mass eigenstates. In that case the CKM matrix is recovered as $V = U_u^* U_d$, where $U_{u/d}$ is the unitary transformation matrices that brings the u/d quarks into their mass eigenstates.

The presence of the complex phase δ_{CP} in the Lagrangian term of the W coupling causes CP violation because, as evident from Eq. (1.4), if δ_{CP} enters the amplitude for some decay mediated by a W boson, $A = |A|e^{i(\delta_0 + \delta_{CP})}$, then it will enter the CP conjugate decay amplitude with the opposite sign: $\bar{A} = |A|e^{i(\delta_0 - \delta_{CP})}$. In these expressions, δ_0 denotes a CP conserving phase that is not caused by complex terms in the Lagrangian, but arises due to potential intermediate states in the decay amplitude.² Usually the underlying mechanism is due to QCD effects, and these CP conserving phases are therefore generally dubbed *strong* phases, as opposed to the CP violating *weak* phase of the W coupling [31]. This terminology will be applied throughout the thesis.

Experimentally, it has been observed that the CKM matrix elements of Eq. (1.5) satisfy $s_{13} \ll s_{23} \ll s_{12}$. This motivates an often used, alternative parameterisation of the matrix, where the elements are expressed as power series in a parameter λ that naturally incorporates this hierarchy: the Wolfenstein parameterisation [32]. The definitions

$$\begin{aligned} s_{12} &\equiv \lambda \\ s_{23} &\equiv \lambda^2 A \\ s_{13} &\equiv \lambda^3 (\rho - i\eta) \end{aligned} \tag{1.6}$$

are made, after which the unitarity conditions (or Eq. 1.5) determine the remaining elements to any order in λ .³ To $\mathcal{O}(\lambda^5)$ the Wolfenstein parameterisation of the CKM matrix is [34, 35]

$$V = \begin{pmatrix} 1 - \frac{\lambda^2}{2} - \frac{\lambda^4}{8} & \lambda & A\lambda^3(\rho - i\eta) \\ -\lambda + \frac{\lambda^5}{2}A^2(1 - 2(\rho + i\eta)) & 1 - \frac{\lambda^2}{2} - \frac{\lambda^4}{8}(1 + 4A^2) & A\lambda^2 \\ A\lambda^3(1 - (\rho + i\eta)(1 - \frac{\lambda^2}{2})) & -A\lambda^2(1 - \frac{\lambda^2}{2}(1 - 2(\rho + i\eta))) & 1 - \frac{1}{2}A^2\lambda^4 \end{pmatrix}. \tag{1.7}$$

The unitarity condition $V^\dagger V = \mathbb{1}$ of the CKM matrix defines 9 relations between the CKM elements of the form

$$\sum_j V_{jq}^* V_{jq} = 1 \quad , \quad q \in \{d, s, b\} \quad \text{along the diagonal} \tag{1.8a}$$

$$\sum_j V_{jq}^* V_{jq'} = 0 \quad , \quad q, q' \in \{d, s, b\}, q \neq q' \quad \text{off-diagonal.} \tag{1.8b}$$

²It is generally true that all phases of a single term in a given amplitude will be convention dependent, but that the phase differences between terms are not.

³Other variants of the Wolfenstein parameterisation do exist [33]. They all agree at the lowest orders of λ .

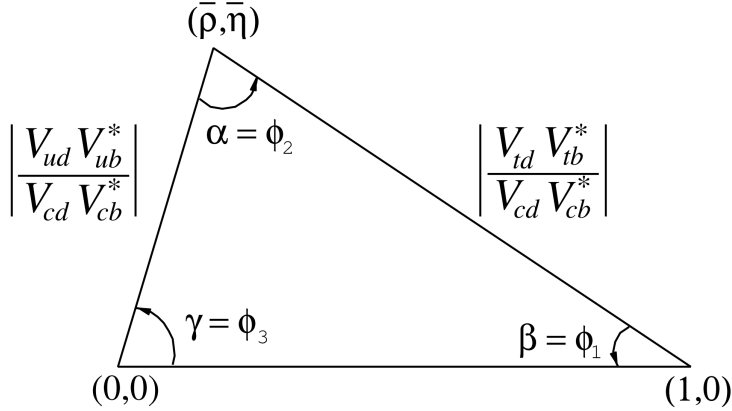


Figure 1.1: Definition of the lengths and sides of the Unitarity Triangle. Figure is taken from the *CKM Quark-Mixing Matrix* review of the PDG [31].

266 The off-diagonal conditions constrain three complex numbers to sum to zero, and
 267 can thus be visualised as triangles in the complex plane, the so-called unitarity
 268 triangles. Of these, the triangle corresponding to the (d, b) elements plays a
 269 special role, because all three sides are of the same order of magnitude, $\mathcal{O}(\lambda^3)$.
 270 When expressed in the form

$$\frac{V_{ud}^* V_{ub}}{V_{cd}^* V_{cb}} + \frac{V_{td}^* V_{tb}}{V_{cd}^* V_{cb}} + 1 = 0, \quad (1.9)$$

271 it is often referred to as the singular Unitarity Triangle, illustrated in Fig. 1.1 where
 272 the usual names for the three angles are also given.

273 Over-constraining the unitarity triangle by making separate measurements of all
 274 sides and angles, in as many different decay channels as possible, is an important,
 275 and non-trivial test of the SM. The current experimental constraints are in agreement
 276 with the SM predictions, as visualised in Fig. 1.2. The CKM angle

$$\gamma \equiv \arg(-V_{ud} V_{ub}^* / V_{cd} V_{cb}^*) = \arg(-V_{cb} V_{cd}^* / V_{ub} V_{ud}^*) \quad (1.10)$$

277 is unique among the CKM parameters, in that it can be measured in tree-level pro-
 278 cesses without significant theoretical uncertainty from lattice QCD calculations [36].
 279 Because tree-level processes are less likely to be affected by Beyond-Standard-Model
 280 (BSM) effects, direct measurements of γ can be considered a SM benchmark, which
 281 can be compared to estimates based on measurements of other CKM elements that
 282 are measured in loop-level processes, and thus are more likely to be affected by
 283 BSM effects [37]. The current, worldwide combination of direct measurements,
 284 published by the CKMFitter group, is $\gamma = (72.1^{+5.4}_{-5.7})^\circ$, to be compared with the
 285 estimate from loop-level observables of $\gamma = (65.66^{+0.90}_{-2.65})^\circ$ [38]. Other world averages

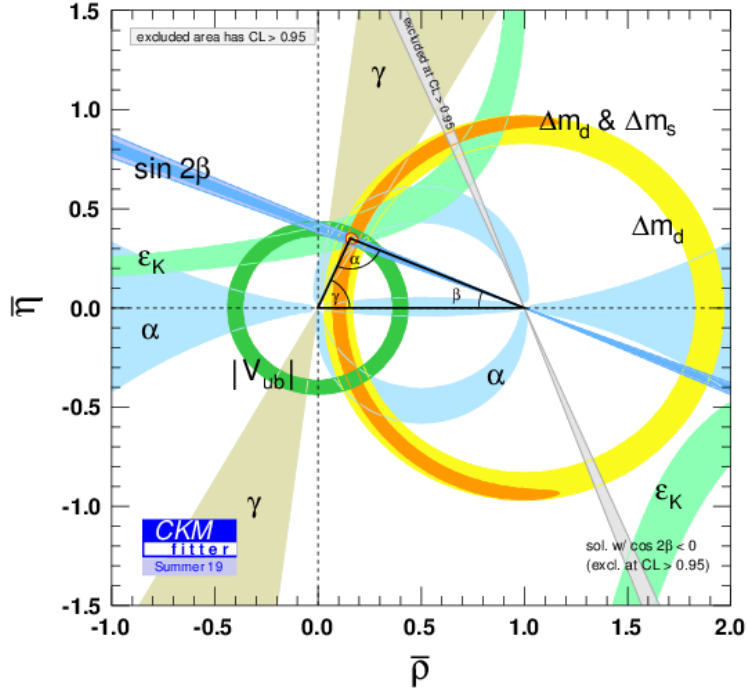


Figure 1.2: Current constraints on the Unitarity Triangle parameters as determined by the CKMFitter group for the EPS 2019 conference [38].

exist [27, 39], but the overall picture is the same: the ability to constrain BSM physics is currently limited by the uncertainty of the direct measurements. Hence further precision measurements of γ are highly motivated. Presently, the precision is driven by time-integrated measurements of direct CP -violation in $B^\pm \rightarrow DK^\pm$ decays; such a measurement is the topic of this thesis and the theory behind is treated in detail in the following section. It is also possible to measure γ in time-dependent mixing analyses of $B_s^0 \rightarrow D_s^\mp K^\pm$, $B^0 \rightarrow D^\mp \pi^\pm$ and related decays, by measuring CP violation in interference between mixing and decay. These modes are expected to provide competitive measurements in the future [40, 41].

1.2.2 Measuring γ in tree level decays

The phase γ can be measured in tree-level processes with interference between $b \rightarrow c\bar{s}u$ and $b \rightarrow \bar{c}s u$ transitions. The canonical example, also the subject of this thesis, is based on measurements sensitive to interference between the $B^\pm \rightarrow D^0 K^\pm$ and $B^\pm \rightarrow \bar{D}^0 K^\pm$ decay amplitudes. As illustrated in Fig. 1.3 for the case of B^- decays, the electro-weak phase difference between the two decays

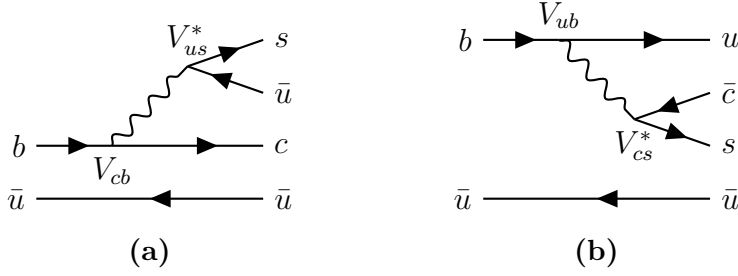


Figure 1.3: Tree level Feynman diagrams describing (a) $B^- \rightarrow D^0 K^-$ and (b) $B^- \rightarrow \bar{D}^0 K^-$ decays. The electro-weak phase difference between the two decays is $\Delta\phi = \arg(V_{cb}V_{us}^*/V_{ub}V_{cs}^*) \simeq \gamma$.

is $\Delta\phi = \arg(V_{cb}V_{us}^*/V_{ub}V_{cs}^*)$. While $\Delta\phi$ is not identical to the definition of γ in Eq. (1.10), the ratio of the involved CKM matrix elements is [42]

$$\begin{aligned} -\frac{V_{cd}^*/V_{ud}^*}{V_{us}^*/V_{cs}^*} &= -\frac{-\lambda[1 - \frac{\lambda^4}{2}A^2(1 - 2(\rho - i\eta))](1 - \frac{\lambda^2}{2} - \frac{\lambda^4}{8}(1 + 4A^2))}{\lambda(1 - \frac{\lambda^2}{2} - \frac{\lambda^4}{4})} \\ &= 1 - \lambda^4 A^2(1 - 2(\rho - i\eta)) + \mathcal{O}(\lambda^5). \end{aligned} \quad (1.11)$$

The ratio equals unity to $\mathcal{O}(\lambda^4) \simeq 2.6 \times 10^{-3}$, and thus $\Delta\phi \simeq \gamma$ is a good approximation within current experimental uncertainties. For the remainder of this thesis the approximation will be used without further comment. The diagrams in Fig. 1.3 describe the leading order contributions to the two amplitudes

$$\begin{aligned} A[B^- \rightarrow D^0 K^-] &\equiv A_B \\ A[B^- \rightarrow \bar{D}^0 K^-] &\equiv \bar{A}_B \equiv r_B A_B e^{i(\delta_B - \gamma)}, \end{aligned} \quad (1.12a)$$

where the last equality introduces two new parameters: the amplitude magnitude ratio $r_B \equiv |\bar{A}_B|/|A_B|$, and δ_B , the strong-phase difference between the decay amplitudes. Since all CP -violation is attributed to the electro-weak phase in the SM, the CP -conjugate decay amplitudes are [43]

$$\begin{aligned} A[B^+ \rightarrow \bar{D}^0 K^+] &= A_B \\ A[B^+ \rightarrow D^0 K^+] &= \bar{A}_B = r_B A_B e^{i(\delta_B + \gamma)}. \end{aligned} \quad (1.12b)$$

In an experimental setting, the D^0 and \bar{D}^0 mesons are reconstructed in some final state, f or its CP -conjugate \bar{f} . In analogy with the B^\pm decays, the D decay amplitude can be related⁴

$$\begin{aligned} A[D^0 \rightarrow f] &= A[\bar{D}^0 \rightarrow \bar{f}] = A_D \\ A[\bar{D}^0 \rightarrow f] &= A[D^0 \rightarrow \bar{f}] = r_D A_D e^{i\delta_D}. \end{aligned} \quad (1.13)$$

⁴In this notation δ_D is thus phase of the suppressed D -decay amplitude minus the phase of the favoured D -decay amplitude. This is the opposite convention to that used in the LHCb measurements with the ADS technique, but aligns with the notation used in the literature on γ measurements in $D \rightarrow K_S^0 \pi^+ \pi^-$ decays.

where the assumption has been made that CP violation in the D decays is negligible, and δ_D denotes a CP -conserving strong-phase difference. While CP -violation in D decays has recently been measured [21], the size of the effect is small and it is considered negligible in this thesis. Based on Eqs. 1.12 and (1.13), the decay rates of B^+ and B^- mesons into the possible final states can be seen to satisfy

$$\Gamma(B^- \rightarrow D(\rightarrow f)K^-) \propto 1 + r_D^2 r_B^2 + 2r_B r_D \cos [\delta_B + \delta_D - \gamma], \quad (1.14a)$$

$$\Gamma(B^+ \rightarrow D(\rightarrow \bar{f})K^+) \propto 1 + r_D^2 r_B^2 + 2r_B r_D \cos [\delta_B + \delta_D + \gamma], \quad (1.14b)$$

$$\Gamma(B^- \rightarrow D(\rightarrow \bar{f})K^-) \propto r_D^2 + r_B^2 + 2r_B r_D \cos [\delta_B - \delta_D - \gamma], \quad (1.14c)$$

$$\Gamma(B^+ \rightarrow D(\rightarrow f)K^+) \propto r_D^2 + r_B^2 + 2r_B r_D \cos [\delta_B - \delta_D + \gamma]. \quad (1.14d)$$

The processes in Eqs. (1.14a) and (1.14b) are CP -conjugate and it is clear how, in the general case where $\delta_B + \delta_D \neq 0$, a non-zero value of γ leads to CP violation in the form of differing decay rates. The same is true for the processes in Eqs. (1.14c) and (1.14d). Depending on the choice of D final state, these expressions can be used to relate γ to various observables that are experimentally accessible. This thesis concerns the choice $f = K_S^0 \pi^+ \pi^-$ or $f = K_S^0 K^+ K^-$, where the terms related to the D decay all have a non-trivial variation over the phase space of the decay. However, it is useful to first analyse the simpler case where f is a two-body state.

The simplest case is when f is chosen to be a CP eigenstate, so that $f = \pm \bar{f}$ and the rate equations of (1.14a)–(1.14d) simplify, because $r_D = 1$ and $\delta_D \in \{0, \pi\}$. Measurements of γ in such decay modes are denoted GLW measurements, after Gronau, London, and Wyler who described the approach in the early 90ies [43, 44]. Experimentally it is preferable to measure yield ratios rather than absolute rates, and the observables of interest are thus the CP asymmetry

$$\begin{aligned} A_{CP=\pm 1} &= \frac{\Gamma[B^- \rightarrow D_{CP} K^-] - \Gamma[B^+ \rightarrow D_{CP} K^+]}{\Gamma[B^- \rightarrow D_{CP} K^-] + \Gamma[B^+ \rightarrow D_{CP} K^+]} \\ &= \frac{\pm r_B \sin \delta_B \sin \gamma}{1 + r_B^2 \pm 2r_B \cos \delta_B \cos \gamma}, \end{aligned} \quad (1.15a)$$

as well as the ratio

$$\begin{aligned} R_{CP=\pm 1} &= 2 \frac{\Gamma[B^- \rightarrow D_{CP} K^-] + \Gamma[B^+ \rightarrow D_{CP} K^+]}{\Gamma[B^- \rightarrow D^0 K^-] + \Gamma[B^+ \rightarrow \bar{D}^0 K^+]} \\ &= 1 + r_B^2 \pm 2r_B \cos \delta_B \cos \gamma. \end{aligned} \quad (1.15b)$$

In practice, A_{CP} and R_{CP} are obtained from measured yield ratios that are corrected with appropriate branching fractions. A measurement of A_{CP} and R_{CP} alone is not sufficient to determine the underlying physics parameters (γ, r_B, δ_B) , and this is not solely due to the number of parameters exceeding the number of constraints:

the equations also allow for multiple, ambiguous solutions for (γ, δ_B) . One way to break the ambiguity, first noted in the original paper [43], is to make further measurements in additional B decays. These can be described with the formalism described above, but will not share the same ambiguous solutions because (r_B, δ_B) are unique to a given B decay. Another method is to analyse D decay final states that are not CP eigenstates.

A few years later, Atwood, Dunietz, and Sonis analysed an alternative choice of D final states: a simultaneous analysis of a Cabibbo-favoured (CF) decay $D^0 \rightarrow f$ and the doubly-Cabibbo-suppressed (DCS) decay $D^0 \rightarrow \bar{f}$ into the CP conjugate final state [45, 46]. Their suggested method is named the ADS method after the authors. The classical example is to take $f = K^-\pi^+$ and $\bar{f} = \pi^-K^+$. The relative suppression means that the r_D of Eq. (1.14) is small, typically of the same order of magnitude as r_B , and thus the CP asymmetry of the suppressed decay is $\mathcal{O}(1)$:

$$\begin{aligned} A_{ADS(\bar{f})} &= \frac{\Gamma[B^- \rightarrow D(\rightarrow \bar{f})K^-] - \Gamma[B^+ \rightarrow D(\rightarrow f)K^+]}{\Gamma[B^- \rightarrow D(\rightarrow \bar{f})K^-] + \Gamma[B^+ \rightarrow D(\rightarrow f)K^+]} \\ &= \frac{r_D r_B \sin(\delta_B - \delta_D) \sin \gamma}{r_D^2 + r_B^2 + 2r_D r_B \cos(\delta_B - \delta_D) \cos \gamma}. \end{aligned} \quad (1.16a)$$

The large CP asymmetry is a prime feature of the ADS method. However, also the suppressed-to-favoured yield ratio is sensitive to the physics parameters of interest:

$$\begin{aligned} R_{ADS(\bar{f})} &= \frac{\Gamma[B^- \rightarrow D(\rightarrow \bar{f})K^-] + \Gamma[B^+ \rightarrow D(\rightarrow f)K^+]}{\Gamma[B^- \rightarrow D(\rightarrow f)K^-] + \Gamma[B^+ \rightarrow D(\rightarrow \bar{f})K^+]} \\ &= \frac{r_B^2 + r_D^2 + 2r_D r_B \cos(\delta_B - \delta_D) \cos \gamma}{1 + r_D^2 r_B^2 + 2r_D r_B \cos(\delta_B + \delta_D) \cos \gamma}. \end{aligned} \quad (1.16b)$$

The interpretation of A_{ADS} and R_{ADS} in terms of (γ, r_B, δ_B) requires knowledge of the r_D and δ_D parameters, but these can be measured independently. In general, the constraints from a single set of ADS observables suffer the same ambiguities as in the GLW case. However, unlike the GLW case, each D decay mode provides an independent set of constraints, because the parameters related to the D decay vary.

The discussion of this section has centred on the classical case of $B^\pm \rightarrow DK^\pm$ decays with a two-body D final state. With minor modifications the techniques have been used to make measurements of γ in B^0 decays [?], with B decay final states including excited D mesons [?], excited kaons [?], or pions [?]. The decay $B^\pm \rightarrow D\pi^\pm$ also is also CP -violating, although the effect is much smaller than in the $B^\pm \rightarrow DK^\pm$ decay, because it is expected that $r_B^{D\pi^\pm} \simeq 0.005$ [47], whereas $r_B^{DK^\pm} \simeq 0.1$. Furthermore, it is possible to use multi-body D final states. However, in some cases, a better precision can then be obtained by exploiting phase-space dependent decay rates. This is the topic of the next section.

367 1.3 Measuring γ using multi-body D final states

368 In multi-body D decays, the r_D and δ_D parameters of the fundamental rate equations
 369 in Eq. (1.14) vary over the phase space of the D decay. This section describes a
 370 model-independent approach to measure γ in $B \rightarrow D(\rightarrow K_S^0\pi^+\pi^-)h^\pm$ decays by
 371 exploiting this variation. The theory is identical for $D \rightarrow K_S^0K^+K^-$ decays, and
 372 similar ideas have been proposed for the $D \rightarrow K_S^0\pi^+\pi^-\pi^0$ [48] and $D \rightarrow 2\pi^+2\pi^-$
 373 modes [49]. First, however, the formalism for describing amplitudes of multi-
 374 body decays is briefly reviewed.

375 1.3.1 Dalitz plots and the phase space of multi-body decays

376 In general, the phase space of the n -body decay $P \rightarrow p_1 + p_2 + \dots + p_n$ consists of n
 377 four momenta, with a total of $4n$ components. The requirement that each of the final
 378 state particles is on-shell provides n constraints on these components, and energy-
 379 momentum conservation removes a further 4 degrees of freedom. If the original
 380 particle P is a scalar, the decay is isotropic, which removes an additional 3 degrees
 381 of freedom, leaving the total number of degrees of freedom at $3n - 7$. For the specific
 382 case of three-body decays, the available phase space can thus be parameterised with
 383 only two parameters. A practical and often used choice is the invariant masses

$$s_{12} = m^2(p_1 p_2) = (p_1^\mu + p_2^\mu)^2, \quad s_{13} = m^2(p_1 p_3) = (p_1^\mu + p_3^\mu)^2. \quad (1.17)$$

384 The choice of particle pairs is arbitrary, and the coordinates easily related

$$m_P^2 + m_{p_1}^2 + m_{p_2}^2 + m_{p_3}^2 = m^2(p_1 p_2) + m^2(p_1 p_3) + m^2(p_2 p_3). \quad (1.18)$$

385 A scatter plot of (s_{12}, s_{13}) values for a sample of particle decays is denoted a Dalitz
 386 plot [50]. It has the very useful feature that the presence of (narrow) resonances
 387 in the decay leads to visible bands in the scatter plot. Figure 1.4 illustrates how
 388 the limits of the Dalitz plot are defined by kinematic constraints, and shows an
 389 example of a Dalitz plot for $D \rightarrow K_S^0\pi^+\pi^-$ decays in which the $K^*(892)^\pm$ and $\rho(770)$
 390 resonances are clearly visible. The plot shows the sample of $B^+ \rightarrow D\pi^+$ decays
 391 used to make the measurement described in Chapter 4 and thus the D meson is in
 392 a superposition of D^0 and \bar{D}^0 states (as detailed in the following section).

393 In terms of the coordinates of Eq. (1.17) the differential decay rate is given by

$$d\Gamma = \frac{1}{32(2\pi)^3 m_P^3} |\mathcal{M}|^2 ds_{12} ds_{13}, \quad (1.19)$$

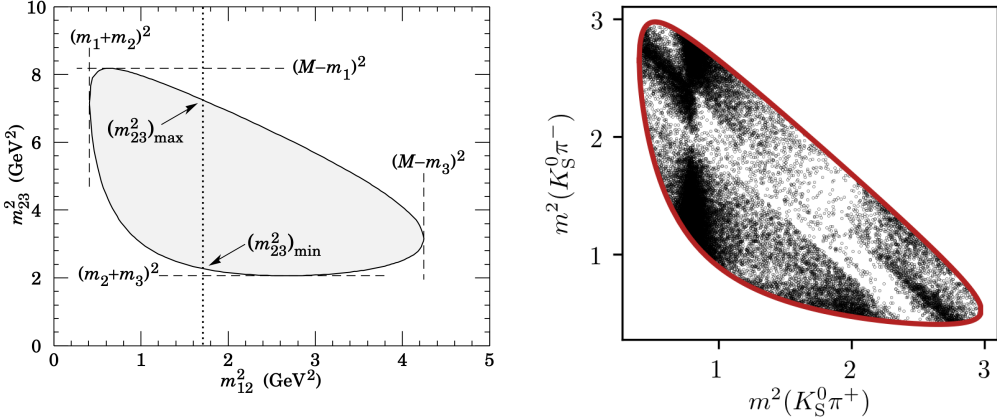


Figure 1.4: (Left) Schematic of a Dalitz plot and the limits of the kinematically allowed phase space limits. (Right) Example of a Dalitz plot for $D \rightarrow K_S^0 \pi^+ \pi^-$ decays where the D meson originates in a $B^+ \rightarrow D \pi^+$ decay; the decaying D meson is in a superposition of the D^0 and \bar{D}^0 states, but predominantly \bar{D}^0 -like.

where \mathcal{M} is the QFT matrix element, or total decay amplitude, corresponding to the decay. In general, it is not possible to calculate \mathcal{M} from first principles. Instead, a model is defined with an empirically well motivated form, in which a number of free parameters must be determined experimentally. The simplest case is that of an *isobar* model, where it is assumed that the full decay can be decomposed into consecutive two-body decays of the form $P \rightarrow R_{12}(\rightarrow p_1 + p_2)p_3$. Thus, \mathcal{M} is expressed as a non-resonant constant amplitude term, k_{NR} , plus a sum of resonance terms

$$\mathcal{M}(s_{12}, s_{13}) = k_{NR} + \sum_r k_r \mathcal{M}^r(s_{12}, s_{13}). \quad (1.20)$$

The exact form of the \mathcal{M}^r function depends on the resonance in question. An overview is given in the PDG review on resonances and references therein [31]. The isobar formalism breaks down when resonances in the decay are not well separated. In this case, models of the form in Eq. (3.27) can still be employed, if the contribution from overlapping resonances are collected in a single term. An example of such a model, is the amplitude model for $D^0 \rightarrow K_S^0 \pi^+ \pi^-$ decays developed by the Belle collaboration for a measurement of the CKM angle β in 2018 [51]. In this model, individual terms are included for $D^0 \rightarrow K^*(\rightarrow K_S^0 \pi^\pm)\pi^\mp$ decays, whereas the $\pi\pi$ and $K\pi$ S -wave contributions are modelled with the so-called K -matrix- and LASS formalisms [52, 53]. The amplitude and phase of \mathcal{M} as predicted by this model are shown in Fig. 1.5.

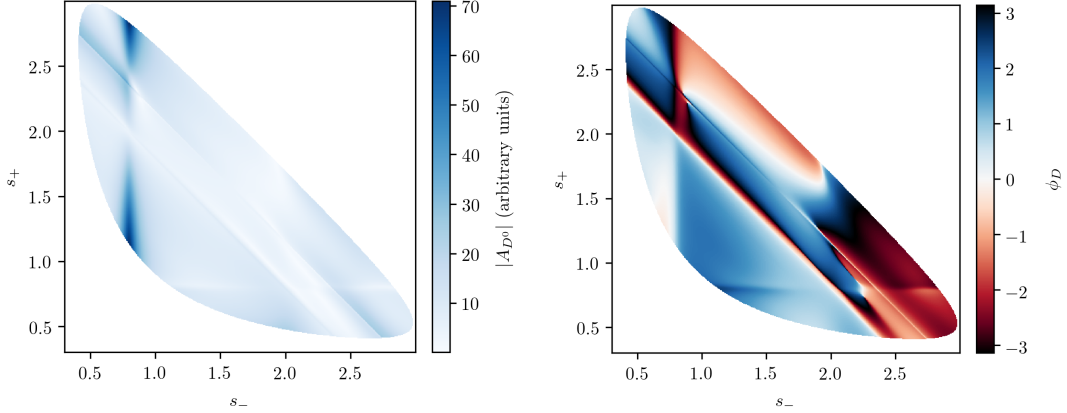


Figure 1.5: The (left) magnitude and (right) phase of the $D \rightarrow K_S^0 \pi^+ \pi^-$ amplitude in the Belle 2018 model [51].

1.3.2 The GGSZ method to measure γ

The non-trivial phase-space dependence of the $D \rightarrow K_S^0 \pi^+ \pi^-$ decay amplitude can be exploited to measure γ with $B^\pm \rightarrow DK^\pm$ or $B^\pm \rightarrow D\pi^\pm$ decays. This approach was proposed independently by Bondar [54], and by Giri, Grossman, Soffer, and Zupan [55] after whom it takes the commonly used acronym GGSZ. For this specific decay s_- and s_+ are used to describe the Dalitz coordinates $m^2(K_S^0 \pi^-)$ and $m^2(K_S^0 \pi^+)$, respectively, and the D decay amplitude is a function of these coordinates

$$A_S^{\bar{D}}(s_-, s_+) = A(\bar{D}^0 \rightarrow K_S^0 \pi^+ \pi^-). \quad (1.21)$$

To a good approximation the K_S^0 meson is a CP eigenstate, meaning that the $K_S^0 \pi^+ \pi^-$ state is self-conjugate. Assuming this approximation to be exact, and that CP violation in the D decay is negligible, the D decay amplitude satisfies the symmetry relation

$$A_S^{\bar{D}}(s_-, s_+) = A_S^D(s_+, s_-). \quad (1.22)$$

The impact of the K_S^0 meson *not* being an exact CP eigenstate is treated in detail in Chapter 3. In order to simplify equations, the short-hand notation

$$(s_{-+}) = (s_-, s_+), \quad (s_{+-}) = (s_+, s_-), \quad (1.23)$$

will be employed for the remainder of the thesis, so that the relation in Eq. (1.22) can be expressed as $A_S^{\bar{D}}(s_{-+}) = A_S^D(s_{+-})$. Thus, the rate equations of Eq. (1.14)

427 for the $D \rightarrow K_S^0\pi^+\pi^-$ decay mode are

$$\begin{aligned} d\Gamma^-(s_{-+}) &\propto |\mathcal{A}_S^-|^2 = |A_B|^2 |A_{K_S^0}|^2 \\ &\times [|A_S^D(s_{-+})|^2 + r_B^2 |A_S^D(s_{+-})|^2 + 2r_B |A_S^D(s_{-+})| |A_S^D(s_{+-})| \\ &\times (\cos[\delta_D(s_{-+})] \cos[\delta_B - \gamma] + \sin[\delta_D(s_{-+})] \sin[\delta_B - \gamma])], \end{aligned} \quad (1.24a)$$

$$\begin{aligned} d\Gamma^+(s_{-+}) &\propto |\mathcal{A}_S^+|^2 = |A_B|^2 |A_{K_S^0}|^2 \\ &\times [|A_S^D(s_{+-})|^2 + r_B^2 |A_S^D(s_{-+})|^2 + 2r_B |A_S^D(s_{-+})| |A_S^D(s_{+-})| \\ &\times (\cos[\delta_D(s_{-+})] \cos[\delta_B + \gamma] - \sin[\delta_D(s_{-+})] \sin[\delta_B + \gamma])]. \end{aligned} \quad (1.24b)$$

428 Here, $\delta_D(s_{-+}) = \phi_D(s_{-+}) - \phi_D(s_{+-}) = -\delta_D(s_{+-})$, where $\phi_D(s_{-+})$ denotes the
 429 complex phase of the $A_S^D(s_{-+})$ amplitude, and a standard trigonometric relation
 430 have been employed to factorise the terms depending on the complex phases of the B
 431 and D decays. It can be seen that in the case where $\gamma = 0$ the B^+ and B^- decay rates
 432 are symmetric if the Dalitz coordinates are exchanged: $\Gamma^+(s_-, s_+) = \Gamma^-(s_+, s_-)$.
 433 The presence of CP violation in the B decay breaks the symmetry. Therefore it is
 434 possible to measure γ (and the nuisance parameters r_B and δ_B) from the phase-space
 435 distribution of $B^\pm \rightarrow D(\rightarrow K_S^0\pi^+\pi^-)K^\pm$ decays, given knowledge of $A_S^D(s_{-+})$.

436 A series of measurements of γ have been made that use amplitude models of the
 437 D decay [56–63]. However, a model-independent approach has been proposed by
 438 Bondar and Poluektov [64, 65] that relies on binning phase-space, in which case the
 439 necessary information on the D decay amplitude can be summarised in a small set
 440 of coefficients that can be measured in a separate experiment. That is the approach
 441 followed in this thesis, and has been used previously by the Belle [66] and LHCb
 442 collaborations [67]. It is described in detail in the following section.

443 Such a model-independent approach is favourable for two reasons. Firstly,
 444 uncertainty estimates related to model inputs and the choice of parameterisation in
 445 an amplitude model are non-trivial, yet would become the leading systematic with
 446 the very high precision expected for γ measurements in the near future. Secondly,
 447 amplitude models are notoriously hard to reproduce, and in a high-precision era it
 448 is favourable that any experiment is easy to reinterpret in various extensions of the
 449 SM. This is a lot easier for an experiment that measures a small set of well-defined
 450 observables, than for an experiment that fits a complicated amplitude model.

451 An alternative model-independent approach has recently been proposed by
 452 Poluektov [68] where the externally measured input on the D -decay phase are
 453 Fourier expansion coefficients, and which therefore avoids binning phase space; this
 454 approach may have the potential to improve the obtainable precision in the future.

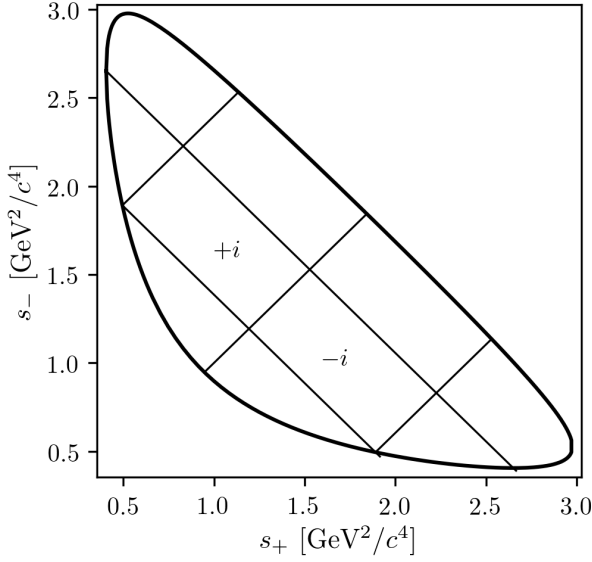


Figure 1.6: Illustration of the binning scheme used in GGSZ measurements: the bins are symmetric around the $m^2(K_S^0\pi^+) = m^2(K_S^0\pi^-)$ diagonal, and numbered so that opposite bins have the same number, but with opposite sign.

1.3.3 A model-independent approach

The phase-space distribution can be analysed in a model-independent way, if the D -decay phase space is split into regions, or bins, and the B decay yield in each bin determined experimentally. A measurement of γ using this approach is the main topic of the thesis. This section describes the fundamental principle, whereas the details pertaining to the exact experimental approach are delegated to Section 1.4.

The amplitude symmetry of Eq. (1.22) is exploited by defining $2N$ bins to be symmetric around the $s_- = s_+$ diagonal of the Dalitz plot, numbered $i = -N$ to N (omitting zero) such that if the point (s_-, s_+) is in bin i , then (s_+, s_-) is in bin $-i$, and by convention $i > 0$ for bins where $s_- > s_+$. The principle is illustrated in Fig. 1.6, but the binning schemes used in actual measurements are more complicated. The decay rates in Eq. (1.24) can be integrated over such bins, and give the bin yields

$$\begin{aligned} N_i^- &\propto h^- \left[K_i + r_B^2 K_{-i} + 2\sqrt{K_i K_{-i}} (c_i x_- + s_i y_-) \right], \\ N_i^+ &\propto h^+ \left[K_{-i} + r_B^2 K_i + 2\sqrt{K_i K_{-i}} (c_i x_+ - s_i y_+) \right], \end{aligned} \quad (1.25)$$

where the parameters describing the B decay have been expressed in terms of the observables

$$x_\pm = r_B \cos(\delta_B \pm \gamma), \quad y_\pm = r_B \sin(\delta_B \pm \gamma), \quad (1.26)$$

⁴⁷⁰ and a number of phase-space integrated quantities related to the D -decay have
⁴⁷¹ been introduced. The K_i parameters denote fractional yield of a flavour-tagged
⁴⁷² D^0 decaying into bin i , defined as

$$K_i = \frac{1}{N_K} \int_i ds^2 |A_S^D(s_{-+})|^2, \quad N_K = \int ds^2 |A_S^D(s_{-+})|^2, \quad (1.27)$$

⁴⁷³ where $\int_i ds^2$ denotes integration over bin i of the Dalitz plot. The c_i and s_i denote
⁴⁷⁴ the amplitude-weighted average of $\cos \delta_D(s_{-+})$ and $\sin \delta_D(s_{-+})$ over bin i

$$\begin{aligned} c_i &= \frac{\int_i ds^2 |A_S^D(s_{-+})| |A_S^D(s_{+-})| \cos[\delta_D(s_{-+})]}{\sqrt{\int_i ds^2 |A_S^D(s_{-+})|^2} \sqrt{\int_i ds^2 |A_S^D(s_{+-})|^2}}, \\ s_i &= \frac{\int_i ds^2 |A_S^D(s_{-+})| |A_S^D(s_{+-})| \sin[\delta_D(s_{-+})]}{\sqrt{\int_i ds^2 |A_S^D(s_{-+})|^2} \sqrt{\int_i ds^2 |A_S^D(s_{+-})|^2}}. \end{aligned} \quad (1.28)$$

⁴⁷⁵ By the symmetry properties of $\delta_D(s_{-+})$ these parameters satisfy $c_i = c_{-i}$ and
⁴⁷⁶ $s_i = -s_{-i}$. The normalisation constants h^+ and h^- are identical in the ideal case,
⁴⁷⁷ but it is convenient to define them separately for practical reasons: depending on
⁴⁷⁸ the experimental setup, there may be overall production and detection asymmetries
⁴⁷⁹ that affect the total signal yields. An experimental analysis can be made insensitive
⁴⁸⁰ to these effects because they can be absorbed into the normalisation constants, as
⁴⁸¹ long as they are constant over the D -decay phase space. This comes at the cost
⁴⁸² that the information on x_\pm and y_\pm from the overall CP asymmetry is lost, but
⁴⁸³ Section 1.3.5 will show the loss in precision to be minimal.

⁴⁸⁴ Thus, for a set of $2N$ bins, the bin yields of Eqs. (1.25) provide $4N$ constraints
⁴⁸⁵ on a total of $4N + 6$ parameters: $(h^\pm, K_i, c_i, s_i, x_\pm, y_\pm)$. However, the K_i , c_i , and
⁴⁸⁶ s_i parameters relate only to the D decay, and can thus, in principle, be measured
⁴⁸⁷ in independent experiments. With such external inputs, a measurement of the
⁴⁸⁸ $B^\pm \rightarrow D(\rightarrow K_S^0 \pi^+ \pi^-) K^\pm$ yields in a set of bins can be used to constrain x_\pm and y_\pm ,
⁴⁸⁹ and thereby (γ, r_B, δ_B) . The measurement presented in this thesis determines the
⁴⁹⁰ K_i parameters directly, but uses externally measured values of c_i and s_i as input,
⁴⁹¹ as measured in quantum correlated D decays by the CLEO [69] and BESIII [70]
⁴⁹² collaborations. Because these measurements are the foundation of the approach,
⁴⁹³ they are described in some detail in the following section. In the future, it is possible
⁴⁹⁴ that the c_i and s_i parameters may be measured in quantum-correlated D decays
⁴⁹⁵ in LHCb [71], and in charm-mixing measurements [72].

496 1.3.4 Measuring strong-phase inputs at charm factories

497 The strong-phase parameters c_i and s_i have been measured by the CLEO and
 498 BESIII collaborations, using quantum correlated $D^0\bar{D}^0$ pairs from decays of the
 499 $\psi(3770)$ resonance state, itself produced in e^+e^- collisions at the resonance energy.
 500 The $\psi(3770)$ has quantum-number $C = -1$, which is conserved in the strong decay
 501 into two D mesons, and thus the two D mesons are produced in an anti-symmetric
 502 wave function. By observing the decay of one D meson into a specific final state,
 503 say a CP eigenstate, the quantum state of the other D meson can be determined.
 504 The measurement is based on decays where both D decays are reconstructed, one
 505 in the $K_S^0\pi^+\pi^-$ final state, the other in one of several different tag categories.
 506 The main principles are outlined below, but most experimental considerations and
 507 implementation details are left out for the sake of brevity.

508 The simplest case is when one D meson decays into a final state that uniquely
 509 tags the flavour, such as $\bar{D}^0 \rightarrow K^+e^-\bar{\nu}_e$. In that case, the D meson decaying to
 510 $K_S^0\pi^+\pi^-$ is known to be in the D^0 state and the decay rate is simply determined by
 511 $A_S^D : \Gamma(s_{-+}) \propto |A_S^D(s_{-+})|^2$. This allows for a measurement of the K_i parameters.

512 If one D meson is reconstructed in a CP -even state, eg. K^+K^- , or a CP -odd
 513 state, eg. $K_S^0\pi^0$, the D meson decaying to $K_S^0\pi^+\pi^-$ is known to be in a state of
 514 opposite CP . Thus, for a tag-decay of $CP = \pm 1$ the decay rate has the form

$$\Gamma_{CP=\pm 1} \propto |A_S^D(s_{-+}) \mp A_S^D(s_{+-})|^2 \quad (1.29a)$$

515 and the bin yields will be given by

$$M_i^\pm \propto K_i + K_{-i} \mp 2\sqrt{K_i K_{-i}} c_i. \quad (1.29b)$$

516 Thus a simultaneous analysis of flavour and CP tagged decays allow for a deter-
 517 mination of the K_i and c_i parameter sets.

518 Finally, the case where both D mesons, for now denoted D and D' , decay into
 519 the $K_S^0\pi\pi$ final state can be considered. The total amplitudes have contributions
 520 from the case where D is in the D^0 state and D' is in the \bar{D}^0 state, as well as the
 521 opposite flavour assignment. Thus the decay rate satisfies

$$\Gamma_{CP=\pm 1} \propto |A_S^D(s_{-+})A_S^D(s'_{+-}) + A_S^D(s_{+-})A_S^D(s'_{-+})|^2 \quad (1.30a)$$

522 where s_{-+} denotes the Dalitz-plot coordinates of the D meson, and s'_{-+} those of
 523 the D' meson. Defining M_{ij} to be the yield of decays where the D decay is in
 524 bin i and the D' in bin j , the bin yields satisfy

$$M_{ij} \propto K_i K_{-j} + K_j K_{-i} - 2\sqrt{K_i K_{-i} K_j K_{-j}} (c_i c_j + s_i s_j). \quad (1.30b)$$

525 Thus, analysing these decays in addition to the CP and flavour tagged decays provide
 526 information on all of K_i , c_i , and s_i . Note, however, that Eqs. (1.29) and (1.30) are
 527 invariant under the transformation $\delta_D \rightarrow -\delta_D$. In practice, the analysis is extended
 528 in a number of ways to enhance the statistics: using "flavour-tag" states that are not
 529 exact flavour tags, such as $K^-\pi^+$, using self-conjugate multi-body D -decay final
 530 states that are not exact CP eigenstates, such as $\pi^+\pi^-\pi^0$, and using the $K_L^0\pi^+\pi^-$
 531 final state as well. However, the main principles are the same as described above.

532 The measurements of c_i and s_i are made for a range of different binning schemes.
 533 It was noted already in Ref. [65] that a rectangular binning scheme, such as the
 534 example in Fig. 1.6, does not provide the optimal sensitivity to γ . A better sensitivity
 535 can be obtained if the bins are defined such that δ_D is approximately constant over
 536 a given bin, by defining bin i out of N via the condition

$$\text{bin}_i = \{(s_-, s_+) \mid 2\pi(i - 3/2)/N < \delta_D(s_-, s_+) < 2\pi \times (i - 1/2)/N\}. \quad (1.31)$$

537 In practice, the binning scheme is defined by splitting the D -decay phase-space
 538 into quadratic *micro bins* with a width of $0.0054 \text{ (GeV}/c^2)^2$ and assigning a bin
 539 number to each micro bin via the condition in (1.31) as evaluated in an amplitude
 540 model of choice. The obtained binning scheme when using an amplitude model
 541 developed by the BaBar collaboration in 2008 [57] is shown in Fig. 1.7a. In Ref [65]
 542 it was also shown that the binning can be even further optimised for sensitivity.
 543 The suggested figure of merit is

$$Q^2 = \frac{\sum_i \left(\frac{1}{\sqrt{N_i^B}} \frac{dN_i^B}{dx} \right)^2 + \left(\frac{1}{\sqrt{N_i^B}} \frac{dN_i^B}{dy} \right)^2}{\int ds^2 \left[\left(\frac{1}{|\Gamma^B(s_-)|} \frac{d|\Gamma^B(s_-)|^2}{dx} \right)^2 + \left(\frac{1}{|\Gamma^B(s_-)|} \frac{d|\Gamma^B(s_-)|^2}{dy} \right)^2 \right]} \quad (1.32)$$

544 which quantifies the statistical sensitivity for a given binning, relative to the one
 545 achievable in an unbinned analysis. The CLEO collaboration defined an *optimal*
 546 binning scheme by an iterative procedure where, starting from the equal binning
 547 scheme, a micro-bin is randomly reassigned new bin numbers in each step, and a
 548 step accepted if Q^2 increases. The optimisation is done for the case where $x = y = 0$
 549 and thus Q^2 simplifies to $Q_{x=y=0}^2 = \sum_i N_i^{x=y=0} (c_i^2 + s_i^2) / N_{total}^{x=y=0}$. The resulting
 550 binning scheme is shown in Fig. 1.7b. An additional binning scheme is defined,
 551 denoted the *modified optimal* scheme and shown in Fig. 1.7c, where the Q^2 figure
 552 of merit is modified to take into account the presence of backgrounds [69]. The
 553 modified optimal binning scheme has proven beneficial to use in measurements with
 554 small signal yields [], but is not employed in the present thesis.

Table 1.1: The experimentally measured c_i and s_i values used in the thesis. The $D \rightarrow K_S^0\pi^+\pi^-$ values are the combined values from the BESIII and CLEO measurements published by BESIII [70]. The $D \rightarrow K_S^0K^+K^-$ values are measured by CLEO [69].

Optimal binning scheme: $D \rightarrow K_S^0\pi^+\pi^-$		
Bin i	c_i	s_i
1	-0.037 ± 0.049	0.829 ± 0.097
2	0.837 ± 0.067	0.286 ± 0.152
3	0.147 ± 0.066	0.786 ± 0.154
4	-0.905 ± 0.021	0.079 ± 0.059
5	-0.291 ± 0.041	-1.022 ± 0.062
6	0.272 ± 0.082	-0.977 ± 0.176
7	0.918 ± 0.017	-0.184 ± 0.065
8	0.773 ± 0.033	0.277 ± 0.118

2-bins binning scheme: $D \rightarrow K_S^0K^+K^-$		
Bin i	c_i	s_i
1	0.818 ± 0.107	-0.445 ± 0.215
2	-0.746 ± 0.083	-0.229 ± 0.220

Both the CLEO and BESIII collaborations have measured the values of c_i and s_i for the equal, optimal, and modified optimal binning schemes. The results are also shown in Fig. 1.7, where they are compared to the expectation from the latest amplitude model [51]. The measurements presented in this thesis are based on a combination of the BESIII and CLEO results for the optimal binning scheme, made by the BESIII collaboration [70] and tabulated in Table 1.1.

While the *definition* and *optimisation* of these binning schemes depend on knowledge of $A_S^D(s_-, s_+)$ via an amplitude model, it is important to note that no model information is needed when the binning schemes are used in the subsequent measurements of strong-phases⁵ or CP -observables. Therefore the measurements will not be biased by any modelling imperfections, although the obtained precision might be lower than expected.

The preceding discussion has been focusing on the $D \rightarrow K_S^0\pi^+\pi^-$ channel, however the $D \rightarrow K_S^0K^+K^-$ channel can be analysed completely analogously. The CLEO collaboration measure c_i and s_i values for this mode as well, in three binning schemes [69]. These are all equal-phase binning schemes, with 2, 3, and 4 bins,

⁵With the exception of minimal model-dependence introduced when the $K_L^0\pi^+\pi^-$ final state is employed to constrain the s_i parameters by the D -factories [69, 70], the impact of which is well under control.

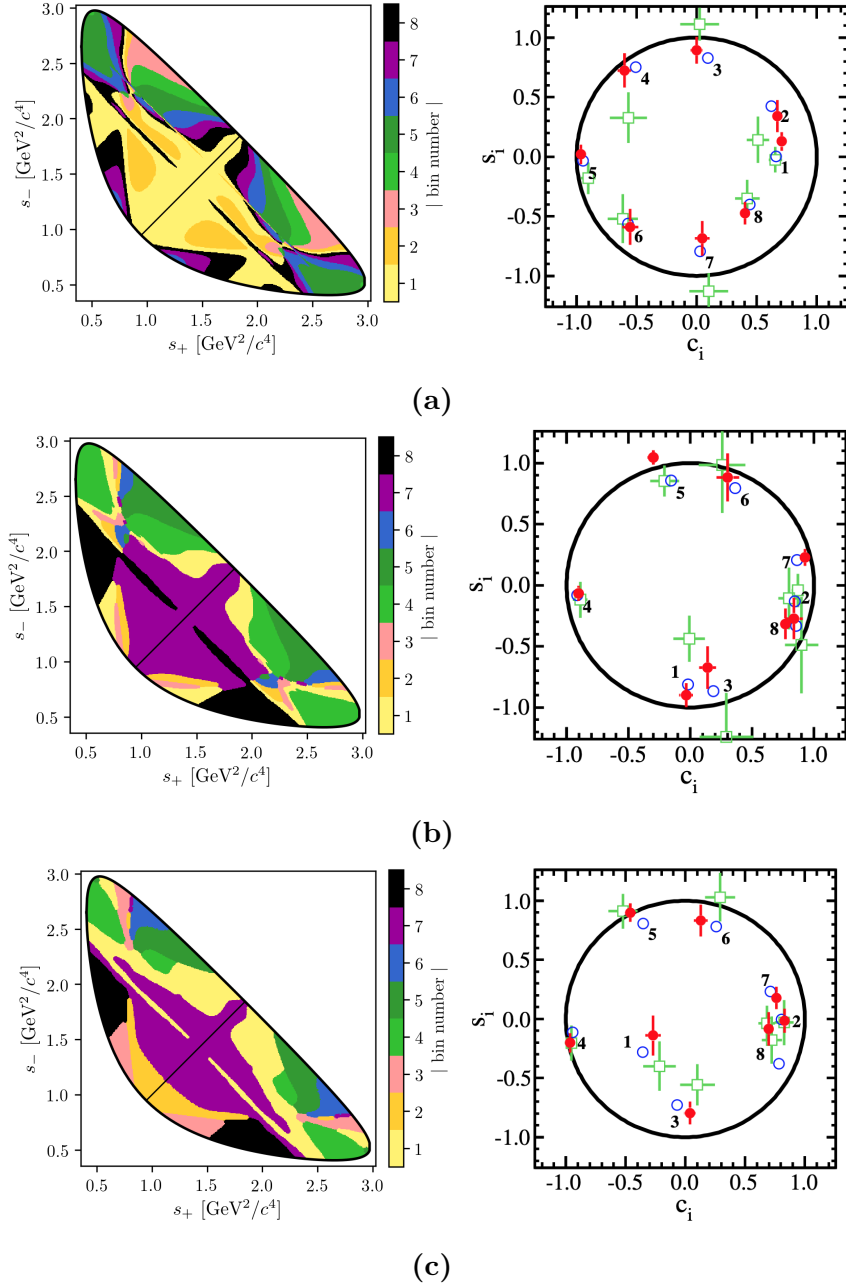


Figure 1.7: The (left) binning schemes and (right) measured values of (c_i, s_i) for (a) equal, (b) optimal, and (c) modified optimal binning schemes for $D \rightarrow K_S^0 \pi^+ \pi^-$ decays. The plots of the measured values are taken from Ref. [70] and show the results obtained by (red) BESIII, (green) CLEO, and (blue) the model expectation using the model from Ref. [51]. The measurement featured in this thesis used the optimal binning scheme.

respectively, shown in Fig. 1.8. The $D \rightarrow K_S^0 K^+ K^-$ decay amplitude is almost completely dominated by two $K^+ K^-$ resonances, the CP -odd $\phi(1020)$ and the CP -even $a_0(980)$, and this means that very little gain in sensitivity can be made by altering the equal-phase binning schemes. The measured c_i and s_i values are also shown in Fig. 1.8 and tabulated in Table 1.1 for the 2-bins scheme, which is used in this thesis. A BESIII measurement is in preparation, but has not been finished at the time of writing.

1.3.5 Global CP asymmetry and the relation to GLW and ADS measurements

The introduction of separate normalisation factors h^+ and h^- in Eq. (1.25) hides the fact that information on γ (in principle) can be obtained from the asymmetry in phase-space-integrated B^+ and B^- yields. In the ideal case where $h^- = h^+$ the total yield asymmetry is

$$\begin{aligned} A_{GGSZ} &= \frac{\sum_i N_- - N_i^+}{\sum_{i=-N}^N N_i - +N_i^+} = \frac{\sum_{i=-N}^N \sqrt{K_i K_{-i}} c_i (x_- - x_+)}{1 + r_B^2 + 2 \sum_{i=-N}^N \sqrt{K_i K_{-i}} c_i (x_- + x_+)} \\ &= \frac{2 \sum_{i=1}^N \sqrt{K_i K_{-i}} c_i (x_- - x_+)}{1 + r_B^2 + 4 \sum_{i=1}^N \sqrt{K_i K_{-i}} c_i (x_- + x_+)}, \end{aligned} \quad (1.33)$$

where it has been exploited that $\sum_{i=-N}^N \sqrt{K_i K_{-i}} s_i = 0$ by definition. The size of the asymmetry is governed by the factor $\sum_{i=1}^N \sqrt{K_i K_{-i}} c_i$, which is small for $D \rightarrow K_S^0 \pi^+ \pi^-$ and $D \rightarrow K_S^0 K^+ K^-$ decays. The underlying reason is that $\delta_D(s_-, s_+)$ varies significantly across phase-space for these decays, as evident by the spread in the values of c_i in Table 1.1, which reduces the *average* of the asymmetry-generating $D^0 - \bar{D}^0$ interference term to being close to zero. The value of $\sum_{i=-N}^N \sqrt{K_i K_{-i}} c_i$ is closely related to the CP content of the final state in question: for a self-conjugate CP even (odd) final state

$$A_{D^0}(s_-, s_+) = {}^{(+)}_{(-)} A_{\bar{D}^0}(s_-, s_+) = {}^{(+)}_{(-)} A_{D^0}(s_+, s_-) \quad (1.34)$$

and thus $\sum_{i=1}^N \sqrt{K_i K_{-i}} c_i = {}^{(+)}_{(-)} 1$. This motivates the definition of the CP -even fraction of the decay

$$\mathcal{F}_+ \equiv \frac{1}{2} \left(1 + \sum_{i=1}^N \sqrt{K_i K_{-i}} c_i \right). \quad (1.35)$$

With \mathcal{F}_+ in hand, the asymmetry in Eq. (1.33) can be rewritten

$$A_{GGSZ} = \frac{(2\mathcal{F}_+ - 1)r_B \sin \delta_B \sin \gamma}{1 + r_B^2(2\mathcal{F}_+ - 1)2r_B \cos \delta_B \cos \gamma}, \quad (1.36)$$

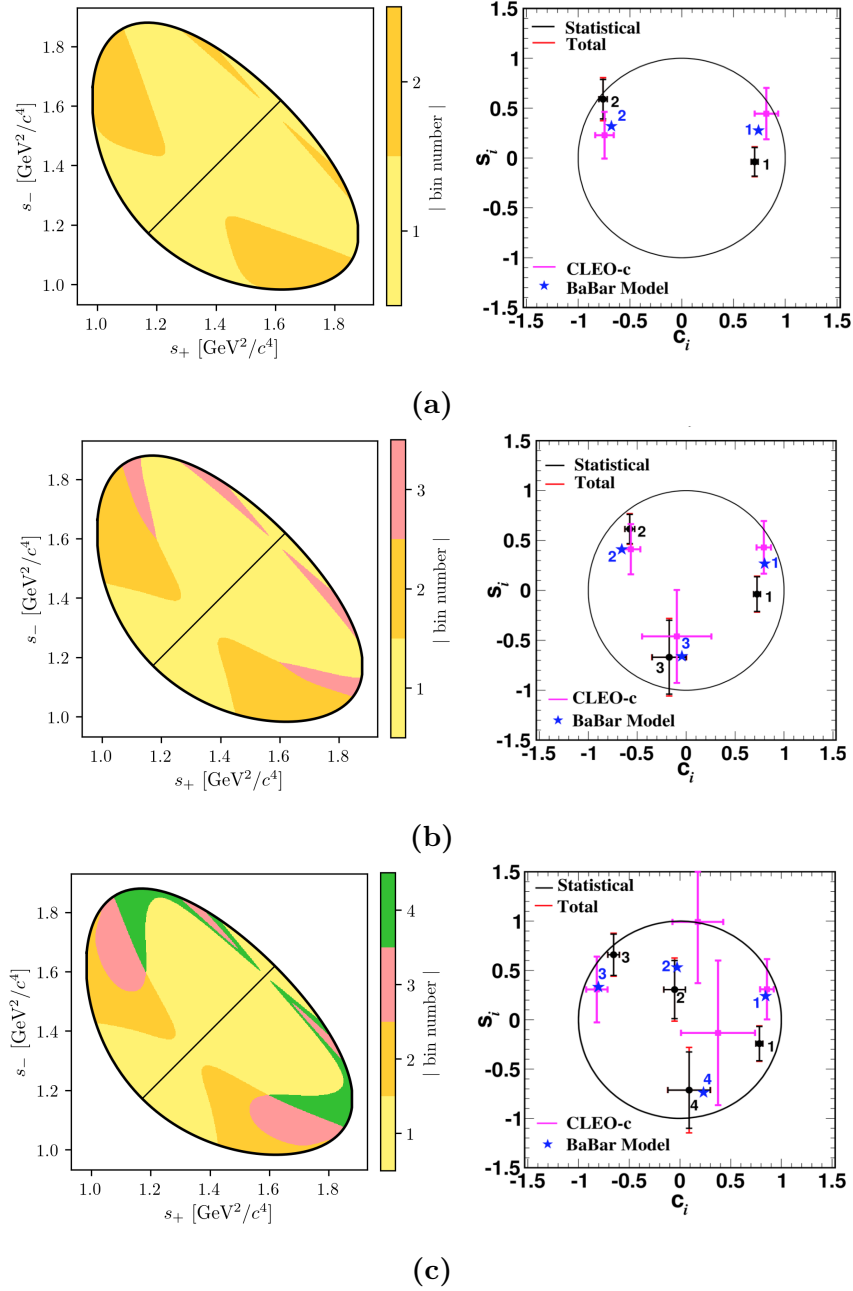


Figure 1.8: The (left) binning schemes and (right) measured values of (c_i, s_i) for the (a) 2-, (b) 3-, and (c) 4-bins binning schemes for $D \rightarrow K_0^0 K^+ K^-$ decays. The plots of the measured values are taken from Ref. [73] and show the (error bars) results obtained by (black) BESIII, (pink) CLEO, and (blue) the model expectation using the model from Ref. [58]. The measurement featured in this thesis uses the 2-bins scheme.

which is the usual form used in quasi-GLW measurements []; for $N = 1$ the definition in Eq. (1.35) is equivalent to \mathcal{F}_+ as defined in Ref. []. The value of \mathcal{F}_+ is independent of the number and shape of bins in a given binning scheme, as long as the bin definitions follow the symmetry principles outlined in Section 1.3.3. For $D \rightarrow K_S^0\pi^+\pi^-$ and $D \rightarrow K_S^0K^+K^-$ decays the values of \mathcal{F}_+ are

$$\begin{aligned}\mathcal{F}_+(K_S^0\pi^+\pi^-) &= X? \\ \mathcal{F}_+(K_S^0K^+K^-) &= X?\end{aligned}\tag{1.37}$$

as evaluated with the Belle 2018 model for $D \rightarrow K_S^0\pi^+\pi^-$ decays and the BaBar 2010 model for $D \rightarrow K_S^0K^+K^-$ decays. Since $r_B^{DK^\pm} \sim 0.1$ the predicted global asymmetries are thus approximately 1–2 %, which is not resolvable with the current experimental yields. As shown in Chapter 3, CP violation in the K_S^0 sector leads to asymmetries of a similar size, further complicating the use of global asymmetries to constrain x_\pm and y_\pm . Thus these modes are ill-suited for quasi-GLW measurements, and ignoring global asymmetries leads to a negligible loss of information on γ in a GGSZ measurement. The reverse is true for a well-suited quasi-GLW mode, such as $D \rightarrow \pi^+\pi^-\pi^0$: if \mathcal{F}_+ is close to either zero or unity, it means that (c_i, s_i) will be close to $(\pm 1, 0)$ in all bins for *any* given binning scheme, and the set of bins will provide almost identical constraints on x_\pm and y_\pm . Thus, the binning of phase space leads to no significant gain in precision compared to a global analysis.

Indeed, a crucial quality of the GGSZ method, is that exactly because each bin-pair provides independent constraints on x_\pm and y_\pm , the method provides a single solution for (γ, r_B, δ_B) that does not suffer the ambiguities of the ADS and GLW approaches. In order to illustrate this further, it is useful to make one more comparison of the model-independent GGSZ formalism to the ADS and GLW formalisms. If there was no CP symmetry the B^+ yield in bin $+i$ would equal the B^- yield in bin $-i$. Therefore the relevant CP asymmetry for a given Dalitz bin is

$$\begin{aligned}A_{GGSZ}^i &\equiv \frac{N_i^- - N_{-i}^+}{N_i^- + N_{-i}^+} \\ &= \frac{\sqrt{K_i K_{-i}}(c_i(x_- - x_+) + s_i(y_- - y_+))}{K_i + r_B^2 K_{-i} + 2\sqrt{K_i K_{-i}}(c_i(x_- + x_+) + s_i(y_- + y_+)})\end{aligned}\tag{1.38}$$

This expression is identical to the ADS asymmetry in Eq. (1.16a) if the effective D -decay parameters r_D^i and δ_D^i are defined via

$$\kappa_i \cos \delta_D^i \equiv c_i \quad , \quad \kappa_i \sin \delta_D^i \equiv s_i \quad , \quad r_D^i \equiv \sqrt{K_i/K_{-i}},\tag{1.39}$$

and a coherence factor, κ , is included in the interference terms of the ADS expression, as is standard for multi-body D decays []. These parameters allow us to classify

Table 1.2: Classification of the bins used in model-independent GGSZ measurements, in terms of whether the interplay between the D^0 and \bar{D}^0 amplitudes in the bin resemble typical GLW or ADS behaviour. The parameters are calculated using the 2018 Belle model [1] for $D \rightarrow K_S^0\pi^+\pi^-$ decays and the 2010 BaBar model [2] for $D \rightarrow K_S^0K^+K^-$ decays.

Optimal binning scheme: $D \rightarrow K_S^0\pi^+\pi^-$					
Bin i	\hat{r}_D	$\hat{\delta}_D$	\mathcal{F}_+	κ	Bin type
1	0.473	91.9°	48.97 %	0.81	Odd-even
2	0.164	11.1°	63.38 %	0.85	ADS-like
3	0.157	79.4°	52.50 %	0.89	ADS-like
4	0.768	175.3°	5.85 %	0.92	GLW-odd-like
5	0.759	-99.9°	42.84 %	0.87	Odd-even
6	0.223	-64.5°	57.92 %	0.87	ADS-like
7	0.651	-13.3°	89.44 %	0.89	GLW-even-like
8	1.745	21.0°	87.08 %	0.92	GLW-even-like

2-bins binning scheme: $D \rightarrow K_S^0K^+K^-$					
Bin i	\hat{r}_D	$\hat{\delta}_D$	\mathcal{F}_+	κ	Bin type
1	0.816	19.8°	86.14 %	0.78	GLW-even-like
2	0.775	154.5°	16.23 %	0.77	GLW-odd-like

623 a given pair of bins with number $\pm i$ as either *GLW-like*, if δ_D^i is close to 0 or π
 624 and r_D^i is close to unity, or *ADS-like* if $0 < r_D^i \ll 1$. The *CP*-even fraction of the
 625 D -decay can also be defined for a given bin-pair:

$$\mathcal{F}_+^i = \mathcal{F}_+^{-i} \equiv \frac{1}{2} \left(1 + 2c_i \frac{\sqrt{K_i K_{-i}}}{K_i + K_{-i}} \right) = \frac{1}{2} \left(1 + 2c_i \frac{r_D^i}{1 + r_D^i} \right). \quad (1.40)$$

626 A GLW-even-like bin pair will have $\mathcal{F}_+^i \simeq 1$ and a GLW-odd-like bin pair will
 627 have $\mathcal{F}_+^i \simeq 0$.

628 Table 1.2 summarises a classification of the bins for the optimal $D \rightarrow K_S^0\pi^+\pi^-$
 629 binning scheme and the 2-bins $D \rightarrow K_S^0K^+K^-$ binning scheme following these
 630 principles. Two bins are classified as *Odd-even*; in these bins, r_D^i is not particularly
 631 small but \mathcal{F}_+^i is close to 0.5. The name refers to the fact that for these
 632 bins A_{GGSZ}^i , as defined in Eq (1.38), will be positive and A_{GGSZ}^{-i} negative (or vice
 633 versa). The fact that multiple bin types appear for both the $D \rightarrow K_S^0\pi^+\pi^-$ and
 634 $D \rightarrow K_S^0K^+K^-$ modes underline that each mode benefits from being analysed in
 635 the GGSZ formalism, and that the bins provide independent constraints, allowing
 636 for a non-ambiguous solution for (γ, r_B, δ_B) .

1.4 Strategy for the LHCb measurement

The main topic of the thesis is a model-independent GGSZ measurement using $B^\pm \rightarrow DK^\pm$ and $B^\pm \rightarrow D\pi^\pm$ decays, and the two D final states $K_S^0\pi^+\pi^-$ and $K_S^0K^+K^-$. The measurement uses the optimal binning scheme for the $D \rightarrow K_S^0\pi^+\pi^-$ mode, with the combined strong-phase inputs from the BESIII [70] and CLEO [69] collaborations published in Ref. [70]. For the $D \rightarrow K_S^0K^+K^-$ channel, the 2-bins scheme is used with the strong-phase parameters measured by the CLEO collaboration [69]. The details of the analysis are presented in Chapter (4), but the overall strategy and a few extensions of the formalism from the previous sections are given here.

Due to the geometry of the LHCb detector, the signal reconstruction efficiency for $B^\pm \rightarrow D(\rightarrow K_S^0h^+h^-)h'^\pm$ decays varies significantly across the D -decay phase space. Denoting the efficiency profile as $\eta(s_-, s_+)$, the yield equations of Eq. (1.25) are therefore modified slightly

$$\begin{aligned} N_i^- &= h^{B^-} \left[F_i + r_B^2 F_{-i} + 2\sqrt{F_i F_{-i}} (c'_i x_- + s'_i y_-) \right], \\ N_i^+ &= h^{B^+} \left[F_{-i} + r_B^2 F_i + 2\sqrt{F_i F_{-i}} (c'_i x_+ - s'_i y_+) \right], \end{aligned} \quad (1.41)$$

where the phase-space integrated quantities now include the efficiency profile

$$F_i = \frac{1}{N_F} \int ds^2 \eta(s_{-+}) |A_S^D(s_{-+})|^2, \quad N_F = \int ds^2 \eta(s_{-+}) |A_S^D(s_{-+})|^2, \quad (1.42)$$

$$c'_i = \frac{\int_i ds^2 \eta(s_{-+}) |A_S^D(s_{-+})| |A_S^D(s_{-+})| \cos[\delta_D(s_{-+})]}{\sqrt{\int_i ds^2 \eta(s_{-+}) |A_S^D(s_{-+})|^2} \sqrt{\int_i ds^2 \eta(s_{-+}) |A_S^D(s_{-+})|^2}}, \quad (1.43)$$

with an analogous definition of s'_i . At leading order, the strong-phase parameters are unaffected by the non-uniform efficiency, and, in addition, the bin definitions favour bins for which $\cos[\delta_D(s_{-+})]$ and $\sin[\delta_D(s_{-+})]$ take on similar values across each bin. Therefore, the c_i and s_i values reported by the charm factories are used directly in the measurement. The impact on the obtained central values is negligible, as described in detail in Section 4.6 where a systematic uncertainty is assigned.

The F_i are significantly different to the K_i due to the experimental acceptance profile in LHCb. Given external inputs for the strong-phase parameters, it is possible to fit the F_i parameters and x_\pm and y_\pm simultaneously in a fit to the LHCb $B^\pm \rightarrow DK^\pm$ data set, in which case the obtained F_i parameters incorporate the correct acceptance profile correction by construction. However, the obtainable precision for the CP observables measured by this procedure is suboptimal. As

an alternative, the first LHCb measurement [67] made a simultaneous analysis of $B^\pm \rightarrow DK^\pm$ and a much larger sample of $B^\pm \rightarrow D\pi^\pm$ decays; since the F_i parameters relate to the D decay, they can effectively be obtained in the $D\pi^\pm$ sample and shared between the two $B^\pm \rightarrow Dh^\pm$ channels. However, there is CP violation present in the $B^\pm \rightarrow D\pi^\pm$ decays, which led to a dominant systematic uncertainty. Later LHCb measurements [3, 74] instead relied on flavour tagged D mesons from $\bar{B}^0 \rightarrow D^{*+}(\rightarrow D^0\pi^+)\mu^-\bar{\nu}_\mu X$ decays to obtain F_i , where no CP violation is possible. However, due to necessarily different triggering paths and selections, the acceptance profile is not exactly identical between semi-leptonic decays and the $B^\pm \rightarrow Dh^\pm$ decays of interest. An efficiency correction based on simulation was therefore applied to obtain the correct F_i , and in this case, the uncertainty related to the correction constituted the largest systematic uncertainty on the measurement.

Both sources of systematic uncertainty can be avoided by making a simultaneous analysis of $B^\pm \rightarrow DK^\pm$ and $B^\pm \rightarrow D\pi^\pm$ decays, where CP -violating observables are measured in *both* channels and the F_i parameters are shared. It is a reasonable assumption that $F_i^{DK} = F_i^{D\pi}$ to a very good approximation, given the similar kinematics of the decays. The assumption is confirmed using simulated decays in Section 4.2.2, for the candidate selection used in the measurement of the thesis. Effectively, the F_i are determined in the high statistics $B^\pm \rightarrow D\pi^\pm$ channel, but with no systematic effect from CP -violation in that channel, since the CP -violation is incorporated in the yield description.

ADD SECTION ON INFORMATION ON GAMMA FROM DPI AND THE TWO SOLUTIONS IN THE LHCb COMBINATION?!

At the start of the work that lead to this thesis, it was not clear to what degree the measured CP -violating observables in $B^\pm \rightarrow D\pi^\pm$ decays were affected by CP violation in the neutral kaon sector. The impact had been shown to scale as $\mathcal{O}(|\epsilon|/r_B)$ [42], which is negligible for the $B^\pm \rightarrow DK^\pm$ channel but suggests potentially large biases in the $B^\pm \rightarrow D\pi^\pm$ channel, where r_B is 20 times smaller. However, the dedicated analysis presented in Chapter 3 has proved the effect on GGSZ measurements to be in fact be *smaller* than $\mathcal{O}(|\epsilon|/r_B)$ and the simultaneous measurement is indeed viable.

The measurement is performed by making extended maximum-likelihood fits to the m_B spectra of $B \rightarrow D(\rightarrow K_S^0 h^+ h^-)h'^\pm$ candidates split by charge and Dalitz bin. The $B^\pm \rightarrow DK^\pm$ signal yields are parameterised using the expressions in Eq. (1.41) directly, thus obtaining values for x_\pm^{DK} and y_\pm^{DK} directly. The Cartesian CP -violating observables x_\pm and y_\pm are employed because they lead to better statistical behaviour than fits to data where the underlying parameters $(\gamma, r_B^{DK^\pm}, \delta_B^{DK^\pm})$ are

determined [], at the cost of introducing a fourth degree of freedom. With the addition of the $B^\pm \rightarrow D\pi^\pm$ mode as a true signal channel, two new underlying parameters are introduced, $r_B^{D\pi^\pm}$ and $\delta_B^{D\pi^\pm}$. There is a choice to be made, in terms of how to define the observables that are measured directly. One is to introduce an additional set of four observables, $(x_-^{D\pi}, y_-^{D\pi}, x_+^{D\pi}, y_+^{D\pi})$, that are analogous to the $B^\pm \rightarrow DK^\pm$ parameters. As an alternative, it is possible to introduce only two Cartesian parameters [75], by defining

$$\xi_{D\pi^\pm} = \left(\frac{r_B^{D\pi^\pm}}{r_B^{DK^\pm}} \right) \exp[i(\delta_B^{D\pi^\pm} - \delta_B^{DK^\pm})] \quad (1.44a)$$

and letting

$$x_\xi^{D\pi} = \text{Re}[\xi_{D\pi^\pm}] \quad y_\xi^{D\pi} = \text{Im}[\xi_{D\pi^\pm}]. \quad (1.44b)$$

In terms of these parameters, the usual Cartesian x_\pm and y_\pm are given by

$$x_\pm^{D\pi} = x_\xi^{D\pi} x_\pm^{DK} - y_\xi^{D\pi} y_\pm^{DK}, \quad y_\pm^{D\pi} = x_\xi^{D\pi} y_\pm^{DK} + y_\xi^{D\pi} x_\pm^{DK}. \quad (1.45)$$

Using this expression, the $B^\pm \rightarrow D\pi^\pm$ yields can also be defined via Eq. (1.41) in the maximum-likelihood fit. Note that ξ does not depend on γ : all information on CP asymmetries in both the $B^\pm \rightarrow DK^\pm$ and $B^\pm \rightarrow D\pi^\pm$ channels is encoded in x_\pm^{DK} and y_\pm^{DK} . In the thesis, the latter parameterisation is chosen, because it allows for a stable fit for all six x and y parameters and the shared F_i ; the choice is described in much greater detail in Section 4.5.1.

The combined analysis of $B^\pm \rightarrow DK^\pm$ and $B^\pm \rightarrow D\pi^\pm$ decays presents a significant step forward, because it solves the problem of obtaining F_i parameters for the appropriate acceptance profile in a manner that avoids leading systematic uncertainties, and almost all reliance on simulation. This is of great importance, if the large data samples that will be collected by LHCb in the future are to be exploited to their full potential.

2

723

724

The LHCb experiment

725 The LHCb experiment is one of the four large experiments at the Large Hadron
726 Collider (LHC), the World’s most powerful accelerator, able to accelerate protons
727 to record centre-of-mass energies of $\sqrt{s} = 13$ TeV in a 27 km long tunnel underneath
728 Geneva. The LHCb experiment is specifically designed to study the large number
729 of particles containing b or c quarks produced in such collisions, which has led
730 to a number of design decisions that make the LHCb unique among the LHCb
731 experiments. The LHCb is not a solid-angle detector like the other three LHC
732 experiments, CMS, ATLAS, and ALICE, but a single-arm spectrometer, instru-
733 mented in the forward region where the majority of $b\bar{b}$ pairs are produced. During
734 data-taking the experiment is operated at a lower instantaneous luminosity than
735 the other experiments, leading to far fewer pp interactions. This, in combination
736 with a vertex detector located extremely close to the interaction point, allows for
737 excellent resolution in the reconstruction of primary and secondary vertex locations,
738 crucial to many of the central measurements of the experiment. Finally, dedicated
739 particle-identification detectors allow for very efficient separation of hadron species,
740 absolutely crucial to isolate a number important signal decays (including the
741 $B^\pm \rightarrow DK^\pm$ decay studied in the thesis). Each of these features is described in
742 much greater detail in the sections below.

743 During operation of the LHC, bunches of about $\mathcal{O}(10^{11})$ protons are accelerated
744 to the desired centre-of-mass energy in a series of linear and circular accelerators,
745 the final one being the LHC itself. This is illustrated in Fig. 2.1. The bunches
746 remain in the LHC for the duration of a *fill*, typically about 12 hours, where they
747 are made to collide at four distinct locations, the collision points, each home to one

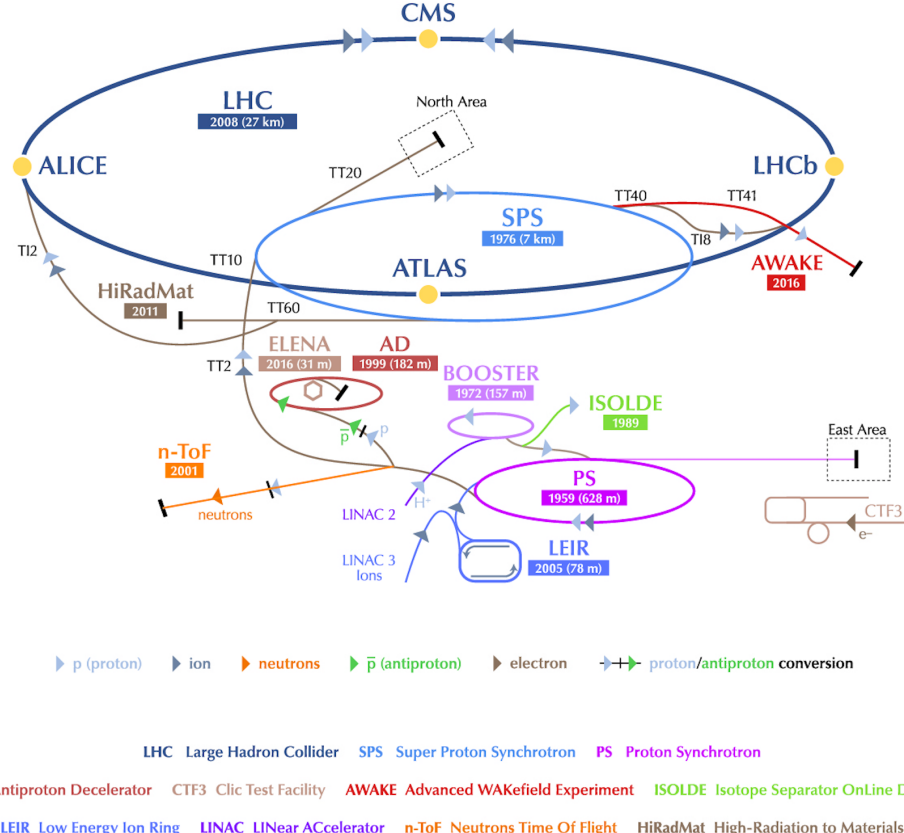


Figure 2.1: The CERN accelerator complex, including the length and construction year for a number of accelerators, not all of which are used in pp operations. During pp operation, the proton acceleration chain is: LINAC 2 → BOOSTER → S → SPS → LHC. The figure is reproduced from Ref. [76].

of the big experiments. The collisions occur with a frequency of up to 40 MHz. A fill ends when the beams are dumped, typically because the average number of protons in the bunches has become too low, after which the whole process begins again.

The LHC has been providing pp collisions during two periods so far: Run 1 during 2011 and 2012, where the centre-of mass energies were $\sqrt{s} = 7 \text{ TeV}$ and 8 TeV respectively, and Run 2 from 2015 to 2018, where $\sqrt{s} = 13 \text{ TeV}$. The instantaneous luminosity at the LHCb collision point has been $4 \times 10^{32} \text{ cm}^{-2} \text{ s}^{-1}$, and has allowed for the collection of data set corresponding to a total of 3 fb^{-1} during Run 1 and 6 fb^{-1} during Run 2. The full data set forms the basis of the thesis. This instantaneous luminosity is significantly lower than at other collision points, for example the peak instantaneous luminosity in the ATLAS detector was about $20 \times 10^{33} \text{ cm}^{-2} \text{ s}^{-1}$ in 2018 [77], about 50 times higher than in LHCb. The lower luminosity is necessary to limit the number of pp interactions per bunch crossing to an average of about 1–1.6, necessary for a vertex reconstruction with the required precision. It is achieved by colliding the proton beams with a traverse off-set at the LHCb collision point.

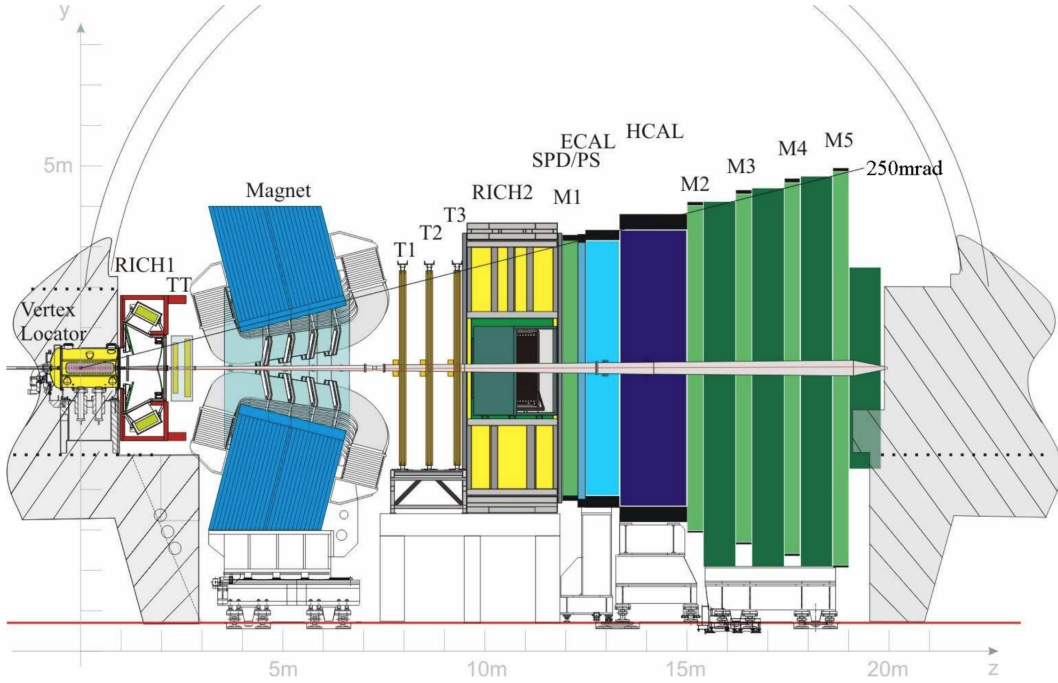


Figure 2.2: Overview of the LHCb detector reproduced from Ref. [78,79]. The individual sub detectors are described in detail in the chapter.

This has the added benefit that the offset can be continuously adjusted during a fill of the LHC, and thus all data can be taken at the same instantaneous luminosity, allowing for simpler trigger configuration, and simpler subsequent analysis because the detector occupancy is constant. The lower luminosity, of course, comes with the downside that the collected data sample is smaller.

2.1 The LHCb subdetectors

The LHCb detector, shown in Fig. 2.2, is able to detect particles in the forward region $\eta \in [2, 5]$, corresponding to an angle θ with respect to the beam line between 15 and 300/250 mrad in the horizontal/vertical direction. As illustrated in Fig. 2.3, the $b\bar{b}$ production cross section is very large within the LHCb acceptance: even though the acceptance covers less than 2% of the solid angle, 24% of all $b\bar{b}$ pairs created at $\sqrt{s} = 14$ TeV are within the acceptance. The detector is described with a coordinate system, where the z -axis is along the beam line and the x (y) axis is in the horizontal (vertical) directions normal to the beam line. The origin is at the collision point. The experiment consists of a number of sub detectors, located in the region from around the interaction point, and up to a distance of $z = 20$ m along the beam line (in the following, the direction from the interaction point towards

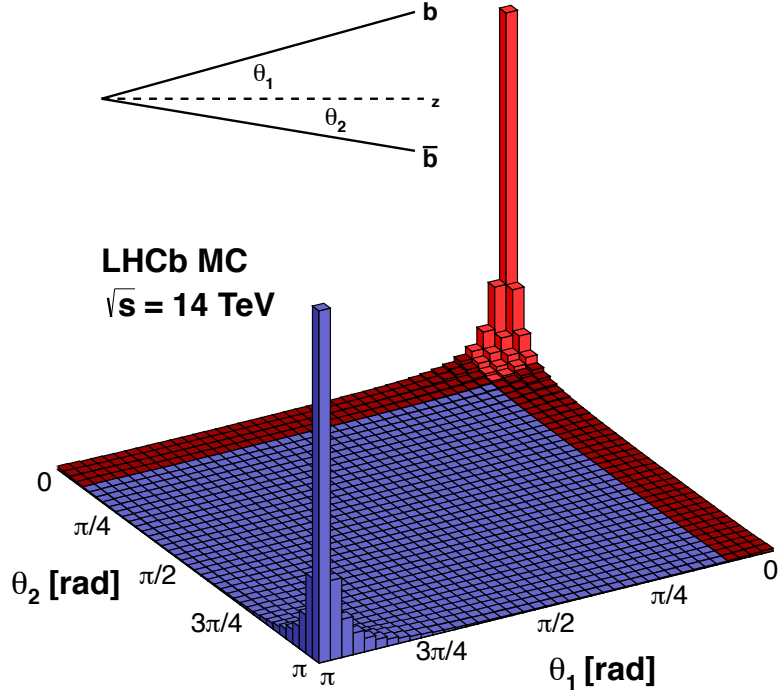


Figure 2.3: Production cross section of $b\bar{b}$ pairs at a centre-of-mass energy of $\sqrt{s} = 14$ TeV, as a function of θ_1 and θ_2 , the angle of the b and \bar{b} quark, respectively, with respect to the beam axis z . The LHCb acceptance is marked in red. The cross-section looks very similar for $\sqrt{s} = 7, 8$ TeV. The figure is taken from Ref. [80].

the sub detectors is denoted *downstream*, and the opposite direction *upstream*). This section describes each of them in detail.

2.1.1 The VELO

The VErtex LOcator (VELO) [81] is a silicon detector located immediately around the collision point, used to provide precise measurements of the particle track coordinates in the interaction region. These are used to reconstruct the production and decay vertices of beauty and charm hadrons with a very high accuracy, allowing for an accurate reconstruction of their life times, and for efficient background rejection. The ability to distinguish tracks originating in secondary vertices also plays a crucial role in efficient triggering, as described further below.

The detector consists of 21 VELO stations positioned along the beam line as illustrated in Fig. 2.4. Each station consists of two *modules*, mounted on each side of the beam line; each module, in turn, consists of two silicon strip detectors, where

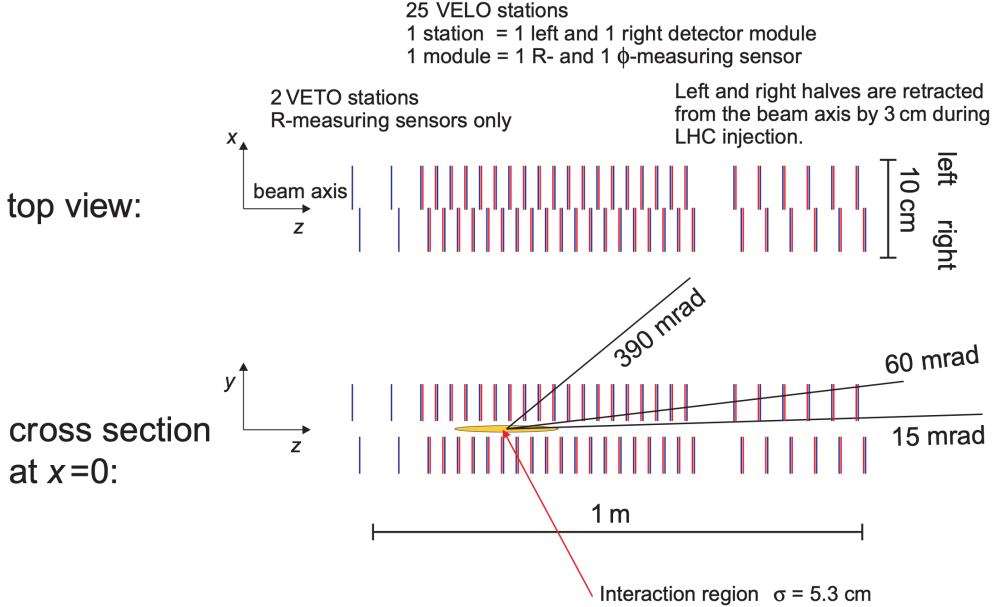


Figure 2.4: Overview of the arrangement of VELO stations from the VELO Technical Design Report (TDR) [81]. The actual detector includes 21 stations instead of 25, but the overall design is identical [82].

the strips are oriented to provide a measurement of r , the radial distance from the beam line, and ϕ , the azimuthal angle, respectively. This is illustrated in Fig. 2.5. The strip pitch varies between 40 and 100 μm depending on the distance from the beam line. The stations are positioned such that all tracks that are within the acceptance region of the downstream detectors and originate at the interaction point are guaranteed to intersect 3 detector segments. During operation, the segments are located only 8 mm from the beam; this is achieved by mounting them on a moving frame that can be retracted during beam commissioning to avoid radiation damage. The detectors are kept in a vacuum, shielded from the beam vacuum by a 0.3 mm thick *RF foil* made of aluminium that also serves to screen the detector from electric fields induced by the proton beam. The silicon sensors were kept at an operating temperature of about -7 $^{\circ}\text{C}$, achieved with a liquid-CO₂ cooling system.

The primary vertex (PV) resolution of the VELO is typically $\sim 10 \mu\text{m}$ in the x and y directions and $\sim 50 \mu\text{m}$ in the z direction, improving with the number of tracks originating at the PV, and deteriorating with the overall number of PVs [82]. The typical uncertainty on the decay length of a B meson is about 230 μm , compared to a typical decay length $O(10)$ mm. The resolution of the *impact parameter*, IP, of a track is well-described by the formula $\sigma_{\text{IP}} = (15 + 29/[p_T/(\text{GeV}/c)]) \mu\text{m}$. This parameter excellently distinguishes particles produced in secondary decays, from those produced in the primary interaction (for which the IP would be zero, were it not for the experimental resolution).

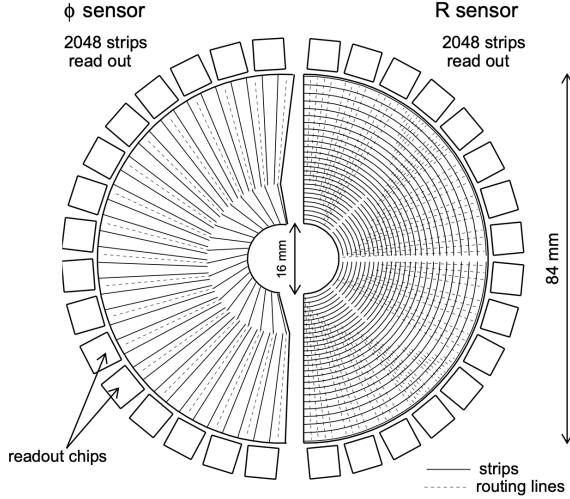


Figure 2.5: Illustration of the silicon strip layout in the VELO modules designed to measure (left) the azimuthal angle, ϕ , of a track, and (right) the radial distance from the beam, r . Reproduced from Ref. [81].

2.1.2 Magnet and tracking stations

The LHCb experiments uses a warm (non-superconducting) dipole magnet to measure the momentum of charged particles, by providing a maximum magnetic field strength of approximate 1T and a total bending power of about 4 T m over the region where $z \in [2.5, 8]$ m. The magnetic field has been measured to a relative precision of about 4×10^{-4} and is uniform within a percent within the tracking volume. The profile of the magnetic field along the z -axis is shown in Fig. 2.14 on page 40, where the track types within LHCb are defined. The magnet can provide a magnetic field in either vertical direction; over the span of a year of data taking approximately equal amounts of data are collected with the magnet in the "Up" and "Down" configurations; this leads to a number of charge-asymmetry effects to cancel, significantly reducing potential systematic uncertainties.

The tracking system consists of the VELO, and four other tracking stations: the Tracker Turicensis (TT) upstream of the magnet, and the tracking stations 1–3 (T1, T2, T3) downstream of the magnet. The downstream tracking stations each consist of an Inner Tracker (IT) based on silicon strips, and an Outer Tracker (OT) that employs drift tubes.

Both the TT and IT are based on silicon strip detectors with a pitch of about 200 μm ; they were developed as a single project and are collectively known as the Silicon Tracker (ST). The TT is a 140 cm wide and 130 cm tall planar tracking station, covering the whole LHCb acceptance. It is shown in Fig. 2.6a. At each

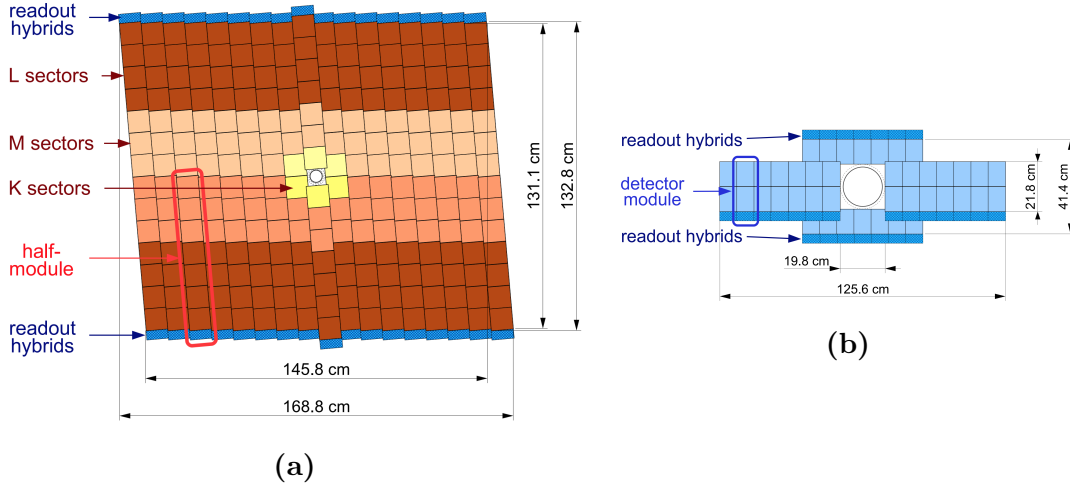


Figure 2.6: Overview of (a) a *v*-layer module of the IT and (b) an *x*-layer module of the IT. Reproduced from Ref. [78]

of the T1–T3 stations, the IT consist of four modules, arranged around the beam pipe as illustrated in Fig. 2.6b. They do now cover the full LHCb acceptance, only the very-forward region where the number of tracks is largest. Each TT or IT module comprises of four layers of silicon strips, where the central two layers are rotated $\pm 5^\circ$ with respect to the first and last layer (an *x-u-v-x* geometry). The ST has a spatial resolution for a given track of approximately 50 μm , chosen because the overall momentum resolution is then dominated by multiple-scattering effects for almost all momenta.

At the T1–T3 stations, the OT covers the part of the overall acceptance of 300 (250) mrad in the horizontal bending (vertical non-bending) plane that is not covered by the IT. The OT consists of arrays of gas-tight drift tubes with inner diameters of 4.9 mm. The OT is shown illustrated in Fig. 2.7. An Ar/CO₂/O₂ (70/28.5/1.5) gas mixture is used to fill the tubes that ensures a drift time below 50 ns and a drift coordinate resolution of 200 μm . The use of a drift-chamber detector is necessary, because it was not economically feasible to instrument the whole LHCb acceptance with silicon strip detectors in T1–T3. The condition that the OT occupancy should not be above 10 % in typical run conditions determined the boundary between the IT and the OT.

The overall relative momentum resolution achieved for most charged tracks in LHCb is less than a percent, as illustrated in Fig. 2.8, where it has been determined from a fit to the mass peak in $J/\psi \rightarrow \mu^+\mu^-$ decays in Run 1 data.

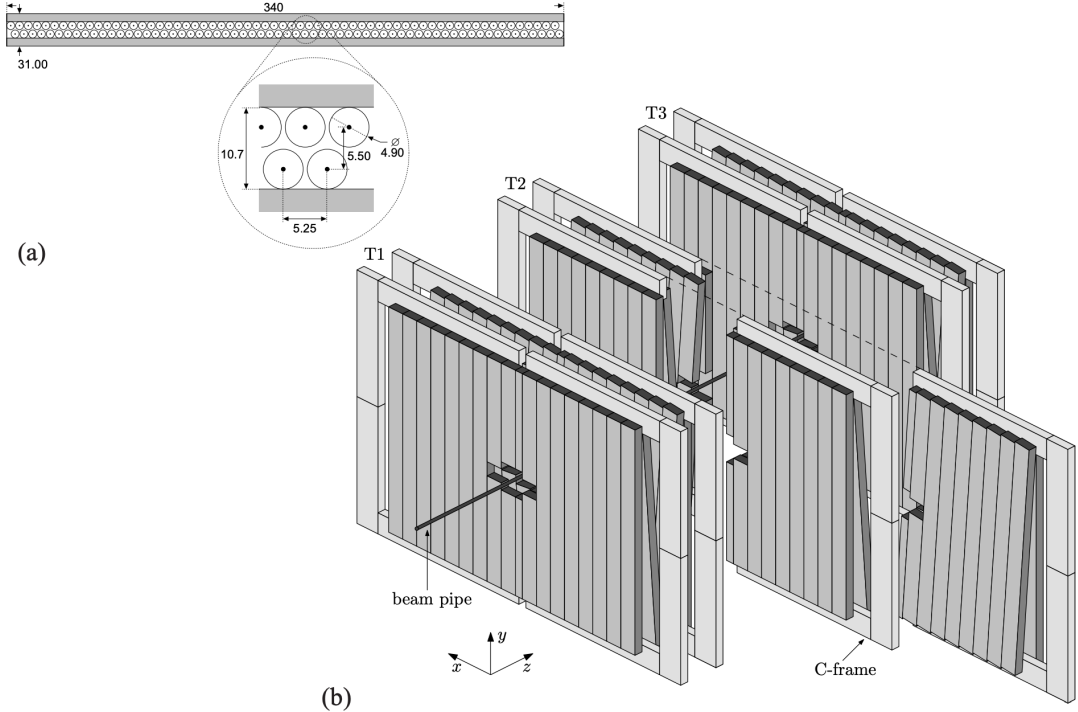


Figure 2.7: (a) Cross section of an OT module. (b) Arrangement of the OT modules in tracking stations. Reproduced from Ref. [83].

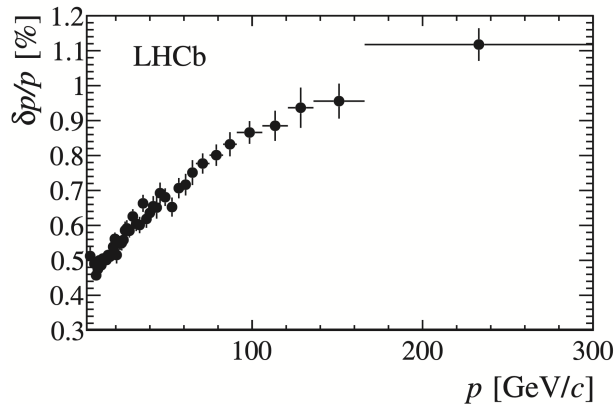


Figure 2.8: Relative uncertainty on the momentum of charged tracks (specifically long tracks, cf. the definitions in Section 2.2) in the LHCb detector, determined via the mass resolution obtained in $J/\psi \rightarrow \mu^+\mu^-$ decays in Run 1 data. Reproduced from Ref. [84]

2.1.3 The RICH detectors

Two Ring Imaging Cherenkov detectors (RICH) provide crucial information for particle identification (PID) in LHCb, in particular the ability to separate pions and kaons that is absolutely essential for the measurement presented in the thesis. The RICH 1 detector is located upstream of the magnet, in between the VELO and the TT tracking station. It is designed to provide PID capability for tracks

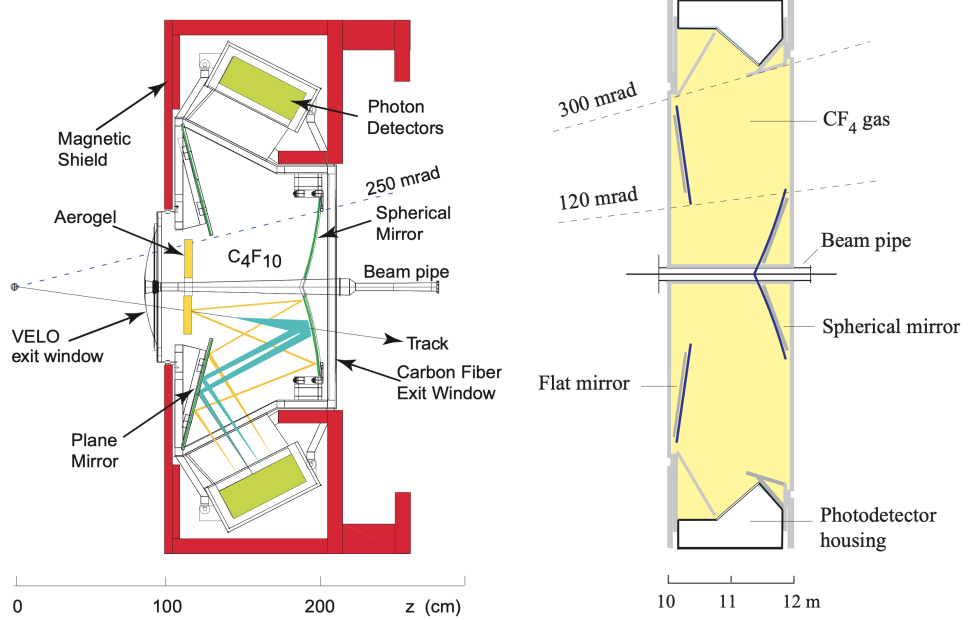


Figure 2.9: Overview of (left) the Rich 1 and (right) the RICH 2 detectors. Reproduced from Ref. [78,85].

in the momentum range $p \in [1 - 60] \text{ GeV}/c$ using a C_4F_{10} radiator, and covers the full LHCb acceptance. During Run 1 the RICH 1 detector also included an Aerogel radiator designed to provide PID for very low momentum particles; however, it was removed before Run 2 because it did not meet the performance requirements during Run 1 [86,87]. The RICH 2 detector is located downstream of the T1–T3 tracking stations. It is designed to provide PID capabilities for higher momentum tracks in the range $p \in [15 - 100] \text{ GeV}/c$ using a CF_4 radiator. It only covers the very forward region where $|\theta| < 120 \text{ mrad}(100 \text{ mrad})$ in the horizontal (vertical) directions, as high momentum particles are produced in that region. In both RICH detectors, mirrors are used to reflect the Cherenkov photons to arrays of Hybrid Photon Detectors (HPDs) located outside the LHCb acceptance. The optics are designed such that photons originating from a given track form rings in the HPD arrays, where the radius is determined by the Cherenkov angle θ_c . The detectors are illustrated in Fig. 2.9.

The resolution on θ_c can be measured by fitting the obtained θ_c distribution in high momentum tracks, where the Cherenkov angle is saturated. It is found to be $1.618 \pm 0.002 \text{ mrad}$ for RICH 1 and $0.68 \pm 0.02 \text{ mrad}$ for RICH 2 in Run 1 data [86], and was essentially unchanged in Run 2 [87]. Figure 2.10 shows the relation between track momentum and θ_c in RICH 1 for *isolated tracks* in Run 1 data; these are tracks where the Cherenkov ring does not overlap with any other

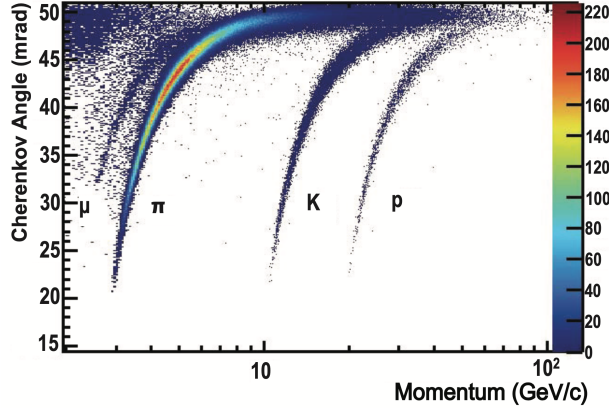


Figure 2.10: Cherenkov angle for isolated tracks in the RICH 1 radiator as a function of track momentum. Reproduced from Ref. [86].

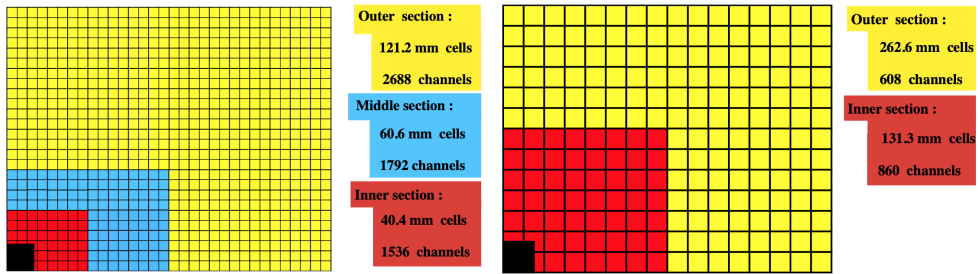


Figure 2.11: Illustration of the calorimeter cell size of (left) the ECAL and (right) the HCAL. Reproduced from Ref. [88].

Cherenkov rings. The bands for each hadron species are clearly visible, and it can be seen that the RICH detector also provide some ability to distinguish muons. The definition of the PID variables used in analysis is discussed in Section 2.2.2, along with the achieved PID performance.

2.1.4 Calorimeters

The calorimeter system of the LHCb detector has four components. Ordered from the interaction point, these are the Scintillating Pad Detector (SPD), Pre-Shower (PS), an Electromagnetic CALorimeter (ECAL), and a Hadron CALorimeter (HCAL). Information from the calorimeters also provide identification of electrons, photons, and hadrons, and measurements of their energies and positions, and also plays a crucial role in the triggering, as described below. In all four cases, light is produced in organic scintillators and transmitted to Photo Multiplier Tubes (PMTs) via optical fibres [78].

The SPD and PS detectors consist of almost identical planes of rectangular scintillator pads, with a 15 mm thick lead absorber located in between. The presence

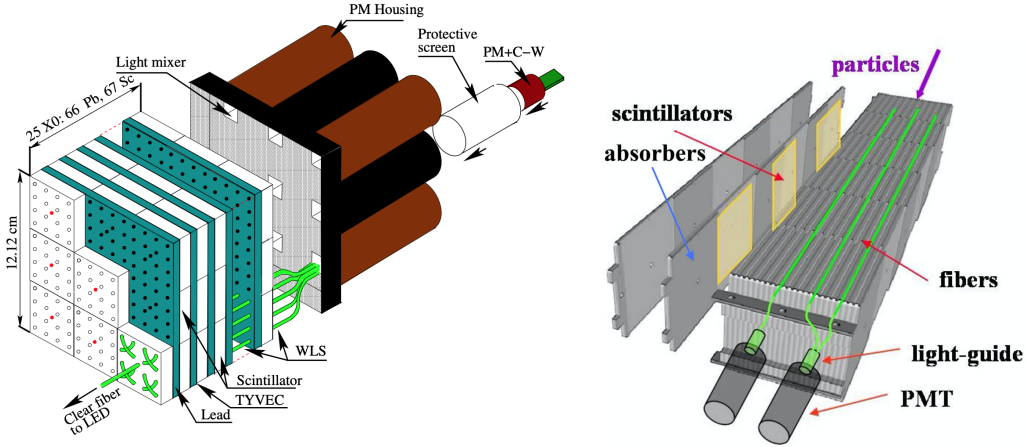


Figure 2.12: Illustration of (left) an ECAL and (right) a HCAL module. Reproduced from Ref. [84, 89].

of the SPD before the first absorption allows for the separation photons and charged particles using trigger information alone, because only electronic showers formed by the latter will deposit energy in the SPD. The PS allows for the separation of pion and electron tracks, as only the latter deposit significant energy in the thin lead layer. The cell divisions of the detectors closely follow that of the ECAL, shown in Fig. 2.11, to allow for the matching of energy deposits.

The ECAL has a Shashlik structure, with 66 layers consisting of 2 mm of lead absorber and 4 mm of scintillator; an example of a calorimeter module is shown in Fig. 2.12. Accurate energy measurements require that the full electronic shower is contained in the ECAL, which is achieved since the structure extends for 25 radiation lengths. The scintillators are divided into cells that allow for the determination of the location and shape of energy deposits; the cell dimensions vary as a function of radial distance from the beam pipe as shown in Fig. 2.11, to take into account the varying occupancy. The resolution of the ECAL has been measured to be $\Delta E/E \simeq (9/\sqrt{E} \oplus 0.8)\%$ (E in GeV/c^2) [78].

The HCAL is located downstream of the ECAL, designed to measure the energy of charged hadrons (which leave relatively little energy in the ECAL). It is constructed with layers of 1 cm iron absorbers inter-spaced with scintillators, oriented *along* the beam direction, such that a typical track will traverse 16 mm of iron per 4 mm of scintillator [88]. As for the ECAL, the cell size varies as a function of distance to the beam line, as shown in Fig. 2.11. An example of a module is shown in Fig. 2.12. The energy resolution required for efficient triggering is moderate; therefore, the HCAL only has a length of 5.6 interaction lengths and can measure the hadron energies at a resolution of $\Delta E/E \simeq (69/\sqrt{E} \oplus 9)\%$ (E in GeV/c^2) [78].

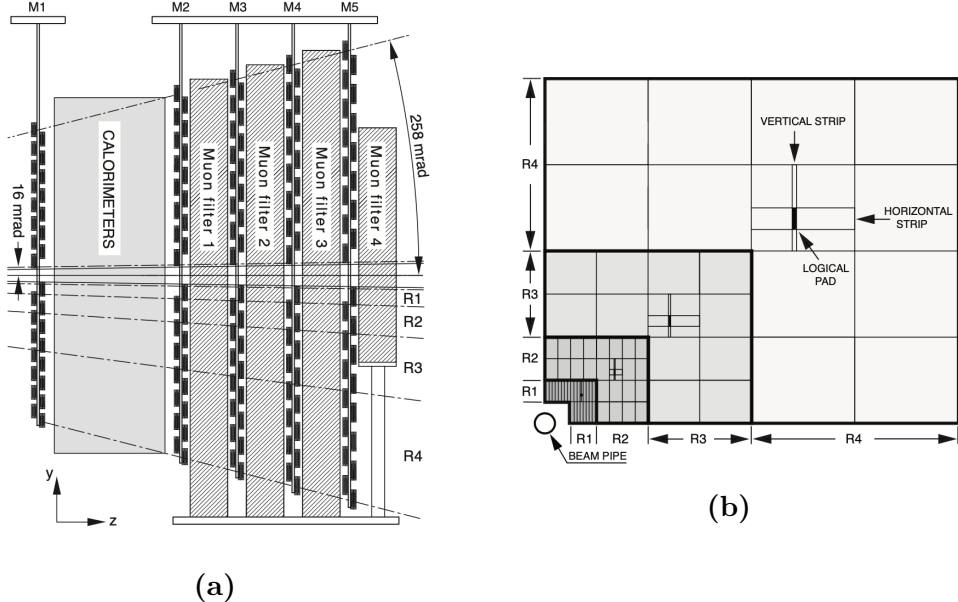


Figure 2.13: Illustration of (a) the location of the muon stations along the z -axis of the experiment, and (b) the geometry of the logical pads of the M3 muon station. Reproduced from Ref. [84].

2.1.5 Muon detectors

Muon identification and triggering is crucial for a range of high-profile LHCb measurements, such as lepton-universality tests or measurements of $B_{(s)}^0 \rightarrow \mu^+ \mu^-$ decays. In the thesis, muon identification plays a role in suppressing a number of backgrounds. The LHCb muon system consists of 5 tracking stations, M1–M5, covering the full LHCb acceptance. M1 is located upstream of the ECAL, whereas M2–M5 are located downstream of the HCAL and inter-spaced with 80 cm thick ion absorbers in order to select penetrating muons. This is illustrated in Fig. 2.13a. The detectors are multiwire proportional chambers (MWPC), organised into logical pads, the dimensions of which define the (x, y) resolution of the measured spatial points. As for the calorimeters, the size of the pads vary as a function of the radial distance from the beam pipe, as illustrated in Fig. 2.13b. The resolution is significantly better in the bending plane (x) than in the non-bending plane (y). The resolution is also significantly better in the M1–3 stations than in M4 and M5, which are mostly used to identify penetrating tracks. The muon system can independently measure the p_T of a muon to within 20 %, which allows for efficient triggering.

2.2 Reconstruction

This section describes the reconstruction algorithms that fit the detector hits in the tracking stations to form track candidates, as well as the algorithms used to

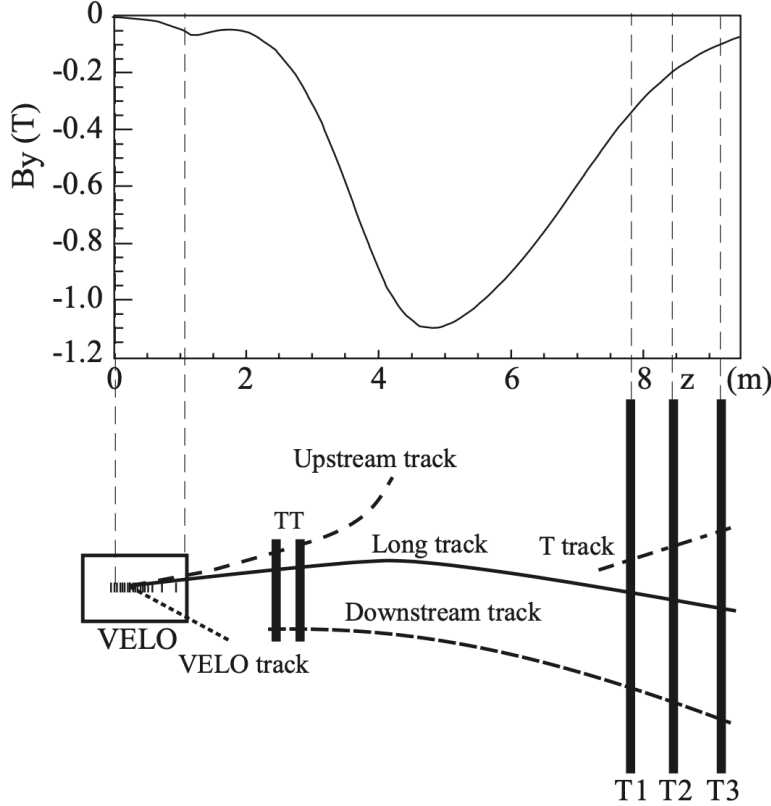


Figure 2.14: Definition of track types within the LHCb detector, depending on which set of tracking detectors the track intersects. The profile of the magnetic field is also shown. Reproduced from Ref. [84].

940 identify the types of the particles that formed these tracks.

941 2.2.1 Track reconstruction

942 The LHCb experiments operates with a number of different particle track types,
 943 depending on which sub detectors a track intersects; these are summarised in
 944 Fig. 2.14. The two track types that are important for this thesis are *long* tracks,
 945 which have hits in the VELO and the TT and T1–T3 tracking stations, and
 946 *downstream* tracks that only have hits in the TT and T1–3 tracking stations. The
 947 analysis depends on both track types because a number of K_S^0 mesons produced in
 948 the signal decay leave the VELO before they decay into the $\pi^+\pi^-$ final state that
 949 is reconstructed; hence these pions necessarily form downstream tracks.

950 The first step is to form track candidates from hits in the VELO (VELO tracks)
 951 and T1–3 stations (T tracks) separately; because the magnetic field is low in
 952 the tracking detectors, these tracks are fairly straight. Long tracks are formed
 953 using two separate search strategies: in one, *forward tracking* [90], VELO tracks

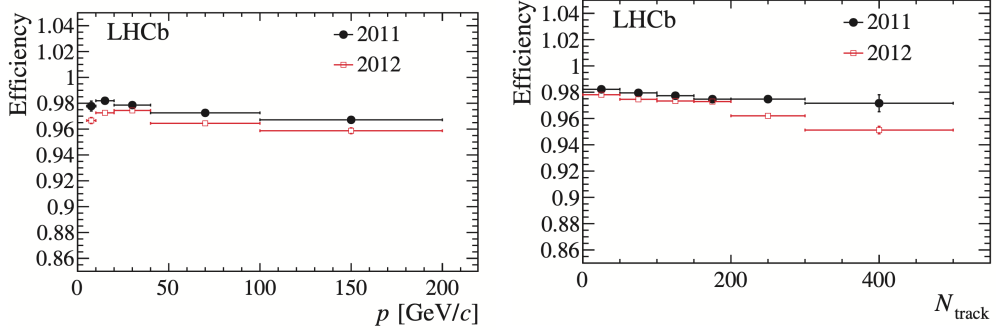


Figure 2.15: The long track reconstruction efficiency as a function of (left) track momentum and (right) the number of charged tracks in the event. The figure is reproduced from Ref. [84].

are used as seeds and matched with hits in the TT and T1–3 tracking stations by extrapolation. These are combined to form long tracks that are required to pass a set of quality conditions. An alternative approach, *track matching* [91, 92], matches VELO and T tracks by extrapolating both through the bending region, and deciding if they below together; finally TT hits are added. The union of tracks found via both approaches is saved, where only the track candidate with the best fit quality is kept in the case where a track appears twice. Downstream tracks are formed based on T tracks as seeds, matched with hits in the TT detector in a search region obtained by extrapolation of the seed [93]. Finally, each track is reprocessed using a Kalman filter that takes into account multiple scattering and corrects for energy loss due to ionisation [94, 95].

Many of the interesting signal decay channels of LHCb have 4–6 charged final state tracks, and therefore it is crucial to have a single-track reconstruction efficiency close to 100 %. The single-track reconstruction efficiency is shown in Fig. 2.15 as a function of track momentum and the number of tracks in an *event* (an *event* denotes a pp collision and all the particles produced therein and in subsequent decays). The efficiencies have been obtained in data, using a tag-and-probe method in $J/\psi \rightarrow \mu^+ \mu^-$ decays [96]. One muon, the *tag*, is fully reconstructed, while the other, the *probe* is only partially reconstructed, allowing for the J/ψ invariant mass to be reconstructed with reasonable resolution. If the partially reconstructed probe track is matched to a full long track, the track is classified as efficient. Similar efficiencies have been achieved in Run 2.

2.2.2 Particle identification

The information from the RICH detectors, the calorimeters, and the muon system is generally combined, for optimal identification of charged tracks as electrons, muons,

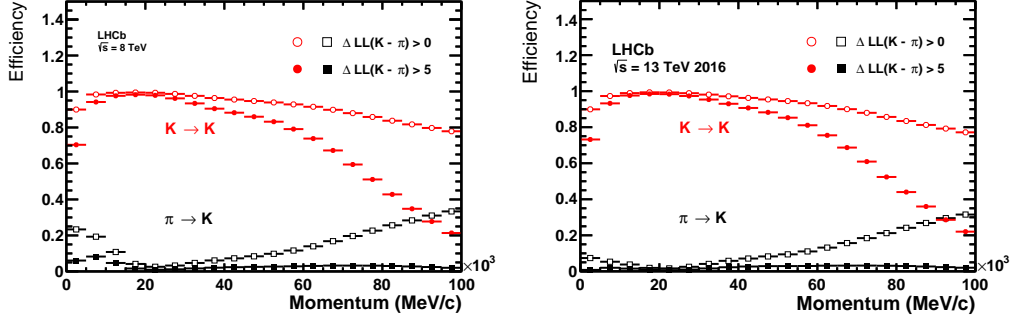


Figure 2.16: The probability to correctly identify a kaon/misidentify a pion as a kaon given two different requirements on $\Delta LL(K)$, as a function of track momentum in (left) Run 1 data from 2012 and (right) Run 2 data from 2016. Reproduced from Ref. [97].

979 pions, kaons, or protons. Photons and neutral pions are identified using the ECAL,
980 but play no role in the thesis, and will not be discussed further.

981 The ability to separate $B^\pm \rightarrow DK^\pm$ and $B^\pm \rightarrow D\pi^\pm$ decays is essential to the
982 measurement presented in this thesis. In LHCb, hadron separation is achieved via
983 information from the RICH detectors, using a likelihood method where the observed
984 pattern of hit pixels in the photo detectors is compared to the expected pattern,
985 given all reconstructed tracks in an event under a given set of particle hypothesis.
986 The likelihood is maximised by varying the particle hypotheses for each track being
987 an electron, muon, pion, kaon, or proton [98]. It is necessary to consider all tracks
988 of an event simultaneously because the Cherenkov rings of different tracks overlap.
989 For each track, the maximum log likelihood of a particle hypothesis, say that the
990 track is a kaon, relative to the hypothesis that it is a pion

$$\Delta LL_{\text{track}_i}^{\text{RICH}}(K) = \ln \mathcal{L}_{\max}^{\text{RICH}}(\text{pattern}|\text{track}_i = K) - \ln \mathcal{L}_{\max}^{\text{RICH}}(\text{pattern}|\text{track}_i = \pi), \quad (2.1)$$

991 is saved to inform PID decisions. In the case of pion-kaon separation, this variable
992 alone is enough to achieve good separation power; in the remainder of the thesis
993 it is denoted PIDK. The PID performance for pion-kaon separation has been
994 measured in calibration data, following a procedure described in Section 4.2.1,
995 and is illustrated in Fig. 2.16.

996 Muons are identified by extrapolating tracks to the muon stations to define
997 fields-of-interest (FOI). A track is considered as a muon candidate when a minimum
998 number of stations (2–4 depending on the track momentum) have hits in the
999 corresponding FOI [99, 100]. This information is encoded in a variable denoted
1000 `isMuon` throughout the thesis. Additional information, such as a comparison of
1001 the slopes of the track in the main tracker and the muon stations, and the average

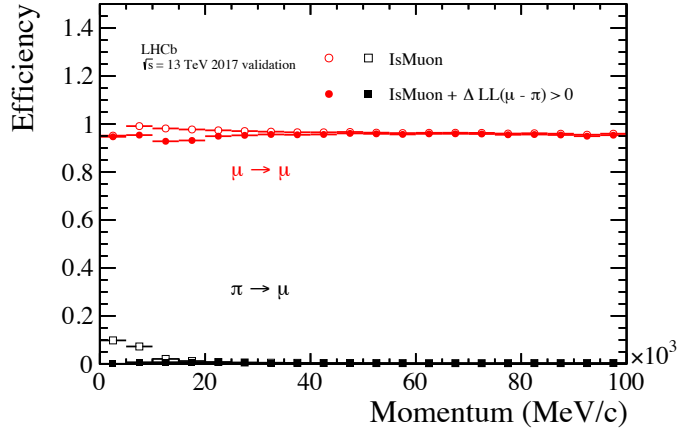


Figure 2.17: The probability to correctly identify a muon/misidentify a pion as a muon given requirements on either `isMuon` or $\Delta LL(\mu)$, as a function of track momentum in Run 2 data from 2017. Reproduced from Ref. [97].

track-hit distance in the FOI is used to form a $\Delta LL^{\text{muon}}(\mu)$ variable analogous to the one defined in Eq. (2.1) for the RICH detectors; it can be combined with $\Delta LL^{\text{RICH}}(\mu)$ to form a PID variable that takes information from both detectors into account, denoted `PIDmu`. The performance of the muon PID variables is shown in Fig. 2.17 as obtained in data. It can be seen that requiring `isMuon=0` rejects muon tracks efficiently at all momenta; this is used in the analysis to veto a number of semi-leptonic backgrounds.

In similar manner, a potential semi-leptonic background with electrons is also vetoed in the analysis presented in the thesis. In LHCb, electron PID is mainly based on the balance between deposited energy and track momentum in the ECAL [101]. This information is combined with information on photon deposits from brehmstrahlung, and energy deposits in the PS and HCAL, as well as information from the RICH and muon detectors, to form yet another ΔLL variable, denoted `PIDE`. As an example of the obtainable performance, an average electron selection efficiency of $(91.9 \pm 1.3\%)$ was achieved in displaced $J/\psi \rightarrow e^+e^-$ decays in Run 1, with a hadron misidentification rate of $(5.54 \pm 0.02)\%$ [84].

2.3 The LHCb trigger system

The collision rate in the LHC is up to 40 MHz, with a visible inelastic collision rate in LHCb of up to 30 MHz. The LHCb uses a multi-stage trigger to reduce rate with which events are stored to a manageable level (of eg. 12.5 kHz during Run 2). The first stage consists of a hardware trigger that selects events with high transverse energy in the calorimeters, or hits in the muon detectors. This

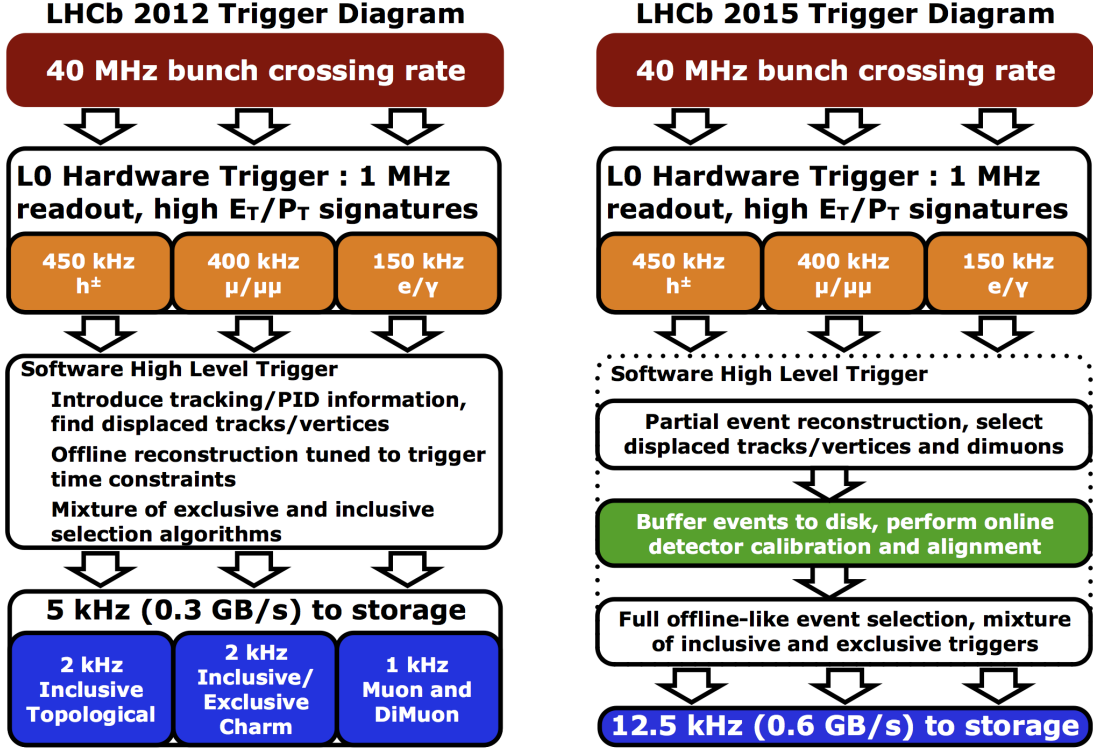


Figure 2.18: Illustration of stages and event processing rates in the LHCb trigger during (left) Run 1 and (right) Run 2.

is followed by two software stages that rely on a reconstruction of tracks in the detector to select events that are likely to include interesting physics. The overall trigger stages were identical in Run 1 and Run 2, however the throughput rate was upgrade significantly between the two data taking period, as was the quality of the reconstruction in the software trigger stages; in Run 2, the final software trigger decisions are in fact based on the full offline event reconstruction [102]. The stages are illustrated in Fig. 2.18, and described in detail in the following.

A further, offline processing and reconstruction step is applied to all events before they are made available to most LHCb analyses, commonly denoted as the *stripping* step. Although the stripping does not form part of the LHCb trigger, it does constitute an additional, centralised filter on the data, and a description is included in Section 2.3.3.

2.3.1 The level-0 hardware trigger

The level-0 (L0) triggers that select physics events are based on the calorimeters and the muon system. The ECAL and HCAL are divided into clusters of 2×2

1039 cells, for which the transverse energy is defined as

$$E_T = \sum_j E_j \sin \theta_j, \quad (2.2)$$

1040 where θ_j is the angle of cell j with respect to the beam axis and the average collision
1041 point. The trigger forms a **L0Hadron** candidate with the highest E_T found in the
1042 HCAL, combined with the ECAL cluster in front of it if such a cluster is present.
1043 Photon and electron candidates are formed based on clusters in the ECAL, identified
1044 by the presence (lack) of hits in the SPD for an elentron (photon). The transverse
1045 energies of the candidates are compared to a fixed set of thresholds, and events
1046 where at least one candidate is above threshold are retained.

1047 The muon trigger searches for straight line tracks in the muon stations, estimating
1048 the associated muon p_T based on the track direction. An event is retained if either
1049 the largest muon p_T is above a given threshold, or the product of the two highest
1050 muon p_T values is above a different threshold.

1051 High-multiplicity events take a long time to process in the subsequent software
1052 stage; therefore it is favourable for the overall retention rate of interesting physics
1053 decays to put a maximum limit on the event multiplicity at the L0 stage. This
1054 is achieved by requiring the number of hits in the SPD detector to be below a
1055 threshold value in most L0 lines.

1056 2.3.2 High-level triggers

1057 The events that pass the L0 trigger are passed to a farm of multiprocessor computing
1058 node, the Event Filter Farm (EFF), tasked with bringing the rate down from
1059 approximately 1 MHz to the $\mathcal{O}(1 - 10)$ kHz rate that can be saved to disk. The EFF
1060 consisted of 900 (1700) nodes during Run 1 (Run 2). The software-based filtering
1061 proceeds in two stages: a first filter (HLT1) brings the rate down to approximately
1062 40 (110) kHz based on a limited reconstruction of the event, after which a second
1063 stage (HLT2) filters the events further based on a more complete reconstruction.
1064 Each step executes a number of different algorithms, each of which can allow an
1065 event to be accepted; these are denoted *trigger lines*.

1066 During both runs, the HLT1 performed a partial event reconstruction by building
1067 long tracks that satisfy a p_T requirement using the forward tracking approach
1068 described in Section 2.2.1, and determining the location of PVs using VELO tracks.
1069 In both runs, the HLT1 included an inclusive trigger that selected a high p_T
1070 track with significant displacement of all PVs (typical of a b or c decay). This
1071 line is denoted HLT1TrackAllL0 in Run 1 [103]; for Run 2 the track requirements

were reoptimised and it is denoted `Hlt1TrackMVA`. Further, an additional inclusive trigger was added that forms a two-prong vertex out of high p_T tracks inconsistent with originating in a PV, and applies a multivariate classifier to determine if it is signal-like based on a number of track and vertex properties. This line is denoted `Hlt1TwoTrackMVA` [102]. These lines triggered all events included in the analysis of the thesis; other lines exist for selecting events that include muons, calibration data, low-multiplicity events, and a number of exclusive lines, for a total of approximately 20 lines during Run 2 [102].

Because the rate of events is reduced significantly by HLT1, the HLT2 decisions can be based in a more complete reconstruction of the event. Indeed, during Run 2 it was based on a complete, fully aligned reconstruction equivalent to the offline reconstruction. During Run 1 the HLT2 reconstruction only included long tracks and did exclude some low momentum tracks; this was a main motivation for the upgrade of the EFF during the shutdown period. The need for full alignment in HLT2 means that it could not be run fully online in Run 2; instead the output events were saved to disk in the EFF, and processed with some delay [102]. The analysis presented in the thesis is based on a number of inclusive "topological" trigger lines, based on combinations of 2, 3, or 4 tracks that satisfy fit quality requirements, have high p_T , are separated from the PVs, and have a distance-of-closes-approach below 0.2 mm. A multivariate classifier is applied to each formed n -body object, to determine if the event should be accepted based on the track momenta, invariant mass, a corrected invariant mass that takes into account missing transverse momentum, distance of closest approach, and the impact parameter and separation with the associated PV. The resulting trigger lines were denoted `Hlt2Topo{2, 3, 4}BodyBBDT` during Run 1 and `Hlt2Topo{2, 3, 4}Body` during Run 2. A large number of other HLT2 lines exist (more than 500 in Run 2), including a significant number of exclusive lines that aim to select specific decays and only save information on the signal decay, not the whole event. This was made possible by the full reconstruction within HLT2 [102], and have allowed for larger signal yields to be collected within the data storage limits.

2.3.3 Offline data filtering: the LHCb stripping

Events that are written to disk are processed with the full detector alignment and calibration. In a further, offline processing step denoted the *stripping*, hundreds of different, dedicated reconstructions are performed; decay candidates for various signal decays are built and a number of requirements are made to reject backgrounds from random track combinations. For example, the $B^\pm \rightarrow D(\rightarrow K_S^0 h'^+ h'^-) h^\pm$

1108 candidates that are analysed in this thesis are built during the stripping stage, as
1109 described further in Section 4.1. The stripping is a centralised computing task,
1110 executed on the Worldwide LHC Computing Grid [104], and allows the analysts
1111 to process much smaller data sets during their individual analysis. Because the
1112 stripping is based on data saved to offline storage it can be repeated; however,
1113 the processing of data collected during a year of data taking takes many weeks,
1114 so this does not happen often.

1115 2.4 Simulation

1116 A centralised LHCb simulation is able to simulate pp collisions with the proper
1117 conditions within LHCb, subsequent secondary decays, and the detector response,
1118 and process it via the full LHCb reconstruction. In this thesis, simulated decays
1119 are used to determine the reconstructed invariant-mass distribution of a number
1120 of decay modes, as well as a number of relative selection efficiencies. The pp
1121 collisions are generated using PYTHIA [105] with a specific configuration specific
1122 to LHCb [106]. The time-dependent evolution and decays of unstable particles
1123 are described by the EVTGEN [107] package, designed specifically for B physics.
1124 Final-state radiation is generated using PHOTOS [108]. The interaction of the
1125 generated particles with the detector, and its response, are implemented using the
1126 GEANT4 toolkit [109] as described in Ref. [110].

1127 The most significant computational cost of the simulation is due to the detector
1128 simulation. A single pp collision produces $\mathcal{O}(100)$ tracks in the detector, out of
1129 which only a handful belong to the signal decay under study. Therefore, significant
1130 computation resources can be saved by reusing the detector simulation of non-signal
1131 tracks a number of times, while redescaying the signal particle, say a B^+ , each time.
1132 This approach is called ReDecay [111], and has been relatively widely adopted
1133 within LHCb. ReDecay has been used to produce simulation samples corresponding
1134 to the conditions in 2017 and 2018 for this thesis. In some cases, the use of ReDecay
1135 necessitates special statistical treatment due the correlated detector occupancies
1136 between signal candidates, but for the analysis in this thesis the impact is negligible.

1137 A number of sub-dominant backgrounds are investigated using the fast-simulation
1138 package RapidSim [112]. This package can decay heavy b and c hadrons with
1139 kinematic distributions similar to those in LHCb pp collisions, or with user defined
1140 input distributions. The decays are typically evenly distributed over phase space,
1141 but can also be handled with EVTGEN [107] to take involved spins and resonant
1142 structure into account. Furthermore, a smearing of the obtained momenta is
1143 implemented, based on the LHCb resolution.

3

1144

1145

1146

Neutral kaon CP violation and material interaction in BPGGSZ measurements

1147 The presence of a K_S^0 meson in the $D \rightarrow K_S^0 h^+ h^-$ final states introduces a small
1148 bias in BPGGSZ measurements due to CP -violation in the neutral kaon sector
1149 and asymmetries caused by the interaction between the neutral kaons and detector
1150 material. These fundamental physics effects are reviewed in Section 3.1, after which
1151 the chapter presents a detailed analysis of the impact on the LHCb measurement
1152 that is the subject of the thesis, as well as future γ measurements with the Belle II
1153 experiment. Prior to this analysis, the only existing work on the effect on γ
1154 measurements suggested a small effect in $B^\pm \rightarrow D K^\pm$ measurements but potentially
1155 very significant effects in measurements based on $B^\pm \rightarrow D \pi^\pm$ decays [42]. However,
1156 as described in Section 3.1.1, the analysis in Ref. [42] does not take into account
1157 the fundamental aspect of the BPGGSZ method: that it relies on the phase-space
1158 distribution of signal decays, not phase-space integrated asymmetries. Furthermore,
1159 the study only considers the CP -violation effect, not material interaction. Therefore,
1160 a more detailed study was necessary before the $B^\pm \rightarrow D \pi^\pm$ decay mode could
1161 reliably be promoted to a signal channel.

1162
1163

3.1 CP violation and material interaction of neutral kaons

1164 A brief review of the general phenomenology of mixing and CP violation in the
1165 neutral kaon system is useful, before analysing the impact on γ measurements.

¹¹⁶⁶ The presentation in this section follows the PDG review of *CP violation in the*
¹¹⁶⁷ *quark section* [31]. The general theory considers any pair of neutral mesons $|M^0\rangle$
¹¹⁶⁸ and $|\bar{M}^0\rangle$ related by CP conjugation

$$CP|M^0\rangle = e^{i\phi_M}|M^0\rangle \quad CP|\bar{M}^0\rangle = e^{-i\phi_M}|\bar{M}^0\rangle, \quad (3.1a)$$

¹¹⁶⁹ where ϕ_M is an arbitrary phase. In this thesis, the convention $\phi_M = 0$ is chosen
¹¹⁷⁰ to equal zero, so that

$$CP|M^0\rangle = |\bar{M}^0\rangle \quad CP|\bar{M}^0\rangle = |M^0\rangle. \quad (3.1b)$$

¹¹⁷¹ A meson state that starts as a general superposition of $|M^0\rangle$ and $|\bar{M}^0\rangle$ states

$$\begin{aligned} \psi_M^0 &\equiv \psi_M(0) = a(0)|M^0\rangle + b(0)|\bar{M}^0\rangle \\ &\equiv \psi_{M^0}^0 + \psi_{\bar{M}^0}^0 \end{aligned} \quad (3.2)$$

¹¹⁷² will, over time, involve into a state that consists of a different superposition of
¹¹⁷³ $|M^0\rangle$ and $|\bar{M}^0\rangle$, as well as components for all possible states the meson system
¹¹⁷⁴ can decay into

$$\begin{aligned} \psi_M(t) &= a(t)|M^0\rangle + b(t)|\bar{M}^0\rangle + \sum c_i(t)f_i \\ &\equiv \psi_{M^0}(t) + \psi_{\bar{M}^0}(t) + \sum c_i(t)f_i. \end{aligned} \quad (3.3)$$

¹¹⁷⁵ For time scales that are longer than the typical strong-interaction, the time evolution
¹¹⁷⁶ of the $M^0 - \bar{M}^0$ superposition can be described by a 2×2 Hamiltonian

$$\frac{d}{dt} \begin{pmatrix} \psi_{M^0}(t) \\ \psi_{\bar{M}^0}(t) \end{pmatrix} = -i\mathcal{H}_0 \begin{pmatrix} \psi_{M^0}(t) \\ \psi_{\bar{M}^0}(t) \end{pmatrix} \quad (3.4)$$

¹¹⁷⁷ that is *non-Hermitian* (to allow for decay) but can be parameterised in terms
¹¹⁷⁸ of two Hermitian matrices \mathcal{M} and Γ_0

$$\mathcal{H}_0 = \mathcal{M} - \frac{i}{2}\Gamma_0. \quad (3.5)$$

¹¹⁷⁹ The quantum states with well-defined (real) masses, m_j , and (real) decay widths,
¹¹⁸⁰ Γ_j , are the two eigenstates of \mathcal{H}_0 with eigenvalues $\lambda_j = m_j - \frac{i}{2}\Gamma_j$. The eigenstates
¹¹⁸¹ (of course) evolve independently in time, so that

$$\psi_j(t) = e^{-i\lambda_j t}\psi_j^0 = e^{-im_j t - \frac{\Gamma_j}{2}t}\psi_j^0. \quad (3.6)$$

¹¹⁸² The eigenstates are denoted H and L according to the size of m_j , the real part
¹¹⁸³ of the eigenvalues, such that $m_H > m_L$. Assuming that \mathcal{H}_0 conserves CPT the
¹¹⁸⁴ eigenstates have the general form

$$\begin{aligned} |M_H\rangle &\equiv p|M^0\rangle - q|\bar{M}^0\rangle \\ |M_L\rangle &\equiv p|M^0\rangle + q|\bar{M}^0\rangle \end{aligned} \quad (3.7)$$

where p and q are complex numbers that satisfy $|q|^2 + |p|^2 = 1$. With the convention in Eq. (3.1b) it follows that if \mathcal{H}_0 also conserves CP , so that $|M_H\rangle$ and $|M_L\rangle$ are CP eigenstates, then $p = \pm q$, where the sign depends on which of the heavy and the light meson states is CP even, and which is CP odd.

The eigenstates of the Hamiltonian governing the neutral kaon system are almost, but not exactly, equal to the CP eigenstates

$$|K_1\rangle = \frac{|K^0\rangle + |\bar{K}^0\rangle}{\sqrt{2}} \quad |K_2\rangle = \frac{|K^0\rangle - |\bar{K}^0\rangle}{\sqrt{2}}, \quad (3.8)$$

which are CP even and odd, respectively. This approximate equality leads to the most prominent feature of the neutral kaon system: the two eigenstates of \mathcal{H}_0 have lifetimes that differ by orders of magnitude. This is best understood by assuming, for a moment, that the states in Eq. (3.8) *do* equal the eigenstates with definite life times. The K_1 state can decay in the CP even $\pi^+\pi^-$ and $\pi^0\pi^0$ modes, and does so almost 100% of the time; these decay modes are not available to the K_2 (in the absence of direct CP violation) which results in a much lower decay rate and much longer life time. Therefore, the eigenstates in the kaon system are labelled the *short-lived* kaon, K_S^0 , which is almost CP even, and the *long-lived* kaon, K_L^0 , which is almost CP odd. The life times are [31]

$$\tau_{K_S^0} = (8.954 \pm 0.004) \times 10^{-11} \text{s} \quad \tau_{K_L^0} = (5.116 \pm 0.021) \times 10^{-8} \text{s}. \quad (3.9)$$

Experimentally, it is found that the K_S^0 corresponds to the light eigenstate, but that the mass splitting [31]

$$\begin{aligned} \Delta m = m_{K_L^0} - m_{K_S^0} &= (0.5289 \pm 0.0009) \times 10^{10} \hbar s^{-1} \\ &\simeq 3.5 \times 10^{-6} \text{ eV} \end{aligned} \quad (3.10)$$

is tiny compared to the neutral kaon masses of $m_{K_S^0} = 497.6 \text{ MeV}/c^2$ [31].

However, the discovery of $K_L^0 \rightarrow \pi\pi$ decays by Kronin and Fitch in 1964 established that the K_S^0 and K_L^0 are *not* exactly equal to the CP eigenstates in Eq. (3.8), because the \mathcal{H}_0 relevant to the kaon system is CP -violating. The CP violation in the kaon sector is conventionally parameterised in terms of the complex parameters ϵ and ϵ' , in terms of which

$$\frac{A(K_L^0 \rightarrow \pi^+\pi^-)}{A(K_S^0 \rightarrow \pi^+\pi^-)} = \epsilon + \epsilon' \quad \frac{A(K_L^0 \rightarrow \pi^0\pi^0)}{A(K_S^0 \rightarrow \pi^0\pi^0)} = \epsilon - 2\epsilon'. \quad (3.11)$$

In these expressions ϵ denotes the contribution from CP violation in mixing and ϵ' the contribution due to direct CP violation in the decays. The ϵ parameter has been measured to be [31]

$$|\epsilon| = (2.228 \pm 0.011) \times 10^{-3}, \quad \arg \epsilon = (43.52 \pm 0.05)^\circ. \quad (3.12)$$

1212 Direct CP violation is ignored for the remainder of the thesis, because ϵ' is measured
1213 to be three orders of magnitude smaller than ϵ . In terms of the CP eigenstates
1214 of Eq. (3.8), the mass eigenstates K_S^0 and K_L^0 are given by

$$\begin{aligned} |K_S^0\rangle &= \frac{|K_1\rangle + \epsilon|K_2\rangle}{\sqrt{1+|\epsilon|^2}} &= \frac{(1+\epsilon)|K^0\rangle + (1-\epsilon)|\bar{K}^0\rangle}{\sqrt{2(1+|\epsilon|^2)}} \\ |K_L^0\rangle &= \frac{|K_2\rangle + \epsilon|K_1\rangle}{\sqrt{1+|\epsilon|^2}} &= \frac{(1+\epsilon)|K^0\rangle - (1-\epsilon)|\bar{K}^0\rangle}{\sqrt{2(1+|\epsilon|^2)}}, \end{aligned} \quad (3.13)$$

1215 corresponding to the definition $p = (1+\epsilon)/\sqrt{2(1+|\epsilon|^2)}$ and $q = (1-\epsilon)/\sqrt{2(1+|\epsilon|^2)}$
1216 in Eq. (3.7).

1217 In an experimental setting, the time evolution of a neutral kaon state is affected
1218 by nuclear interactions with the detector. The interaction is governed by the strong
1219 force, and therefore sensitive to the *flavour* of the kaon state; the interaction
1220 strength is thus different for K^0 and \bar{K}^0 mesons. This difference introduces a
1221 non-zero $K_S^0 \leftrightarrow K_L^0$ transition amplitude for neutral kaons traversing a detector
1222 segment. This effect was predicted early in the history of kaon physics [113] and is
1223 commonly denoted *kaon regeneration*. The effect can be described by including a
1224 material-interaction term in the Hamiltonian that is diagonal in the $(|K^0\rangle, |\bar{K}^0\rangle)$
1225 basis, so that the equation governing the time evolution is [114, 115]

$$\frac{d}{dt} \begin{pmatrix} \psi_{K^0}(t) \\ \psi_{\bar{K}^0}(t) \end{pmatrix} = -i \left[\mathcal{H}_0 + \begin{pmatrix} \chi & 0 \\ 0 & \bar{\chi} \end{pmatrix} \right] \begin{pmatrix} \psi_{K^0}(t) \\ \psi_{\bar{K}^0}(t) \end{pmatrix}. \quad (3.14)$$

1226 The complex parameters χ and $\bar{\chi}$ describe the material interaction of the K^0
1227 and \bar{K}^0 flavour eigenstates and are related to their scattering cross section, as
1228 described further in Section 3.3.4. The solution of Eq. (3.14) for the time evolution
1229 in the K_S^0 and K_L^0 states is [115]

$$\begin{aligned} \psi_S(t) &= e^{-i\Sigma t} \left(\psi_S^0 \cos \Omega t + \frac{i}{2\Omega} (\Delta\lambda\psi_S^0 - \Delta\chi\psi_L^0) \sin \Omega t \right), \\ \psi_L(t) &= e^{-i\Sigma t} \left(\psi_L^0 \cos \Omega t - \frac{i}{2\Omega} (\Delta\lambda\psi_L^0 + \Delta\chi\psi_S^0) \sin \Omega t \right), \end{aligned} \quad (3.15)$$

1230 in terms of the parameters

$$\begin{aligned} \Delta\chi &= \chi - \bar{\chi}, \\ \Delta\lambda &= \lambda_L - \lambda_S = (m_L - m_S) - \frac{i}{2}(\Gamma_L - \Gamma_S), \\ \Sigma &= \frac{1}{2}(\lambda_S + \lambda_L + \chi + \bar{\chi}), \\ \Omega &= \frac{1}{2}\sqrt{\Delta\lambda^2 + \Delta\chi^2}. \end{aligned} \quad (3.16)$$

1231 In the vacuum limit where $\chi = \bar{\chi} = 0$, the expressions in Eq. (3.6) and Eq. (3.15) are
1232 equal.

3.1.1 A first look at the impact on γ measurements

The effects described above have an impact on measurements of CP asymmetries in modes with a neutral kaon in the final state. This was analysed for the first time in relation to γ measurements by Grossman and Savastio in 2014 [42]. The authors point out two sources of corrections to be included:

- the fact that K_S^0 is not an exact CP eigenstate can break potential symmetry relations employed in an analysis, and
- that when the neutral kaon is reconstructed in a $\pi\pi$ final state there will be contributions from both K_S^0 and K_L^0 decays.

The analysis in this chapter considers yet another effect, not treated by Grossman and Savastio, namely that

- material interaction can emulate the effect of neutral kaon CP violation, because it couples the almost- CP -even K_S^0 and the almost- CP -odd K_L^0 states.

Due to the presence of $K_L^0 \rightarrow \pi\pi$ decays, Grossman and Savastio point out that the relevant decay rates to consider in an experimental setting are of the form

$$d\Gamma(t) \propto |\psi_S(t) + \epsilon\psi_L(t)|^2. \quad (3.17)$$

The time dependence of the decay rates considered in Chapter 1 was left out because all terms shared a common time dependence. That is not the case in Eq. (3.17), due to the very different decay rates of the K_S^0 and K_L^0 components of the kaon state. As a consequence, the time-integrated yields have the form

$$N \propto \int dt \eta(t) |\psi_S(t) + \epsilon\psi_L(t)|^2, \quad (3.18)$$

where $\eta(t)$ is the time acceptance in a given experimental setting. Thus, the acceptance is crucial to model in order to correctly estimate the impact of kaon CP -violation effects on a given measurement.

Considering BPGBSZ measurements, the main effect of neutral kaon CP violation is a breakdown of the fundamental Dalitz-plot symmetry that is exploited in the derivation of the bin yield equations. Extending the amplitude definition of Eq. (1.21) to include K_L^0 decays

$$A_{S(L)}^{(\overline{D})}(s_-, s_+) = A((\overline{D})^0 \rightarrow K_{S(L)}^0 \pi^+ \pi^-), \quad (3.19)$$

the authors point out that CP -violation in the K_S^0 system means that the relation $A_S^{(\overline{D})}(s_{-+}) = A_S^D(s_{+-})$ is not exactly true; and in addition, there is now a

dependence on $A_L^D(s_{-+})$ which satisfies a different approximate symmetry, namely $A_L^{\bar{D}}(s_{-+}) \simeq -A_L^D(s_{+-})$. Grossman and Savastio describe these symmetry breaking effects in detail, but do not explicitly derive the corrections to the yield equations of Chapter 1, nor try to quantify the potential bias on γ in a measurement based on the binned yields. Instead, they derive expressions for the bias in a measurement obtained from phase-space integrated CP asymmetries. This is done for both GLW measurements that use $D \rightarrow K_S^0 X$ final states and for the $D \rightarrow K_S^0 h^+ h^-$ final states; however, for their quantitative estimate of $\Delta\gamma$ the authors make an approximation that corresponds to assuming that the $D \rightarrow K_S^0 h^+ h^-$ final state is a CP eigenstate, making the two results identical. The authors find that in this case, assuming a uniform experimental acceptance for all kaon decay times, the asymmetry has the form¹

$$A = \frac{2r_B \sin \gamma \sin \delta_B + 2\text{Re}[\epsilon]}{1 + r_B^2 - 2r_B \cos \gamma \cos \delta_B}, \quad (3.20)$$

If a measured value of A is interpreted to obtain γ without taking the ϵ term into account, it leads to a bias of

$$\Delta\gamma = -\frac{\text{Re}[\epsilon]}{r_B \cos \gamma \sin \delta_B} + O(|\epsilon|). \quad (3.21)$$

The scaling $\Delta\gamma \sim \mathcal{O}(r_B/|\epsilon|)$ is the main result of the analysis by Grossman and Savastio. For $B^\pm \rightarrow D K^\pm$ decays, where $r_B^{DK^\pm} \simeq 0.1$ this suggests a bias at the percent level, which is negligible compared to current experimental uncertainties. However, in the $B^\pm \rightarrow D \pi^\pm$ case, where $r_B^{D\pi^\pm} \simeq 0.005$ [47], their result suggests relative biases that are potentially of $\mathcal{O}(1)$.

The conclusions are lacking on two accounts, however. Firstly, as made clear in Section 1.3.5, the $K_S^0 \pi^+ \pi^-$ and $K_S^0 K^+ K^-$ states are *far from* CP eigenstates. From the asymmetry expression in that section, it is clear that the bias in a determination of γ based on phase-space asymmetries will in fact scale as

$$\Delta\gamma \sim \mathcal{O}\left(\frac{|\epsilon|}{(2\mathcal{F}_+ - 1)r_B}\right), \quad (3.22)$$

which suggests that Grossman and Savastio severely *underestimates* the potential impact. This is described in detail in Section 3.2.3. More importantly, the analysis of the phase-space integrated asymmetry is in fact *irrelevant* to BPGGSZ measurements as they are currently performed: as described in Section 1.3.5 the information from

¹In fact the expression in Eq. (3.20) is missing a term, as will be clear when an analogous expression is derived in detail in Section 3.2.3.

the global asymmetry is completely discarded. Therefore it is necessary to analyse the effects of kaon CP -violation on a full, binned analysis of $D \rightarrow K_S^0 h^+ h^-$ decays, which is done in detail in the following sections. While the aim is to extend the analysis if Grossman and Savastio, the treatment in the following sections is completely independent of that in Ref. [42].

3.2 Impact on BPGBSZ measurements of γ : principles

The analysis of the impact on BPGBSZ measurements is carried out in two stages. This section treats the leading order effects analytically, and derives the overall order of magnitude of the expected bias in a general setting. Then Section 3.3 presents a detailed numerical study of the expected effect in measurements with the LHCb and Belle II experiments specifically, because these will be crucial to constrain γ during the coming decade [40, 41].

3.2.1 Modified symmetry relations

In order to derive the corrections to the asymmetry relation $A_S^D(s_{-+}) \simeq A_S^{\bar{D}}(s_{+-})$, it is beneficial to express $A_{S(L)}^D$ in terms of the amplitudes

$$A_{1/2}^{\bar{D}} = A(\overline{D}^0 \rightarrow K_{1/2}^0 \pi^+ \pi^-), \quad (3.23)$$

because these amplitude satisfy the exact symmetries $A_1^D(s_{-+}) = A_1^{\bar{D}}(s_{+-})$ and $A_2^D(s_{-+}) = -A_2^{\bar{D}}(s_{+-})$. This approach is different to that of Grossman and Savastio, but the final results are equivalent. After the decay of a D^0 meson to a neutral kaon, the kaon state is

$$\begin{aligned} \psi^0 &= A_1^D |K_1\rangle + A_2^D |K_2\rangle \\ &= N \left[(A_1^D - \epsilon A_2^D) |K_S^0\rangle + (A_2^D - \epsilon A_1^D) |K_L^0\rangle \right], \end{aligned} \quad (3.24)$$

with the normalisation constant $N = \sqrt{1 + |\epsilon|^2}/(1 - \epsilon^2)$. Thus it can be seen that

$$\begin{aligned} A_S^D(s_{-+}) &= N \left[(A_1^D(s_{-+}) - \epsilon A_2^D(s_{-+})) \right], \\ A_L^D(s_{-+}) &= N \left[(A_2^D(s_{-+}) - \epsilon A_1^D(s_{-+})) \right], \end{aligned} \quad (3.25)$$

1309 with an analogous expression for the \bar{D}^0 decay amplitudes. Therefore, the generalised
1310 relations between the D^0 and \bar{D}^0 amplitudes are

$$\begin{aligned} A_S^{\bar{D}}(s_{+-}) &= N[A_1^{\bar{D}}(s_{+-}) - \epsilon A_2^{\bar{D}}(s_{+-})] \\ &= N[A_1^D(s_{-+}) + \epsilon A_2^D(s_{-+})] = A_S^D(s_{-+}) + 2N\epsilon A_2^D(s_{-+}), \\ A_L^{\bar{D}}(s_{+-}) &= N[A_2^{\bar{D}}(s_{+-}) - \epsilon A_1^{\bar{D}}(s_{+-})] \\ &= -N[A_2^D(s_{-+}) + \epsilon A_1^D(s_{-+})] = -A_L^D(s_{-+}) - 2N\epsilon A_1^D(s_{-+}). \end{aligned} \quad (3.26)$$

1311 3.2.2 Relationship between the K_S^0 and K_L^0 amplitudes

1312 The decay amplitude $A(D^0 \rightarrow K_S^0 \pi^+ \pi^-)$ has been carefully studied, and a number
1313 of amplitude models have been published [51, 56–58, 61]. No models have been
1314 published for $D^0 \rightarrow K_L^0 \pi^+ \pi^-$ decays. However, following an approach laid out by
1315 the CLEO collaboration [69], the two amplitudes can be related. Again, this is
1316 most easily done by relating the $A_1^D(s_{+-})$ and $A_2^D(s_{+-})$ amplitudes. In the isobar
1317 formalism, the decay amplitude $A(D^0 \rightarrow K_1 \pi^+ \pi^-)$ is expressed as a non-resonant
1318 constant amplitude plus a sum of resonances

$$A(D^0 \rightarrow K_1 \pi^+ \pi^-) = k_{NR} + \sum_{CF} k_i R^i(s_{K\pi^-}) + \sum_{DCS} k_j R^j(s_{K\pi^+}) + \sum_{R_{\pi\pi}} k_k R^k(s_{\pi^+\pi^-}). \quad (3.27)$$

1319 The resonances are split into Cabibbo-favoured (CF) K^{*-} resonances, doubly
1320 Cabibbo-suppressed (DCS) K^{*+} resonances and $\pi\pi$ resonances.² The CF resonances
1321 couple to the \bar{K}^0 component of $K_1 (\propto K^0 + \bar{K}^0)$, and therefore the corresponding
1322 k_i in the $K_2 (\propto K^0 - \bar{K}^0)$ amplitude will have a relative minus sign. The DCS
1323 resonances couple to the K^0 component of K_1 , and so the corresponding k_j in the
1324 K_2 amplitude will have a relative plus sign. For the $h^+ h^-$ resonances, there will be
1325 a coupling to both the K^0 and \bar{K}^0 components, however the coupling to the K^0
1326 component is expected to be suppressed with a Cabibbo suppression factor $r_k e^{i\delta_k}$,
1327 where $r_k \simeq \tan^2 \theta_C \simeq 0.05$ is determined by the Cabibbo angle θ_C and δ_k can take
1328 any value. Therefore, the k_k for these resonances have a relative $-(1 - 2r_k e^{i\delta_k})$
1329 factor in the K_2 amplitude. The same effect leads to the differences in decay rates
1330 between $D^0 \rightarrow K_S^0 \pi^0$ and $D^0 \rightarrow K_L^0 \pi^0$ decays [116, 117]. Thus, given a model of the

²In modern models, the $\pi\pi$ and $K\pi$ S -wave components are modelled via the K -matrix formalism and LASS parametrisations, respectively, instead of sums of individual resonances [51]. This does not alter the arguments below, as the R functions of Eq. (3.27) can equally well represent such terms.

¹³³¹ form in Eq. (3.27), a model for the $A(D^0 \rightarrow K_2\pi^+\pi^-)$ amplitude will have the form

$$A(D^0 \rightarrow K_2\pi^+\pi^-) = k_{NR} + \sum_{CF} (-k_i) R^i(s_{K\pi^-}) + \sum_{DCS} (+k_j) R^j(s_{K\pi^+}) + \sum_{R_{\pi\pi}} (-(1 - 2r_k e^{i\delta_k}) k_k) R^k(s_{\pi^+\pi^-}). \quad (3.28)$$

¹³³² An important consequence of these substitution rules is that

$$A_2^D(s_{+-}) = -A_1^D(s_{+-}) + r_A \Delta A(s_{+-}), \quad (3.29)$$

¹³³³ where $r_A \simeq \tan^2 \theta_C$ and $\Delta A(s_{+-}) \sim A_1^D(s_{+-})$ are of the same order of magnitude
¹³³⁴ (at least when averaged over the bins used in γ measurements). This relation is
¹³³⁵ sufficient to make the qualitative arguments of this section, while the full set of
¹³³⁶ substitution rules above are used in the quantitative studies of Section 3.3.

¹³³⁷ 3.2.3 Modification of the BPGBSZ yield equations

¹³³⁸ With suitable models to calculate $A_{S(L)}^{\bar{D}}$ (or $A_{1/2}^{\bar{D}}$) and knowledge of $\Delta\chi$ for the
¹³³⁹ materials relevant to an experimental setting, the relations derived in the preceding
¹³⁴⁰ sections can be employed to calculate the expected phase-space bin yields, N_i^\pm ,
¹³⁴¹ including the effects of kaon CP violation and material interaction. The decay
¹³⁴² rates have additional terms compared to those in Eq. (1.24), because the K_L^0
¹³⁴³ contribution must be taken into account

$$d\Gamma(t, s_{+-}) \propto |\psi_S(t, s_{+-}) + \epsilon\psi_L(t, s_{+-})|^2, \quad (3.30)$$

¹³⁴⁴ where the time-dependence of $\psi_{S/L}(t, s_{+-})$ is governed by Eq. (3.15), and the phase-
¹³⁴⁵ space dependence is included in the state component, by defining $\psi_{S/L}^0$ in terms of
¹³⁴⁶ $A_{S(L)}^{\bar{D}}(s_{+-})$. For example, for the case of a $B^- \rightarrow DK^-$ decay, the definition is

$$\begin{aligned} \psi_{S/L}^{0,B^-}(s_{+-}) &= A_S^D(s_{+-}) + r_B e^{i(\delta_B - \gamma)} A_S^{\bar{D}}(s_{+-}) \\ &= A_1^D(s_{+-}) - \epsilon A_2^D(s_{+-}) + r_B e^{i(\delta_B - \gamma)} (A_1^{\bar{D}}(s_{+-}) - \epsilon A_2^{\bar{D}}(s_{+-})) \\ &= A_1^D(s_{+-}) - \epsilon A_2^D(s_{+-}) + r_B e^{i(\delta_B - \gamma)} (A_1^D(s_{+-}) + \epsilon A_2^D(s_{+-})). \end{aligned} \quad (3.31)$$

¹³⁴⁷ It is useful to look at the corrections to the BPGBSZ yield expressions in Eq. (1.25)
¹³⁴⁸ to lowest order in ϵ and $r_\chi = \frac{1}{2} \frac{\Delta\chi}{\Delta\lambda}$, the dimensionless parameter governing material
¹³⁴⁹ interactions. For LHCb and Belle II the average $|r_\chi| \simeq 10^{-3}$, as detailed in the
¹³⁵⁰ Section 3.3. To first order in r_χ , the time-dependent kaon states within a material,
¹³⁵¹ given in Eq. (3.15), simplify to [115]

$$\begin{aligned} \psi_S(t, s_{+-}) &= e^{-\frac{i}{2}(x+\bar{x})t} e^{-i\lambda_{St}} (\psi_S^0(s_{+-}) - r_\chi (1 - e^{-i\Delta\lambda t}) \psi_L^0(s_{+-})), \\ \psi_L(t, s_{+-}) &= e^{-\frac{i}{2}(x+\bar{x})t} e^{-i\lambda_{Lt}} (\psi_L^0(s_{+-}) + r_\chi (1 - e^{+i\Delta\lambda t}) \psi_S^0(s_{+-})). \end{aligned} \quad (3.32)$$

By inserting these expressions into Eq. (3.30) and employing the definition in Eq. (3.31) (and a similar definition for B^+ decays), the binned yields can be calculated by an integration over time and phase space. In the remainder of this section, it is assumed that the experimental time acceptance is $\eta(t) = 1$ for all times and that r_χ is constant at all times; more realistic assumptions are introduced in Section 3.3. In this case, the binned yields are given by the expression

$$\begin{aligned} N_i^- &= h_B^{-'} \left(\hat{K}_{+i} + r_B^2 \hat{K}_{-i} + 2\sqrt{\hat{K}_{+i} \hat{K}_{-i}} (x_- \hat{c}_i + y_- \hat{s}_i) + O(r\epsilon) \right), \\ N_i^+ &= h_B^{+'} \left(\hat{K}_{-i} + r_B^2 \hat{K}_{+i} + 2\sqrt{\hat{K}_{+i} \hat{K}_{-i}} (x_+ \hat{c}_i - y_+ \hat{s}_i) + O(r\epsilon) \right), \end{aligned} \quad (3.33)$$

where a number of new parameters have been defined, and where $O(r\epsilon)$ denotes terms of $O(r_A\epsilon)$, $O(r_B\epsilon)$, $O(r_A r_\chi)$, and $O(r_B r_\chi)$. Since $r_B \sim r_A \sim 10^{-1}$ (in $B^\pm \rightarrow D K^\pm$ decays) and $r_\chi \sim \epsilon \sim 10^{-3}$, these terms are all of the same order of magnitude.

The new normalisation constants $h_B^{\pm'} = h_B^\pm (1 + |\epsilon + r_\chi|^2 \frac{\Gamma_S}{\Gamma_L} \mp \Delta h)$ are defined in terms of

$$\Delta h = 2\text{Re}[\epsilon + r_\chi] - 4 \frac{\Gamma_S}{\Gamma_L + \Gamma_S} \frac{\text{Re}[\epsilon + r_\chi] + \mu \text{Im}[\epsilon + r_\chi]}{1 + \mu^2}, \quad \mu = 2 \frac{m_L - m_S}{\Gamma_L + \Gamma_S}. \quad (3.34)$$

The \hat{K}_i parameters are defined to be

$$\hat{K}_i = \frac{1}{1 + |\epsilon + r_\chi|^2 \frac{\Gamma_S}{\Gamma_L}} \left(K_i^{(1)} + |\epsilon + r_\chi|^2 \frac{\Gamma_S}{\Gamma_L} K_i^{(2)} \right), \quad (3.35)$$

in which the $K_i^{(1/2)}$ parameters are phase-space integrals, defined as in Eq. (1.27) but for $A_{1/2}^D$. To lowest order, the \hat{K}_i correspond to the fractional D^0 decay yield in each bin, as obtained in a measurement that averages D^0 and \bar{D}^0 decays, and assumes the $A_S^D(s_{-+}) = A_S^D(s_{+-})$ symmetry to be exact:

$$K_i^{\text{meas}} \equiv \frac{N_i^D + N_{-i}^{\bar{D}}}{\sum_j N_j^D + N_{-j}^{\bar{D}}} = \hat{K}_i + \mathcal{O}(r\epsilon). \quad (3.36)$$

Here, N_i^D ($N_i^{\bar{D}}$) is the expected yield of flavour tagged D^0 (\bar{D}^0) mesons into bin i of the D decay phase-space.

In similar fashion, the parameters (\hat{c}_i, \hat{s}_i) have been introduced to denote the measured average strong-phases, which are expected to differ from (c_i, s_i) at $O(\epsilon)$, since neutral kaon CP violation is not taken into account in the measurements by CLEO. Thus, any corrections arising if (\hat{c}_i, \hat{s}_i) and (c_i, s_i) are substituted in Eq. (3.33) will appear in the $O(r_B\epsilon)$ terms.

Two observations can be made from the expression in (3.33). The first is that the phase-space distribution is only changed at $O(r\epsilon)$ compared to the expression in

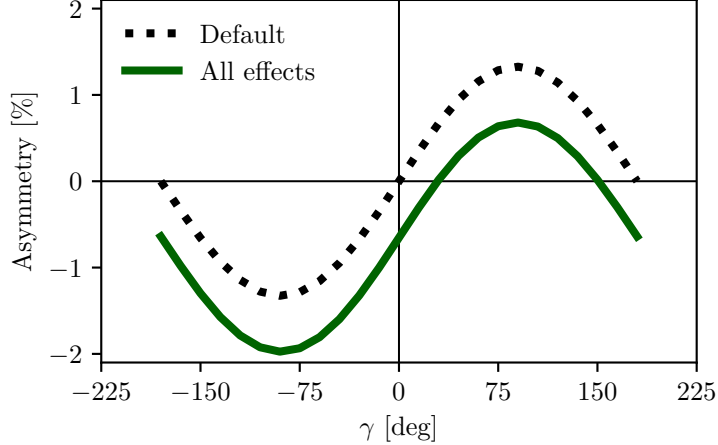


Figure 3.1: The asymmetry A_{total} as a function of γ calculated to $O(\epsilon)$ using Eq. (3.37). The calculation is made using for (black dotted line) the default case where $\Delta h = 0$ and (green) including neutral kaon CP -violation and material interaction with $r_\chi = \epsilon$.

Eq. (1.25), if the measured \hat{K}_i are used in the experimental analysis. This equally true whether the K_i are fitted in the signal channel along with x_\pm and y_\pm , as is the case in the measurement presented in the thesis, or if they are obtained in a control channel with flavour tagged D decays, according to Eq. (3.36). As the $D^0 - \bar{D}^0$ interference term that provides sensitivity to γ enters at order $O(r_B)$, the impact on γ measurements can be expected to be $\Delta\gamma/\gamma \sim O(r\epsilon/r_B)$. For $B \rightarrow DK$ analyses, where $r_B \simeq 0.1$, this is at the permille level, so the induced $\Delta\gamma$ bias can be expected to be smaller than 1° . Even in the case of $B^\pm \rightarrow D\pi^\pm$ decays, this suggests biases that are maximally a few percent. This is the main result of the chapter, because it means that the effect of neutral kaon CP violation and material interaction is small compared to the precision of the measurement that is the main subject of the thesis.

The second observation relates to potential future measurements of γ , which may also include sensitivity from the total, phase-space-integrated yield asymmetry

$$A_{\text{total}} = \frac{N^- - N^+}{N^- + N^+} = \frac{2(2\mathcal{F}_+ - 1)r_B \sin \delta_B \sin \gamma + \Delta h}{1 + r_B^2 + 2(2\mathcal{F}_+ - 1)r_B \cos \delta_B \cos \gamma} + O(r\epsilon), \quad (3.37)$$

where the definition of \mathcal{F}_+ from Section 1.3.5 has been employed. In the limit $r_B \rightarrow 0$ the expression agrees with the result for the analogous asymmetry in $D^\pm \rightarrow \pi^\pm K_S^0$ decays in Ref. [118], evaluated to $O(\epsilon)$ for an infinite and uniform time-acceptance. As hinted at above, the fact that $\mathcal{F}_+ \simeq 0.5$ means that the asymmetry due to γ being non-zero is not $\mathcal{O}(r_B)$, but of approximately the same order of magnitude as the asymmetry due to CP violation in the neutral kaon sector, governed by Δh . This is illustrated in Fig. 3.1, where the expression in Eq. (3.37) is plotted in the default

case where $\Delta h = 0$, using the model in Ref. [51] to calculate K_i and c_i , as well as including neutral kaon CP violation and material interaction effects, calculated using $r_\chi = \epsilon$, with ϵ taking the value in Eq. (3.12). The asymmetry changes significantly when including the latter effects. Therefore, measurements based only on the global asymmetry will suffer relative biases of tens of degrees, not a few degrees, if neutral kaon CP violation and material interaction is not taken into account.

3.3 Impact on BPGBGSZ measurements of γ : LHCb and Belle II measurements

The previous section has established that the bias due to neutral kaon CP violation and material interaction is at the sub-percent level for measurements based on $B^\pm \rightarrow DK^\pm$ decays, and just a few percent in $B^\pm \rightarrow D\pi^\pm$ decays. Thus, the effects only contribute a manageable systematic uncertainty in the measurement that is the subject of the thesis. However, the expected precision on γ measurements will increase significantly in the coming decade, as both the LHCb [41] and Belle II [40] collaborations expect to make BPGBGSZ measurements that measure γ with a precision of 1–3°. Therefore a deeper understanding of the expected bias for these specific experiments is important.

This section details a study, where the equations of the previous section are evaluated numerically to all orders, and care is taken to realistically model the experiment specific conditions. The scope of the original analysis, published in Ref. [2], was a stand-alone paper that covers both LHCb and Belle II, and which therefore does not rely on full detector simulation. Instead the following approaches are taken to model the necessary input

- the experimental time-acceptance is modelled based on the detector geometry and typical neutral kaon momentum spectrum
- the material interaction is included, using the material budget information available in the technical design reports on each experiment
- both the time-acceptance and material interaction depends on the neutral kaon momentum, for which realistic distributions are estimated using the `RapidSim` simulation package [112].

Each input is described in detail in the following sections. The study has been repeated to assign a systematic uncertainty to the LHCb measurement in Chapter 4, with slight adjustments to match the exact fit setup and with the inputs above extracted from full LHCb simulation. This is described further in Section 3.3.7.

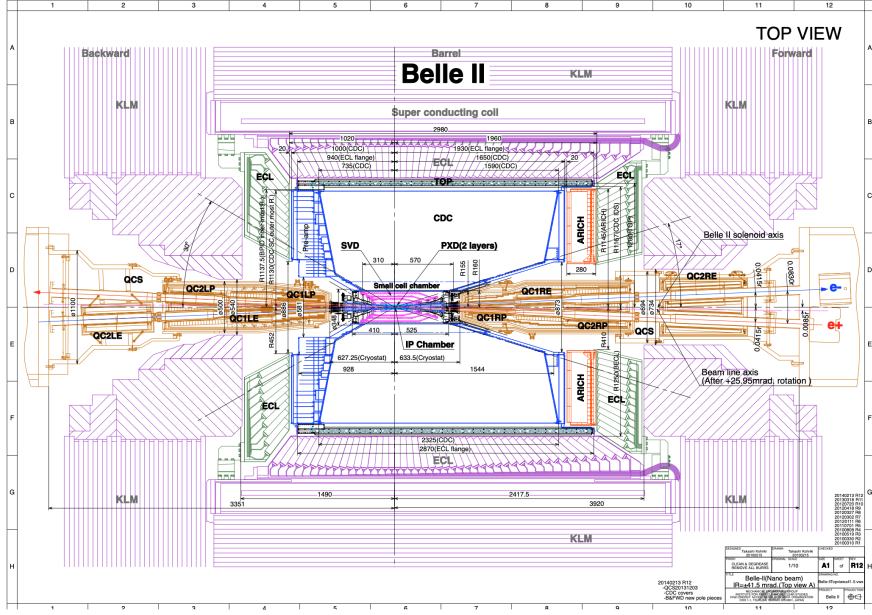


Figure 3.2: Schematic of the Belle II detector, reproduced from Ref. [40].

1431 3.3.1 Detector geometries

1432 The LHCb geometry and sub detectors are described in details in Chapter 2. In the
 1433 LHCb measurement discussed in Chapter 4, the K_S^0 mesons are reconstructed in
 1434 the $\pi^+\pi^-$ final state and two distinct categories of decay are considered, depending
 1435 on where in the detector the K_S^0 decay occurs. The categories have very different
 1436 decay-time acceptance, and therefore two scenarios are considered for LHCb: one
 1437 in which the decay products of the K_S^0 leave reconstructed tracks in both the silicon
 1438 vertex detector and downstream tracking detectors (denoted *long-long* or LL), and
 1439 one in which the decay products of the K_S^0 only leave tracks in the downstream
 1440 tracking detectors (denoted *down-down* or DD).

1441 The Belle II detector is a general purpose spectrometer, built to collect data
 1442 from asymmetric e^+e^- collisions made by the SuperKEKB accelerator in Japan [40].
 1443 A schematic of the detector is shown in Fig. 3.2. The relevant sub detectors for
 1444 the present study are the tracking detectors: a central silicon vertex detector,
 1445 comprised of a total of six layers within 140 mm of the beam, and a large volume
 1446 drift chamber with 56 wire layers, extending to a radius of 1130 mm [40]. A single
 1447 scenario is considered for Belle II, because essentially all the K_S^0 mesons produced
 1448 in signal decays in Belle II decay within the tracking volume, with more than 90 %
 1449 decaying in the vertex detector according to the studies described below. Thus,
 1450 three scenarios are considered in total: LL LHCb, DD LHCb, and Belle II.

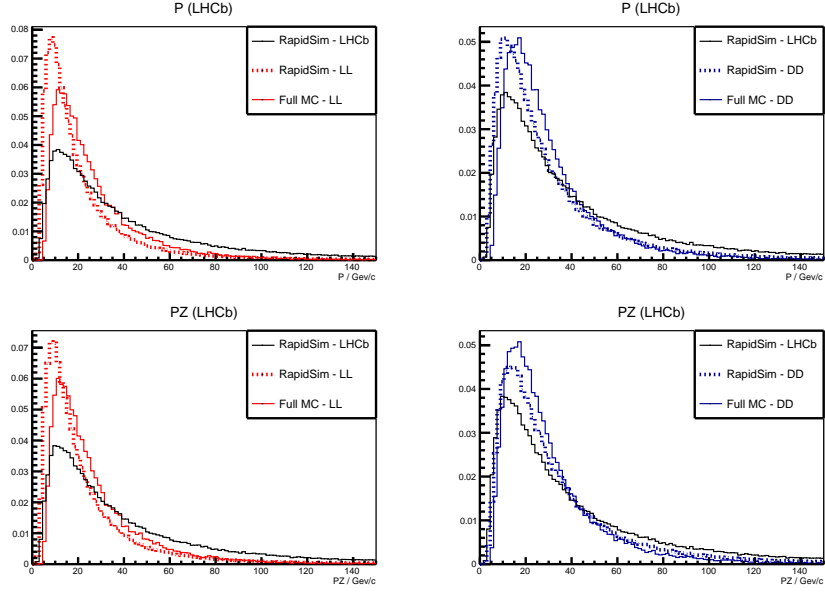


Figure 3.3: Momentum spectra for the K_S^0 meson in LHCb, as generated using **RapidSim** (black lines) directly, as well as reweighted to match decay time acceptance in the (red) LL and (blue) DD data categories of LHCb. The LHCb spectra are compared with the spectra in fully simulated signal decays, for both (dotted red lines) LL and (dotted blue lines) DD data categories.

3.3.2 Kaon momentum distributions

The neutral kaon momentum distributions are obtained using **RapidSim** [112], a simple tool to generate MC samples. **RapidSim** has an inbuilt capability to generate decays of B mesons with the kinematic distribution found in LHCb collisions and falling in the LHCb acceptance. However, the distributions need to be reweighted to take the kaon-decay-time acceptance into account. After being reweighted, the **RapidSim** momentum spectra are reasonably close to those found in full LHCb simulation samples of $B^\pm \rightarrow D(\rightarrow K_S^0\pi^+\pi^-)K^\pm$ decays, as seen in Fig. 3.3

At Belle II, the signal B mesons stem from decays of $\Upsilon(4S)$ mesons produced in asymmetric electron-positron collisions. This leads to substantially different decay kinematics in comparison to those found at LHCb. The momentum distribution in Belle II is estimated by letting **RapidSim** decay B mesons with a momentum of 1.50 GeV/ c along the z -axis using **RapidSim**, corresponding to the $\gamma\beta = 0.28$ boost of the centre-of-mass system in Belle II when operated at the $\Upsilon(4S)$ resonance [40]. A perfect 4π angular acceptance is assumed. It is not necessary to reweigh the Belle II momentum spectrum to account for the kaon-decay-time acceptance because all produced K_S^0 mesons decay in the tracking volume.

The resulting momentum distributions for the three types of sample are shown in Fig. 3.4.

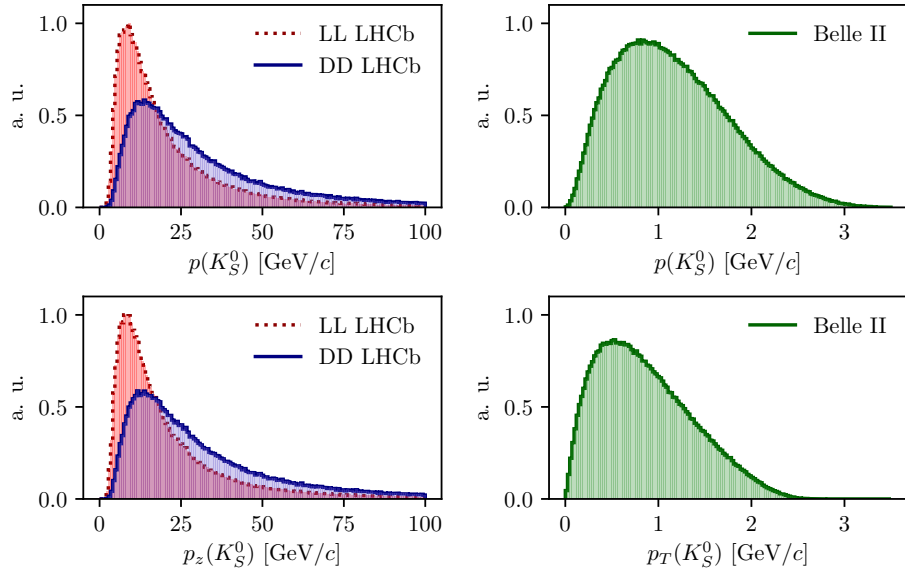


Figure 3.4: Momentum distributions for the LHCb (red dotted line) LL and (blue) DD categories, as well as (green) Belle II, obtained using `RapidSim`.

3.3.3 Experimental time acceptance

In order to model the experimental time acceptance, the time-dependent decay rates are only integrated over a finite time interval (τ_1, τ_2) . The intervals are defined for each of the three experimental categories, by requiring that a neutral kaon, if produced at $x = y = z = 0$ with momentum $p = (p_T, p_z)$, decays within the relevant part of the corresponding detector. For the LL LHCb category, it is required that the kaon decays before reaching $z_{max} = 280$ mm, corresponding to a decay where the decay products traverse at least 3 VELO segments (ignoring a number of widely spaced VELO segments placed at a distance of up to $z = 750$ mm from the interaction point) [79]. For the DD LHCb category a decay at $z \in [280, 2350]$ mm is required, corresponding to decay between the LL cut-off and the first downstream tracking station [119]. The time acceptance has a significant impact for the LHCb categories, where some 20 % of the kaons escape the tracking stations completely before decaying.

For Belle II, it is assumed that the K_S^0 reconstruction is similar to the Belle K_S^0 reconstruction, which is based on a neural network and reconstructs K_S^0 decays for which the decay product leave tracks in both the drift chamber and silicon vertex detectors, as well as decays that leave tracks in the drift chamber only [120, 121]. Therefore, the K_S^0 decay is required to be within $r_{max} = 1130$ mm of the beam axis, corresponding to a decay within the outer radius of the drift-chamber. In practice,

most of the kaons decay inside the silicon vertex detector, and requiring a decay before 1130 mm is essentially equivalent to having no time cut-off.

3.3.4 Detector material budget

The effect of the material interaction is governed by parameter $\Delta\chi$ of Eq. (3.16). The parameter varies along a given kaon path, as the kaon intersects detector components made of different materials. In these studies, the calculations are simplified by using a single average material parameter for each experimental scenario. The average material parameters can be estimated for a given experimental scenario by considering the type and length of material traversed by a kaon in the relevant sub-detector(s). The average value is estimated, by exploiting that $\Delta\chi$ is related to the forward scattering amplitude f (\bar{f}) of K^0 (\bar{K}^0) mesons in a given material [114, 115]

$$\Delta\chi = -\frac{2\pi\mathcal{N}}{m_K}(f - \bar{f}) = -\frac{2\pi(N_A\rho/A)}{m_K}(f - \bar{f}), \quad (3.38)$$

where $\mathcal{N} = N_A\rho/A$ is the scattering centre density of the material, m_K is the mass of the kaon state, A and ρ are the nucleon number and density of the material, and N_A is Avogadro's number. Measurements made for a range of nuclei [122] show that in the momentum range $p_K \in [20, 140] \text{ GeV}/c$

$$\left| \frac{f - \bar{f}}{p_K} \right| = 2.23 \frac{A^{0.758}}{p_K^{0.614}(\text{GeV}/c)} \text{ mb}, \quad \arg[f - \bar{f}] = -\frac{\pi}{2}(2 - 0.614), \quad (3.39)$$

where the phase of Δf is determined via a phase-power relation [123]. In the numerical studies presented here, Eq. (3.39) is also used for the low momentum neutral kaons in the Belle II calculations, as a more detailed modelling of the low momentum $\Delta\chi$ based on Ref. [124] is found to yield very similar results. The scattering centre density \mathcal{N} is approximated as being constant, equal to the average density along a neutral kaon path due to its intersection with different detector segments. This average is estimated using the simplifying assumption that the total detector material budget is due to silicon. In practice, $\mathcal{N} = N_A\rho/A$ is calculated using $A = 28$ and $\rho = f^{\text{Si}}\rho^{\text{Si}}$, where $f^{\text{Si}} < 1$ is the average fraction of a neutral kaon path length that is inside detector material, estimated via the known dimensions of the detector, the average nuclear interaction length seen by a track traversing it cf. the technical design reports [79, 85], and the nuclear interaction length of silicon $\lambda_I^{\text{Si}} = 465.2 \text{ mm}$ [31]. The average value of $r_\chi = \frac{1}{2}\frac{\Delta\chi}{\Delta\lambda}$, which governs the size of the matter regeneration effect, can be calculated for the three considered experimental scenarios and satisfy $|r_\chi^{\text{LL}}| = 2.7 \times 10^{-3}$, $|r_\chi^{\text{DD}}| = 2.2 \times 10^{-3}$, and $|r_\chi^{\text{Belle II}}| = 1.0 \times 10^{-3}$.

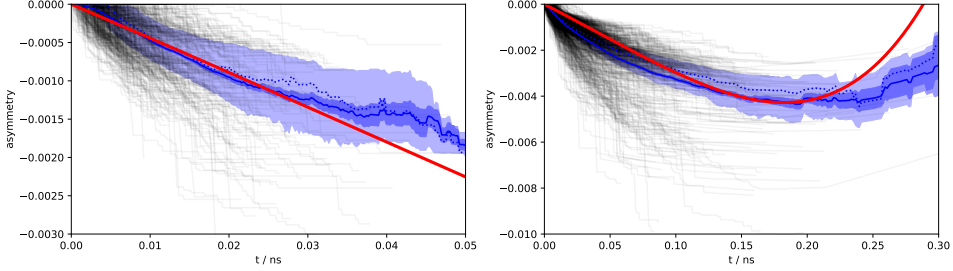


Figure 3.5: The asymmetry in Eq. (3.40) as a function of time for (left) LL and (right) DD K_S^0 tracks in a simulated LHCb sample. The black lines show individual tracks. The light blue area is the central 50 % quantile, the dark blue area is the 1σ uncertainty band on the mean. The red lines are calculated using the average $\Delta\chi$ values that are also used in the calculation of biases in BPGGSZ measurements.

1521 The neutral kaon tracks in LHCb generally pass through somewhere between
1522 zero (for a significant amount of the LL tracks) and a hundred (for some DD tracks)
1523 distinct detector segments. Therefore it is worth examining the degree to which
1524 using a single average $\Delta\chi$ value, obtained following the procedure outlined above,
1525 provides a reasonable description of the average material interaction. This can be
1526 done using full LHCb simulation, where the kaon state for a simulated track can be
1527 evaluated at all times, by applying Eq. (3.15) iteratively for each detector segment
1528 the track traverses, using a $\Delta\chi$ value appropriate for that segment. This is done
1529 in Fig. 3.5 for a simple observable: the yield asymmetry

$$A_{K^0} = \frac{|\psi_K^0(t)|^2 - |\psi_{\bar{K}^0}(t)|^2}{|\psi_K^0(t)|^2 + |\psi_{\bar{K}^0}(t)|^2}, \quad (3.40)$$

1530 where $\psi_K^0(t)$ ($\psi_{\bar{K}^0}(t)$) is the amplitude for an initial K^0 (\bar{K}^0) to decay to two pions at
1531 time t . In this calculation, it is assumed that $\epsilon = 0$ to isolate the material effect with
1532 no asymmetry contribution from the inherent CP -violation in the neutral kaon sector.
1533 While the track-by-track asymmetries are found to differ significantly depending on
1534 the exact detector segments a track intersects, the average asymmetry is seen to
1535 evolve smoothly as a function of decay time, and in reasonable agreement with the
1536 asymmetry value that is calculated using the average $\Delta\chi$ values estimated above.

1537 The LHCb detector is undergoing a significant upgrade prior to the start of
1538 the LHC Run 3. However, the material budget and geometry of the relevant sub-
1539 detectors will be similar to the sub-detectors used during Run 1 and 2 [125, 126].
1540 Hence the results of this study will be valid for measurements during the upgrade
1541 phases of LHCb, even though the detector parameters presented in this section
1542 relate to the original LHCb detector.

¹⁵⁴³ **3.3.5 Calculation procedure**

¹⁵⁴⁴ The main idea in the bias study is to calculate the BPGBSZ bin yields including
¹⁵⁴⁵ the full effect of neutral kaon CP violation and material, fit them using the default
¹⁵⁴⁶ equations of Chapter 1, and obtain the bias $\Delta\gamma = \gamma - \gamma^0$ due to the kaon effects not
¹⁵⁴⁷ being considered in the parameter extraction. For the purpose of Ref. [2], a simple
¹⁵⁴⁸ fit setup of a single $B^\pm \rightarrow Dh^\pm$ mode is investigated, where the K_i parameters are
¹⁵⁴⁹ determined in a control channel with the relevant experimental acceptance. This
¹⁵⁵⁰ setup is modified in the study used to assign a systematic uncertainty on the LHCb
¹⁵⁵¹ measurement of Chapter 4, as described in Section 3.3.7 below.

¹⁵⁵² In practice, the amplitude model for $D^0 \rightarrow K_S^0 \pi^+ \pi^-$ decays in Ref. [51] is taken
¹⁵⁵³ to represent the $A_1(s_{+-})$ amplitude. Then $A_2(s_{+-})$ is obtained as described in
¹⁵⁵⁴ Section 3.2.2. In terms of A_1 and A_2 , the amplitudes $A_{S(L)}^{(\bar{D})}(s_{+-})$ can be expressed
¹⁵⁵⁵ and related via Eqs. (3.25) and (3.26), and the full signal decay amplitudes as a
¹⁵⁵⁶ function of phase-space coordinates, time, and the material interaction parameter
¹⁵⁵⁷ $\Delta\chi$ can be calculated for a given set of input parameters $(\gamma^0, r_B^0, \delta_B^0)$. The squared
¹⁵⁵⁸ decay amplitudes are then integrated over phase space and the kaon decay times
¹⁵⁵⁹ to obtain the binned signal yield.

¹⁵⁶⁰ The signal yields depend on the momentum via the time-acceptance parameters
¹⁵⁶¹ τ_1 and τ_2 , and because the material interaction parameter $\Delta\chi$ is momentum
¹⁵⁶² dependent. Therefore, the yields are averaged over the K_S^0 momentum distributions
¹⁵⁶³ of LHCb and Belle II.

¹⁵⁶⁴ The parameters x_\pm and y_\pm are determined by a maximum likelihood fit to the
¹⁵⁶⁵ calculated yields, after which the fit result and covariance matrix are interpreted
¹⁵⁶⁶ in terms of the physics parameters (γ, r_B, δ_B) using another maximum likelihood
¹⁵⁶⁷ fit [127]. In the fits, the K_i are obtained using the definition $K_i = K_i^{\text{meas}} =$
¹⁵⁶⁸ $(N_i^D + N_{-i}^{\bar{D}})/(\sum_j N_j^D + N_{-j}^{\bar{D}})$, in terms of the expected yields N_i^D ($N_i^{\bar{D}}$) of a flavour-
¹⁵⁶⁹ tagged D^0 (\bar{D}^0) decays in bin i of the D decay phase space, calculated as described
¹⁵⁷⁰ above for $r_B^0 = 0$. This corresponds to experimentally measuring the K_i in a control
¹⁵⁷¹ channel, and takes the effect of neutral kaon CP violation and material interaction
¹⁵⁷² on K_i measurements into account, as well the experimental time acceptance. The
¹⁵⁷³ (c_i, s_i) are calculated using $A_1(s_{+-})$ and the experimental time acceptance is taken
¹⁵⁷⁴ into account in this calculation as well.

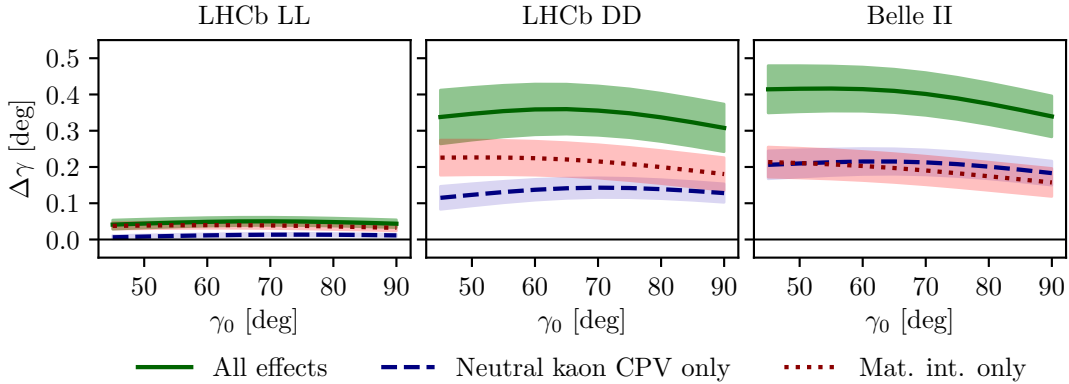


Figure 3.6: The bias $\Delta\gamma$ as a function of input γ_0 for (left) the LL LHCb category, (centre) the DD LHCb category, and (right) Belle II. The bias is calculated due to (blue, dashed line) neutral kaon CP violation alone, (red, dotted line) material interaction alone, and (green line) both effects. The shaded region shows the estimated 1σ uncertainty band.

1575 3.3.6 Results

1576 The obtained bias $\Delta\gamma$ is shown as a function of input γ^0 for the various experimental
1577 conditions in Fig. 3.6. The calculations are made using $(r_B^0, \delta_B^0) = (0.1, 130^\circ)$,
1578 approximately equal to the physics parameters relevant for $B^\pm \rightarrow DK^\pm$ decays [27,
1579 39]. The bias does not vary significantly with γ^0 in the plotted range, which includes
1580 the world average value of direct γ measurements as well as the values obtained in
1581 full unitarity-triangle fits [27, 38, 39], and for all cases, the bias is found to be below
1582 0.5° , corresponding to relative biases of about half a percent. Thus the biases are
1583 of $O(r\epsilon/r_B)$ as expected, given the arguments of Section 3.2.3. The contributions
1584 from the individual K_S^0 CPV and material interaction effects are also shown. It
1585 is seen that the neutral kaon CP violation and material interaction effects leads
1586 to approximately equal biases in all three cases.

1587 Given the decay-time acceptance and momentum distribution for each experimen-
1588 tal category, the mean life time, $\langle\tau\rangle$, of the reconstructed kaons can be calculated.
1589 In terms of the K_S^0 lifetime $\tau_{K_S^0} = (0.895 \pm 0.004) \times 10^{-11}$ s [31], $\langle\tau_{LL}\rangle \simeq 0.1\tau_{K_S^0}$
1590 for the LHCb LL category, $\langle\tau_{DD}\rangle \simeq 0.8\tau_{K_S^0}$ for the LHCb DD category, and at
1591 Belle II $\langle\tau_{Belle\,II}\rangle \simeq \tau_{K_S^0}$. The difference in average kaon lifetime is reflected in
1592 the observed biases, which are found to be larger in the samples with longer lived
1593 kaons. The very small effect in the LL category is to be expected because the
1594 CP -violation effect due to K_S^0 not being CP -even is approximately cancelled by
1595 the CP -violation effect arising from $K_S^0 - K_L^0$ interference for kaons with decay
1596 times much smaller than $\tau_{K_S^0}$ [118].

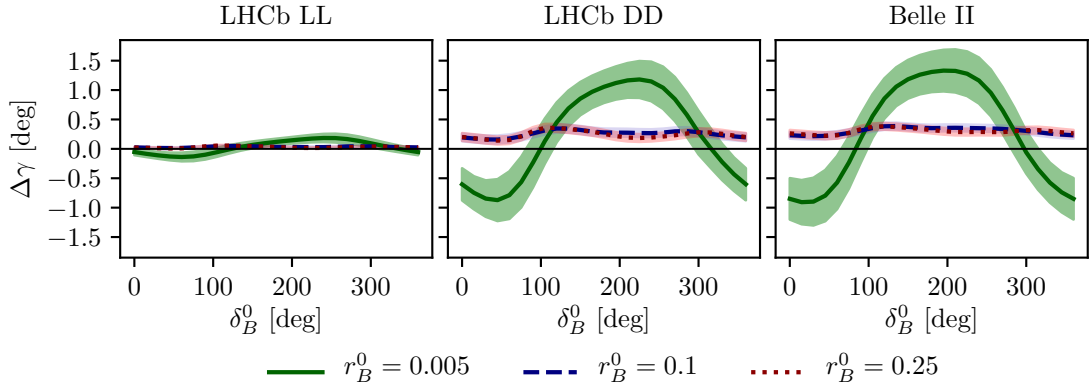


Figure 3.7: The bias $\Delta\gamma$ as a function of input δ_B for (left) the LL LHCb category, (centre) the DD LHCb category, and (right) Belle II. The bias is calculated for $\gamma = 75^\circ$ and (green line) $r_B = 0.005$, (blue, dashed line) $r_B = 0.1$, and (red, dotted line) $r_B = 0.25$. The shaded region shows the estimated 1σ uncertainty band.

1597 The uncertainty bands in Fig. 3.6 are calculated by repeating the study while
1598 varying some of the inputs. The model dependence of the predicted biases is
1599 probed by repeating the study using two other amplitude models as input for
1600 $A_1(s_{+-})$ and $A_2(s_{+-})$: the model published in Ref. [61] and the model included in
1601 EVTGEN [107]. When defining $A_2(s_{+-})$ in terms of $A_1(s_{+-})$, there is an uncertainty
1602 due to the unknown (r_k, δ_k) parameters used to describe the $\pi\pi$ resonance terms.
1603 This uncertainty is assessed by making the study with several different random
1604 realisations of the parameter set. The studies are repeated while varying the time
1605 acceptances and material densities with $\pm 10\%$. There is an additional uncertainty
1606 due to the use of simulation samples generated with `RapidSim` to describe the kaon
1607 momentum distribution, in lieu of full detector simulations.

1608 There is also an uncertainty from the use of (c_i, s_i) as calculated using $A_1(s_{+-})$.
1609 It is to be expected that the measured values (\hat{c}_i, \hat{s}_i) from the CLEO collaboration
1610 differ by those calculated using $A_1^D(s_-, s_+)$ by terms of $O(\epsilon)$ due to neutral kaon
1611 CP violation, which is not taken into account in the measurement [69]. These
1612 corrections can be calculated via a procedure analogous to the one used to estimate
1613 the corrections on measurements of γ in this paper. However, as these corrections
1614 are much smaller than the experimental uncertainties in the measurement, they
1615 have not been studied further.

1616 For the purpose of this thesis, it is important to consider the bias in measurements
1617 that use $B^\pm \rightarrow D\pi^\pm$ decays as well, and other B decay modes can also be used in
1618 BPFGSZ measurements, such as $B^\pm \rightarrow D^*K^\pm$, $B^\pm \rightarrow DK^{*\pm}$, and $B^0 \rightarrow DK^{*0}$.
1619 For the purpose of the study presented here, the main difference between the decay

channels is that they have different values of r_B and δ_B . Figure 3.7 shows $\Delta\gamma$ as a function of input δ_B^0 , for $\gamma^0 = 75^\circ$ and three different values of r_B^0 . Aside from $r_B^0 = 0.1$, the results are shown for $r_B^0 = 0.005$, which corresponds to the expectation in $B^\pm \rightarrow D\pi^\pm$ decays [47] and $r_B^0 = 0.25$, which corresponds to $B^0 \rightarrow DK^{*0}$ decays [128]. The most notable feature is that the biases are significantly larger in the $B^\pm \rightarrow D\pi^\pm$ case. This is expected: the r_B^0 dependent behaviour is governed by the relative importance of different $O(r\epsilon)$ correction terms to the phase-space distribution. There are terms of both $O(r_A\epsilon)$ and $O(r_B\epsilon)^3$, which lead to expected biases of size $O(r_A\epsilon/r_B)$ and $O(r_B\epsilon/r_B) = O(\epsilon)$, respectively, cf. the discussion of Section 3.2.3. In the $B^\pm \rightarrow D\pi^\pm$ case, the $O(r_A\epsilon)$ correction terms dominate because $r_A/r_B \simeq (0.05/0.005) = 10$. This explains the relatively large bias, as $|r_A\epsilon/r_B^{D\pi}| \simeq 4\%$. The bias is seen to be up to $\pm 1.5^\circ$, but only about $+0.2^\circ$ with the expected value of $\delta_B^{D\pi} \simeq 300^\circ$ [47, 127]. These biases are *much smaller* than the precision on γ that is obtainable in a $B^\pm \rightarrow D\pi^\pm$ analysis with current experimental yields, and do thus not pose a problem. In the $r_B^0 = 0.1$ and $r_B^0 = 0.25$ cases the $O(r_B\epsilon)$ correction terms dominate, and the biases are of $O(\epsilon)$, independent of the r_B^0 value. Therefore both cases have biases of similar size.

Further, it is clear that the biases depend on δ_B^0 and that the oscillation period of the δ_B dependence is different between the $r_B^0 = 0.005$ case and the $r_B^0 \in \{0.1, 0.25\}$ cases. It is to be expected that $\Delta\gamma$ oscillates as a function of δ_B^0 , because δ_B^0 enters the yield equations via $\cos(\delta_B^0 \pm \gamma)$ and $\sin(\delta_B^0 \pm \gamma)$ terms. As explained above, the $O(r_A\epsilon)$ terms dominate the $B^\pm \rightarrow D\pi^\pm$ bias, and these are independent of δ_B^0 . The $O(r_B\epsilon)$ terms, however, are important for the bias corrections for larger r_B values, and the terms include factors of $\cos(\delta_B^0 \pm \gamma)$ and $\sin(\delta_B^0 \pm \gamma)$. This explains the different bias dependence on δ_B^0 .

While the input value of $\gamma^0 = 75^\circ$ was chosen for these studies, there is minimal variation in the results if another value of γ^0 in the range $[60^\circ, 85^\circ]$ is used.

3.3.7 Coupled $B^\pm \rightarrow DK^\pm$ and $B^\pm \rightarrow D\pi^\pm$ measurements

The studies presented above have been extended on two accounts in order to assign a systematic uncertainty to the LHCb measurement presented in Chapter 4. Firstly, full LHCb simulation has been used to obtain the momentum distributions, as well as to fit a better description of the time acceptance and the reconstruction efficiency profile over the D -decay phase space. Secondly, the fit setup is modified

³There are similar terms of $O(r_A r_\chi)$ and $O(r_B r_\chi)$, but as ϵ and r_χ are of the same order of magnitude, these terms can be treated completely analogously to the $O(r_A\epsilon)$ and $O(r_B\epsilon)$ terms, and have been left out of the discussion for brevity.

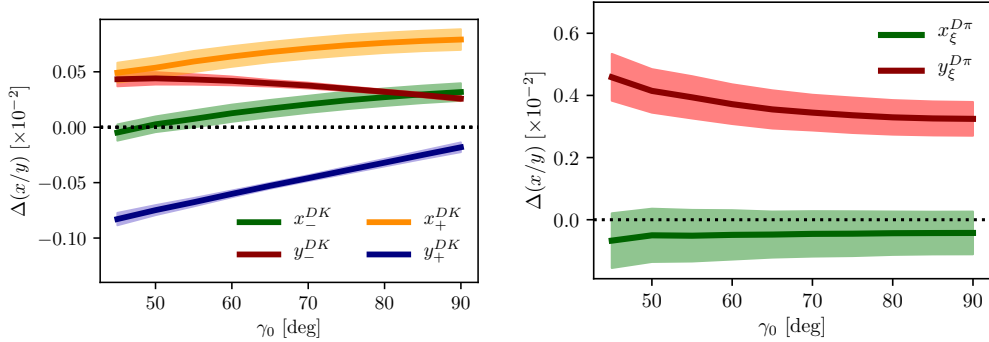


Figure 3.8: The bias on (left) the $B^\pm \rightarrow DK^\pm$ and (right) $B^\pm \rightarrow D\pi^\pm$ CP -violation observables in the LHCb DD category, evaluated in bias studies with inputs based on full LHCb simulation, calculated as a function of input γ_0 .

to correspond to the experimental approach described in Section 1.4 and Chapter 4: the signal yields are calculated for both the $B^\pm \rightarrow DK^\pm$ and $B^\pm \rightarrow D\pi^\pm$ channels, and fitted in a combined fit to obtain $(x_\pm^{DK}, y_\pm^{DK}, x_\xi^{D\pi}, y_\xi^{D\pi})$, where the F_i parameters are allowed to float in the fit. The biases obtained for each observable are shown in Fig. 3.8, evaluated using the time-acceptance, momentum distribution, and material budget relevant for the DD category (since the effect in the LL category is much smaller). As will be clear in Chapter 4, these biases are all significantly smaller than the corresponding statistical uncertainties. Thus, the effects of neutral kaon CP violation and material interactions contribute a manageable systematic uncertainty in current BPGGSZ measurements, even if the $B^\pm \rightarrow D\pi^\pm$ channel is promoted to a signal channel.

As the statistical uncertainty becomes comparable with the bias effects described in this chapter, the systematic uncertainty should be assigned by a more accurate study, incorporating the traversed material on a track-by-track basis in full detector simulation. Such a detailed calculations can also be used to apply a bias correction if desired.

3.4 Concluding remarks

The analysis presented in this chapter has shown the expected impact of neutral kaon CP violation and material interaction on current BPGGSZ measurements to be small compared to the statistical uncertainties; first by simple order-of-magnitude estimates and then by a detailed calculation of the expected effect in LHCb and Belle II.

While the calculations were made for the case of $D \rightarrow K_S^0 \pi^+ \pi^-$ decays, the BPGGSZ approach can of course also be applied in other D -decay final states,

such as $D \rightarrow K_S^0 K^+ K^-$ and $D \rightarrow K_S^0 \pi^+ \pi^- \pi^0$. The biases on measurements of γ based the D decay phase-space distributions should be of similar size in these decay channels. The impact on γ measurements based on the phase-space-integrated yield asymmetry can be expected to be tens of degrees for the $D \rightarrow K_S^0 K^+ K^-$ channel, where the yield asymmetry is expected to be around 2 %, for the reasons explained in Section 3.2.3. The $D \rightarrow K_S^0 \pi^+ \pi^- \pi^0$ decay, however, is dominantly CP -odd [129], and the bias in measurements based on the total asymmetry is therefore expected to be $O(\epsilon/r_B)$, ie. a few degrees [42]. More precise calculations of the biases would require a repeat of the study included here, with relevant amplitude models and binning schemes in place.

The chapter focuses on the model-independent, binned approach that is the subject of the thesis. However, the underlying mechanism that determines the scale of the bias, namely that the phase-space *distribution* of signal decays is unaffected at $\mathcal{O}(\epsilon)$ and $\mathcal{O}(r_\chi)$, is independent on the exact measurement approach. Therefore it is expected that amplitude-model-based measurements and measurements made with new unbinned methods such as those in Ref [68] will be similarly biased if kaon CP violation and regeneration are not accounted for.

4

1694

1695

1696

A BPGBGSZ measurement of γ with $B^\pm \rightarrow Dh^\pm$ decays

1697 This chapter describes a model-independent BPGBGSZ measurement of γ with
1698 $B^\pm \rightarrow DK^\pm$ and $B^\pm \rightarrow D\pi^\pm$ decays where $D \rightarrow K_S^0\pi^+\pi^-$ and $D \rightarrow K_S^0K^+K^-$,
1699 commonly denoted $B^\pm \rightarrow D(\rightarrow K_S^0h^+h^-)h'^\pm$ decays. The measurement is made
1700 with the full LHCb data set collected during Run 1 and 2 of the LHC, corresponding
1701 to an integrated luminosity of about 9 fb^{-1} . The analysis is under review for
1702 publication in the Journal of High Energy Physics at the time of writing [1]
1703 (one can hope).

1704 4.1 Candidate reconstruction and selection

1705 The $B^\pm \rightarrow D(\rightarrow K_S^0h^+h^-)h'^\pm$ candidates are constructed during the offline *stripping*
1706 stage described in Section 2.3.3. The candidates are defined by first combining
1707 tracks to form a $K_S^0 \rightarrow \pi^+\pi^-$ vertex, then a $D \rightarrow K_S^0h^+h^-$ vertex, and finally
1708 the $B^\pm \rightarrow Dh'^\pm$ candidate. Each final state track is required to satisfy certain
1709 momentum thresholds and track-quality requirements, and to be separated from all
1710 primary interaction vertices. Each decay vertex is required to satisfy a fit-quality
1711 threshold and to be separated from the primary vertex. Momentum thresholds
1712 are applied to the composite particles and they are required to have reconstructed
1713 invariant masses close to their known masses¹ except that the B candidate is
1714 required to have a reconstructed invariant mass in the interval $4750\text{--}7000\text{ MeV}/c^2$.

¹The exact mass window depends on the particle type and reconstruction category; narrower mass windows are applied at a later stage, as described below.

1715 The B candidate is required to satisfy $\chi^2_{\text{IP}} < 25$, where χ^2_{IP} is the difference in χ^2
1716 value of the primary vertex fit, when the vertex is formed with- and without the B
1717 candidate. As the final *stripping* stage, a multivariate algorithm is applied to the
1718 formed B candidate to reduce the amount of random track combinations, denoted
1719 combinatorial background, even further than the aforementioned requirements.

1720 Two data categories are defined, depending the tracks used to form the K_S^0
1721 candidate: the LL category where both pions are long tracks, and DD category where
1722 both pions are downstream tracks, using the track classifications of Section 2.2.1.

1723 Each candidate is re-analysed with the `DecayTreeFitter` (DTF) frame work [130],
1724 where a simultaneous fit of the full decay chain is made with a number of constraints
1725 applied: the momenta of the composite D and K_S^0 particles are required to form
1726 invariant masses exactly equal to the known particle masses [31], and the momentum
1727 of the B candidate is required to point in the direction defined by the B decay
1728 vertex and the primary vertex. This refit results in improved resolution of the
1729 invariant masses of the composite particles and, very importantly, of the Dalitz
1730 coordinates in the D -decay phase space. It also ensures that all candidates fall in the
1731 kinematically allowed region of the D -decay phase space. Unless otherwise specified,
1732 all results in this chapter are based on the refitted track momenta; for reasons
1733 explained below, some studies have to be based on parameters that are obtained
1734 without the constraints described above, or with only a subset of them applied.

1735 Following the stripping stage, the further selection of signal candidates is
1736 performed in three steps: an initial set of requirements that remove a large fraction
1737 of candidates that are very likely to be background and veto a number of specific
1738 backgrounds, the application of a multivariate analysis algorithm designed to allow
1739 for filtering combinatorial background, and finally a set of particle-identification
1740 requirements. The requirements are summarised in Table 4.1, and each step is
1741 described in detail in the following sections.

1742 4.1.1 Initial requirements

1743 At the hardware trigger level, it is required that a particle associated with the
1744 signal decay triggered the hadronic L0 trigger (classifying the event as *Trigger on*
1745 *Signal*, or TOS), or that the level-0 trigger decision was caused by a particle that
1746 is not associated with the signal decay (e^\mp *Trigger Independent of Signal*, or TIS).
1747 The inclusion of the latter category increases the data sample about 50 %. At the
1748 software trigger level, a particle belonging to the signal decay is required to have
1749 caused one of each of the inclusive HLT1 and HLT2 lines to accept the events.
1750 Specifically, the Run 1 events are required to be TOS on the `HLT1TrackAllL0` and

Table 4.1: Summary of requirements applied to data. The base requirements are applied to all data samples before training or applying the BDT.

Base requirements		
Variable	Cut	Comment
Bachelor momentum, p	$< 100 \text{ GeV}/c$	
Bachelor has RICH	<i>true</i>	
K^\pm in D decay: momentum, p	$< 100 \text{ GeV}/c$	In $D \rightarrow K_S^0 K^+ K^-$
K^\pm in D decay: have RICH	<i>true</i>	In $D \rightarrow K_S^0 K^+ K^-$
DecayTreeFit converged	<i>true</i>	
D mass	$m_{D^0} \in m_{D^0}^{PDG} \pm 25 \text{ MeV}/c^2$	From DTF with constrained K_S^0 mass
K_S^0 mass	$m_{K_S^0} \in m_{K_S^0}^{PDG} \pm 15 \text{ MeV}/c^2$	From DTF with constrained D^0 mass

Background suppressing requirements		
Variable	Cut	Comment
K_S^0 flight distance χ^2	> 49	for LL only
$\Delta z_{\text{significance}}^{DB}$	> 0.5	for all candidates

PID requirements		
Channel	Cut	Comment
$B^\pm \rightarrow DK^\pm$	PIDK > 4	for bachelor
$B^\pm \rightarrow D\pi^\pm$	PIDK < 4	for bachelor
$B^\pm \rightarrow Dh^\pm$	IsMuon = 0	for bachelor
$B^\pm \rightarrow D(\rightarrow K_S^0 \pi^+ \pi^-)h^\pm$	PIDe < 0 & IsMuon = 0	for charged D decay products
$B^\pm \rightarrow D(\rightarrow K_S^0 K^+ K^-)h^\pm$	PIDK > -5 & IsMuon = 0	for charged D decay products

BDT requirements		
Channel	Cut	Comment
Run 1, DD	> 0.6	
Others	> 0.8	

1751 Hlt2Topo{2, 3, 4}BodyBBDT lines and the Run 2 events are required to be TOS on
 1752 the Hlt1{Track, TwoTrack}MVA and Hlt2Topo{2, 3, 4}Body lines. These trigger
 1753 lines were described in Section 2.3.

1754 Before any processing of the data, a loose preselection is applied to remove
 1755 obvious background candidates. The reconstructed D (K_S^0) mass is required to
 1756 be within 25 (15) MeV/c^2 of the known values [31]. The *companion* particle, the
 1757 pion or kaon produced in the $B^\pm \rightarrow Dh^\pm$ decay, is required to have associated
 1758 RICH information and a momentum less than $100 \text{ GeV}/c$; this ensures good particle-
 1759 identification performance. Finally, all of the DTF fits of the full decay chain
 1760 are required to have converged properly.

1761 Two additional requirements are made at this stage in order to suppress specific
 1762 backgrounds. In order to suppress decays of the type $B^\pm \rightarrow K_S^0 h^+ h^- h'^\pm$ with
 1763 no intermediate D meson, so called *charmless* decays, it is required that the
 1764 significance of the z -separation of the D^0 decay vertex and the B^\pm decay vertex
 1765 is above 0.5 . The significance of the z -separation of the D^0 decay vertex and

1766 the B^\pm decay vertex is defined as

$$\Delta z_{\text{significance}}^{D-B} = \frac{z_{vtx}^D - z_{vtx}^B}{\sqrt{\sigma^2(z_{vtx}^D) + \sigma^2(z_{vtx}^B)}}. \quad (4.1)$$

1767 This source of background described further in section 4.3.1. In order to suppress
1768 a background from $D \rightarrow 4\pi$ and $D \rightarrow \pi\pi KK$ decays, it is required that the K_S^0
1769 flight distance χ_{FD}^2 is greater than 49, where

$$\chi_{\text{FD}}^2 = \left(\frac{\Delta r}{\sigma(\Delta r)} \right)^2, \quad (4.2)$$

1770 and Δr is the measured flight distance of the K_S^0 meson. This background is
1771 described in further detail in section 4.3.2.

1772 4.1.2 Boosted decision tree

1773 A Gradient Boosted Decision Tree [131] (abbreviated BDT in the following) is
1774 applied to classify each candidate on a scale from -1 to $+1$ as signal-like ($+1$)
1775 or combinatorial-background-like (-1), based on the values of a number of input
1776 parameters for candidate in question. The BDT is implemented in the TMVA
1777 frame work [132, 133].

1778 A boosted decision tree classifier consists of a number of sequentially trained
1779 decision trees, each of which classify events as either signal or background. Each tree
1780 bases the decision on an individual subset of variables, out of an overall set of input
1781 variables. At each training step, the input events are weighted when training a new
1782 tree, so that events that the already-trained trees classify incorrectly are given a
1783 higher weight; this is denoted boosting. The term *gradient boosting* denotes a specific
1784 weight calculation scheme [133]. The final score is the average over all decision trees.

1785 The full set of input variables are given in Table 4.2. It includes the momenta
1786 of particles in the decay; a number of geometric parameters such a absolute and
1787 relative vertex positions, and distances of closest approach between tracks; χ_{IP}^2
1788 values for a number of particles in the decay chain; the χ^2 per degree of freedom
1789 of the DTF refit; DIRA values, which denote the angle between the fitted particle
1790 momenta and the vector spanned by it's production ad decay vertices; and finally
1791 an isolation variable, defined as

$$A_{p_T} = \frac{p_T(B) - \sum p_T(\text{other})}{p_T(B) + \sum p_T(\text{other})} \quad (4.3)$$

1792 where the sum is over all other tracks in a cone around the B -candidate. The cone
1793 is defined as being within a circle with a radius of 1.5 units around the B candidate

1794 in the (η, ϕ_{azim}) -plane. This variable is highly efficient in rejecting combinatorial
1795 background. Two algorithms are trained, one for the LL category of K_S^0 mesons and
1796 one for the DD category, because some input parameters relate to the K_S^0 meson
1797 and have very different distributions between the two categories.

Table 4.2: Input parameter set used in BDTG trained to separate signal and combinatorial background, sorted according to importance in LL BDT.

Variable name	Importance LL/DD (Rank in DD)	Description
$\log(1-K_{\text{S}}\text{DIRA_BPV})$	7.2 % / 3.5 % (16)	$\log \cos \theta_{\text{DIRA}}$ for K_{S}^0
$\log(B_{\text{U}}\text{RHO_BPV})$	5.7 % / 5.5 % (5)	Radial distance of B vertex to beam line
$\log(\text{Bach_PT})$	5.2 % / 6.9 % (1)	p_T of the bachelor particle
$\log(1-D_{\text{O}}\text{DIRA_BPV})$	4.9 % / 5.8 % (4)	$\log \cos \theta_{\text{DIRA}}$ for D
$\log(1-B_{\text{U}}\text{DIRA_BPV})$	4.9 % / 6.4 % (3)	$\log \cos \theta_{\text{DIRA}}$ for B^\pm
$\log(D_{\text{O}}\text{RHO_BPV})$	4.8 % / 5.3 % (6)	Radial distance of D vertex to beam line
Bu_PTASY_1.5	4.7 % / 4.9 % (7)	Asymmetry parameters of B^\pm
$\log(D_{\text{O}}\text{PT})$	4.7 % / 6.6 % (2)	p_T of the D meson
$\log(\text{Bu_constDOKSPV_CHI2NDOF})$	4.2 % / 4.5 % (9)	$\chi^2/\text{d.o.f}$ of kinematical refit with DecayTreeFitter
$\log(\text{Bu_FDCHI2_OWNPV})$	3.9 % / 4.1 % (11)	Flight distance χ^2 of the B^\pm
$\log(\max_{\text{Ksh1h2_IPCHI2_OWNPV}})$	3.9 % / 3.0 % (20)	Largest χ^2_{IP} of the K_{S}^0 decay products
$\log(D_{\text{O}}\text{IPCHI2_OWNPV})$	3.8 % / 3.3 % (17)	χ^2_{IP} of the D
$\log(\min_{\text{Ksh1h2_IPCHI2_OWNPV}})$	3.7 % / 0.9 % (26)	Smallest χ^2_{IP} of the K_{S}^0 decay products
$\log(\text{Bu_P})$	3.7 % / 3.9 % (12)	p of the B^\pm meson
$\log(\text{Bu_IPCHI2_OWNPV})$	3.6 % / 4.6 % (8)	χ^2_{IP} of the B^\pm
Bu_MAXDOCA	3.6 % / 3.3 % (18)	"Distance of closest approach" for B^\pm vertex
$\log(\text{Bach_IPCHI2_OWNPV})$	3.3 % / 4.3 % (10)	χ^2_{IP} of the bachelor particle
$\log(\text{Bu_PT})$	3.3 % / 3.7 % (14)	p_T of the B^\pm meson
$\log(\max_{\text{h1h2_IPCHI2_OWNPV}})$	3.1 % / 3.8 % (13)	Largest χ^2_{IP} of the D decay products
$\log(\min_{\text{h1h2_IPCHI2_OWNPV}})$	3.0 % / 3.4 % (19)	Smallest χ^2_{IP} of the D decay products
$\log(K_{\text{S}}\text{VTXCHI2DOF})$	2.9 % / 2.3 % (21)	χ^2 of vertex fit for K_{S}^0
$D_{\text{O}}\text{MAXDOCA}$	2.9 % / 1.0 % (25)	"Distance of closest approach" for D vertex
$\log(D_{\text{O}}\text{VTXCHI2DOF})$	2.7 % / 1.6 % (24)	χ^2 of vertex fit for D
$\log(D_{\text{O}}\text{P})$	2.7 % / 1.8 % (22)	p of the D meson
$\log(\text{Bach_P})$	2.2 % / 3.6 % (15)	p of the bachelor particle
$\log(\text{Bu_VTXCHI2DOF})$	1.8 % / 1.7 % (23)	χ^2 of vertex fit for B^\pm

The BDTs are trained and tested with input samples representing typical signal and background decay candidates: a signal sample that consists of simulated $B^\pm \rightarrow D(\rightarrow K_S^0\pi^+\pi^-)\pi^\pm$ decays corresponding to the LHCb running conditions for the years 2012–2018, and a sample of combinatorial background candidates from real data, where the reconstructed invariant mass of the B meson is larger than 5800 MeV/ c^2 . The candidates in both samples were required to have passed the initial requirements described in the preceding section. The input-parameter distributions in the signal and background training samples are shown in Figs. 4.1 and 4.2. The signal and background samples are each split into two before the training stage: one sub sample, the training sample, is used to train the BDT, after which the trained algorithm is applied to the other sub sample, the test sample. The classifier is found to perform well on the test sample, not just the training sample, which ensures that it does not suffer significant overtraining. The BDT output distribution are shown for both test and training samples in Fig. 4.3, where it is clear that the classifier very effectively separates signal and background candidates.

Each candidate in data is classified using the BDT, and candidates that are assigned a score below some threshold value are discarded. The threshold values are chosen in a set of pseudo experiments, such that the expected sensitivity to γ is maximised. This is done by performing preliminary fits to the data set for a range of different BDT threshold values, then generating many pseudo data sets with the obtained yields, and applying the full fit and interpretation procedure described in Sections 4.4–4.7 to each data set. Thus, the expected uncertainty on γ is obtained for a range of threshold values. The procedure is applied independently for the LL and DD categories, as well as for the Run 1 and Run 2 data sets, because some parameter distributions differ slightly between the two runs. The optimal threshold values are found to be 0.8 in all situations, except for LL candidates in Run 1 where it is 0.6. This is illustrated in Fig. 4.4 where the results of the threshold scans are shown. The same classifier is applied to both $B^\pm \rightarrow D\pi^\pm$ and $B^\pm \rightarrow DK^\pm$ candidates, and both D final state categories. While the classifiers were trained using samples of $B^\pm \rightarrow D(\rightarrow K_S^0\pi^+\pi^-)\pi^\pm$ simulation and data, the decays are similar enough that no significant improvement in performance was obtained when considering a more elaborate setup. Across all categories, the requirement on the BDT output is found to remove approximately 98 % of the combinatorial background, while being approximately 93 % efficient on signal.

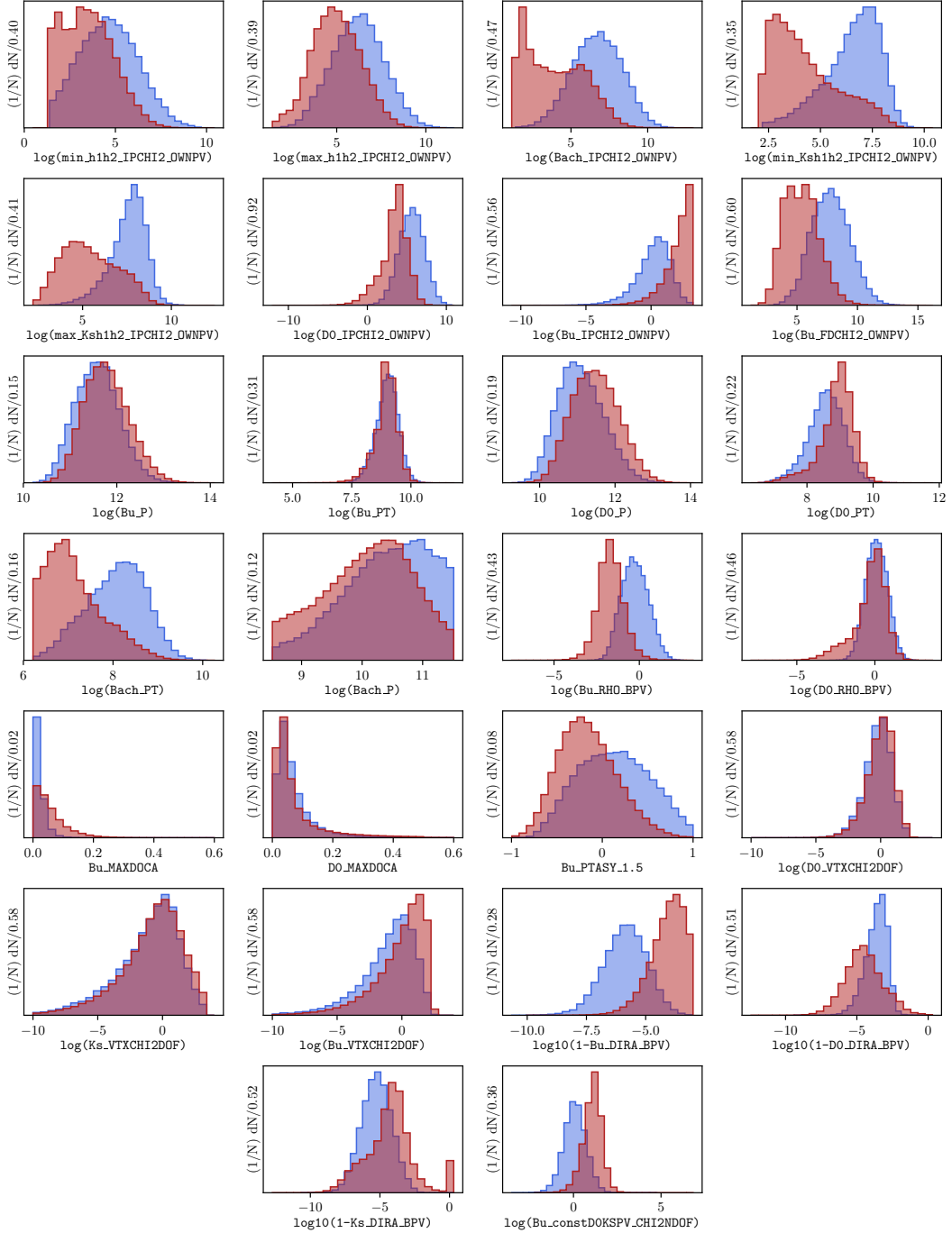


Figure 4.1: Distribution of input parameters in the LL training samples of (blue) signal decays from simulation and (red) background decays from the upper B sideband. The variable names described further in Table 4.2.

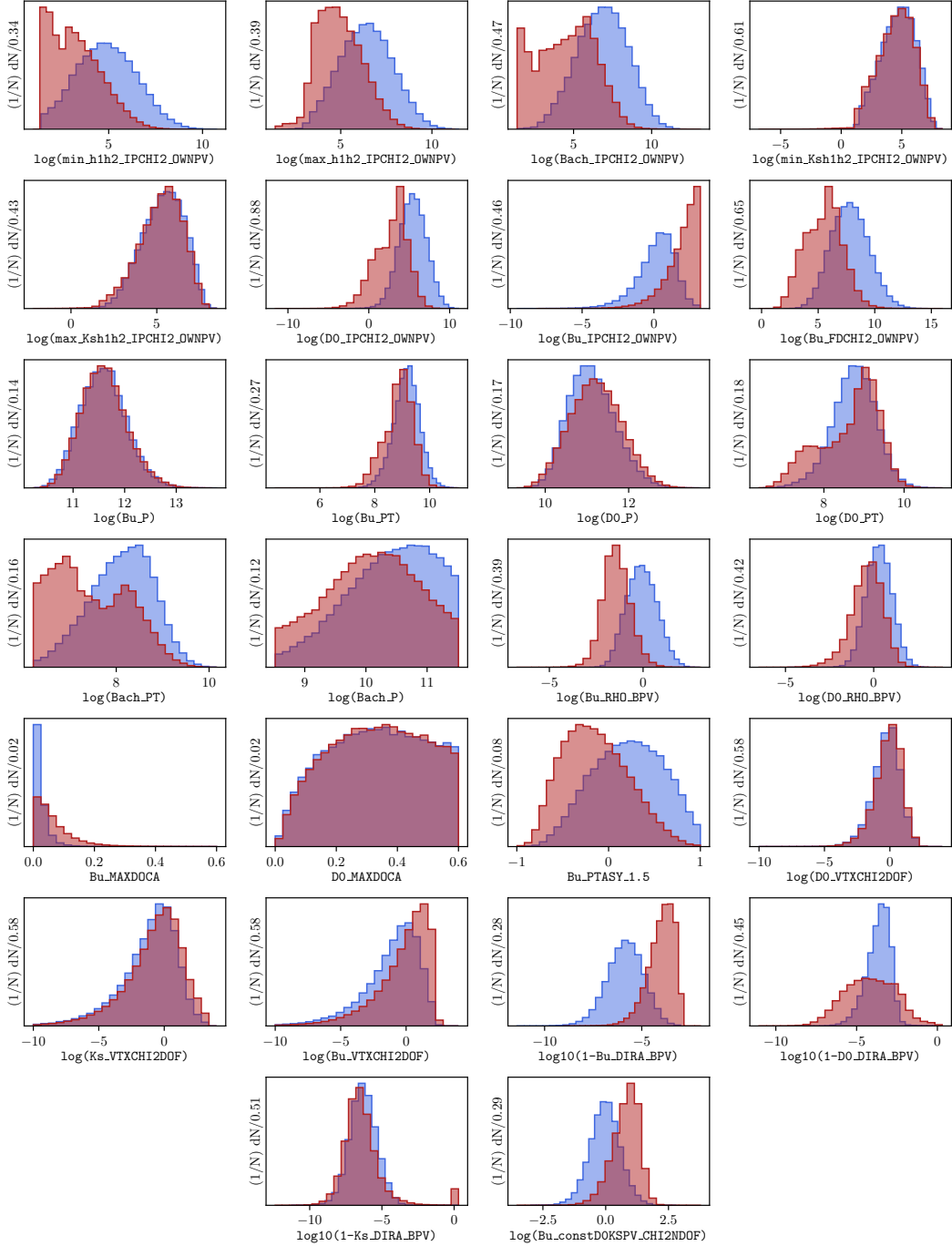


Figure 4.2: Distribution of input parameters in the DD training samples of (blue) signal decays from simulation and (red) background decays from the upper B sideband. The variable names described further in Table 4.2.

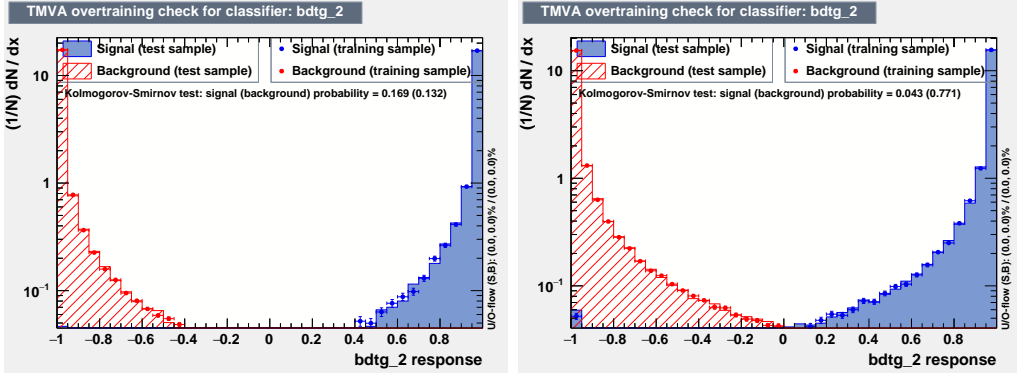


Figure 4.3: Distribution of BDT variable on test and training samples for (left) the LL and (right) the DD category, with logarithmic y -scale.

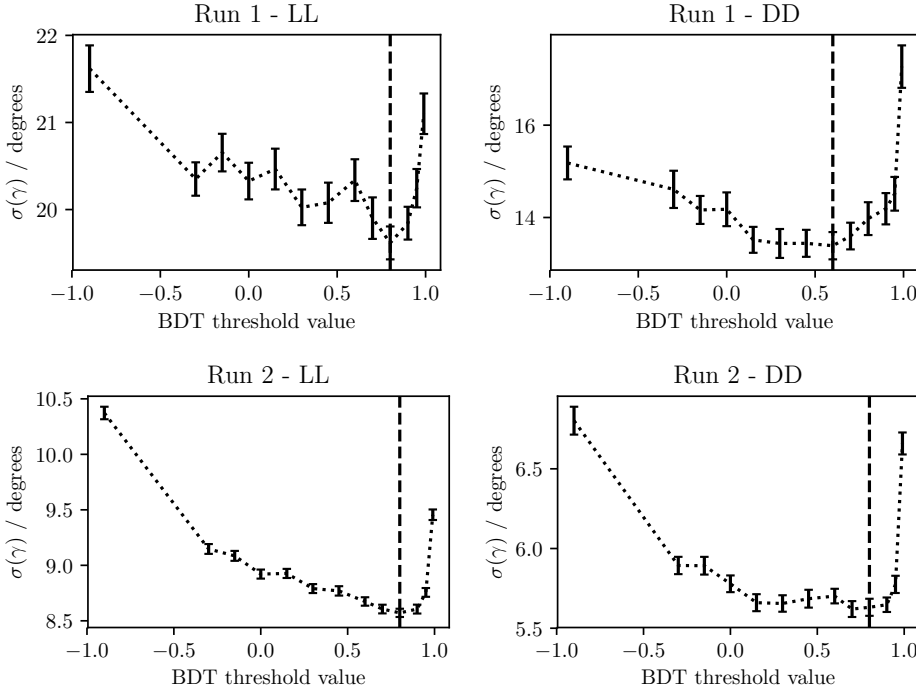


Figure 4.4: The mean uncertainty on γ in toy studies, performed with the signal and background yields corresponding to a given BDT requirement, using (top) the Run 1 and (bottom) Run 2 datasets, using only candidates in (left) the LL category and (right) the DD category. The dashed line shows the threshold value employed to discard background-like candidates in the selection.

4.1.3 Particle-identification requirements

- 1832 A PID requirement is made to separate $B^\pm \rightarrow DK^\pm$ and $B^\pm \rightarrow D\pi^\pm$ candidates in
- 1833 the data sample, by requiring that the PIDK of the companion particle satisfies
- 1834 $\text{PIDK} < 4$ for $B^\pm \rightarrow D\pi^\pm$ candidates and $\text{PIDK} > 4$ for $B^\pm \rightarrow DK^\pm$ candidates.
- 1835 The PIDK variable was defined in Section 2.1.3. This ensures that any given
- 1836 candidates is selected into only one of these samples.
- 1837

1838 Further to the requirement on the companion, PID requirements are made to
 1839 suppress semi-leptonic backgrounds as well as decays where a final state particle
 1840 decays in flight, and a loose PID requirement is made in the $D \rightarrow K_S^0 K^+ K^-$
 1841 channels where it leads to a higher signal purity:

- 1842 • the companion particle is required to satisfy `IsMuon` = 0.
- 1843 • For the $B \rightarrow D(\rightarrow K_S^0 \pi^+ \pi^-) h^\pm$ samples it is require that the charged pion
 1844 track from the D decay with opposite charge to the companion satisfies
 1845 $\text{PIDe} < 0 \& \text{IsMuon} = 0$, and for the other charged pion that `IsMuon` = 0.
- 1846 • For the $B \rightarrow D(\rightarrow K_S^0 K^+ K^-) h^\pm$ samples it is required that the charged kaon
 1847 tracks from the D decay have RICH information, a momentum less than 100
 1848 GeV/c and $\text{PIDK} > -5 \& \text{IsMuon} = 0$.

1849 These backgrounds are described in Section 4.3.3.

1850 4.1.4 Final requirements

1851 For a small fraction of candidates in the final sample, it is the case that two
 1852 or more candidates originate in the same pp collision. In order to make sure
 1853 that all candidates are completely independent, a single, arbitrary candidate from
 1854 each pp collision is kept for these collisions, and the other candidates discarded.
 1855 This requirements results in the removal of less than 0.7% of candidates in
 1856 each data category.

1857 Furthermore, the D mass used to define the binning schemes described in Ref. [69]
 1858 differs slightly from the mass used in the DTF refit. Therefore a few of the decays are
 1859 reconstructed with Dalitz coordinates outside the allowed kinematic region. Because
 1860 this problem only concerns a handful of candidates, they are simply discarded.

1861 4.1.5 Selected candidates

1862 In total, about 47,000 $B^\pm \rightarrow DK^\pm$ candidates and 400,000 $B^\pm \rightarrow D\pi^\pm$ candidates
 1863 are selected, as summarised in Table 4.3. An example of the B mass distribution in
 1864 one of the data categories is shown in Fig. 4.5; it is clear that a significant number
 1865 of these candidates are background decays. The Dalitz plots for candidates in the
 1866 signal region where $m_B \in [5249, 5309] \text{ MeV}/c^2$ are shown in Fig. 4.6 and 4.7. Due to
 1867 the large yields in the full Run 1 and 2 LHCb data set, the asymmetries between
 1868 the B^+ and B^- distributions are visible to the eye in the $B^\pm \rightarrow DK^\pm$ plots.

Table 4.3: Final candidate yield in each data category after the full selection has been applied, including removing candidates outside the region $m_B \in [5080, 5800] \text{ MeV}/c^2$.

B Decay	D final state	K_S^0 type	Run 1	Run 2	Total
$B^\pm \rightarrow DK^\pm$	$K_S^0\pi^+\pi^-$	LL	2275	10525	12800
		DD	5097	23508	28605
	$K_S^0K^+K^-$	LL	383	1610	1993
		DD	772	3397	4169
$B^\pm \rightarrow D\pi^\pm$	$K_S^0\pi^+\pi^-$	LL	18209	90509	108718
		DD	40167	205807	245974
	$K_S^0K^+K^-$	LL	2879	13757	16636
		DD	6033	29790	35823

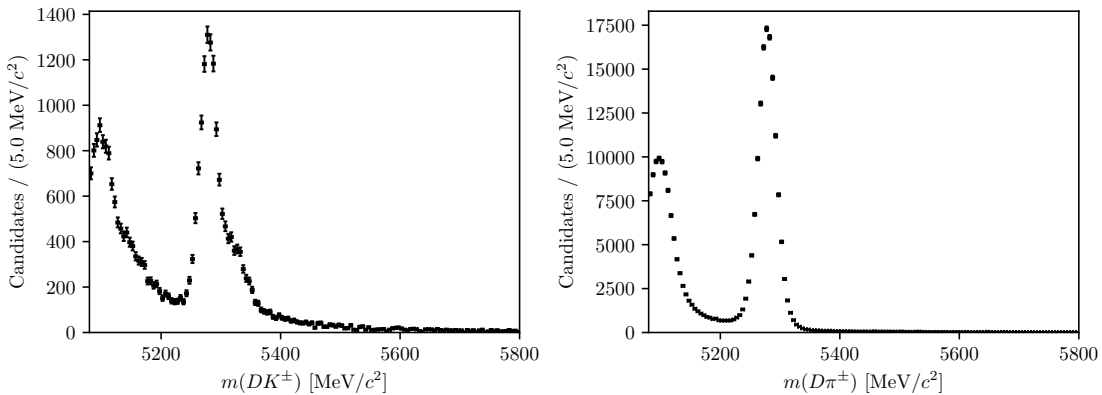


Figure 4.5: The spectrum of m_B in the (left) $B^\pm \rightarrow DK^\pm$ and (right) $B^\pm \rightarrow D\pi^\pm$ samples where $D \rightarrow K_S^0\pi^+\pi^-$ and the K_S^0 meson is reconstructed in the DD category, after the full selection has been applied.

4.2 Signal selection efficiencies

The efficiency of each step of the selection on signal decays can be investigated using simulated decays. In the $B^\pm \rightarrow D\pi^\pm$ channel, only decays that were placed in the "test" sample when training the BDT are used, in order to avoid overestimating the efficiency.

In general, the total selection efficiency up until the PID requirements, including the offline stage and the effect of the geometrical LHCb acceptance, is about 1 permille, slightly higher for $B^\pm \rightarrow DK^\pm$ than $B^\pm \rightarrow D\pi^\pm$ decays, and slightly higher for $D \rightarrow K_S^0K^+K^-$ than $D \rightarrow K_S^0\pi^+\pi^-$ decays. The PID requirements are investigated separately in Section 4.2.1 below, using samples of calibration data. The overall selection efficiency does not impact the measurement at all, because the observables of interest are sensitive *only* to the distribution of decays over the Dalitz plot (except, of course, in the sense that a higher signal efficiency is desirable).

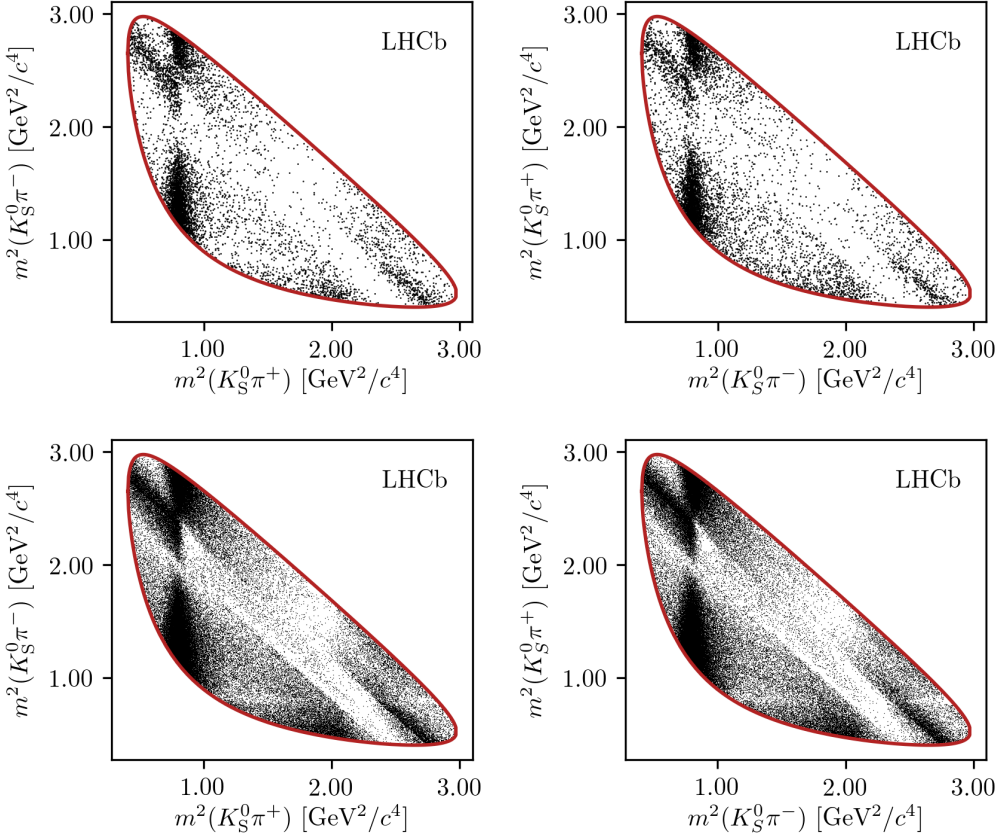


Figure 4.6: Dalitz plots of (left) $B^+ \rightarrow Dh^+$ and (right) $B^- \rightarrow Dh^-$ candidates in the signal region, in the (top) $B^\pm \rightarrow DK^\pm$ and (bottom) $B^\pm \rightarrow D\pi^\pm$ channels where $D \rightarrow K_S^0 \pi^+ \pi^-$. The LL and DD categories have been combined.

because it leads to larger signal yields). Likewise, it makes no difference that the overall selection efficiencies differ slightly between $B^\pm \rightarrow DK^\pm$ and $B^\pm \rightarrow D\pi^\pm$ decays, as long as the efficiency profile over the Dalitz plot is identical between the two decay channels. This is confirmed separately in Section 4.2.2 below.

The efficiencies of each individual selection step are shown in Fig. 4.8, obtained using simulated $B^\pm \rightarrow D\pi^\pm$ decays. The main reason that some signal decays do not survive the base requirement is the $p_{\text{companion}} < 100 \text{ GeV}/c$ requirement, which is in place to ensure that the PID performance for the companion is good. For decays with $p_{\text{companion}} > 100 \text{ GeV}/c$, only about 60 % of $B^\pm \rightarrow DK^\pm$ decays survive the subsequent $PIDK > 4$ requirement and the cross-feed from misidentified $B^\pm \rightarrow D\pi^\pm$ decays is 50 % larger than in the current selection. Thus, loosening this requirement leads to little statistical gain, while leading to larger systematic effects from the crossfeed background.

An equivalent plot for the combinatorial background is shown in Fig. 4.9, using $B^\pm \rightarrow D(\rightarrow K_S^0 \pi^+ \pi^-)\pi^\pm$ candidates in data with a reconstructed B mass

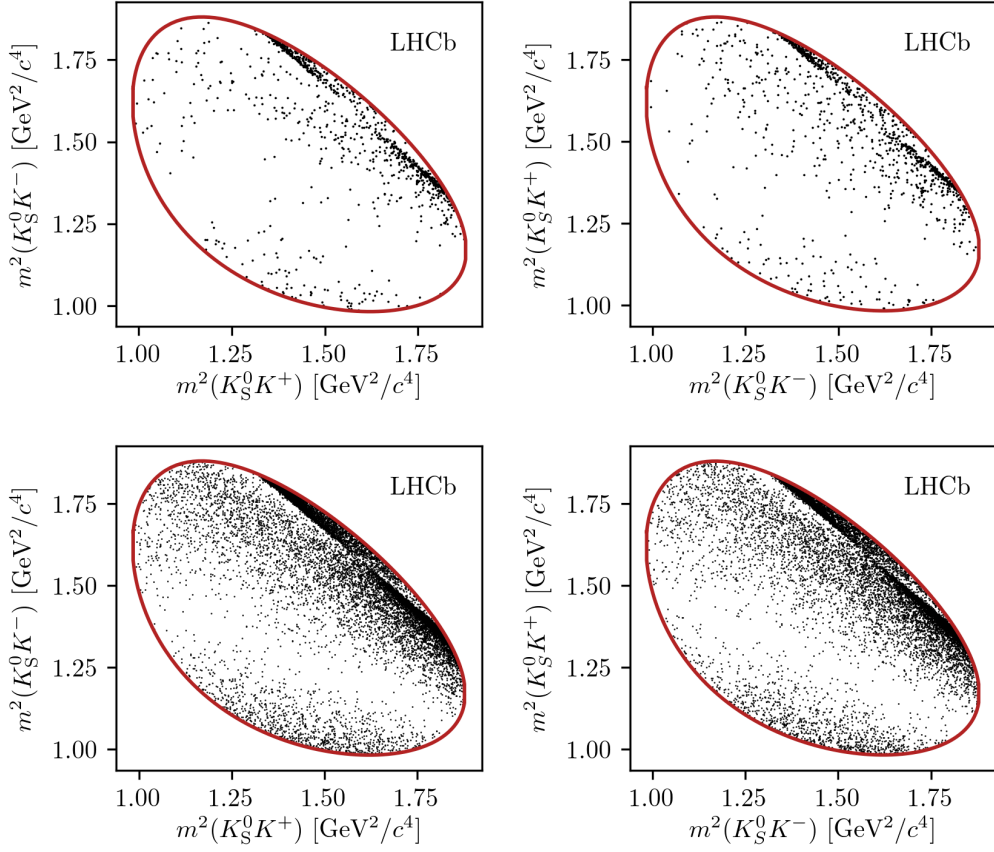


Figure 4.7: Dalitz plots of (left) $B^+ \rightarrow Dh^+$ and (right) $B^- \rightarrow Dh^-$ candidates in the signal region, in the (top) $B^\pm \rightarrow DK^\pm$ and (bottom) $B^\pm \rightarrow D\pi^\pm$ channels where $D \rightarrow K_S^0 K^+ K^-$. The LL and DD categories have been combined.

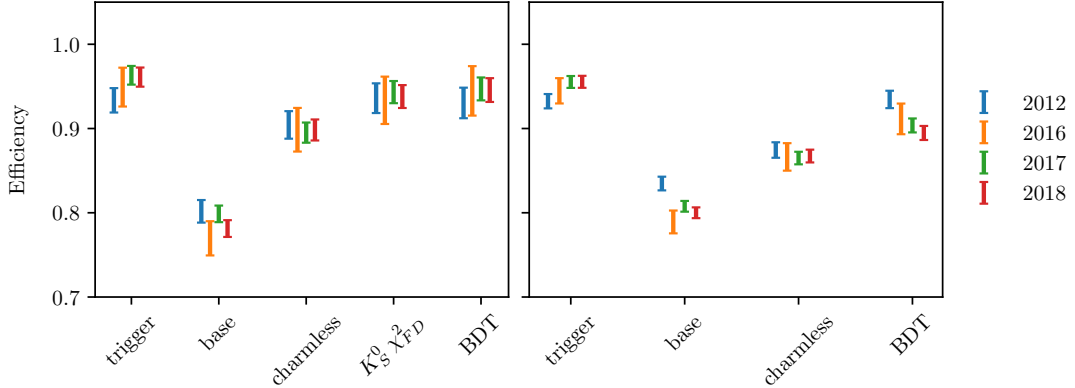


Figure 4.8: The efficiency of each selection step in samples of simulated $B^\pm \rightarrow D(\rightarrow K_S^0 \pi^+ \pi^-) \pi^\pm$ signal decays in the (left) LL and (right) DD categories. The selection steps are applied on top of each other, from left to right on the horizontal axis. The samples are split by year.

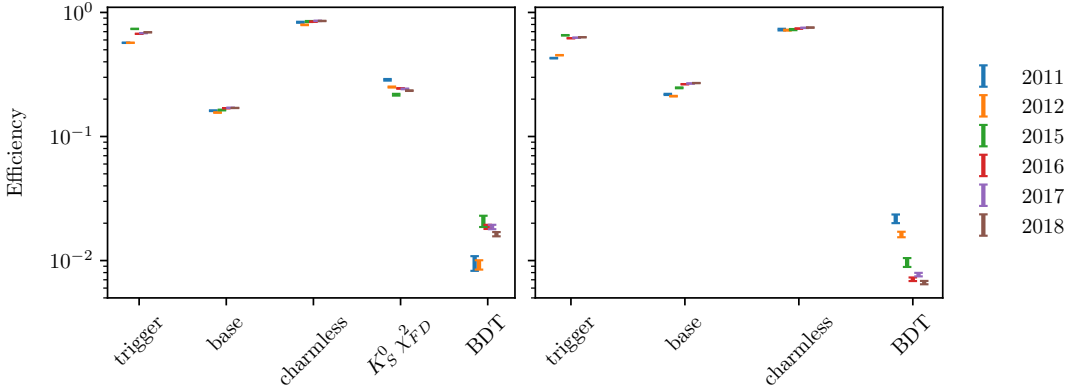


Figure 4.9: The efficiency of each selection step in samples of $B^\pm \rightarrow D(\rightarrow K_S^0 \pi^+ \pi^-) \pi^\pm$ candidates in data where the reconstructed B mass is above $5600 \text{ MeV}/c^2$, meaning the candidates stem from combinatorial background. The efficiency is shown for candidates in the (left) LL and (right) DD categories. The selection steps are applied on top of each other, from left to right on the horizontal axis. The samples are split by year. Notice the logarithmic scale on the vertical axis.

above $5600 \text{ MeV}/c^2$; it can be seen that the BDT is extremely efficient at rejection combinatorial background, but that the base requirements and the requirement on the K_S^0 flight distance also remove a decent amount of background.

4.2.1 Efficiency of the PID requirements

The efficiencies of the PID requirements on the companion enter the yield parameterisations of the mass fits in Section 4.4 and 4.5 and must therefore be known. They are determined using samples of calibration data selected without relying on PID variables, as implemented in the `PIDCalib` frame work [134]. Reasonably pure samples of pion and kaon tracks are obtained from $D^0 \rightarrow K^-\pi^+$ decays, where the D meson originates in a $D^{*+} \rightarrow D^0\pi^+$ decay and can therefore be flavour tagged. The remaining background is subtracted via the `sPlot` [135] procedure, based on a two-dimensional fit of the $m(K^-\pi^+)$ and $m(D^0\pi^+) - m(D^0)$ distributions. The obtained weights are employed to calculate the average efficiency of the requirement on PIDK for a number of bins in the momentum and pseudorapidity of the calibration tracks, and the number of charged tracks in the detector, thus constructing a three-dimensional efficiency lookup table. The procedure is carried out for each PID requirement, companion species, data-taking year, track charge, and magnet polarity. Based on these tables, expected PID efficiencies for the $B^\pm \rightarrow D\pi^\pm$ and $B^\pm \rightarrow DK^\pm$ signal decays are calculated that take the kinematical distribution and detector occupancy in the BPGBS data samples into account, by using the high-purity sample of $B^\pm \rightarrow D\pi^\pm$ candidates in the signal region as a reference.

Table 4.4: PID efficiencies obtained with the `PIDCalib` tool. The uncertainty incorporates statistical uncertainty due to the size of the reference sample, the systematic uncertainty due to the choice of binning scheme in `PIDCalib`, and a systematic uncertainty due to the `sWeight` calculation in `PIDCalib` of 0.1 %.

Efficiency	Particle	D final state	$\varepsilon_{\text{PID}} (\%)$	
			LL	DD
Run I and II				
Correct ID	Kaon	$D \rightarrow K_S^0 \pi^+ \pi^-$	86.74 ± 0.13	86.90 ± 0.22
		$D \rightarrow K_S^0 K^+ K^-$	86.22 ± 0.26	86.56 ± 0.30
	Pion	$D \rightarrow K_S^0 \pi^+ \pi^-$	97.11 ± 0.11	97.17 ± 0.13
		$D \rightarrow K_S^0 K^+ K^-$	97.07 ± 0.11	97.16 ± 0.14

1918 The dominating uncertainty on the efficiencies is statistical in nature, due to
 1919 the finite size of the reference sample. In addition, systematic uncertainties are
 1920 included due to the `sPlot` procedure, estimated at 0.1 % [134], and due to the
 1921 choice of binning scheme, estimated by repeating the procedure using a number of
 1922 alternative binning schemes. The final efficiency estimates are shown in Table 4.4,
 1923 including all sources of uncertainty.

1924 4.2.2 Efficiency profile over the Dalitz plot

1925 The analysis strategy depends on sharing the F_i parameters between the $B \rightarrow D\pi$
 1926 and $B \rightarrow DK$ channels. This is reasonable, since the phase-space dependence
 1927 of the reconstruction efficiency is expected to be very similar between the two
 1928 decays, given the similar kinematics; an assumption that is verified using samples
 1929 of simulated decays. The full selection is applied to the samples. The $B \rightarrow D\pi$
 1930 sample of LL (DD) candidates includes about 63,000 (146,000) decays, and the
 1931 $B \rightarrow DK$ samples include 60,000 (142,000) decays. For the $B \rightarrow D\pi$ mode, this is
 1932 approximately equal to the number of decays in the full Run 1+2 data sample, and
 1933 for $B \rightarrow DK$ this is a factor of about 12 larger than the data sample. The decays
 1934 were simulated with an equal decay probability across the D -decay phase space, so
 1935 that any non-uniform distribution of reconstructed decays is completely determined
 1936 by a phase-space dependent reconstruction and selection efficiency. Therefore the
 1937 assumption that the phase-space dependence is identical between the $B \rightarrow D\pi$ and
 1938 $B \rightarrow DK$ channels is verified by seeing if the Dalitz coordinates are distributed
 1939 differently between the samples of simulated $B \rightarrow D\pi$ and $B \rightarrow DK$ decays.

1940 This is investigated with two statistical tests. The first is a χ^2 comparison of 2D
 1941 histograms of the distribution of $m^2(K_S^0 \pi^+)$ and $m^2(K_S^0 \pi^-)$ in the different $B \rightarrow D\pi$
 1942 and $B \rightarrow DK$ channels. These histograms, and the ratio between them, are shown

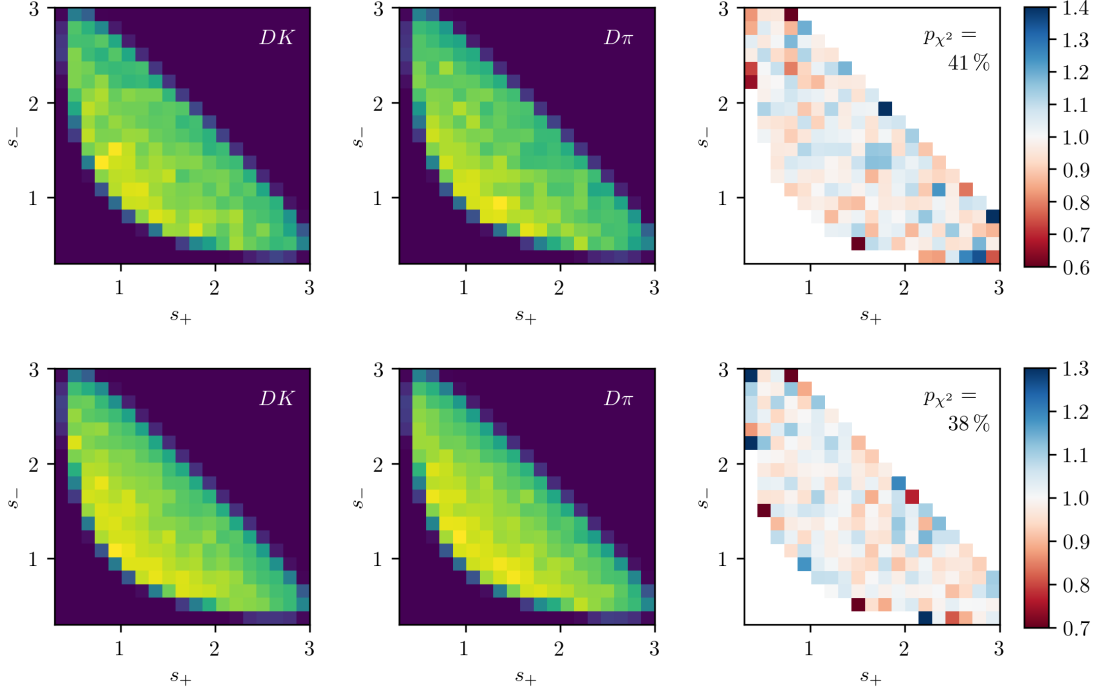


Figure 4.10: The (s_+, s_-) distribution in simulated samples of (left) $B \rightarrow DK$ decays and (center) $B \rightarrow D\pi$ decays where $D \rightarrow K_S^0\pi^+\pi^-$, as well as (right) the ratio between the two histograms (corrected for differences in sample sizes). The plots are shown for candidates in the (top) LL and (bottom) DD categories. The p values are the results of χ^2 compatibility tests between the two histograms.

in Figs. 4.10 and 4.11, along with the p -values from the χ^2 tests. It can be seen that, in all cases, the probability of obtaining the two histograms assuming that they share the same underlying distribution has a reasonable value, and that there is no clear trend in the ratio plots. The second test is a Kolmogorov-Smirnov test [] of the compatibility of the one-dimensional distributions of $m^2(K_S^0\pi^+)$, $m^2(K_S^0\pi^-)$, and $m^2(\pi^+\pi^-)$. These distributions, and the corresponding p -values, are shown in Fig. 4.12 and 4.13. Again, all the p values are reasonable. Therefore, it is concluded that there are no statistically significant differences between the phase-space dependence of the reconstruction and selection efficiency between the $B \rightarrow D\pi$ and $B \rightarrow DK$ channels, given the present sample sizes. Because the simulation samples have approximately the same amount of decays as data (or significantly more, in the $B \rightarrow DK$ case), any potential differences will be negligible with data yields. Thus, sharing the F_i parameters between the $B \rightarrow D\pi$ and $B \rightarrow DK$ channels is viable, and no efficiency correction is necessary.

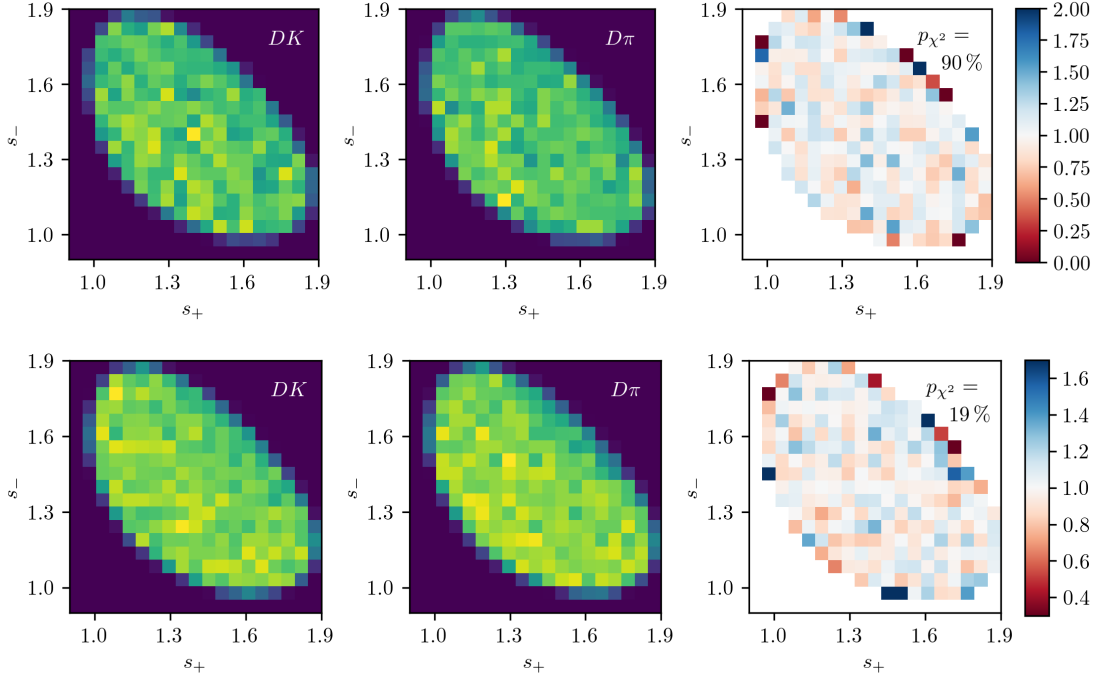


Figure 4.11: The (s_+, s_-) distribution in simulated samples of (left) $B \rightarrow DK$ decays and (center) $B \rightarrow D\pi$ decays where $D \rightarrow K_S^0 K^+ K^-$, as well as (right) the ratio between the two histograms (corrected for differences in sample sizes). The plots are shown for candidates in the (top) LL and (bottom) DD categories. The p values are the results of χ^2 compatibility tests between the two histograms.

4.3 Background studies

A wide range of backgrounds can potentially pollute the sample of signal candidates. The backgrounds group into three categories depending on how they are treated in the analysis:

- Backgrounds that can be effectively removed in the selection
- Backgrounds that are only present at a level where the impact on the measurement result is small, and which do therefore not have to be modelled
- Backgrounds that are present at a level where they have to be modelled in the fit to data, and cannot effectively be rejected further in the selection

The latter category comprises of combinatorial background, which remains present at a non-negligible level after the application of the BDT described in Section 4.1.2; contributions from a number of partly reconstructed $B \rightarrow Dh^\pm X$ decays, where X denotes a pion or photon that is not included in the reconstructed decay, and which can only be separated from signal decays by their $m(Dh)$ distribution; and

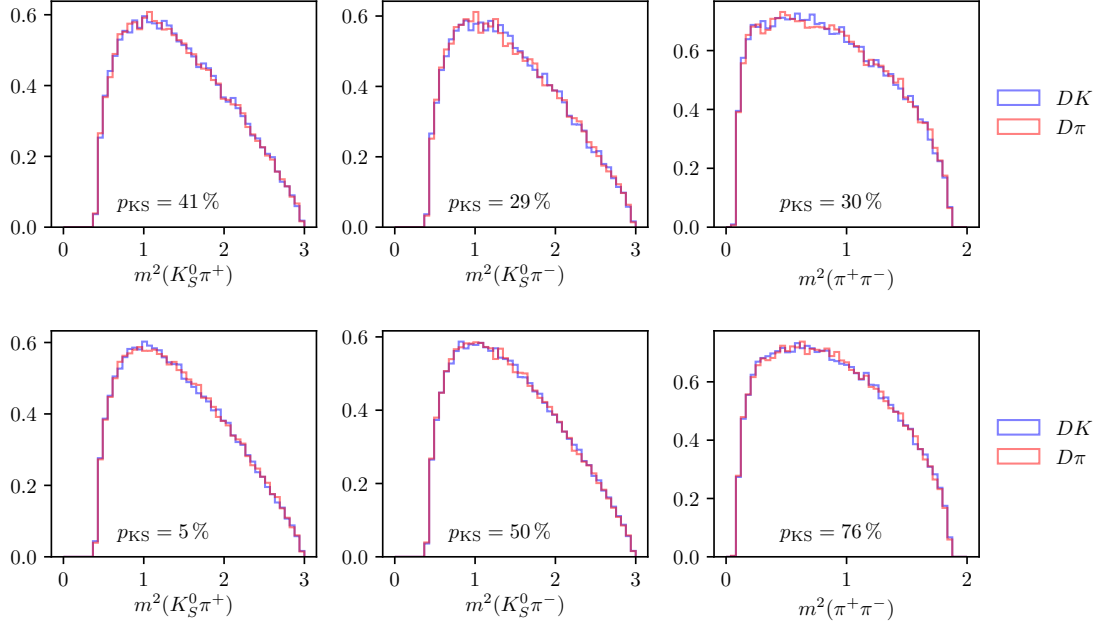


Figure 4.12: One-dimensional distributions of $m^2(K_S^0\pi^+)$, $m^2(K_S^0\pi^-)$, and $m^2(\pi^+\pi^-)$ in simulated (blue) $B^\pm \rightarrow DK^\pm$ and (red) $B^\pm \rightarrow D\pi^\pm$ decays where $D \rightarrow K_S^0\pi^+\pi^-$ in the (top) LL and (bottom) DD categories. The p values are the results of Kolmogorov-Smirnov compatibility tests between the distributions.

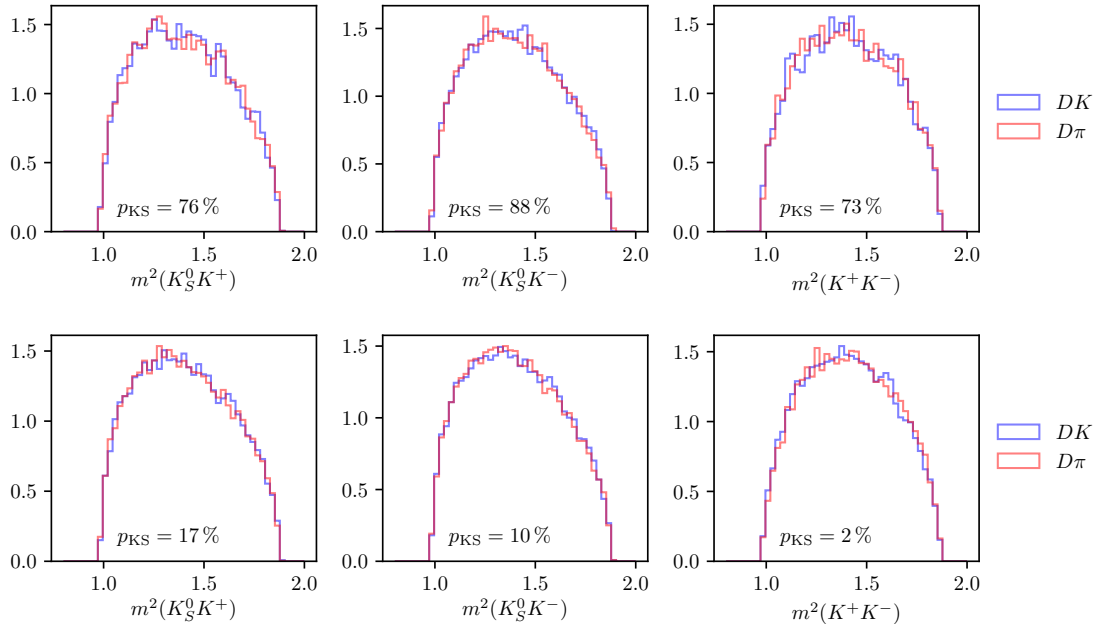


Figure 4.13: One-dimensional distributions of $m^2(K_S^0K^+)$, $m^2(K_S^0K^-)$, and $m^2(\pi^+\pi^-)$ in simulated (blue) $B^\pm \rightarrow DK^\pm$ and (red) $B^\pm \rightarrow D\pi^\pm$ decays where $D \rightarrow K_S^0K^+K^-$ in the (top) LL and (bottom) DD categories. The p values are the results of Kolmogorov-Smirnov compatibility tests between the distributions.

1971 finally $B^\pm \rightarrow D\pi^\pm$ decays that are categorised as $B^\pm \rightarrow DK^\pm$ decays in the particle-
1972 identification step and vice-versa. These background sources are described in detail
1973 in Section 4.4. This section focuses on backgrounds that led to specific requirements
1974 in the selection or proved to be small enough to not merit special treatment.

1975 4.3.1 Charmless decays

1976 There is potentially a so-called *charmless* background present in data, consisting
1977 of $B^\pm \rightarrow K_S^0 h^+ h^- h'^\pm$ decays. These have the same final state as the signal decay,
1978 but no intermediate D meson. Because all final state particles are reconstructed,
1979 this background peaks in the B mass spectrum. This background is suppressed
1980 by requiring the reconstructed B and D decay vertices to be separated in the
1981 z direction; specifically by requiring that $\Delta z_{\text{significance}}^{D-B} > 0.5$, where $\Delta z_{\text{significance}}^{D-B}$
1982 was defined in Eq. (4.1). The remaining background level can be investigated
1983 by investigating the D mass sidebands.

1984 However, the use of the DecayTreeFitter χ^2 as an input variable in the BDT
1985 removes essentially all of the D (and K_S^0) sideband, due to the mass constraints
1986 in the decay chain fit. Therefore separate BDT's are trained for LL and DD
1987 candidates without the χ^2 as an input variable, and used when selecting candidates
1988 for the background studies presented in this section, and the following. In a similar
1989 manner, all mass window requirements are made on the *default* reconstructed
1990 masses, obtained with no use of DecayTreeFitter. The overlap of the two sets of
1991 selected candidates in the signal B -mass window is above 95 %.

1992 The reconstructed B mass spectrum is shown for $B^\pm \rightarrow D\pi^\pm$ candidates in the
1993 D sidebands in Fig. 4.14, both before and after making a requirement on $\Delta z_{\text{significance}}^{D-B}$.
1994 A peak is clearly visible, the size of which is reduced by the requirement. This peak
1995 is partly due to a contribution from $B^\pm \rightarrow K_S^0 \pi^+ \pi^- \pi^\pm$ decays ($B^\pm \rightarrow K_S^0 K^+ K^- \pi^\pm$
1996 decays) in the $D \rightarrow K_S^0 \pi^+ \pi^-$ ($D \rightarrow K_S^0 K^+ K^-$) channel, and partly due to real
1997 signal decays that leak into the D sidebands. The number of real signal decays can
1998 be calculated from the yield obtained in the fit of Section 4.4, and the reconstructed
1999 m_D distribution in simulated signal decays. Subtracting this contribution, it is
2000 estimated that approximately 450 (200) charmless decays are present in the $K_S^0 \pi^+ \pi^-$
2001 ($K_S^0 K^+ K^-$) data samples. In similar fashion, Fig. 4.15 shows the m_B spectra for
2002 $B^\pm \rightarrow DK^\pm$ candidates in the D sidebands. In these plots, the peaks are at
2003 m_B values that are lower (higher) than the B mass in the $K_S^0 \pi^+ \pi^-$ ($K_S^0 K^+ K^-$)
2004 categories, because they stem from real $B^\pm \rightarrow K_S^0 K^+ K^- \pi^\pm$ decays where a kaon is
2005 mis-reconstructed as a pion or a pion is misreconstructed as a kaon, respectively.
2006 The total contribution of charmless decays in the $B^\pm \rightarrow DK^\pm$ data samples is

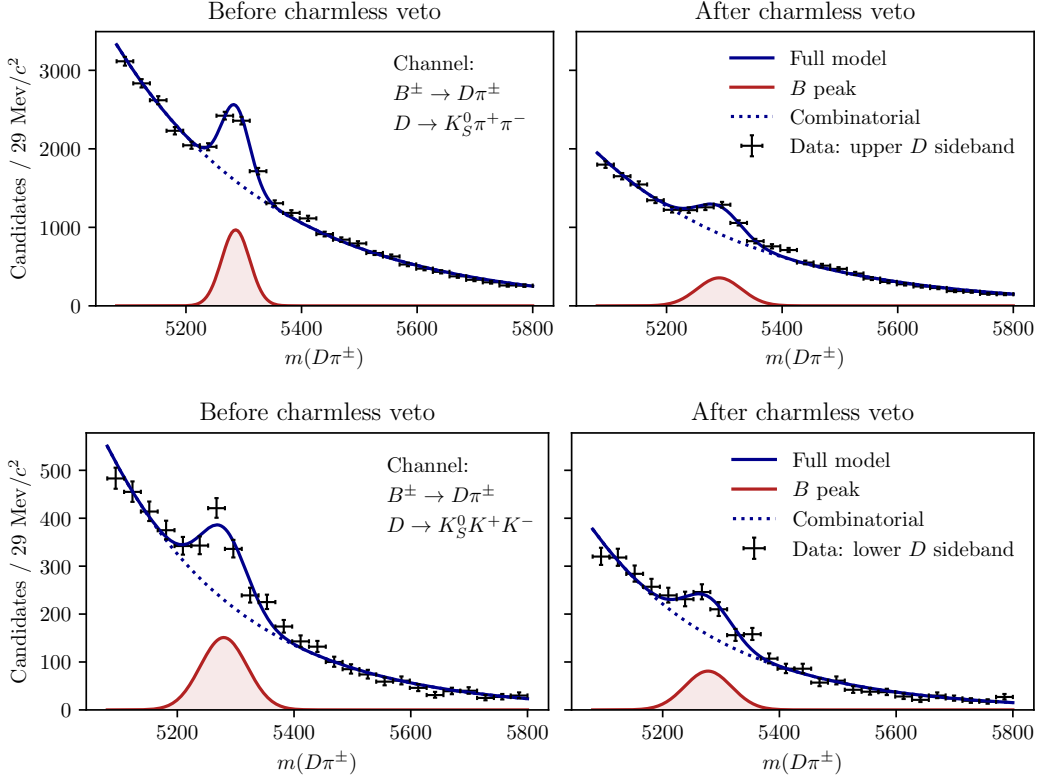


Figure 4.14: The B mass distribution of (top) $B^\pm \rightarrow D(\rightarrow K_S^0 \pi^+ \pi^-)\pi^\pm$ and (bottom) $B^\pm \rightarrow D(\rightarrow K_S^0 K^+ K^-)\pi^\pm$ candidates reconstructed in both the LL and DD categories, residing in the upper D mass sideband $m_D \in [1910, 1960] \text{ MeV}/c^2$ for $D \rightarrow K_S^0 \pi^+ \pi^-$ and in the lower sideband $m_D \in [1910, 1960] \text{ MeV}/c^2$ for $D \rightarrow K_S^0 K^+ K^-$, with (left) no requirement on $\Delta z_{\text{significance}}^{BD}$ and (right) after a requirement of $\Delta z_{\text{significance}}^{BD} > 0.5$.

estimated to be about 200 decays. As described further in Section 4.6.11, the presence of a charmless background at these levels has a negligible impact on the measurement results.

4.3.2 Background from four-body D decays

A similar potential background is from real $B^\pm \rightarrow Dh^\pm$ decays where the D meson decays directly to the $\pi^+\pi^-h^+h^-$ final state, without an intermediate K_S^0 meson. This background can be investigated by looking for a peak in the B mass spectrum for candidates in the K_S^0 sideband, as illustrated in Fig. 4.16. The figure shows the spectrum in the final data sample, illustrating the significant effect of making the requirement on the K_S^0 flight distance that was discussed in Section 4.1.1. The BDT that does *not* rely on the DTF χ^2 has been used to suppress combinatorial background. The remaining peak after requiring $\chi_{\text{FD}}^2 > 49$ is completely accounted for by real signal decays that leak into the K_S^0 sideband.

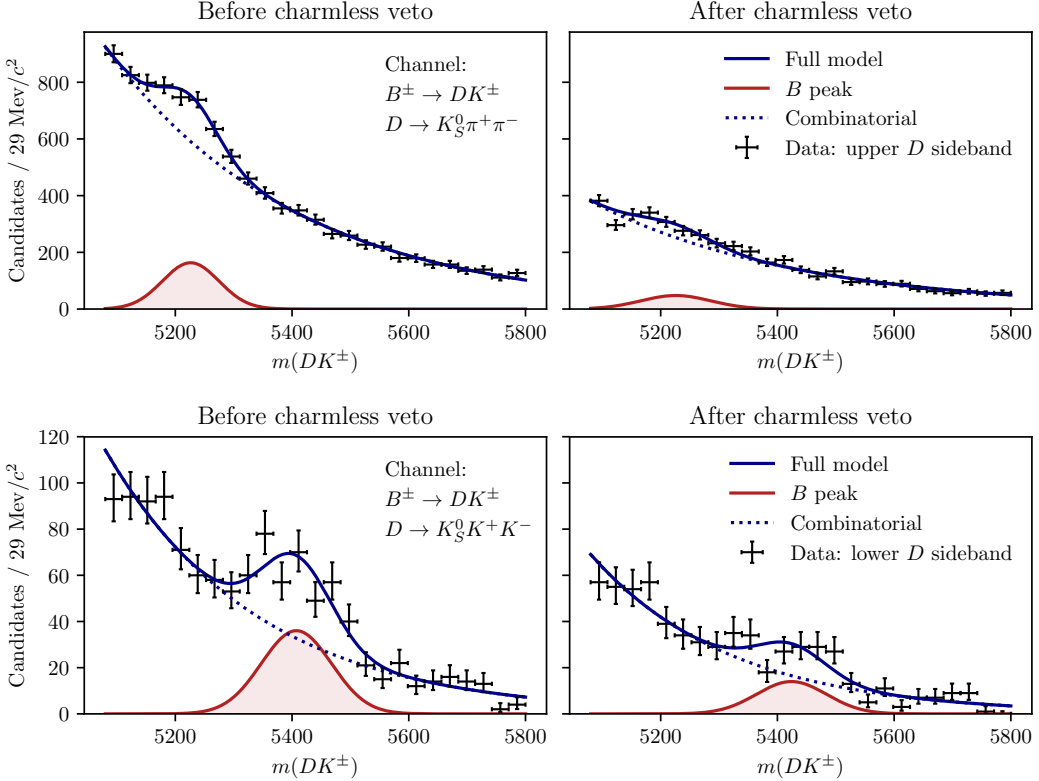


Figure 4.15: The B mass distribution of (top) $B^\pm \rightarrow D(\rightarrow K_S^0 \pi^+ \pi^-)K^\pm$ and (bottom) $B^\pm \rightarrow D(\rightarrow K_S^0 K^+ K^-)K^\pm$ candidates reconstructed in both the LL and DD categories, residing in the upper D mass sideband $m_D \in [1910, 1960] \text{ MeV}/c^2$ for $D \rightarrow K_S^0 \pi^+ \pi^-$ and in the lower sideband $m_D \in [1910, 1960] \text{ MeV}/c^2$ for $D \rightarrow K_S^0 K^+ K^-$, with (left) no requirement on $\Delta z_{\text{significance}}^{BD}$ and (right) after a requirement of $\Delta z_{\text{significance}}^{BD} > 0.5$.

2020 4.3.3 Semi-leptonic backgrounds

2021 The data sample has a minor background from $B \rightarrow D\mu\nu_\mu X$ decays, visible
 2022 in the B mass spectrum when the companion is required to satisfy `isMuon=1`.
 2023 This is shown in Fig. 4.17 for both the $B^\pm \rightarrow DK^\pm$ and $B^\pm \rightarrow D\pi^\pm$ channels
 2024 where $D \rightarrow K_S^0 \pi^+ \pi^-$. The B mass spectra for simulated $B^\pm \rightarrow D\mu^\pm \nu_\mu$ decays
 2025 reconstructed in each category are also shown, from simulation samples produced via
 2026 `RapidSim`. The background is very efficiently vetoed by requiring `IsMuon=0` on the
 2027 companion. This requirement removes approximately 85 % of the background decays,
 2028 as estimated using the `PIDCalib` calibration samples and the (p, p_T) distribution
 2029 for the muon in the `RapidSim` samples. The fraction of signal candidates for
 2030 which the companion satisfies `IsMuon=1` in simulated signal samples is $\leq 0.9\%$
 2031 so the impact on signal yield is small.

2032 The analogous $B \rightarrow D e \nu_e X$ background is investigated by inspecting the B
 2033 mass spectra after making requirements on `PIDE` for the companion candidate, but

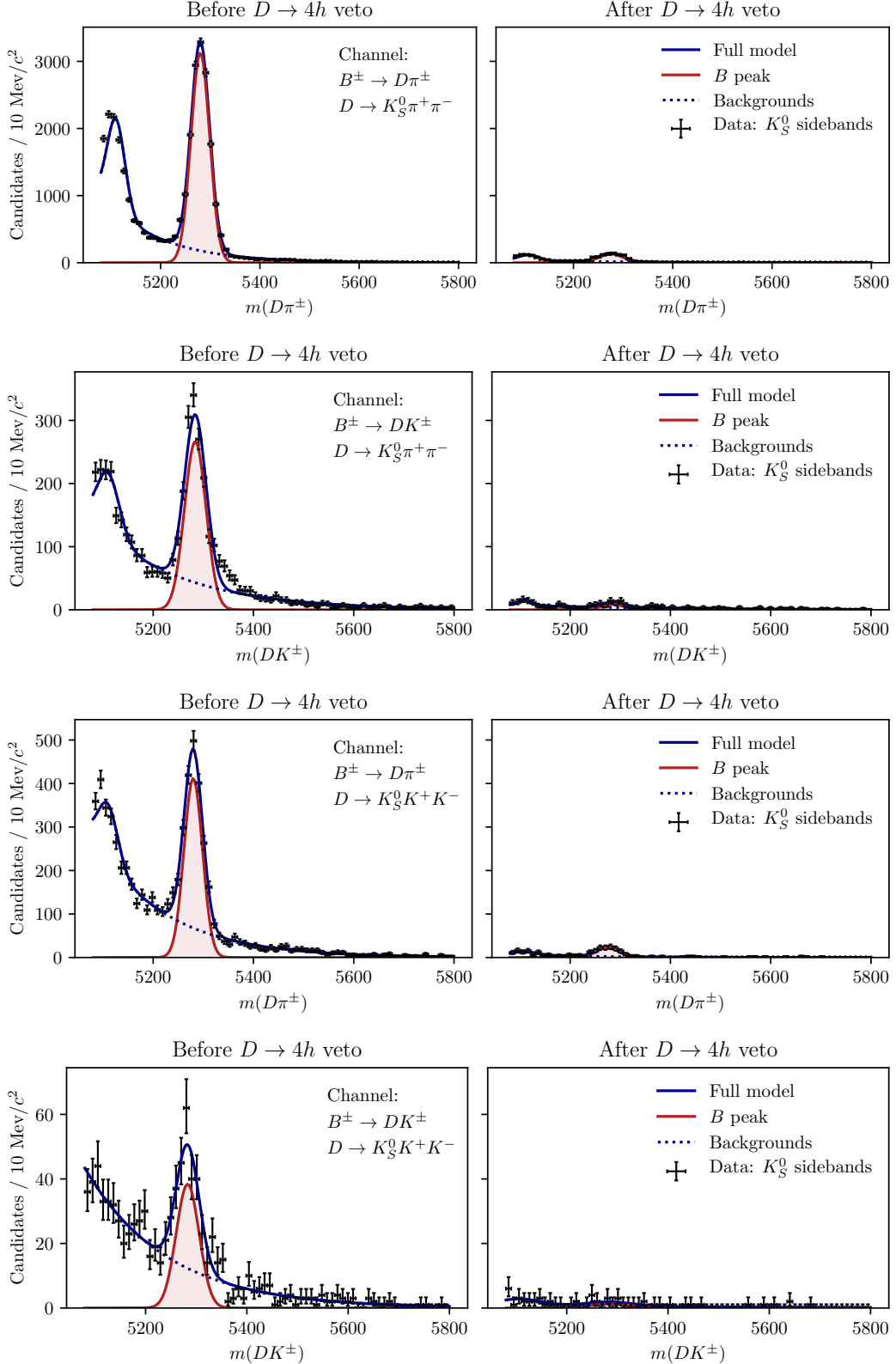


Figure 4.16: The B mass spectrum in the K_S^0 sideband where $m_{K_S^0} \in [467, 482] \text{ MeV}/c^2$ or $m_{K_S^0} \in [512, 527] \text{ MeV}/c^2$ (left) without a requirement on the K_S^0 flight distance significance, and (right) after the requirement implemented in the analysis.

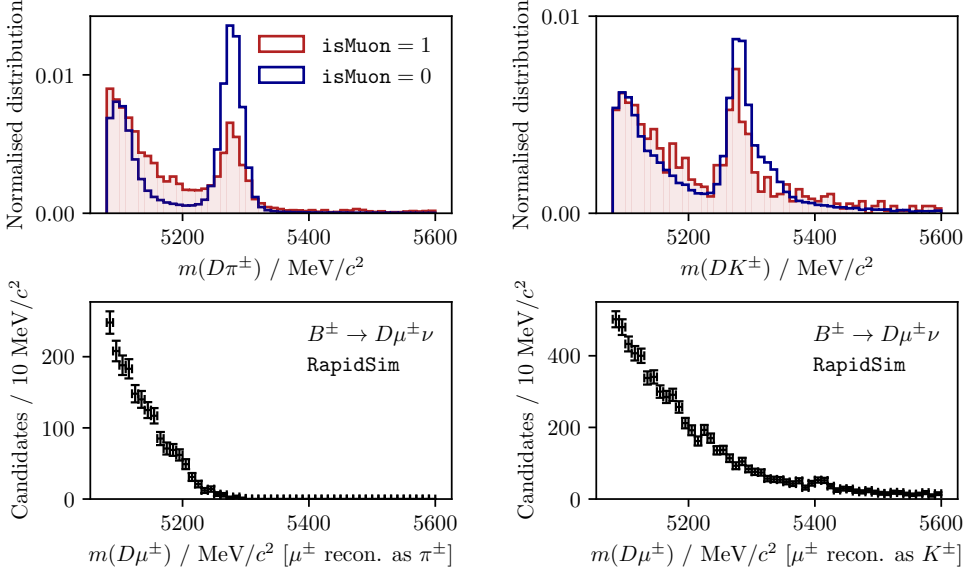


Figure 4.17: (Top) The m_B spectra in data split by the value of `Bach_isMuon` for (left) the $D\pi^\pm$ and (right) the DK^\pm samples where $D \rightarrow K_S^0\pi^+\pi^-$. The two histograms are normalised independently, so that the distributions can be compared. The fractions candidates in data (with $m_B \in [5080, 5800] \text{ MeV}/c^2$) that satisfy `Bach_isMuon=1` are 1.6% and 1.8% for the $D\pi^\pm$ and DK^\pm channels respectively. (Bottom) the Rapidsim mass spectra for $B^\pm \rightarrow D^0\mu^\pm\nu_\mu$ decays reconstructed in the (left) $D\pi^\pm$ and (right) DK^\pm categories.

2034 a presence of the semi-leptonic background in data is not visible and no electron
 2035 veto is applied to the companion.

2036 Background from semi-leptonic D decays

2037 There is a potential background from real $B^\pm \rightarrow Dh^\pm$ decays where the D
 2038 meson decays semi-leptonically: $D^0 \rightarrow K_S^0\pi^-\ell^+\nu_\ell$. This background is particularly
 2039 dangerous because it peaks at the B mass, when the D -mass requirement is applied
 2040 and it is reconstructed in the $D \rightarrow K_S^0\pi^+\pi^-$ category. This is illustrated in Fig. 4.18
 2041 using Rapidsim samples of $B^\pm \rightarrow D(\rightarrow K^{*-}(X)(\rightarrow K_S^0\pi^-)\ell^+\nu_\ell)h^\pm$ decays for
 2042 $X = 892, 1430, 1680$. The expected background yields relative to signal can be
 2043 estimated by applying the B and D mass cuts to decays in the Rapidsim samples,
 2044 and using the relative branching ratios. Only the $D^0 \rightarrow K^{*-}(892)\ell\nu_\ell$ branching
 2045 fractions have been measured [31], but there is no reason to expect that higher
 2046 K^* resonances should not contribute. To estimate their potential contribution,

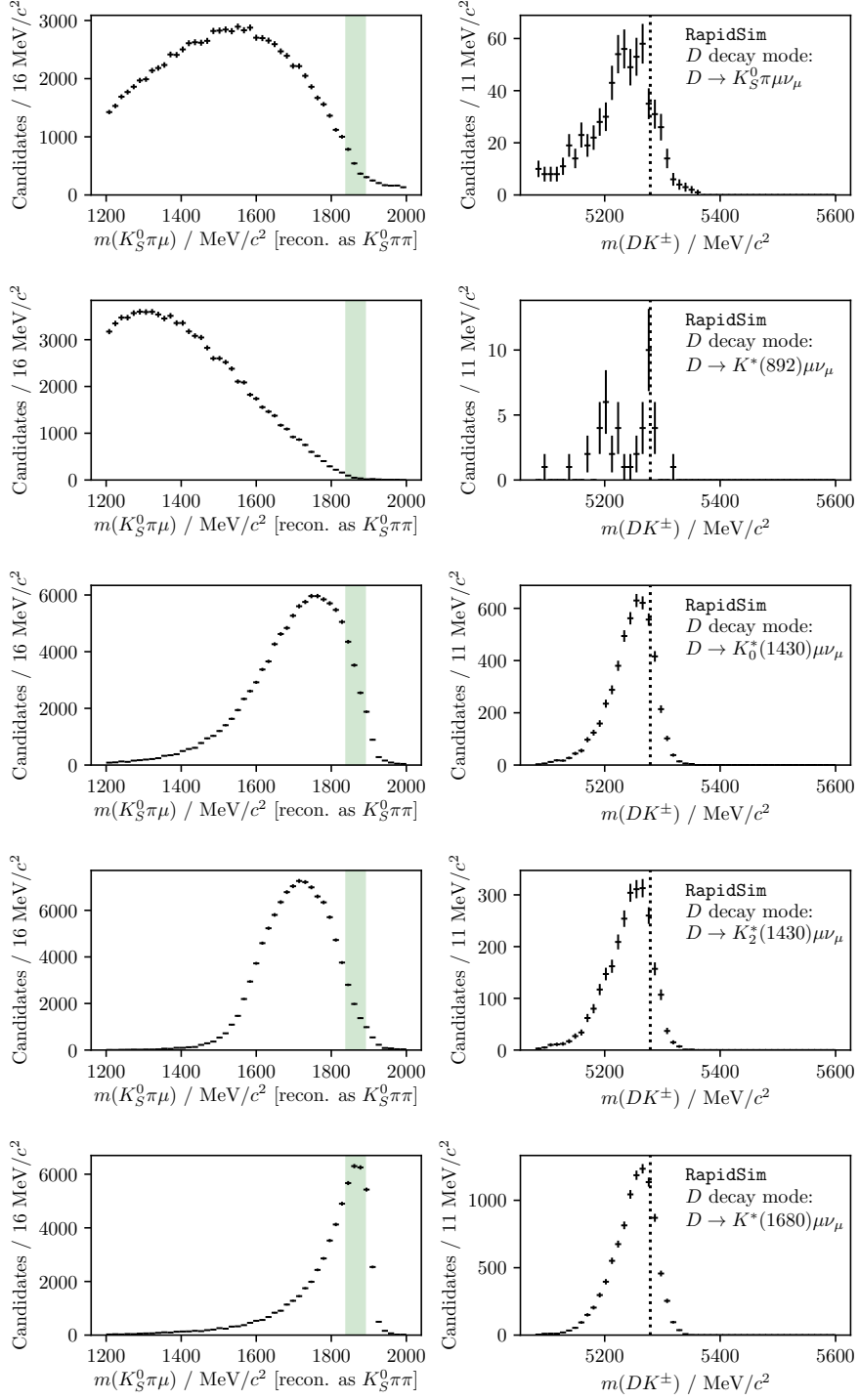


Figure 4.18: The reconstructed (left) $m(K_S^0 \pi^+ \pi^-)$ and (right) $m(Dh)$ distributions in RapidSim samples of $B^\pm \rightarrow DK^\pm$ decays where $D^0 \rightarrow K_S^0 \pi^- \mu^+ \nu_\mu$. The top plot is for PHSP decays, and the following plots show the distribution where the $K_S^0 \pi^-$ originate in the resonances $K^{*-}(892)$, $K^{*-}_0(1430)$, $K^{*-}_2(1430)$, and $K^{*-}(1680)$. The shapes for the $D^0 \rightarrow K_S^0 \pi^- e^+ \nu_e$ case are almost identical.

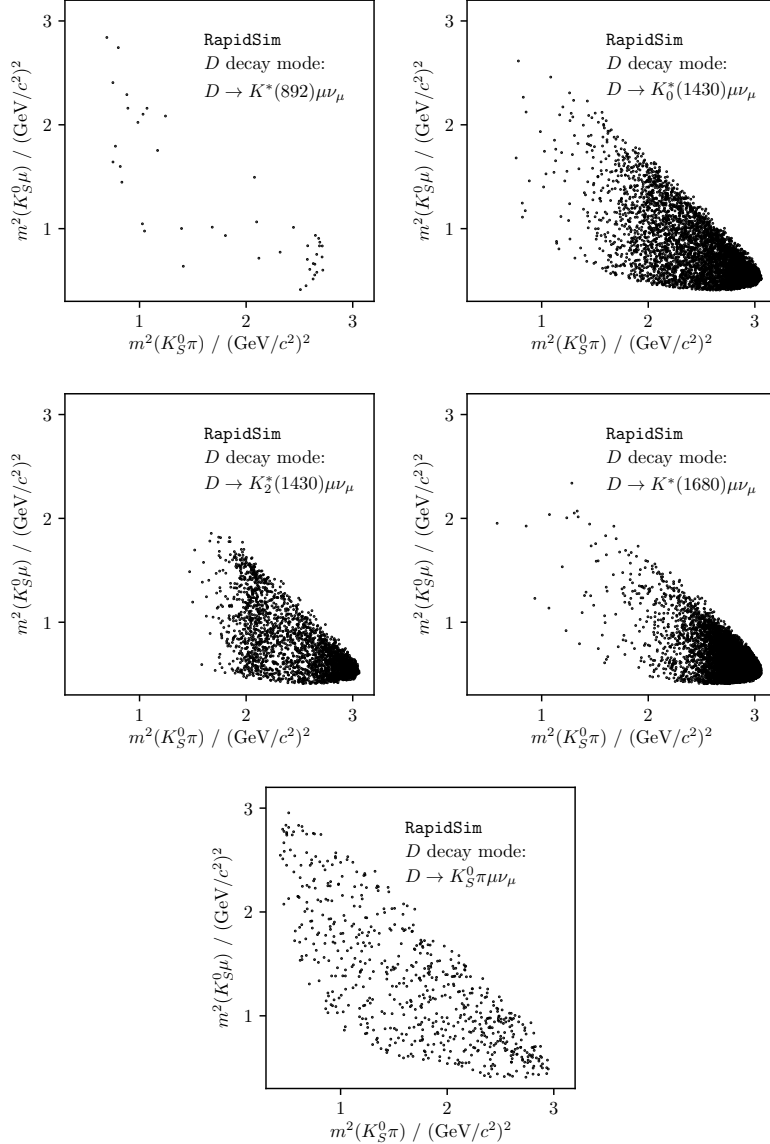


Figure 4.19: Dalitz distribution for $D \rightarrow K_S^0 \pi \mu \nu_\mu$ decays in RapidSim, where the $K_S^0 \pi^-$ originate in the resonances $K^{*-}(892)$, $K^{*-}_0(1430)$, $K^{*-}_2(1430)$, and $K^{*-}(1680)$, as well as for a flat PHSP distribution.

2047 the branching ratios are approximated by

$$\begin{aligned} \text{BR}[D^0 \rightarrow K^{*-}(X)(\rightarrow K_S^0 \pi^-) \ell \nu_\ell] &\simeq \\ \frac{\text{BR}[D^0 \rightarrow K^{*-}(X)(\rightarrow K_S^0 \pi^-) \pi^+]}{\text{BR}[D^0 \rightarrow K^{*-}(892)(\rightarrow K_S^0 \pi^-) \pi^+]} \text{BR}[D^0 \rightarrow K^{*-}(892)(\rightarrow K_S^0 \pi^-) \ell \nu_\ell] \end{aligned}$$

2048 because all the relevant $D^0 \rightarrow K^{*-}(\rightarrow K_S^0 \pi^-) \pi^+$ branching fractions are known [31].
 2049 The efficiencies and branching ratios relative to the signal channel are given in
 2050 Table 4.5. It is clear that the higher K^* resonances are important: the smaller
 2051 branching ratios are compensated for by a higher selection efficiency, due to the

Table 4.5: The selection efficiencies of $B^\pm \rightarrow DK^\pm$ decays where $D^0 \rightarrow K_S^0\pi^-\ell^+\nu_\ell$ when reconstructed in the $D \rightarrow K_S^0\pi^+\pi^-$ mode in RapidSim relative to the signal selection efficiencies, for a number of decay modes: PHSP as well as resonant production where the $K_S^0\pi^-$ pair originates in one of several K^* resonances. The relative branching ratios are also shown, calculated as explained in the main text, as well as the predicted relative yields.

Mode	$\epsilon_{bkg}/\epsilon_{signal}$ (%)	$\Gamma_{bkg}/\Gamma_{signal}$ (%)	N_{bkg}/N_{signal} (%)
$D \rightarrow K_S^0\pi^-\mu^+\nu_\mu$ (PHSP)	0.92 ± 0.05	18.3 ± 14.8	0.17 ± 0.14
$D \rightarrow (K_S^0\pi^-)_{K^{*-}(892)}\mu^+\nu_\mu$	0.06 ± 0.01	22.3 ± 3.2	0.013 ± 0.003
$D \rightarrow (K_S^0\pi^-)_{K_0^{*-}(1430)}\mu^+\nu_\mu$	7.3 ± 0.1	3.7 ± 0.8	0.27 ± 0.06
$D \rightarrow (K_S^0\pi^-)_{K_2^{*-}(1430)}\mu^+\nu_\mu$	3.7 ± 0.1	0.5 ± 0.3	0.02 ± 0.01
$D \rightarrow (K_S^0\pi^-)_{K^{*-}(1680)}\mu^+\nu_\mu$	24.4 ± 0.3	0.6 ± 0.5	0.15 ± 0.12
$D \rightarrow K_S^0\pi^-e^+\nu_e$ (PHSP)	0.53 ± 0.02	20.8 ± 16.3	0.11 ± 0.09
$D \rightarrow (K_S^0\pi^-)_{K^{*-}(892)}e^+\nu_e$	0.15 ± 0.02	25.6 ± 2.5	0.04 ± 0.01
$D \rightarrow (K_S^0\pi^-)_{K_0^{*-}(1430)}e^+\nu_e$	6.3 ± 0.1	4.2 ± 0.8	0.26 ± 0.05
$D \rightarrow (K_S^0\pi^-)_{K_2^{*-}(1430)}e^+\nu_e$	4.12 ± 0.08	0.5 ± 0.3	0.02 ± 0.01
$D \rightarrow (K_S^0\pi^-)_{K^{*-}(1680)}e^+\nu_e$	10.0 ± 0.2	0.7 ± 0.5	0.07 ± 0.05
Total	-	-	1.1 ± 0.4

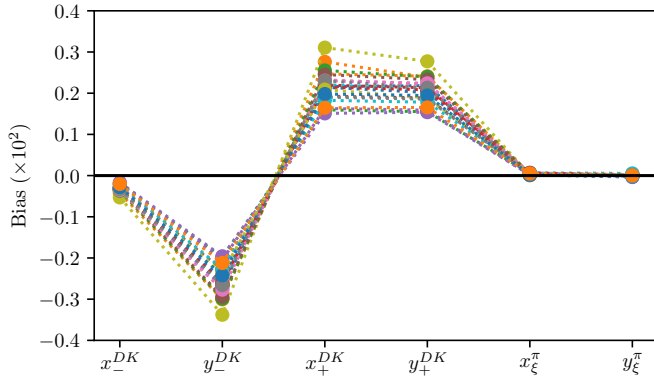


Figure 4.20: Estimated biases on the measured observables due to the presence of $D \rightarrow K_S^0\pi\ell\nu_\ell$ backgrounds, calculated while varying efficiencies and branching ratios within uncertainties.

2052 smaller phase-space of the missed neutrino. The total background yield is 1.1 %
 2053 of the signal yield in both the $B^\pm \rightarrow D\pi^\pm$ and $B^\pm \rightarrow DK^\pm$ channels. However,
 2054 there will be an additional contribution in the $B^\pm \rightarrow DK^\pm$ channel from real
 2055 $B^\pm \rightarrow D\pi^\pm$ decays with semi-leptonic D decays and a mis-identification of the
 2056 companion. This background also peaks, and the yield is approximately 0.4 %
 2057 of the $B^\pm \rightarrow DK^\pm$ signal yield.

2058 The potential impact from the presence of the background is estimated by

- 2059 1. calculating the expected $B^\pm \rightarrow D\pi^\pm$ and $B^\pm \rightarrow DK^\pm$ yields in each bin for
 2060 physics parameters similar to the world average values
- 2061 2. then calculating the background bin yields in each bin, using the relative
 2062 branching fractions and efficiencies described above and taking the bin-
 2063 distribution from the RapidSim samples. The RapidSim samples are produced
 2064 using the ISGW2 model in EvtGen [107], yielding the Dalitz distributions in
 2065 Fig. 4.19.
- 2066 3. adding the signal and background yields, and fitting the new $B^\pm \rightarrow D\pi^\pm$ and
 2067 $B^\pm \rightarrow DK^\pm$ yields back with the default signal-yield expressions (including a
 2068 fit of the F_i parameters)

2069 The obtained biases are shown in Fig. 4.20, where they are calculated a number
 2070 of times, each time varying the efficiencies within statistical uncertainties and the
 2071 relevant branching fractions within the measurement uncertainties. The systematic
 2072 uncertainty due to the unknown branching fractions and the use of RapidSim in
 2073 lieu of full simulation is not included, but is of course significant. Nevertheless
 2074 it is clear that the potential biases are significant compared to the size of the
 2075 systematic uncertainties of the analysis presented in Section 4.6. Therefore the
 2076 backgrounds are vetoed by requiring `IsMuon=0` and `PIDe < 0` on the pions from
 2077 the D -decay with opposite charge to the bachelor in the $D \rightarrow K_S^0 \pi^+ \pi^-$ channel.
 2078 This requirement removes 88 % of the muonic background and 99 % of the electron
 2079 background, according to PID efficiencies obtained via the `PIDCalib` package,
 2080 using the (p, p_T) distribution for the muon/electron in the RapidSim samples. The
 2081 survival rate for signal decays in full simulation is 94 %, so the impact on the
 2082 obtainable precision is only about 3 %. A systematic uncertainty is assigned to
 2083 account for the potential remaining background.

2084 In the $D \rightarrow K_S^0 K^+ K^-$ channel an analogous study shows the relative yields
 2085 to be similar. The selection efficiencies are higher, as are the relative branching
 2086 ratios due to the lower $D \rightarrow K_S^0 K^+ K^-$ branching fraction, but in this mode the
 2087 $\text{PIDK} > -5$ requirement placed on the pion and lepton remove approximately 90 %
 2088 of the background, leaving the relative rate similar to in $D \rightarrow K_S^0 \pi^+ \pi^-$. However,
 2089 importantly, *the background is not peaking*, as shown in Fig. 4.21. The presence
 2090 of a percent-level, *non-peaking* background in the $D \rightarrow K_S^0 K^+ K^-$ channel is safe
 2091 to ignore and thus no veto is applied in the $D \rightarrow K_S^0 K^+ K^-$ channel.

2092 The muon-veto for the semi-leptonic background does remove some signal
 2093 decays, where an original pion or kaon results in hits in the muon detectors. A

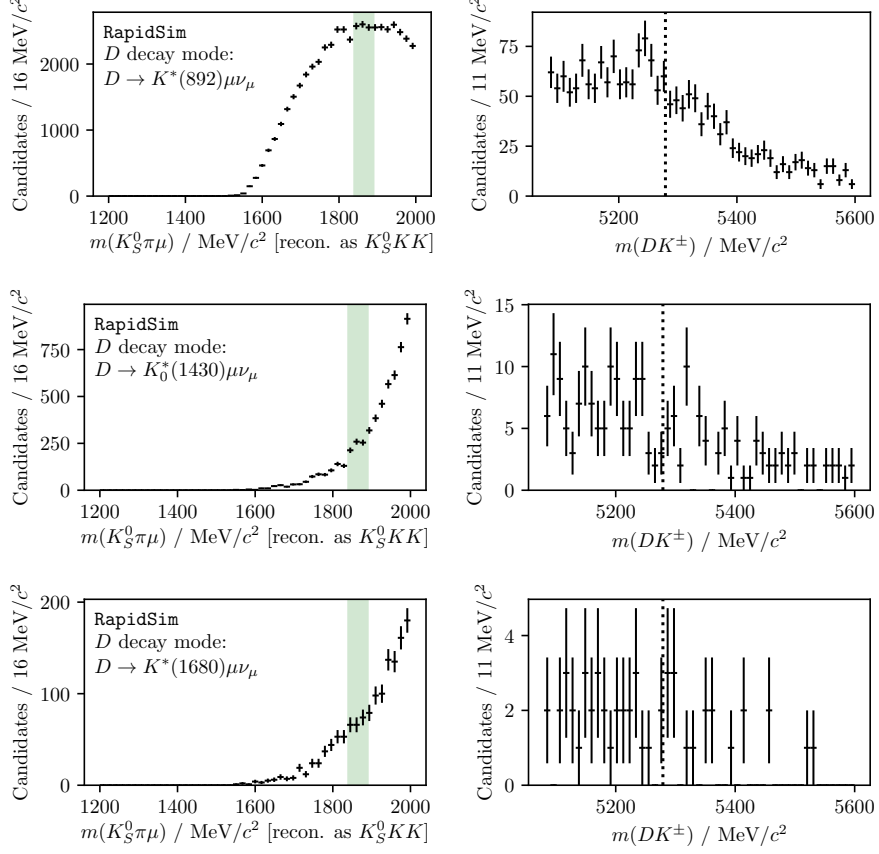


Figure 4.21: The reconstructed (left) $m(K_S^0 K^+ K^-)$ and (right) $m(Dh)$ distributions in RapidSim samples of $B^\pm \rightarrow DK^\pm$ decays where $D^0 \rightarrow K_S^0 \pi^- \mu^+ \nu_\mu$, where the $K_S^0 \pi^-$ originate in (top to bottom) the resonances $K^{*-}(892)$, $K^{*-}_0(1430)$, and $K^{*-}(1680)$. The shapes for the $D^0 \rightarrow K_S^0 \pi^- e^+ \nu_e$ case are almost identical.

2094 significant contribution is from particles that decay in flight. The track quality
 2095 of these decays is worse than for nominal decays, which affects the resolution on
 2096 the reconstructed Dalitz coordinates. In simulated signal decays the standard
 2097 deviation of $\Delta m_\pm^2 = m_{\text{reco}}^2(K_S^0 \pi^\pm) - m_{\text{TRUE}}^2(K_S^0 \pi^\pm)$ is 50 % larger for decays where
 2098 one of the D -decay products has `IsMuon=1` than in decays where this is not the
 2099 case. This can lead to systematic biases on the observables, as described further in
 2100 Section 4.6.7. The overall effect is small, as evidenced by the systematic uncertainty
 2101 described in that section; nevertheless this fact motivates removing decay-in-flight
 2102 decays of the D -decay products. Therefore it is also required that `IsMuon=0` for
 2103 the D -decay pion with the same charge as the companion in the $D \rightarrow K_S^0 \pi^+ \pi^-$
 2104 channels, and on the D -decay kaons in the $D \rightarrow K_S^0 K^+ K^-$ channels. This veto
 2105 removes about 2 % of signal candidates in simulation that survive the lepton vetoes
 2106 described in the previous sections.

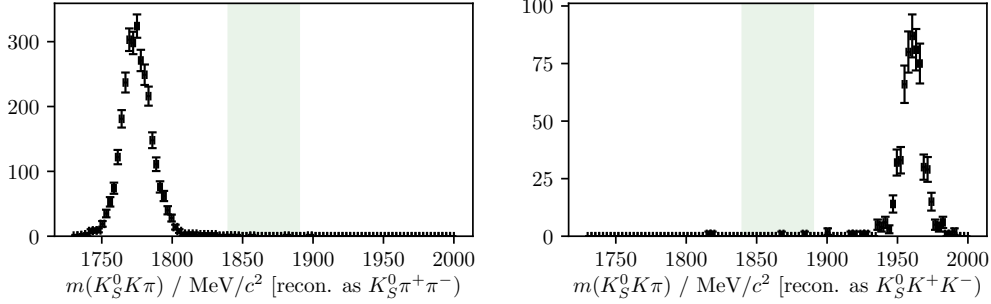


Figure 4.22: Simulated samples of $B^\pm \rightarrow D(\rightarrow K_S^0 K\pi)K^\pm$ decays reconstructed in the (left) $D \rightarrow K_S^0 \pi^+ \pi^-$ and (right) $D \rightarrow K_S^0 K^+ K^-$ channels, combining the LL and DD categories. The D -mass region included in the selection of signal decays is illustrated with the green band. The plots in the $B^\pm \rightarrow DK^\pm$ channels look almost identical.

2107 4.3.4 Cross-feed from other $D \rightarrow K_S^0 h^+ h^-$ decays

2108 Misidentification of a D decay product can lead to background from cross-feed be-
 2109 tween the $B^\pm \rightarrow D(\rightarrow K_S^0 \pi^+ \pi^-)h^\pm$ and $B^\pm \rightarrow D(\rightarrow K_S^0 K^+ K^-)h^\pm$ signal channels,
 2110 or cross-feed from $B^\pm \rightarrow D(\rightarrow K_S^0 K\pi)h^\pm$ decays into either of the signal channels.
 2111 However, this background is very highly suppressed by the employed requirement
 2112 on the D mass. This is illustrated in Fig. 4.22, where the D mass distribution in
 2113 samples of simulated $B^\pm \rightarrow D(\rightarrow K_S^0 K\pi)K^\pm$ decays are shown, when reconstructed
 2114 as $D \rightarrow K_S^0 \pi^+ \pi^-$ and $D \rightarrow K_S^0 K^+ K^-$ decays. Essentially no decays that fall in
 2115 the selected D mass window survive the full selection. Therefore this background
 2116 is not considered further. Neither is the background due to cross-feed between
 2117 $B^\pm \rightarrow D(\rightarrow K_S^0 \pi^+ \pi^-)h^\pm$ and $B^\pm \rightarrow D(\rightarrow K_S^0 K^+ K^-)h^\pm$, since it involves two
 2118 misidentified particles, and therefore will result in reconstructed D masses even
 2119 further away from the selected mass window. A very loose PID requirement on the
 2120 charged D decay products is nonetheless included in the $D \rightarrow K_S^0 K^+ K^-$ channel,
 2121 because it helps reduce the level of combinatorial background.

2122 4.3.5 Swapped-track backgrounds

2123 A possible peaking background stems from real $B \rightarrow DhX$ decays with the same
 2124 final state tracks as in the signal case, but where some tracks are mis-assigned in the
 2125 reconstruction. Examples are $B^\pm \rightarrow (K_S^0 h^+ h^-)_D h^\pm$ decays where the companion
 2126 and a D -decay product track are swapped, or $B^\pm \rightarrow (K^- \pi^+)_D K_S^0 h^\pm$ decays, where
 2127 the K_S^0 is assigned to the D decay and the real companion is swapped with the
 2128 D -decay product of the same charge. The signature of this background type is
 2129 a peak at the D mass, when the invariant mass corresponding to the companion

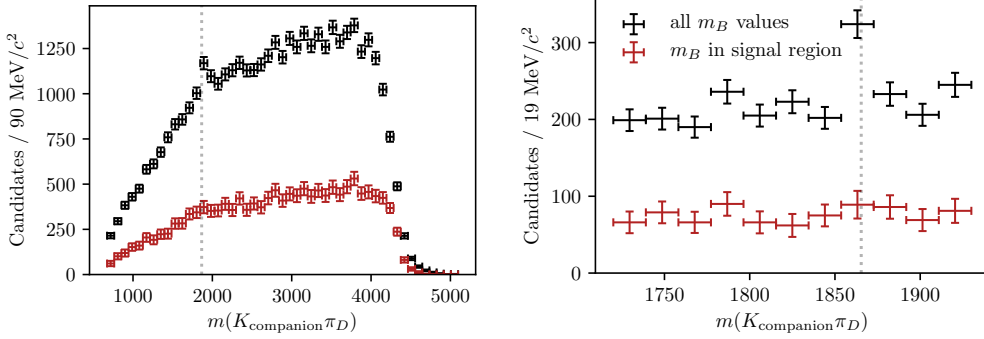


Figure 4.23: Invariant mass spectrum of the $m^2(K^\pm\pi^\mp)$ combination in the $B^\pm \rightarrow (K_S^0\pi^+\pi^-)K^\pm$ data sample for (black) all candidates and (red) candidates for which $m_B \in m_B^{PDG} \pm 30 \text{ MeV}/c^2$. The LL and DD categories are combined. The only difference between the left and right plots is the $m(K\pi)$ mass range on the horizontal axis. The dotted line indicated the known D mass [31].

track and some subset of the D -decay tracks is formed. The presence of the background has been investigated by forming all such combinations, for all data categories, after the full selection has been applied. Only in a single channel is a peak visible: the $B^\pm \rightarrow (K_S^0\pi^+\pi^-)K^\pm$ channel, where $m(K^\pm\pi^\pm)$ has a peak, as shown in Fig. 4.23. Thus, a background is present from the favoured two-body D decay $B^\pm \rightarrow (K^\pm\pi^\mp)_D K_S^0\pi^\pm$, where the K^\mp is reconstructed as the companion, and the pions assigned to the D decay.

Is not favourable to veto this background, because a requirement on the invariant mass of a track combination that includes the companion track would impact the Dalitz-plot acceptance differently in the DK^\pm and $D\pi^\pm$ channels. Thus it would break a fundamental underlying feature of the measurement: the identical selection efficiency profile between these modes. However, the yield excess in the $m(K_{\text{companion}}^\pm\pi^\mp_D)$ range around m_D , attributed to the background, corresponds to only about 0.5% of the signal yield. A background at this level does not lead to a limiting systematic uncertainty on the measurement, as described in Section 4.6.9.

4.4 Signal and background mass shapes

The measurement employs *extended maximum-likelihood fits* [136] to the $m(Dh^\pm)$ distribution of signal candidates to determine the observables of interest. The analysis implements a two-step fit procedure: first the data samples are analysed without separating the candidates by B charge or Dalitz bin, in order to determine appropriate parametrisations of the $m(Dh^\pm)$ distribution of the signal and relevant background components. The parameterisations are then kept fixed in a subsequent

2152 fit of the observables of interest, where the candidates are split by B charge
2153 and Dalitz bin. This section describes the first step, whereas the latter fit is
2154 the subject of Section 4.5.

2155 In both steps, the candidates are split in 8 categories depending on whether
2156 the companion is categorised as a kaon or pion, whether the K_S^0 meson is in the
2157 LL or DD category, and by whether the D meson is reconstructed in the $K_S^0\pi^+\pi^-$
2158 or $K_S^0K^+K^-$ final state. In the remained of this text, these categories are indexed
2159 with the letter c . For each category, c , the expected number of observed decays
2160 at a given B mass, $F^c(m)$, is given by the sum of a signal contribution and a
2161 number of background distributions

$$F^c(m|\theta) = N_s^c(\theta)f_s^c(m|\theta) + \sum_b N_b^c(\theta)f_b^c(m|\theta), \quad (4.4)$$

2162 where θ denotes a set of parameters that describe the mass shapes and expected
2163 yields, in which some parameters are shared between categories. The distributions
2164 $f_{s/b}^c$ are normalised to integrate to unity, and the expected signal (background)
2165 yields are denoted N_s^c (N_b^c). A total, normalised distribution can then be defined

$$f^c(m|\theta) = \frac{1}{N_{\text{tot}}^c(\theta)}F^c(m|\theta), \quad N_{\text{tot}}^c(\theta) = N_s^c(\theta) + \sum_b N_b^c(\theta). \quad (4.5)$$

2166 Given a set of N_{observed}^c measured B masses, $\{m_i^c\}$, in a given category, the extended
2167 log-likelihood function is defined

$$\ln \mathcal{L}_c(\theta|\{m_i^c\}) \equiv \sum_i \ln f^c(m_i^c|\theta) + \ln \text{Poisson}(N_{\text{tot}}^c(\theta), N_{\text{observed}}^c) \quad (4.6)$$

2168 In a simultaneous fit the total, negative log-likelihood is $-\ln \mathcal{L} = -\sum_c \mathcal{L}_c$, and
2169 this function can be minimised to find the maximum-likelihood estimates of the
2170 parameters in θ , as well as their confidence regions and correlation coefficients.
2171 This is handled with the `RooFit` package [137].

2172 Apart from signal decays, the fit includes components that describe combinatorial
2173 background, backgrounds from decays where a companion pion is misidentified
2174 as a kaon or vice versa, and partially reconstructed backgrounds. Each of these
2175 components are described in detail in the following, before the results of the
2176 first-stage fit are presented in Section 4.4.5.

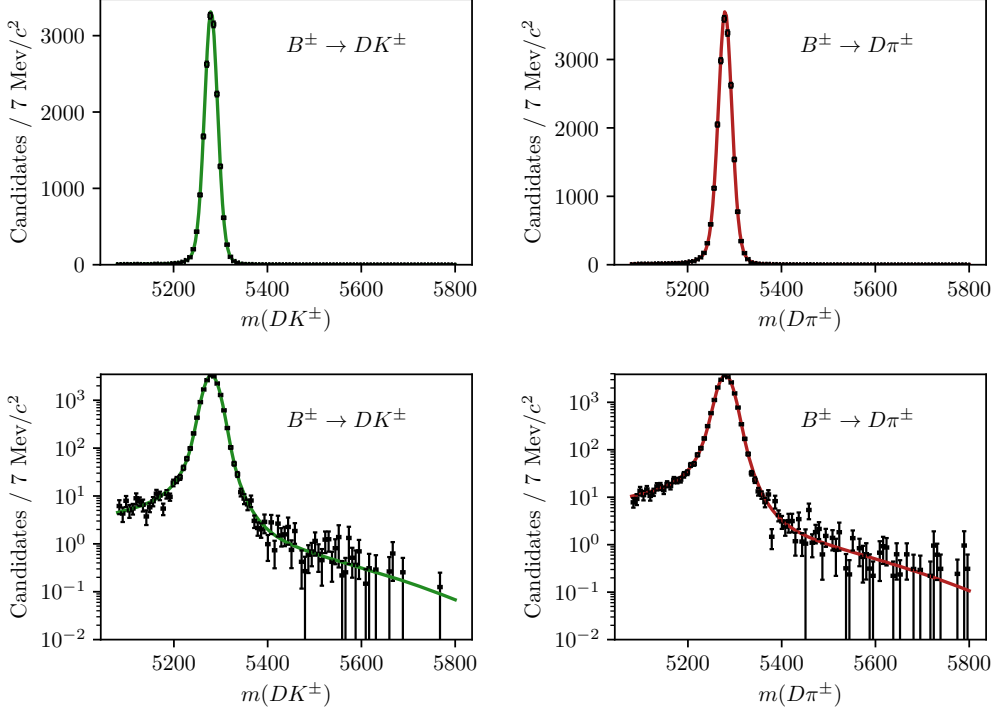


Figure 4.24: Fit projection of the signal shape to simulated $B^\pm \rightarrow D(\rightarrow K_S^0 \pi^+ \pi^-)h^\pm$ samples reconstructed in the LL category. (Left) shows DK shapes, and (right) shows $D\pi$ shapes. The shapes are shown with both linear and logarithmic y -axis scales.

2177 4.4.1 Signal decays

2178 The signal component is modelled with a sum of a Gaussian density function,
 2179 $f_G(m|m_B, \sigma)$, and a modified Gaussian distribution with the parameterisation

$$f_C(m|m_B, \sigma, \alpha_L, \alpha_R, \beta) \propto \begin{cases} \exp \left[\frac{-\Delta m^2(1+\beta\Delta m^2)}{2\sigma^2 + \alpha_L \Delta m^2} \right], & \Delta m = m - m_B < 0 \\ \exp \left[\frac{-\Delta m^2(1+\beta\Delta m^2)}{2\sigma^2 + \alpha_R \Delta m^2} \right], & \Delta m = m - m_B > 0, \end{cases} \quad (4.7)$$

2180 which is Gaussian when $\Delta m^2 \ll \sigma^2/\alpha_{L/R}$ or $\Delta m^2 \gg \beta^{-1}$ (with widths of σ and
 2181 $\sqrt{\alpha_{L/R}/\beta}$ respectively), with an exponential-like transition that is able to model the
 2182 effect of the experimental resolution of LHCb very well. For the case $\beta = 0$ the shape
 2183 is denoted the *Cruijff* shape; however, in this case it tends to a uniform distribution
 2184 for large Δm^2 values, and cannot model the tails of the signal distribution well.
 2185 Thus, the full density function is

$$f_s(m|m_B, \sigma, \alpha_L, \alpha_R, \beta) = k_C f_C(m|m_B, \sigma, \alpha_L, \alpha_R, \beta) + (1 - k_C) f_G(m|m_B, \sigma). \quad (4.8)$$

2186 The tail parameters $(\alpha_{L/R}, \beta)$ and the constant k_C are determined in fits to simulated
 2187 signal decays that have passed the full selection. The parameters are shared

2188 between the $K_S^0\pi^+\pi^-$ and $K_S^0K^+K^-$ channels, but otherwise independent in the
 2189 fit categories. An example of a fit to simulated $B^\pm \rightarrow D(\rightarrow K_S^0\pi^+\pi^-)h^\pm$ decays
 2190 is given in Fig. 4.24. The resolution parameters σ are determined in the fit to
 2191 actual data. Separate parameters are determined in the LL and DD categories,
 2192 because the LL category has a better resolution on the K_S^0 momentum, and
 2193 therefore a narrow peak in reconstructed B mass. Likewise, separate resolution
 2194 parameters are used for $B^\pm \rightarrow D\pi^\pm$ and $B^\pm \rightarrow DK^\pm$ decays, because the smaller
 2195 Q value in the latter case leads to smaller momenta of the decay products, and
 2196 a correspondingly better resolution.

2197 The signal yields are determined independently in each $B^\pm \rightarrow D\pi^\pm$ category.
 2198 The yields in the $B^\pm \rightarrow DK^\pm$ categories are then parameterised in terms of a single
 2199 yield-ratio $\mathcal{R}_{K/\pi}$, and ϵ^c , the corresponding selection efficiency for a given category

$$N_{DK^\pm}^c = \mathcal{R}_{K/\pi} \times N_{D\pi^\pm}^c \times \frac{\epsilon_{DK^\pm}^c}{\epsilon_{D\pi^\pm}^c}. \quad (4.9)$$

2200 The selection efficiency is obtained in simulation, except for the PID efficiencies
 2201 which are obtained in calibration data as described in Section 4.1.3. The parameter
 2202 $\mathcal{R}_{K/\pi}$ is shared between all categories, and corresponds to the branching ratio
 2203 between $B^\pm \rightarrow DK^\pm$ and $B^\pm \rightarrow D\pi^\pm$ decays. Therefore, it can be compared to
 2204 the branching ratio ratio measured in dedication measurements, which serves as
 2205 an important cross check of the efficiency determination.

2206 4.4.2 Cross-feed between $B^\pm \rightarrow Dh^\pm$ channels

2207 There is a cross-feed between the $B^\pm \rightarrow D\pi^\pm$ and $B^\pm \rightarrow DK^\pm$ channels, where real
 2208 $B^\pm \rightarrow D\pi^\pm$ decays are reconstructed as $B^\pm \rightarrow DK^\pm$ decays, or where $B^\pm \rightarrow DK^\pm$
 2209 decays are reconstructed as $B^\pm \rightarrow D\pi^\pm$ decays. Due to relative branching fractions
 2210 the former contribution is by far the most important, but both are modelled.

2211 The cross-feed shapes are obtained in a data-driven manner using the sPlot
 2212 method [135], and fixed in the fit to data. Separate shapes are determined for
 2213 each category, using the following steps:

- 2214 • The procedure is based on the reasonably pure $B^\pm \rightarrow D\pi^\pm$ sample obtained
 2215 when the full selection is applied. A simple mass fit is performed to the
 2216 invariant mass spectrum and the sPlot method [135] is used to obtain the
 2217 sWeights, w_s , for the signal component. The mass fit uses the same components
 2218 for signal, low mass shape, and combinatorial background as described in this
 2219 section.

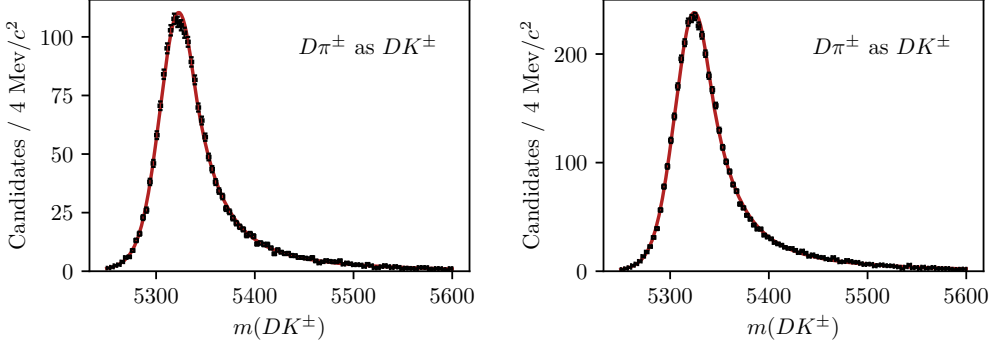


Figure 4.25: Fitted shape of the B^\pm invariant mass spectrum for $B^\pm \rightarrow D\pi^\pm$ decays misidentified as $B^\pm \rightarrow DK^\pm$ decays for (left) LL and (right) DD candidates in the $D \rightarrow K_S^0 \pi^+ \pi^-$ mode.

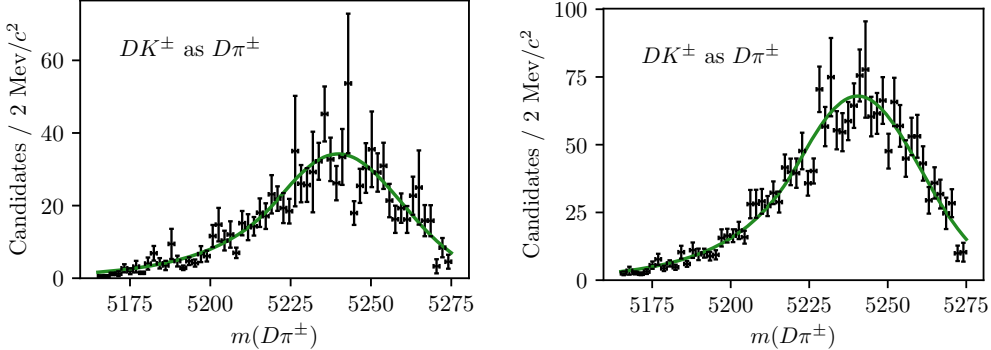


Figure 4.26: Fitted shape of the B^\pm invariant mass spectrum for $B^\pm \rightarrow DK^\pm$ decays misidentified as $B^\pm \rightarrow D\pi^\pm$ decays for (left) LL and (right) DD candidates in the $D \rightarrow K_S^0 \pi^+ \pi^-$ mode.

- 2220 • A set of weights are defined, based on the candidate-by-candidate PID
 2221 efficiencies obtained as described in Section 4.1.3:
 2222 – The extracted PID efficiencies of the $\text{PIDK} < 4$ cut $\epsilon_{D\pi \rightarrow D\pi}(p, \eta, n_{\text{tracks}})$
 2223 are used to reverse-weight the $B^\pm \rightarrow D\pi^\pm$ sample, in order to obtain the
 2224 bachelor kinematic distributions before the $\text{PIDK} < 4$ cut is applied.
 2225 – The extracted PID efficiencies of the $\text{PIDK} > 4$ cut $\epsilon_{D\pi \rightarrow DK}(p, \eta, n_{\text{tracks}})$
 2226 are used to obtain the bachelor kinematic distribution of the $B^\pm \rightarrow D\pi^\pm$
 2227 candidates mis-identified as $B^\pm \rightarrow DK^\pm$.
 2228 • The raw distribution of the invariant mass of B^\pm particles with a misidentified
 2229 bachelor, m_B^{mis-ID} , is produced by also doing the DecayTreeFit kinematic refit
 2230 while swapping the companion mass hypothesis of each $B^\pm \rightarrow D\pi^\pm$ candidate
 2231 to a kaon hypothesis.

- 2232 • Each candidate is reweighted by the overall weight $w = w_s^{cand.}/\epsilon_{D\pi \rightarrow D\pi}^{cand.} \cdot$
 2233 $\epsilon_{D\pi \rightarrow DK}^{cand.}$, and the reweighed m_B^{mis-ID} distribution is fitted to obtain the cross-
 2234 feed mass distribution function.

2235 The distributions are modelled with a sum of two Crystal Ball density functions,
 2236 each defined by the parameterisation [138]

$$f_{CB}(m, \mu, \sigma, \alpha, n) \propto \begin{cases} \exp \left[-\frac{1}{2} \left(\frac{m-\mu}{\sigma} \right)^2 \right] & \text{if } (m-\mu)/\sigma > -\alpha \\ A \left(B - \frac{m-\mu}{\sigma} \right)^{-n} & \text{otherwise,} \end{cases} \quad (4.10)$$

2237 where $\alpha > 0$, and

$$A = \left(\frac{n}{\alpha} \right)^n \exp[-\alpha^2/2], \quad B = \frac{n}{\alpha} - \alpha. \quad (4.11)$$

2238 The obtained m_B^{mis-ID} spectrum and obtained mass shape is given in Fig. 4.25
 2239 for the $D \rightarrow K_S^0 \pi^+ \pi^-$ category; the $D \rightarrow K_S^0 K^+ K^-$ shapes are very similar. An
 2240 analogous procedure is used to obtain the mass distribution of $B^\pm \rightarrow DK^\pm$ decays
 2241 reconstructed in the $B^\pm \rightarrow D\pi^\pm$ category. In the first stage where sPlots are
 2242 extracted by a fit to the $B^\pm \rightarrow DK^\pm$ mass spectrum, the cross-feed component
 2243 determined as described above is included. An example of one of the resulting
 2244 shapes is given in Fig. 4.26

2245 The yield of cross-feed from $B^\pm \rightarrow D\pi^\pm$ decays in a given $B^\pm \rightarrow DK^\pm$ category
 2246 is parameterised in terms of the yield of correctly identified $B^\pm \rightarrow D\pi^\pm$ decays and
 2247 the mis-identification probability extracted from calibration samples as described
 2248 in Section 4.1.3. Denoting the rate at which a pion is reconstructed as a kaon
 2249 by $\epsilon_{\pi \rightarrow K}^c$ in a given category, c , the yield is

$$N_{\pi \rightarrow K}^c = N_{D\pi^\pm}^c \frac{\epsilon_{\pi \rightarrow K}^c}{1 - \epsilon_{\pi \rightarrow K}^c}, \quad (4.12)$$

2250 with an analogous definition of the yield of the cross-feed component from
 2251 $B^\pm \rightarrow DK^\pm$ decays in the $B^\pm \rightarrow D\pi^\pm$ spectrum.

2252 4.4.3 Partially reconstructed backgrounds

2253 A number of background candidates stem from partly reconstructed B decays of the
 2254 type $B \rightarrow DhX$, where X denotes a photon or a pion that is not reconstructed. It
 2255 is not possible to reject these decays in the selection, due to the similarity to signal
 2256 decays. However, the missing momentum results in reconstructed B masses below
 2257 the actual B mass, and the backgrounds are also denoted *lowmass* backgrounds.
 2258 These mass distributions are modelled with analytic shapes, derived based on two

principles. Firstly, the kinematic endpoints of the distributions are fully defined by the particle masses in the decay. Secondly, the angular distribution of the missing particle has a one-to-one relation to the missing momentum, and therefore to the reconstructed B mass. Depending on the spin-parity of the particles and resonances involved in the decay, two different mass distributions arise.

In B decays where the missing particle is a scalar that is produced in the decay of a vector resonance (eg. $B^\pm \rightarrow D^{*0}(\rightarrow D^0\pi^0)\pi^\pm$ decays where the π^0 is not reconstructed), the $m(D^0\pi^\pm)$ distribution has a double-peak structure. The D^{*0} helicity angle θ is defined as the angle between the π^0 momentum vector in the D^{*0} rest frame and the D^{*0} boost vector in the B rest frame. The helicity of D^{*0} means that the π^0 will travel predominantly in the direction where $\theta = 0$ or $\theta = \pi$. When $\theta = 0$ the fraction of momentum carried by the missing π^0 is lower, leading to a higher reconstructed $m(D^0\pi^\pm)$. When $\theta = \pi$ the converse occurs. The resulting B mass distribution is a parabola $f_{\text{HORNS}}^0(m)$ peaking near both kinematic endpoints a and b

$$f_{\text{HORNS}}^0(m) = \begin{cases} (m - \frac{a+b}{2})^2, & \text{if } a < m < b \\ 0, & \text{otherwise.} \end{cases} \quad (4.13)$$

Due to the double-peaking structure, and the fact that was developed by Paolo Gandini for the two-body ADS/GLW analyses [], this shape is denoted a *HORNSdini* shape when convolved with a resolution function as described below.

The second relevant decay situation is where the missing particle is a vector, again produced via the intermediate decay of a vector resonance (eg. $B^\pm \rightarrow D^{*0}(\rightarrow D^0\gamma)\pi^\pm$ decays where the photon is not reconstructed). In this case, the spin-parity of the photon (1^-) means that it will decay preferentially in the $\theta = \frac{\pi}{2}$ or $\theta = \frac{3\pi}{2}$ directions, and so a double-peak structure is not seen. In this case the parabolic distribution $f_{\text{HILL}}^0(m)$ with kinematic endpoints a, b has negative curvature and can be described by

$$f_{\text{HILL}}^0(m) = \begin{cases} -(m - a)(m - b), & \text{if } a < m < b \\ 0, & \text{otherwise.} \end{cases} \quad (4.14)$$

Resolution effects mean that the parabolic shapes must be convolved with a resolution function, chosen to be a sum of two Gaussians. For a single Gaussian shape $f_G(x|\mu, \sigma)$ with mean μ and width σ , the double Gaussian is expressed as

$$f_{DG}(x) = f_G(x|\mu, \sigma) + k_G f_G(x|\mu, R_\sigma \sigma). \quad (4.15)$$

where σ is the width of the first Gaussian, and k_G is the relative fractions between the two Gaussians and R_σ is their relative widths. Further, selection effects can

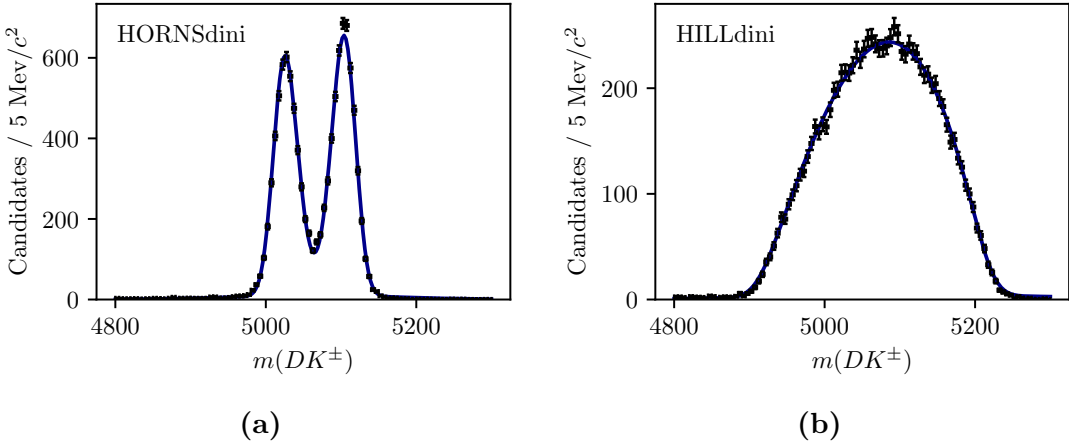


Figure 4.27: Examples of (a) the *HORN**sini* distribution fit to simulated $B^\pm \rightarrow (D^{*0} \rightarrow D^0[\pi^0])K^\pm$ decays, and (b) the *HILL**sini* distribution fit to simulated $B^\pm \rightarrow (D^{*0} \rightarrow D^0[\gamma])K^\pm$ decays. The fits in this figure are made to illustrate the features of each shape, but do not enter the actual fit to data.

distort the horns shape such that one of the peaks is higher than the other. This is taken into account by introducing a linear polynomial with slope parameter ξ . As $\xi \rightarrow 0$, the left hand peak decreases in size relative to the right hand peak. The resulting *HORN_Sdini* and *HILLdini* distributions are therefore

$$f_{\text{HORNS/HILL}}(m) = \int_a^b dx f_{\text{HORNS/HILL}}^0(x) f_{DG}(m|x, \sigma, k_G, R_\sigma) \left(\frac{1-\xi}{b-a}x + \frac{b\xi - a}{b-a} \right). \quad (4.16)$$

Examples of the shapes are given in Fig. 4.27. These shapes are used to fit all partially reconstructed backgrounds, as described in the following section.

2294 Determination of the partially reconstructed background distributions

In both the $B^\pm \rightarrow DK^\pm$ and $B^\pm \rightarrow D\pi^\pm$ categories, components are included to describe contributions from the partially reconstructed decays (where the particle in square brackets is not reconstructed)

- $B^\pm \rightarrow (D^{*0} \rightarrow D^0[\pi^0])h^\pm$, described using a *HORNSdini* distribution
 - $B^\pm \rightarrow (D^{*0} \rightarrow D^0[\gamma])h^\pm$: described using a *HILLdini* distribution
 - $B^0 \rightarrow (D^{*\pm} \rightarrow D^0[\pi^\pm])h^\mp$: described using a *HORNSdini* distribution
 - $B^{\pm(0)} \rightarrow D^0 h^\pm [\pi^{0(\mp)}]$: described using a *HORNSdini* distribution

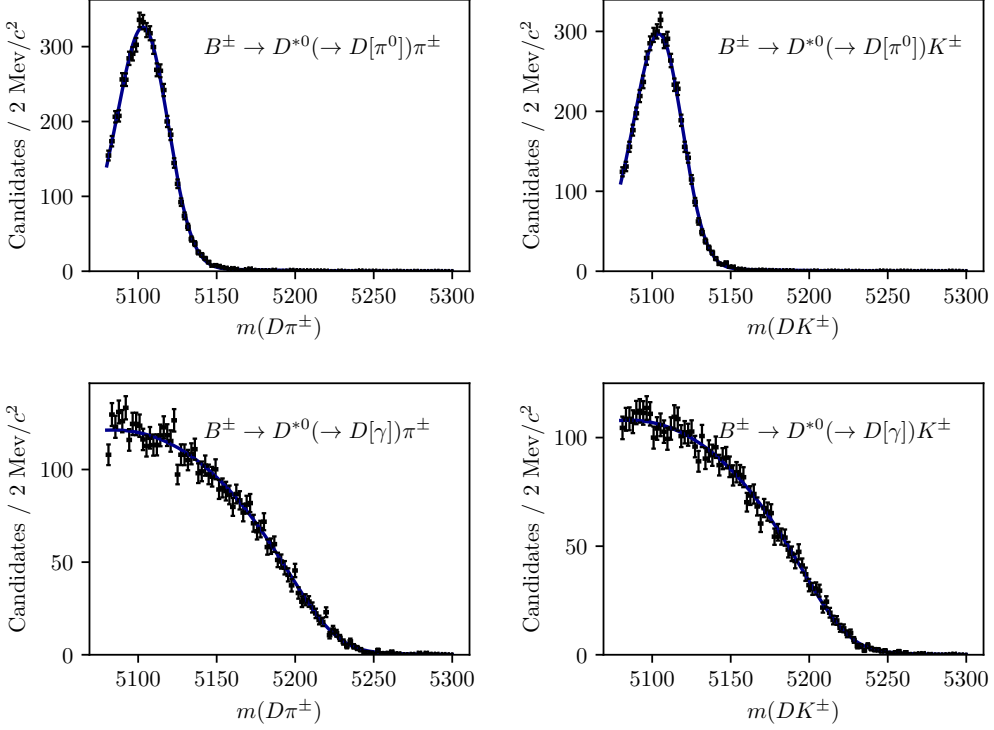


Figure 4.28: Fit projection of the fit to (top) simulated $B^+ \rightarrow D^{*0}(\rightarrow D^0[\pi^0])h^\pm$ decays and (bottom) simulated $B^+ \rightarrow D^{*0}(\rightarrow D^0[\gamma])h^\pm$ decays, all reconstructed in the DD category. Both the (left) DK and (right) $D\pi$ shapes are shown.

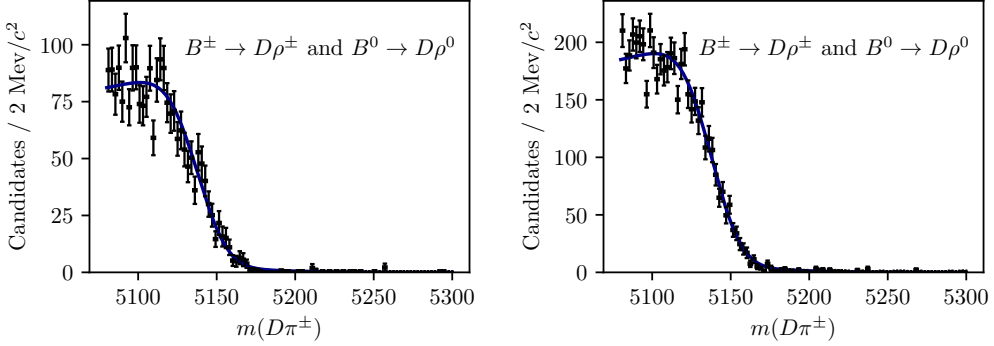


Figure 4.29: Projections of the fit to simulated $B^\pm \rightarrow D\rho^\pm$ and $B^0 \rightarrow D\rho^0$ samples reconstructed as $B^\pm \rightarrow D\pi^\pm$ decays for the (left) LL and (right) DD categories.

2302 The mass distributions of all the $B \rightarrow D^*h^\pm$ contributions are obtained from
 2303 fits to samples of full LHCb simulation. Examples of these fits are shown in
 2304 Fig. 4.28. All shape parameters are kept fixed in the fit to data, except for the
 2305 parameter σ of the resolution function in Eq. (4.15) which is allowed to obtain
 2306 the value preferred by data.

2307 The mass distribution of $B^{\pm(0)} \rightarrow D^0 h^\pm [\pi^{0(\mp)}]$ decays reconstructed in the

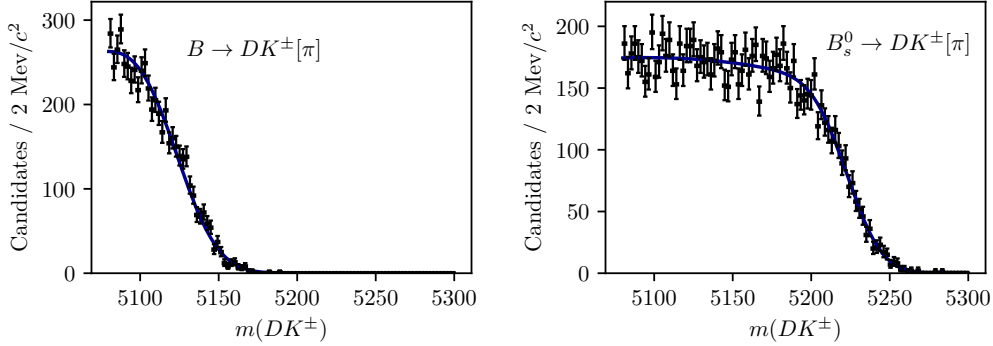


Figure 4.30: Fit projection for the fit used to obtain a shape for the partly reconstructed background from (left) $B \rightarrow DK\pi$ decays and (right) $B_s^0 \rightarrow DK^\pm\pi^-$ decays where a pion is not reconstructed.

2308 $B^\pm \rightarrow D\pi^\pm$ categories is obtained from full LHCb simulation samples of $B^\pm \rightarrow D^0\rho^\pm$
 2309 and $B^0 \rightarrow D^0\rho^0$ decays. The shapes were compared to those predicted by an
 2310 amplitude model for $B^0 \rightarrow D^0 \rightarrow \pi^\pm\pi^\mp$ decays developed by LHCb [139], but
 2311 found to be very similar for the $m(D\pi^\pm)$ range relevant to this analysis. The
 2312 obtained shapes are shown in Fig. 4.29.

2313 The mass distribution of $B^{\pm(0)} \rightarrow D^0 K^\pm[\pi^{0(\mp)}]$ decays reconstructed in the
 2314 $B^\pm \rightarrow DK^\pm$ categories, on the other hand, is obtained from a sample of signal
 2315 decays, generated via a amplitude model for $B^0 \rightarrow D^0 \rightarrow K^\pm\pi^\mp$ decays developed
 2316 by LHCb [140] and smeared to take the LHCb resolution into account. This follows
 2317 an approach developed in the context of a GLW analysis based on partially recon-
 2318 structed decays made within LHCb [141]. The obtained shape is shown in Fig. 4.30.

2319 The background yields of these backgrounds are parameterised in terms of
 2320 one total yield parameter, accounting for all partially reconstructed B^\pm and
 2321 B^0 decays, and a number of parameters that describe the relative rates of the
 2322 different contributions. In the $B^\pm \rightarrow D\pi^\pm$ channels, the relative rates of the
 2323 $B^\pm \rightarrow (D^{*0} \rightarrow D^0[\pi^0])h^\pm$ and $B^0 \rightarrow (D^{*\pm} \rightarrow D^0[\pi^\pm])h^\mp$ backgrounds are fixed
 2324 from the known branching fractions, and relative selection efficiencies in simulation.
 2325 These backgrounds have almost identical mass distributions and it is not possible to
 2326 determine the ratio in the fit to data. The relative yield of $B^\pm \rightarrow D^*(\rightarrow D^0[\gamma])\pi^\pm$
 2327 compared to the $B \rightarrow D^*(\rightarrow D^0[\pi])\pi^\pm$ is denoted $f_{D^*\gamma}^{D\pi}$ and is floated in the fit to
 2328 data, as is the relative yield of $B \rightarrow D^0\pi^\pm[\pi]$ decays compared to the $B \rightarrow D^*\pi$
 2329 modes, denoted $f_{D\pi\pi}^{D\pi}$. In the $B^\pm \rightarrow DK^\pm$ channels, all the relative background
 2330 rates are fixed via known branching fractions and relative selection efficiencies; this
 2331 is necessary to obtain a stable fit, due to the lower yields.

In the $B^\pm \rightarrow DK^\pm$ categories, an additional partially reconstructed background is considered from $B_s^0 \rightarrow \bar{D}^0[\pi^+]K^-$ (an conjugate) decays. The mass shape is obtained from simulated decays, generated using an amplitude model published by LHCb [142] and smeared to account for the experimental resolution. The obtained shape is shown in Fig. 4.30. The yield of this background component is fixed relative to the signal yields in the corresponding $B^\pm \rightarrow D\pi^\pm$ category, taking the relative branching ratios and hadronisation factors into account.

In the $B^\pm \rightarrow DK^\pm$ channels there is a contribution from partially reconstructed $B \rightarrow D^*\pi^\pm X$ decays where the companion pion is misidentified as a kaon. The reverse contribution is negligible due to the relative branching fractions, and the fact that it is mostly shifted below the mass range of the fit. These are modelled using analytic, empirical mass distributions (essentially sums of a number of regular *HORNs/HILLdini* distributions), with parameters that are determined in fits to simulated $B \rightarrow D^*\pi^\pm$ and $B \rightarrow D\rho$ decays where the pion is reconstructed with the kaon mass hypothesis. The shapes are fixed in the fit to data.

2347

2348 Partially reconstructed backgrounds that are not modelled

2349 It was considered whether a background from $\Lambda_b^0 \rightarrow D^0p\pi^-$ decays where a pion
 2350 is not reconstructed, and the proton is misidentified as the companion, can be
 2351 expected to contribute significantly. This has been investigated in full LHCb
 2352 simulation samples, for the D final state $K_S^0\pi^+\pi^-$. Taking into account the selection
 2353 efficiencies, branching fractions, and hadronisation fraction of this background, the
 2354 expected relative yield of the Λ_b^0 background compared to signal of 0.03 % in the
 2355 $B^\pm \rightarrow D\pi^\pm$ channel, which is completely negligible. In the $B^\pm \rightarrow DK^\pm$ channel,
 2356 total of about 200 decays are expected, combined for the LL and DD categories.
 2357 However, most of these lie at B masses smaller than the signal peak, and their impact
 2358 is small. Therefore it is not necessary to model the background in the nominal fit;
 2359 a systematic uncertainty is assigned that accounts for the small potential impact.

2360 In the analogous case of $\Lambda_b^0 \rightarrow D^0pK^-$ decays, the missing energy of the non-
 2361 reconstructed kaon results in a reconstructed B mass below the fit range.

2362 It has also been investigated whether a background from $\Lambda_b^0 \rightarrow \Lambda_c^+\pi^-$ or $\Lambda_b^0 \rightarrow$
 2363 $\Lambda_c^+K^-$ decays can be expected, where $\Lambda_c^+ \rightarrow pK_S^0\pi^+\pi^-$, a pion is missed and the
 2364 proton is misidentified as a pion or kaon from the D decay. Since no PID requirement
 2365 is made on the D decay products in the $D \rightarrow K_S^0\pi^+\pi^-$ channels, and only a loose
 2366 one for $D \rightarrow K_S^0K^+K^-$, this is possible in principle. In practice, the background is
 2367 sufficiently suppressed from the applied D mass requirement to have no significant
 2368 impact, and is therefore not modelled. A systematic uncertainty is assigned that
 2369 accounts for any potential impact on the measurement due to this choice.

2370 **4.4.4 Combinatorial background**

2371 The combinatorial background is modelled with an exponentially falling density
2372 function, where both the yield and exponential slope are determined independently
2373 for each category. This shape is found to model the combinatorial well in all
2374 categories, most evident in the high- m_B regions where this background dominates.

2375 **4.4.5 Fit results**

2376 The fit range is chosen to be $m_B \in [5080, 5800] \text{ MeV}/c^2$. The low end of this
2377 interval includes the high-mass peak of the double-peak structure in the partially
2378 reconstructed background, which helps the fit constrain the relative contributions of
2379 backgrounds in the lowmass regions. A number of additional backgrounds exist at
2380 even lower m_B values, thus extending the fit range to lower masses would necessitates
2381 an extended model, but not benefit the description of the signal region. The high
2382 end of the interval includes enough combinatorial background to allow the fit to
2383 determine the exponential slope parameter accurately.

2384 A large number of pseudoexperiments are carried out to verify that the fit
2385 procedure is self-consistent, in which toy data sets are generated according to
2386 the expected B mass distributions, and then fitted. None of the parameters
2387 obtained in the fit exhibit a mean bias different from zero. For most parameters
2388 the uncertainties are well estimated. This is the case for the signal yields, and
2389 the $DK^\pm\text{-}D\pi^\pm$ yield ratio \mathcal{R} , as evidenced by the pull plots in Fig. 4.31. The
2390 fit underestimates the uncertainty by 10-20 % for some of the parameters related
2391 to the partly reconstructed backgrounds, as shown in Fig. 4.32, but this is taken
2392 into account when the uncertainties are propagated to the observables in the
2393 second-stage fit, as described in Section 4.6.3.

2394 The projections of the fit to data are shown in Figs. 4.33 and 4.34, for the
2395 $D \rightarrow K_S^0\pi^+\pi^-$ and $D \rightarrow K_S^0K^+K^-$ data sets, respectively. The obtained yields for
2396 each fit component are given in Table 4.6. The total yield of $B^\pm \rightarrow D\pi^\pm$ decays is
2397 approximately 230,000 across all channels. The obtained value of the yield ratio is
2398 $\mathcal{R}_{K/\pi} = (7.7 \pm 0.1) \%$, corresponding to a total $B^\pm \rightarrow DK^\pm$ yield of 16,500, of which
2399 about 14,300 pass the PID requirement and are reconstructed in the $B^\pm \rightarrow DK^\pm$
2400 category. This value of \mathcal{R} is in excellent agreement with expectation from the
2401 known branching fractions [31], which predict $\mathcal{R}_{K/\pi}^{\text{PDG}} = (7.8 \pm 0.3) \%$.² The shape
2402 parameters determined in the fit to data are summarised in Table 4.7.

²While it would seem this measurement thus determines the yield ratio $\mathcal{R}_{K/\pi}$ with a much better precision than the current world average uncertainty, that is because the result quoted here does not include any systematic uncertainties; it is only included to serve as a, successfully passed, cross check.

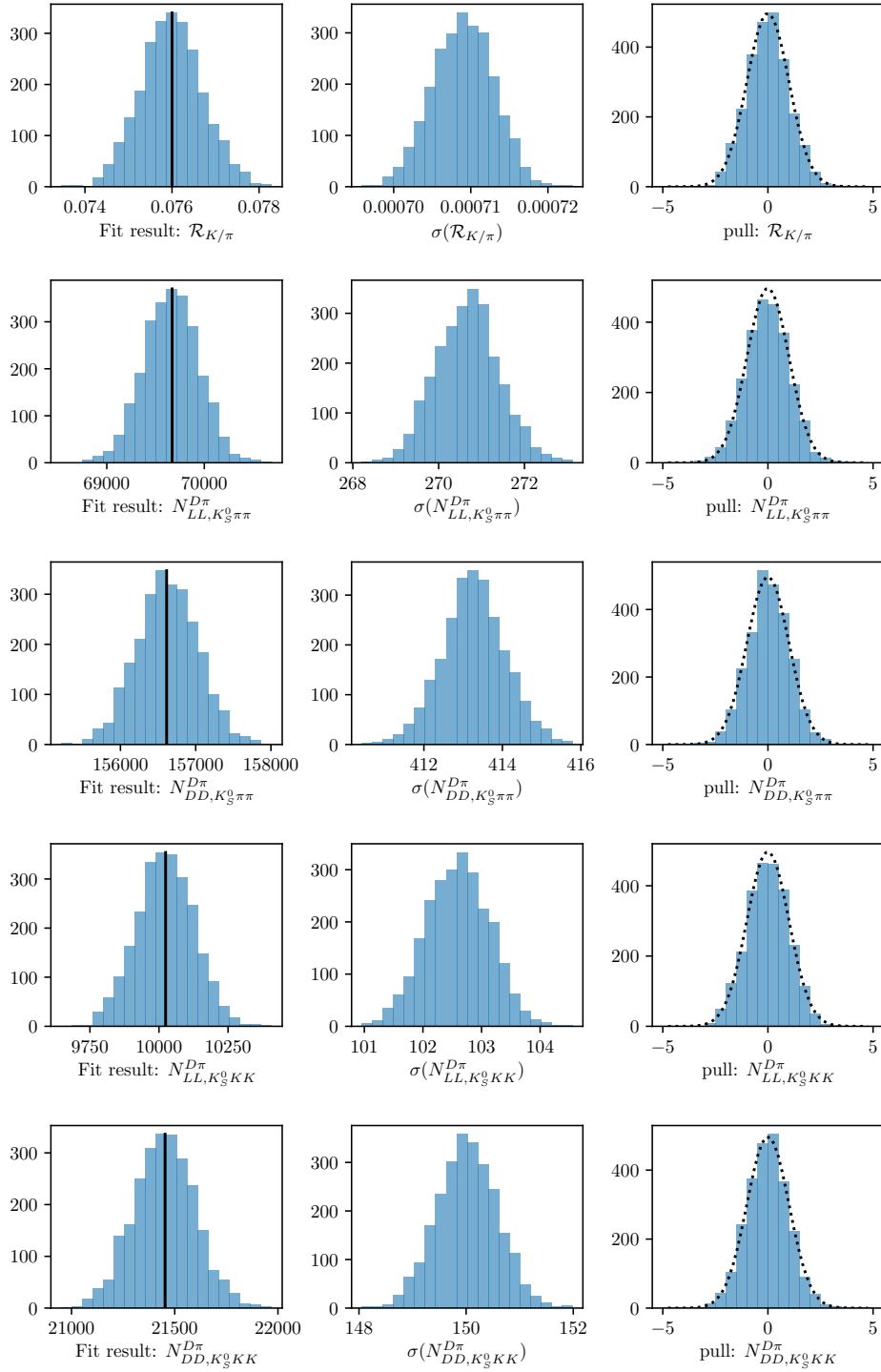


Figure 4.31: The (left) fitted value, (centre) estimated statistical uncertainty, and (right) pull plots for the signal yield parameters, as obtained in a number of pseudo experiments. The black line on the left shows the value used to generate the pseudo data sets; the dotted line on the right shows a Gaussian distribution with mean equal to zero and a standard deviation equal to unity.

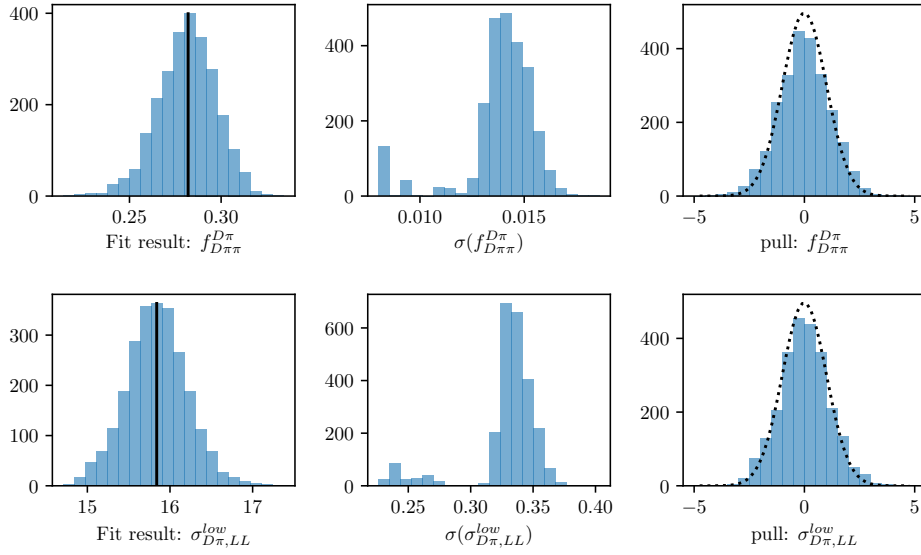


Figure 4.32: The (left) fitted value, (centre) estimated statistical uncertainty, and (right) pulls obtained in a number of pseudo experiments for two examples of parameters relating to the partially reconstructed backgrounds, where the uncertainties are slightly underestimated on average. The standard deviation of the pull distributions is approximately 1.15 in both cases.

Table 4.6: Fitted total candidate yields. The quoted signal yields are for the number of candidates that survive the respective PID cut, whereas the DK^\pm - $D\pi^\pm$ ratio is corrected for PID and selection efficiencies so that it corresponds to the branching ratio.

Component	LL	DD
Signal		
$B^\pm \rightarrow D(\rightarrow K_S^0\pi^+\pi^-)\pi^\pm$	$61,573 \pm 254$	$139,080 \pm 389$
$B^\pm \rightarrow D(\rightarrow K_S^0K^+K^-)\pi^\pm$	$9,160 \pm 98$	$19,910 \pm 144$
$R_{K/\pi} = n(DK)/n(D\pi)$ (%)	7.72 ± 0.08	
Combinatorial		
$B^\pm \rightarrow D(\rightarrow K_S^0\pi^+\pi^-)\pi^\pm$	$3,479 \pm 198$	$9,928 \pm 376$
$B^\pm \rightarrow D(\rightarrow K_S^0K^+K^-)\pi^\pm$	$1,103 \pm 94$	$2,545 \pm 155$
$B^\pm \rightarrow D(\rightarrow K_S^0\pi^+\pi^-)K^\pm$	$1,826 \pm 107$	$3,987 \pm 177$
$B^\pm \rightarrow D(\rightarrow K_S^0K^+K^-)K^\pm$	380 ± 39	655 ± 58
Part. Reco.		
$B^\pm \rightarrow D(\rightarrow K_S^0\pi^+\pi^-)\pi^\pm$	$43,004 \pm 242$	$95,452 \pm 403$
$B^\pm \rightarrow D(\rightarrow K_S^0K^+K^-)\pi^\pm$	$6,247 \pm 99$	$13,241 \pm 157$
$R_{K/\pi}^{low} = n_{low}(DK)/n_{low}(D\pi)$ (%)	6.65 ± 0.12	

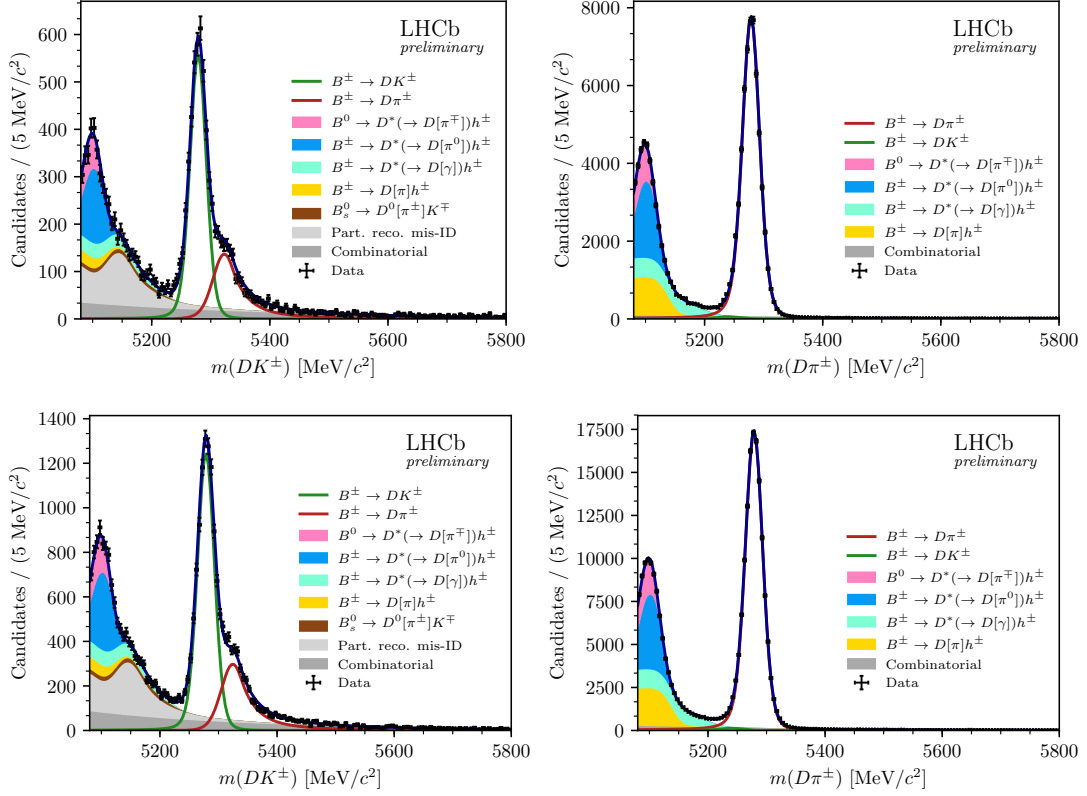


Figure 4.33: The invariant mass distribution for the (left) $B^\pm \rightarrow DK^\pm$ channel and (right) $B^\pm \rightarrow D\pi^\pm$ channel, where $D \rightarrow K_S^0\pi^+\pi^-$ and the K_S^0 is in the (top) LL and (bottom) the DD categories. The particle within square brackets in the legend denotes the particle that has not been reconstructed.

4.5 Measurement of the CP-violation observables

The section describes the second fit stage, in which the CP -violation observables of interest are determined. Compared to the first fit stage, the candidates are further split by B charge, and by the assigned Dalitz bin number, making for a total of 160 categories. Another extended maximum-likelihood fit is carried out, in which shape parameters of all signal and background components are fixed to those determined in the first fit stage, and thus all floating parameters relate to the signal and background yields. The signal yields are expressed in terms of the observables of interest, $(x_\pm^{DK}, y_\pm^{DK}, x_\xi^{D\pi}, y_\xi^{D\pi})$, allowing the fit to determine their optimal values. The details of the fit setup are summarised in the following section, along with a number of studies that lead to the specific setup being chosen. The results are presented in Section 4.5.2, and a wide range of consistency checks are described in Section 4.5.3.

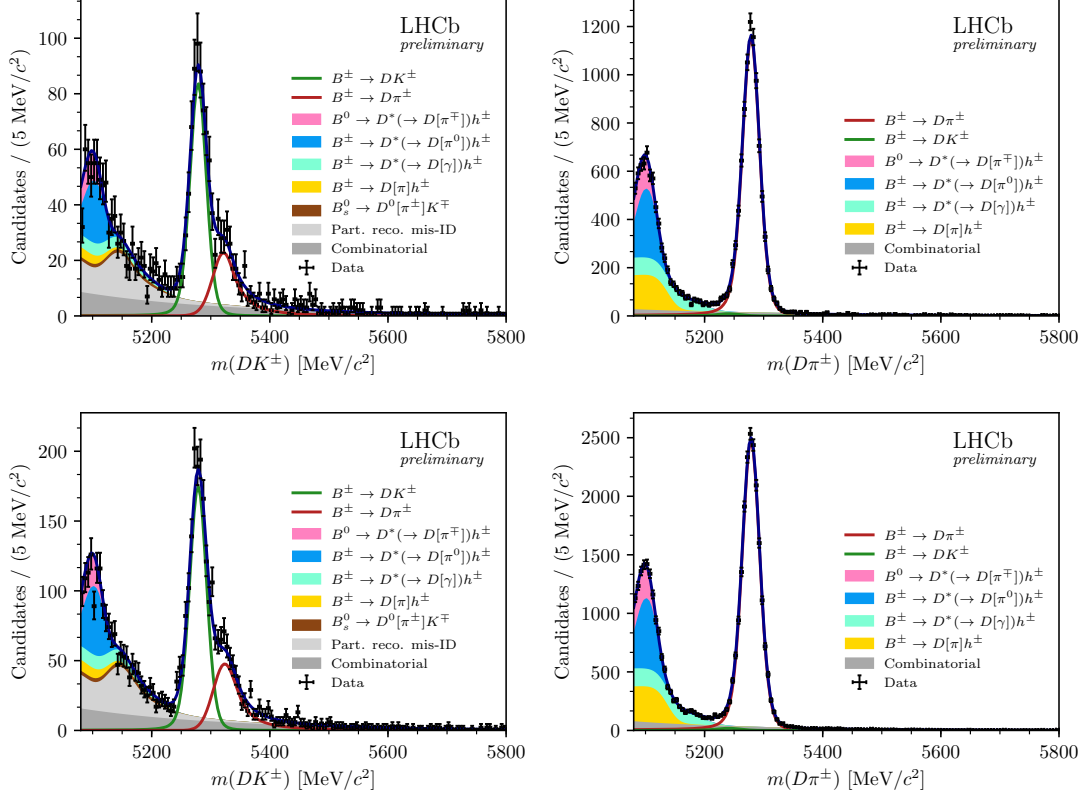


Figure 4.34: The invariant mass distribution for the (left) $B^\pm \rightarrow DK^\pm$ channel and (right) $B^\pm \rightarrow D\pi^\pm$ channel, where $D \rightarrow K_S^0 K^+ K^-$ and the K_S^0 is in the (top) LL and (bottom) the DD categories. The particle within square brackets in the legend denotes the particle that has not been reconstructed.

4.5.1 Fit setup

The basic principle of the measurement is that the signal yields in each bin (in a given category) are defined using the equations of Chapter 1, in order to allow for the determination of the CP -violation observables. In practice, a set of variables are defined

$$Y_{c,i}^- = F_{c,-i} + [(x_-^c)^2 + (y_-^c)^2]F_{c,-i} + 2\sqrt{F_{c,i}F_{c,-i}}(c_i^c x_-^c + s_i^c y_-^c), \quad (4.17)$$

$$Y_{c,i}^+ = F_{c,-i} + [(x_+^c)^2 + (y_+^c)^2]F_{c,-i} + 2\sqrt{F_{c,i}F_{c,-i}}(c_i^c x_+^c - s_i^c y_+^c), \quad (4.18)$$

for each data category, c , in terms of which the bin yields that enter the likelihood are given by

$$N_{c,i}^\pm = \frac{Y_{c,i}^\pm}{\sum_j Y_{c,j}^\pm} \times N_{c,\text{total}}^\pm. \quad (4.19)$$

This parameterisation is essentially identical to the expressions in Section 1.4, slightly modified so that the phase-space-integrated yields of B^+ and B^- decays

Table 4.7: Fitted parameter values.

	LL	DD
$\sigma_{D\pi}$ (MeV/ c^2)	14.27 ± 0.05	14.58 ± 0.04
σ_{DK} (MeV/ c^2)	13.61 ± 0.24	14.19 ± 0.17
μ (MeV/ c^2)		5278.60 ± 0.04
Combinatorial Slopes		
Decay mode	Slope ($10 \times 10^{-3} GeV^{-1}c^2$)	
$B^\pm \rightarrow D(\rightarrow K_S^0\pi^+\pi^-)\pi^\pm$	-3.1 ± 0.2	-4.0 ± 0.1
$B^\pm \rightarrow D(\rightarrow K_S^0K^+K^-)\pi^\pm$	-4.1 ± 0.4	-5.5 ± 0.3
$B^\pm \rightarrow D(\rightarrow K_S^0\pi^+\pi^-)K^\pm$	-3.2 ± 0.2	-3.9 ± 0.2
$B^\pm \rightarrow D(\rightarrow K_S^0K^+K^-)K^\pm$	-4.2 ± 0.4	-4.3 ± 0.4
Part. Reco.		
$\sigma_{D\pi}^{low}$ (MeV/ c^2)	13.73 ± 0.33	13.78 ± 0.28
$f_{D\pi\pi}^{D\pi}$		0.268 ± 0.013
$f_{D^*\gamma}^{D\pi}$		0.317 ± 0.005

in a given category are determined directly, in lieu of the normalisation constants h^\pm of that section. As discussed briefly in Section 1.4, there are choices to be made in terms of how the x and y are parameterised in the $B^\pm \rightarrow D\pi^\pm$ channel, and how the F_i parameters are determined. A series of feasibility studies were carried out to determine the optimal setup; these are presented in the following section, before the final fit setup is described in detail.

2431 Feasibility of alternative fit setups

2432 The motivation for promoting the $B^\pm \rightarrow D\pi^\pm$ channel to a signal channel is two-fold:
2433 one aim is to extract the information on γ from the $B^\pm \rightarrow D\pi^\pm$ data, even the
2434 precision gain is limited, and another is to be able to the F_i parameters directly
2435 from the $B^\pm \rightarrow Dh^\pm$ channels, to avoid the need for a control channel and a
2436 simulation-reliant efficiency correction. Two different sets of observables can be
2437 defined to describe the CP -violation effects in the $B^\pm \rightarrow D\pi^\pm$ channel:

- 2438 • one option, defined the 8-parameters setup below, is to define a new set of four
2439 Cartesian for the $B^\pm \rightarrow D\pi^\pm$ mode, $(x_-^{D\pi}, y_-^{D\pi}, x_+^{D\pi}, y_+^{D\pi})$, defined analogously
2440 to the $B^\pm \rightarrow DK^\pm$ observables

$$x_\pm^{D\pi} = r_B^{D\pi} \cos(\delta_B^{D\pi} \pm \gamma), \quad y_\pm^{D\pi} = r_B^{D\pi} \sin(\delta_B^{D\pi} \pm \gamma), \quad (4.20)$$

2441 • another, proposed in Refs. [75, 143], is to introduce the parameter

$$\xi_{D\pi^\pm} = \left(\frac{r_B^{D\pi^\pm}}{r_B^{DK^\pm}} \right) \exp[i(\delta_B^{D\pi^\pm} - \delta_B^{DK^\pm})] \quad (4.21a)$$

2442 and determining the observables

$$x_\xi^{D\pi} = \text{Re}[\xi_{D\pi^\pm}] \quad y_\xi^{D\pi} = \text{Im}[\xi_{D\pi^\pm}]. \quad (4.21b)$$

2443 This is denoted the 6-parameters setup below. In terms of $x_\xi^{D\pi}$ and $y_\xi^{D\pi}$, the
2444 usual Cartesian x_\pm and y_\pm are given by

$$x_\pm^{D\pi} = x_\xi^{D\pi} x_\pm^{DK} - y_\xi^{D\pi} y_\pm^{DK}, \quad y_\pm^{D\pi} = x_\xi^{D\pi} y_\pm^{DK} + y_\xi^{D\pi} x_\pm^{DK}. \quad (4.22)$$

2445 The former parameterisation has the benefit that information on γ from the
2446 $B^\pm \rightarrow DK^\pm$ and $B^\pm \rightarrow D\pi^\pm$ channels is encoded in separate sets of observables,
2447 whereas the latter parameterisation encodes information on CP violation from both
2448 channel in the (x_\pm^{DK}, y_\pm^{DK}) parameters. In combinations of many measurements, it
2449 is a useful cross check to be able to compare constraints obtained from individual
2450 modes; a good example is the LHCb combination from 2016 [127] where both
2451 $B^\pm \rightarrow DK^\pm$ and $B^\pm \rightarrow Dh^\pm$ combinations are made, and compared in detail. This
2452 is only possible with the former parameterisation. On the other hand, the latter
2453 parameterisation avoids introducing two non-physical degrees of freedom, which,
2454 as seen below, leads to better statistical behaviour.

2455 In order to inform the choice of parameterisation, a series of pseudoexperiments
2456 have been carried out to compare the obtainable precision on γ (these studies
2457 were performed, and discussed within LHCb, prior to the publication of Ref. [143];
2458 thus, the results presented here constitute independent work, even if there is some
2459 overlap in scope and conclusions with that reference). Many simulated data sets
2460 were generated, constituting of a number signal yields approximately equal to the
2461 expected yields in the full Run 1 and 2 LHCb data set: approximately 15,000
2462 $B^\pm \rightarrow DK^\pm$ decays and 210,000 $B^\pm \rightarrow D\pi^\pm$ decays.³ The signal decays were
2463 distributed between Dalitz bins according to $(\gamma, r_B^{DK}, \delta_B^{DK}) = (75^\circ, 0.1, 130^\circ)$ in the
2464 $B^\pm \rightarrow DK^\pm$ mode, which is to the world average values of direct γ measurements
2465 at the time. In the $B^\pm \rightarrow D\pi^\pm$ mode, the behaviour is investigated for different sets
2466 of input values; of most importance is the case $(r_B^{D\pi}, \delta_B^{D\pi}) = (0.005, 300^\circ)$, because it
2467 corresponds to the solution in the LHCb combination [127] that is in agreement with

³No backgrounds were included in these studies, and thus the quoted uncertainties on γ are better than what is obtainable in the final measurement; a similar study including realistic backgrounds is presented for the final setup below.

the theoretical expectation $r_B^{D\pi} \simeq 0.005$ [47]. The behaviour at larger $r_B^{D\pi}$ values is also investigated. The generated data sets are fitted using both parameterisations, and the observables are interpreted in terms of the underlying physics parameters using a maximum-likelihood fit, essentially following the procedure outlined in Section 4.7.1. These studies are performed in two modes: with the F_i floating in the fit, emulating a realistic fit to data, and also with the F_i fixed to the input values used in data generation. This emulates a setup where the F_i parameters are determined in an ultra-high statistics control channel, and perfect efficiency corrections are applied. In all cases, a single set of F_i parameters is shared between the $B^\pm \rightarrow DK^\pm$ and $B^\pm \rightarrow D\pi^\pm$ modes.

In these studies, the 6-parameter setup shows significantly better statistical performance than the 8-parameter setup, in the realistic case where the F_i parameters are determined in the fit and $r_B^{D\pi} \lesssim 0.03$. The fits that employ the 6-parameter setup behave well in this case, whereas the additional degrees of freedom in the 8-parameter fit leads to essentially all parameters being 100% (anti-)correlated, and a significant number of fits not converging. For the fits that do converge, the uncertainties on γ are correspondingly larger, as shown in Fig. ???. This essentially determines the choice: it is only possible to simultaneously model *CP* violation in the $B^\pm \rightarrow D\pi^\pm$ channel *and* determine the F_i parameters by using the 6-parameter setup.

However, in the studies where the F_i parameters are kept fixed, both setups lead to fits that behave well, and the resulting uncertainties on γ are essentially identical. This is illustrated in Fig. ???. Thus the 6-parameter setup does not inherently lead to a gain in precision over the 8-parameter setup; the strength of the parameterisation is that it allows for the determination of the F_i parameters. This conclusion differs somewhat from the one drawn in Ref. [143].

The fixed- F_i studies allow for an assessment of the gain in precision on γ due to the inclusion of the $B^\pm \rightarrow D\pi^\pm$ mode, by comparing the precision obtained in the simultaneous fits, with that obtained when only the (x_\pm^{DK}, y_\pm^{DK}) parameters determined in the 8-parameter fits are used to constrain γ . In the realistic case where $r_B^{D\pi} = 0.005$, the gain in precision is about 0.1° . The reason for the small impact, in spite of the yield being approximately 14 times larger in the $B^\pm \rightarrow D\pi^\pm$ channel than in the $B^\pm \rightarrow DK^\pm$ channel, is that r_B is 20 times smaller, and the *CP* asymmetries are proportional to r_B . Thus, the main improvement to the analysis from including $B^\pm \rightarrow D\pi^\pm$ as a signal channel comes from the ability to determine the F_i parameters without adding a large systematic uncertainty.⁴

⁴If this comparison is made using the alternative parameter set $(r_B^{D\pi}, \delta_B^{D\pi}) = (0.03, 330^\circ)$, which corresponds to the alternative, non-physical solution in the LHCb combination [127], the gain in precision is 1.3° instead; this fact made the statistical interpretation of the $B^\pm \rightarrow Dh^\pm$ combination in Ref. [127] non-trivial.

Finally, it is worth considering whether any precision can be gained by including information on the F_i parameters from a control channel, even if the fit is well behaved without external information. The potential yield in the $\bar{B}^0 \rightarrow D^{*+}(\rightarrow D^0\pi^+)\mu^-\bar{\nu}_\mu X$ control channel is approximately three times larger than in the $B^\pm \rightarrow D\pi^\pm$ channel, and it does therefore offer a better statistical handle on the F_i values (at the significant cost of having to worry about efficiency corrections). This can be gauged by comparing the obtained precision in the fits where F_i parameters were floating, to the precision in the case where they were kept fixed. In the realistic case where $r_B^{D\pi} = 0.005$, the difference in the average $\sigma(\gamma)$ is *less than* 0.05° , which is of course completely negligible. Therefore, it is concluded that no gain in precision is obtained by including the control channel, and it is not considered further.

Final choice of observables and the determination of the F_i parameters

In the chosen setup, a single set of four parameters, $(x_-^{DK}, y_-^{DK}, x_+^{DK}, y_+^{DK})$, are shared between *all* $B^\pm \rightarrow DK^\pm$ categories; they enter the expressions of Eq. (4.17) directly, and are thus determined in the fit. In the $B^\pm \rightarrow D\pi^\pm$ categories, the four corresponding parameters, $(x_-^{D\pi}, y_-^{D\pi}, x_+^{D\pi}, y_+^{D\pi})$, are parameterised in terms of (x_\pm^{DK}, y_\pm^{DK}) and the additional two observables $(x_\xi^{D\pi}, y_\xi^{D\pi})$. The F_i parameters are determined in the fit, being shared between the $B^\pm \rightarrow DK^\pm$ and $B^\pm \rightarrow D\pi^\pm$ channels. However, separate parameter sets are determined for the LL and DD categories because the acceptance profile over the Dalitz plot differs between them.

Because the F_i are subject to the constraint that $\sum_{i=-N}^N F_i^c = 1$, it is beneficial to introduce a reparameterisation in the likelihood function. The F_i are re-expressed in terms of a set of recursive fractions

$$\mathcal{R}_i = \begin{cases} F_i & , \quad i = -N \\ F_i / (\sum_{j \geq i} F_j) & , \quad -N < i < +N \end{cases} , \quad (4.23)$$

for which the constraint is much simpler, namely that each \mathcal{R}_i lies in the interval $[0, 1]$. This results in much better convergence behaviour in the minimisation of the negative log likelihood.

Strong-phase inputs

The strong-phase parameters (c_i, s_i) are fixed in the fit to data. In the $D \rightarrow K_S^0\pi^+\pi^-$ channels, the combined CLEO [69] and BESIII [70] measurement results are used, as reported in Ref. [70]. The $D \rightarrow K_S^0K^+K^-$ categories also use combined CLEO [70] and BESIII results [73], which are reported in Ref. [73]. The experimental uncertainty on these measurements is propagated to the measured CP -violation observables as part of the systematic uncertainties in Section 4.6.1.

2537 **Treatment of backgrounds**

2538 The yield of combinatorial background decays is determined independently in each
2539 bin. A single, overall bin yield of partially reconstructed background from B^\pm and
2540 B^0 decays is determined in each of the 160 categories; the relative contribution
2541 from each individual background is fixed from the results of the first-stage fit,
2542 corrected for the different fit region (a systematic uncertainty is assigned due to this
2543 choice). In the $B^\pm \rightarrow DK^\pm$ channels, the bin yields of the partially reconstructed
2544 background from $B_s^0 \rightarrow \bar{D}^0[\pi^+]K^-$ decays are expressed via the F_i , exploiting that
2545 a positive companion particle is always produced along with a \bar{D}^0 meson (and vice
2546 versa). The overall yield is fixed from the results of the first stage fit. Finally,
2547 the yield of the $D\pi^\pm \leftrightarrow DK^\pm$ cross-feed components in each bin are determined
2548 via the obtained yield of correctly identified decays in the corresponding bin, and
2549 the known PID efficiencies. This is true for both fully and partially reconstructed
2550 decays, although only a $D\pi^\pm \rightarrow DK^\pm$ component is included in the latter case.

2551 **The choice of fit range**

2552 The fit range is decreased to $m_B \in [5150, 5800] \text{ MeV}/c^2$. The information from
2553 candidates with lower reconstructed B masses was useful in determining the relative
2554 rates and free mass shape parameters of the partially reconstructed background
2555 components in the first-stage fit; however, with these fixed in the second-stage
2556 fit, this is no longer the case. Furthermore, the setup assumes that the shape of
2557 the partially reconstructed background is identical across the Dalitz bins. This
2558 assumption is not perfectly true, but the impact is minimal when the lower limit of
2559 the fit range is taken to be $5150 \text{ MeV}/c^2$, as described further in Section 4.6.3.

2560 **Self-consistency check**

2561 In order to establish the fit stability and investigate a potential bias, a series of
2562 pseudoexperiments are run, in which toy datasets are generated using the model,
2563 and then fitted back. The total yields are taken from the first-stage fit. The signal
2564 yields are distributed between Dalitz bins using input physics parameters that
2565 approximately equal the values obtained in Section 4.5.2 from the results of the fit
2566 to data. The F_i parameters are taken from a fit to data. The partly reconstructed
2567 background is distributed as "D⁰-like", ie. in the B^\pm channels $N_i^\pm \propto F_{\mp i}$, except for
2568 the B_s^0 background, which is " \bar{D}^0 -like" ($N_i^\pm \propto F_{\pm i}$). The combinatorial background
2569 includes real D mesons paired with a random bachelor, as well as fake D mesons
2570 that are themselves made up of random tracks. The former is distributed as 50/50

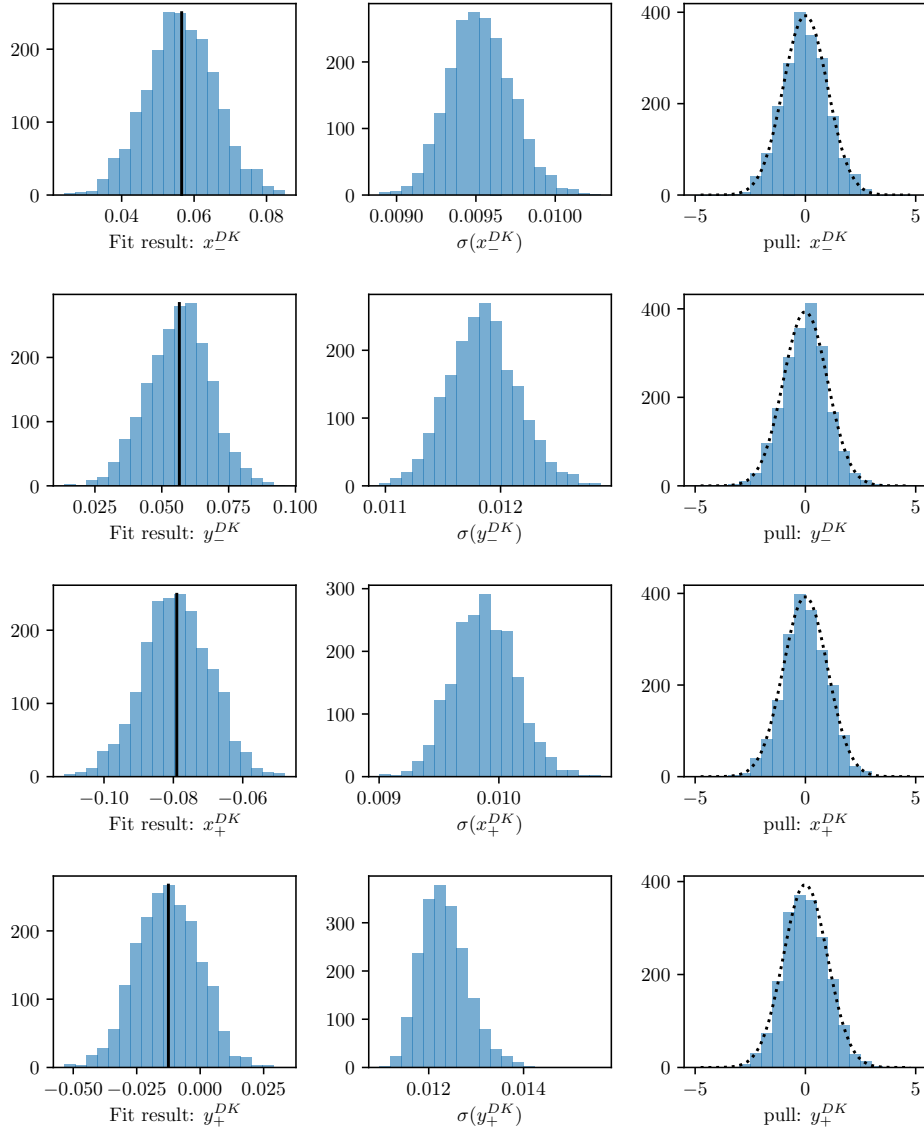


Figure 4.35: The (left) fitted value, (centre) estimated statistical uncertainty, and (right) pulls for the $B^\pm \rightarrow DK^\pm$ observables, as obtained in a number of pseudo experiments. The black line on the left shows the value used to generate the pseudo data sets; the dotted line on the right shows a Gaussian distribution with mean equal to zero and a standard deviation equal to unity.

Table 4.8: Mean biases and pulls for the observables of interest in the final, binned fit, obtained in a large number of pseudoexperiments.

Parameter	Name in code	Mean bias ($\times 10^{-2}$)	Mean pull	Pull width
x_-^{DK}	A_xm_dk	-0.018 ± 0.022	-0.01 ± 0.02	1.01 ± 0.02
y_-^{DK}	A_ym_dk	-0.014 ± 0.026	-0.00 ± 0.02	0.99 ± 0.02
x_+^{DK}	A_xp_dk	-0.018 ± 0.022	-0.01 ± 0.02	1.00 ± 0.02
y_+^{DK}	A_yp_dk	-0.016 ± 0.028	0.01 ± 0.02	1.00 ± 0.02
$x_\xi^{D\pi}$	A_Re_xi_dpi	0.029 ± 0.052	0.06 ± 0.02	1.00 ± 0.02
$y_\xi^{D\pi}$	A_Im_xi_dpi	0.000 ± 0.060	0.01 ± 0.02	1.00 ± 0.02

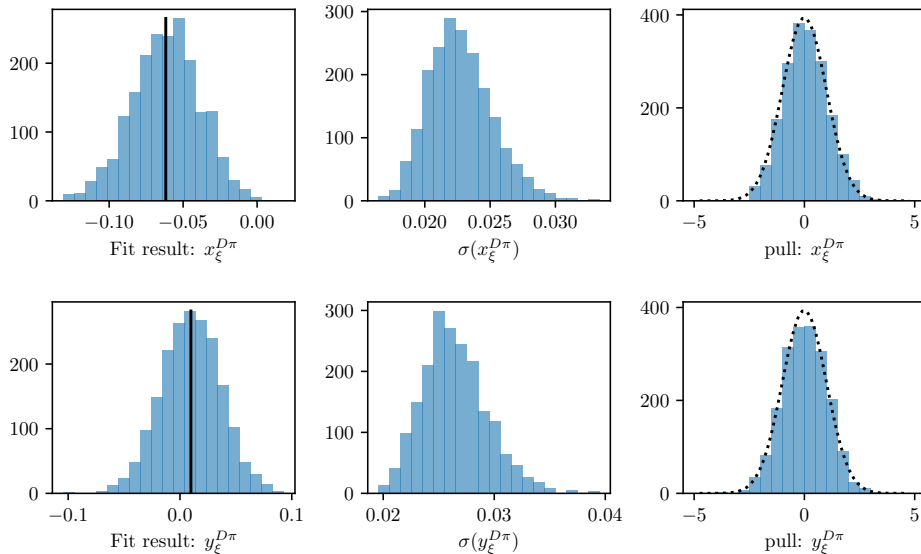


Figure 4.36: The (left) fitted value, (centre) estimated statistical uncertainty, and (right) pulls for the $B^\pm \rightarrow D\pi^\pm$ observables, as obtained in a number of pseudo experiments. The black line on the left shows the value used to generate the pseudo data sets; the dotted line on the right shows a Gaussian distribution with mean equal to zero and a standard deviation equal to unity.

2571 D^0 -like and \bar{D}^0 -like in the toy generation, whereas the latter is assumed to be evenly
 2572 distributed over the Dalitz plot (ie. the bin yield is proportional to the bin area).

2573 A set of 2000 pseudoexperiments has been run, out of which 98.8% con-
 2574 verged properly. The pull plots for the observables of interest are shown in
 2575 Figs. 4.35 and 4.36; the mean biases and pulls are summarised in Table 4.8. No
 2576 biases are statistically significant, and the uncertainties are seen to be well estimated.

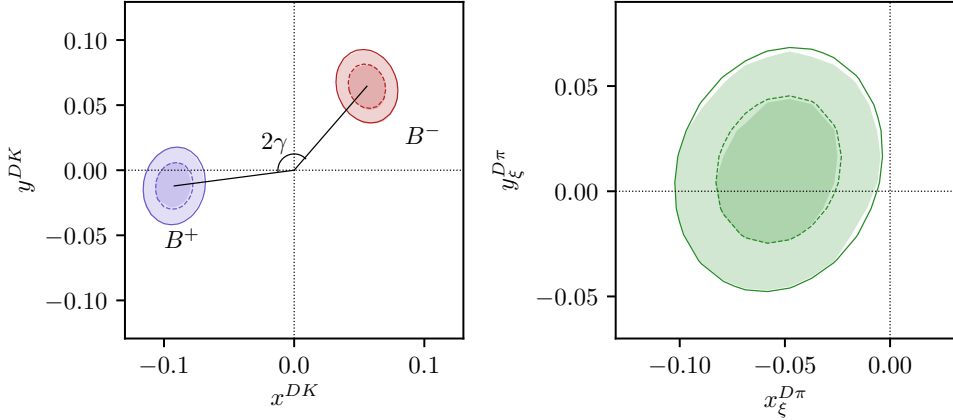


Figure 4.37: The 68 % and 95 % confidence regions for the fitted observables. The lines show the regions estimated from the covariance matrix returned by the default fit. The shaded areas are obtained in a likelihood scan, where the binned fit is run many times with all observables held at fixed values, scanning pairs of observables over the relevant ranges. The scan is made separately for the three pairs (x_{-}^{DK}, y_{-}^{DK}) , (x_{+}^{DK}, y_{+}^{DK}) , and $(x_{\xi}^{D\pi}, y_{\xi}^{D\pi})$, holding the four other parameters fixed at their default-fit central values during a given scan. Then the minimum log-likelihood is related to a χ^2 via $\mathcal{L}_{\min} = \frac{1}{2}\chi^2$ (discarding an irrelevant constant), and the confidence region limits placed at $\chi^2 = 2.30$ and $\chi^2 = 6.18$, yielding the relevant percentiles for a χ^2 distribution with 2 degrees of freedom.

2577 4.5.2 Main results

2578 The values and statistical uncertainties of observables obtained in the fit are

$$\begin{aligned} x_{-}^{DK} &= (-5.68 \pm 0.96) \times 10^{-2}, & y_{-}^{DK} &= (-6.55 \pm 1.14) \times 10^{-2}, \\ x_{+}^{DK} &= (-9.30 \pm 0.98) \times 10^{-2}, & y_{+}^{DK} &= (-1.25 \pm 1.23) \times 10^{-2}, \\ x_{\xi}^{D\pi} &= (-5.47 \pm 1.99) \times 10^{-2}, & y_{\xi}^{D\pi} &= (0.71 \pm 2.33) \times 10^{-2}. \end{aligned} \quad (4.24)$$

2579 The statistical correlation matrix for the observables is given in Table 4.9. The
2580 2D log-likelihood profile for the observables is shown in Fig. 4.37.

2581 The full set of fit projections in all 160 categories is included in Appendix A.
2582 While the CP asymmetry of the phase-space integrated yield is small, this is not the
2583 case for all individual bin-pairs. This is shown in Fig. 4.38 where, as an example,
2584 the fit projections for the $B^+ \rightarrow DK^+$ decays in bin +2 and the $B^- \rightarrow DK^-$
2585 decays in bin -2 of the $D \rightarrow K_S^0 \pi^+ \pi^-$ Dalitz plot are compared. The presence
2586 of CP violation is clearly visible.

2587 The obtained F_i parameter values are shown in Table 4.10. These parameters can
2588 be useful in other BPNGGSZ measurements made within the LHCb collaboration:
2589 it is expected that the systematic uncertainty due to differences between the

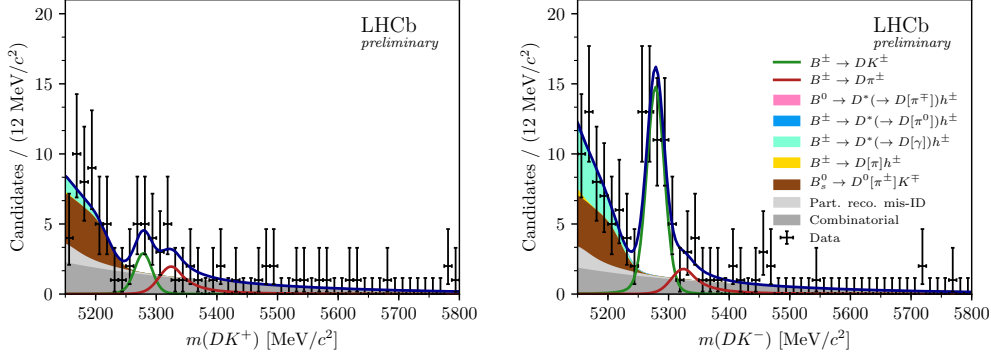


Figure 4.38: The invariant mass distribution for the (left) $B^+ \rightarrow DK^+$ candidates in bin -2 and (right) the $B^- \rightarrow DK^-$ candidates in bin +2, where $D \rightarrow K_S^0\pi^+\pi^-$ and the K_S^0 is reconstructed in the DD category.

Table 4.9: Statistical uncertainties and correlation matrix for the fit to data.

Uncertainty ($\times 10^{-2}$)						
	$x_-^{DK^\pm}$	$y_-^{DK^\pm}$	$x_+^{DK^\pm}$	$y_+^{DK^\pm}$	$x_\xi^{D\pi^\pm}$	$y_\xi^{D\pi^\pm}$
σ	0.96	1.14	0.96	1.20	1.99	2.34

Correlations						
	$x_-^{DK^\pm}$	$y_-^{DK^\pm}$	$x_+^{DK^\pm}$	$y_+^{DK^\pm}$	$x_\xi^{D\pi^\pm}$	$y_\xi^{D\pi^\pm}$
$x_-^{DK^\pm}$	1.000	-0.125	-0.013	0.019	0.028	-0.165
$y_-^{DK^\pm}$		1.000	-0.011	-0.009	0.105	0.030
$x_+^{DK^\pm}$			1.000	0.088	-0.099	0.038
$y_+^{DK^\pm}$				1.000	-0.076	-0.141
$x_\xi^{D\pi^\pm}$					1.000	0.146
$y_\xi^{D\pi^\pm}$						1.000

2590 Dalitz-plot acceptance profile in $B^\pm \rightarrow Dh^\pm$ decays and, say, $B \rightarrow D^*K$ or
 2591 $B \rightarrow DK^*$ decays is smaller than the systematic arising from extracting the
 2592 efficiency profile from simulated decays. Therefore, the obtain central values and
 2593 uncertainties have been made public [1], including a set of systematic uncertainties
 2594 discussed in Section 4.6.12.⁵

2595 4.5.3 Cross checks

2596 A series of cross checks are performed to verify that the fit to data is behav-
 2597 ing as expected.

⁵In practice, it is the obtained \mathcal{R}_i values that are made public, related to the F_i parameters via Eq. (4.23).

Table 4.10: The fitted F_i values including statistical uncertainties. The associated systematic uncertainties are negligible, as discussed in Section 4.6.12.

F_i values: $D \rightarrow K_S^0 \pi^+ \pi^-$		
bin	LL	DD
-8	0.024 ± 0.001	0.024 ± 0.000
-7	0.127 ± 0.001	0.133 ± 0.001
-6	0.062 ± 0.001	0.056 ± 0.001
-5	0.046 ± 0.001	0.042 ± 0.001
-4	0.095 ± 0.001	0.095 ± 0.001
-3	0.160 ± 0.001	0.160 ± 0.001
-2	0.153 ± 0.001	0.153 ± 0.001
-1	0.095 ± 0.001	0.097 ± 0.001
1	0.022 ± 0.001	0.020 ± 0.000
2	0.005 ± 0.000	0.005 ± 0.000
3	0.004 ± 0.000	0.004 ± 0.000
4	0.055 ± 0.001	0.056 ± 0.001
5	0.027 ± 0.001	0.022 ± 0.000
6	0.004 ± 0.000	0.003 ± 0.000
7	0.055 ± 0.001	0.057 ± 0.001
8	0.067 ± 0.001	0.072 ± 0.001

F_i values: $D \rightarrow K_S^0 K^+ K^-$		
bin	LL	DD
-2	0.207 ± 0.004	0.202 ± 0.003
-1	0.222 ± 0.004	0.230 ± 0.003
1	0.290 ± 0.005	0.296 ± 0.003
2	0.281 ± 0.005	0.271 ± 0.003

2598 Comparison to results of earlier analyses

2599 It is confirmed that the results obtained in fits of the Run 1 or 2015+16 data
 2600 sets in isolation are compatible with the results obtained in the original LHCb
 2601 analyses of those data sets [3, 74]. In order to do so, the whole analysis procedure
 2602 is carried out using only the relevant subset of data, and the strong-phase inputs
 2603 from the CLEO collaboration are used in the fit. Two effects need to be taken
 2604 into account when comparing the central values.

2605 The overlap between the samples need to be taken into account. The overlap
 2606 is not 100 % due to changes in the candidate selection. The overlap between the
 2607 new selection and the data set of the original analysis of Run 1 data is about
 2608 70 %, whereas it is about 90 % for the 2015+16 data set. In order to determine the

Table 4.11: Comparison between the results on the Run 1 analysis [74] and the central values obtained when fitting the Run 1 dataset with the selection and fit setup described in this note. The pull is calculated using the 1σ expected difference, which takes the sample overlap and the systematic uncertainty on the F_i parameters in the previous analysis into account, but assumes all other systematic uncertainties to be perfectly correlated. The new fits are performed using the CLEO strong-phase inputs.

Observable	Run 1 result [74]	New Fit (central value $\times 10^{-2}$)	Pull
x_-^{DK}	2.50	4.04	0.85
y_-^{DK}	7.50	9.14	1.02
x_+^{DK}	-7.70	-9.40	-0.91
y_+^{DK}	-2.20	0.80	1.77
<i>p</i> -value: 0.057			

expected difference between the observables fitted from data sets with significant overlap, a large number of toy data sets were generated in sets of two, where 70 (90) % of decays were shared between the data sets. Both data sets were fitted and the difference between the obtained central values for each observable tabulated; the standard deviation of these distributions are used to calculate the pulls between the old analysis results and the new fits to data. This check does not take into account that the semi-leptonic PID cuts were introduced to remove a potential peaking background, which may have had a small systematic effect on the earlier measurement results. Thus the expected differences are likely to be slightly underestimated and the check conservative.

Furthermore, the F_i parameters were determined in a semi-leptonic control channel in the earlier analyses. Therefore, the expected difference obtained above is adjusted by adding the F_i -related systematic uncertainty of the original analysis in quadrature, when comparing the old results to those in new fits to the Run 1 and 15+16 data sets. No further corrections have been made to the expected differences, which effectively assumes all other systematic uncertainties to be 100 % correlated. Also for this reason can the check be considered conservative. As can be seen in Tables 4.11 and 4.12, neither the Run 1 and 2015+16 comparisons show unreasonable differences in central values.

Directly fitting the signal yields

As a cross-check, the fit is run in an alternative mode, in which the signal yields of each bin are independent parameters. The obtained yields are compared to those predicted from the results of the default fit in Fig. 4.39. The yields are shown for

Table 4.12: Comparison between the results on the 2015+16 analysis [3] and the central values obtained when fitting the 2015+16 dataset with the selection and fit setup described in this note. The pull is calculated using the 1σ expected difference, which takes the sample overlap and the systematic uncertainty on the F_i parameters in the previous analysis into account, but assumes all other systematic uncertainties to be perfectly correlated. The new fits are performed using the CLEO strong-phase inputs.

Observable	15+16 result [3] (central value $\times 10^{-2}$)	New Fit	Pull
x_-^{DK}	9.00	8.36	-0.50
y_-^{DK}	2.10	1.16	-0.62
x_+^{DK}	-7.70	-8.58	-0.56
y_+^{DK}	-1.00	-2.82	-1.39
<i>p</i> -value: 0.239			

2632 each "effective bin", where effective bin i is defined as bin $+i$ for B^+ decays and bin
 2633 $-i$ for B^- decays; in the CP symmetric case, these bins are expected to have equal
 2634 yields (modulo production and detection asymmetries). The agreement between the
 2635 two fit set-ups is seen to be excellent. The normalised yield asymmetries, defined as

$$A^i \equiv \frac{N_{-i}^- - N_i^+}{N_{-i}^- + N_i^+} \quad (4.25)$$

2636 are shown in Fig. 4.40 for all decay channels. Again, the agreement between
 2637 the nominal fit, and the alternative fit with independent yields is found to be
 2638 excellent. It is also clear how, in the case of $B^\pm \rightarrow DK^\pm$ decays, the asymmetry
 2639 is significantly different from zero for a number of bin pairs.

2640 Fitting subsets of the data separately

2641 One cross check is carrying out, by determining the CP observables using a number
 2642 of independent sub samples of the data set separately. This is done for the
 2643 following following data splits

- 2644 • Fig. 4.41a shows the same plots, comparing the fits to the data set split by
 2645 K_S^0 track type.
- 2646 • Fig. 4.41b shows the same plots, comparing the fits to the data set split by
 2647 whether the D meson decays to the $K_S^0\pi^+\pi^-$ or $K_S^0K^+K^-$ final state.
- 2648 • Fig. 4.42a shows the two dimensional log likelihood contours for the observables
 2649 for fits to the Run 1, 2015+16, 2017 and 2018 datasets separately

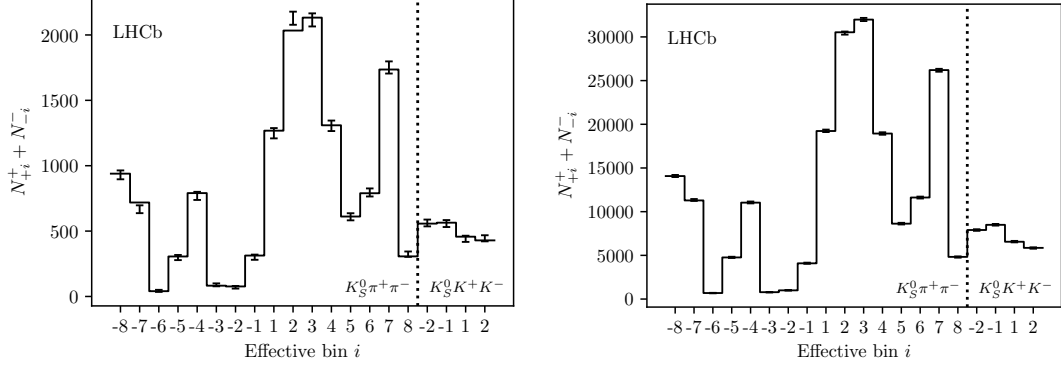


Figure 4.39: Comparison of (lines) the predicted yield given the determined CP observables and (error bars) the yield obtained in fits to data where each yield is an independent parameter. The yields are shown for (left) $B^\pm \rightarrow DK^\pm$ decays and (right) $B^\pm \rightarrow D\pi^\pm$ decays. The LL and DD categories have been combined, as has the B^+ and B^- yields for each effective Dalitz bin, defined as bin $+i$ for B^+ decays and bin $-i$ for B^- decays.

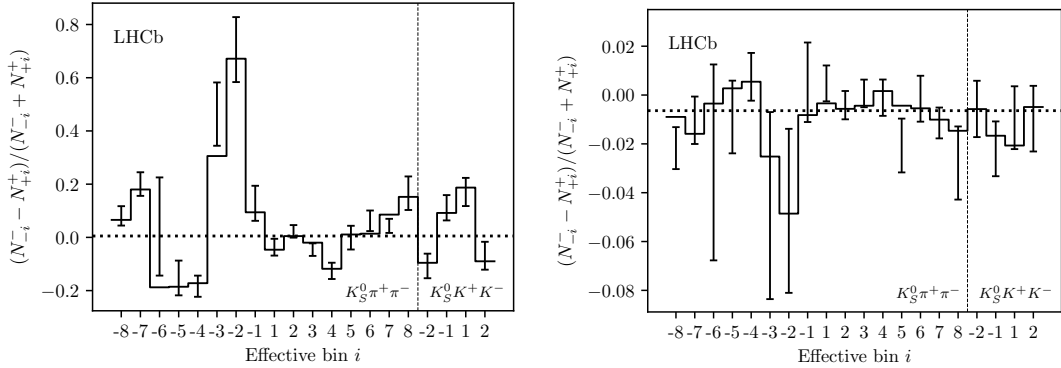


Figure 4.40: The bin-by-bin asymmetries $(N_{-i}^- - N_{+i}^+) / (N_{-i}^- + N_{+i}^+)$ for each Dalitz-plot bin number for (left) $B^\pm \rightarrow DK^\pm$ decays and (right) $B^\pm \rightarrow D\pi^\pm$ decays. The prediction from the central values of the CP -violation observables is shown with a solid line and the asymmetries obtained in fits with independent bin yields are shown with the error bars. The predicted asymmetries in a fit that does not allow for CP violation are shown with a dotted line.

- 2650 • Fig. 4.42b shows the same plots, comparing the fits to the data set split by
- 2651 whether the candidate event was triggered by one of the signal particles at the
- 2652 hardware level (TOS), or by another particle in the underlying event (TIS).
- 2653 • Fig. 4.42c shows the same plots, comparing the fits to the data set split the
- 2654 magnet polarity during data taking.
- 2655 All figures show the Gaussian likelihood contours corresponding to the statistical
- 2656 uncertainties. There is good agreement between the results in all cases, given

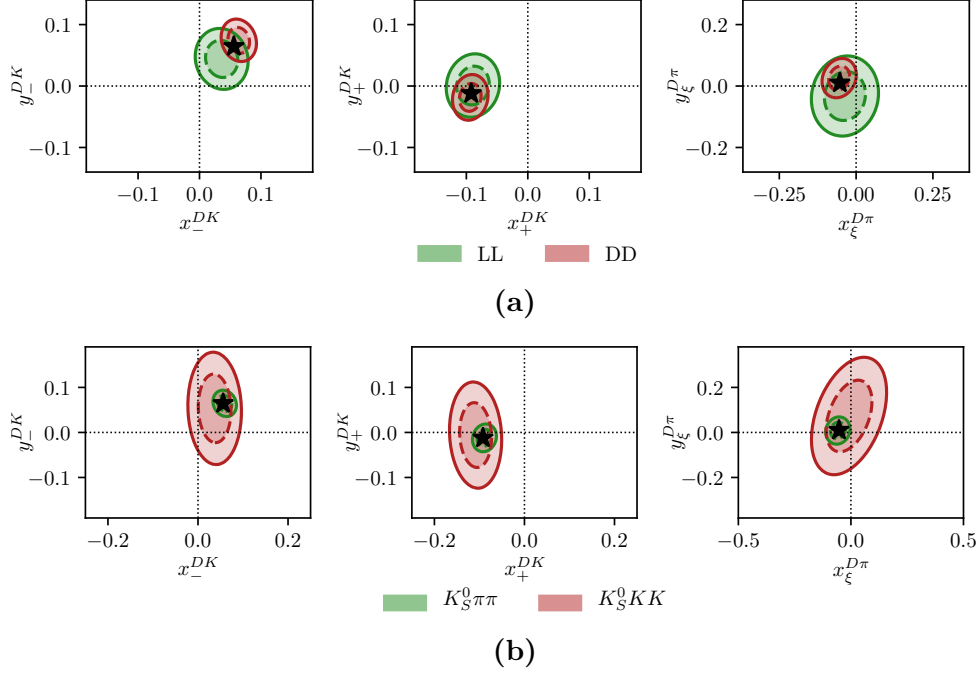


Figure 4.41: Comparison of the 68 % and 95 % confidence regions for (left) (x_{-}^{DK}, y_{-}^{DK}) , (centre) (x_{+}^{DK}, y_{+}^{DK}) , and (right) $(x_{\xi}^{D\pi}, y_{\xi}^{D\pi})$ obtained from fits to sub sets of the data set. The uncertainties are statistical only. The central values of the default fit are shown with a black star. The dataset is split by (a) LL and DD K_S^0 types and (b) D decay mode.

that in each cases the sub datasets are independent and therefore the statistical errors are uncorrelated.

Constraints from a subset of bins

An alternative way to subdivide the data is to examine the constraints from a subset of bins individually; this forms as a cross check, seeing that the observables favoured by each sub set should be compatible, and also serves as a useful illustration of the features of the BPGBSZ method. Likelihood contours for $(x_{\pm}^{DK}, y_{\pm}^{DK})$ are shown in Fig. 4.43, obtained using the binned yields in the $D \rightarrow K_S^0\pi^+\pi^-$ bins, determined in the fits of individual bin yields described in Section 4.5.3. The bins are split by whether they are ADS-like, GLW-like, or Odd-even according to the classification in Section 1.3.5. It is clear that the likelihood regions show a reasonable overlap, and also how it is the GLW bins that constrain the x_{\pm} parameter, while the Odd-even and ADS-like bins provide the ability to constrain the y_{\pm} parameters.

Significantly reducing the $B^\pm \rightarrow D\pi^\pm$ to $B^\pm \rightarrow DK^\pm$ cross feed

One of the dominant backgrounds in the signal region of the $B^\pm \rightarrow DK^\pm$ channel is from partly reconstructed $B \rightarrow D\pi X$ decays where the bachelor pion is misidentified

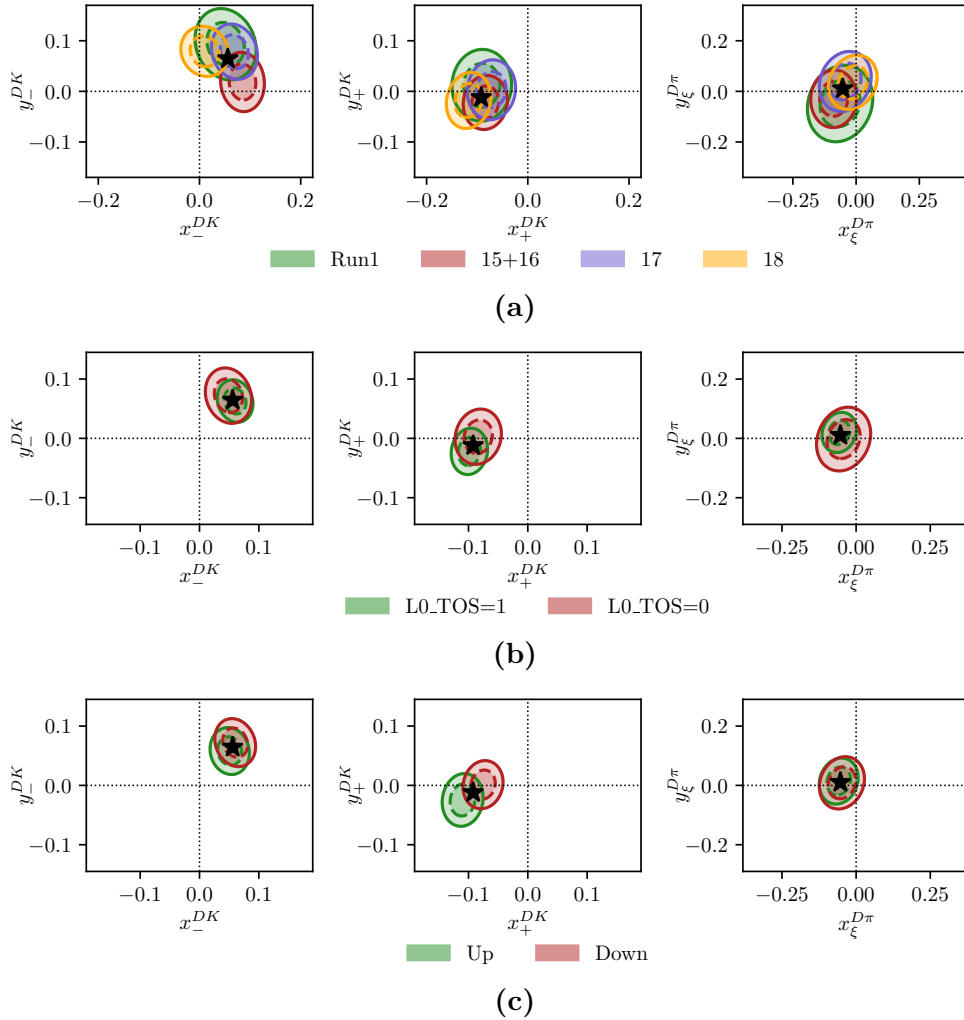


Figure 4.42: Comparison of the 68 % and 95 % confidence regions for (left) (x_-^{DK}, y_-^{DK}) , (centre) (x_+^{DK}, y_+^{DK}) , and (right) $(x_\xi^{D\pi}, y_\xi^{D\pi})$ obtained from fits to sub sets of the data set. The uncertainties are statistical only. The central values of the default fit are shown with a black star. The dataset is split by (a) data taking year, (b) trigger category, and (c) magnet polarity.

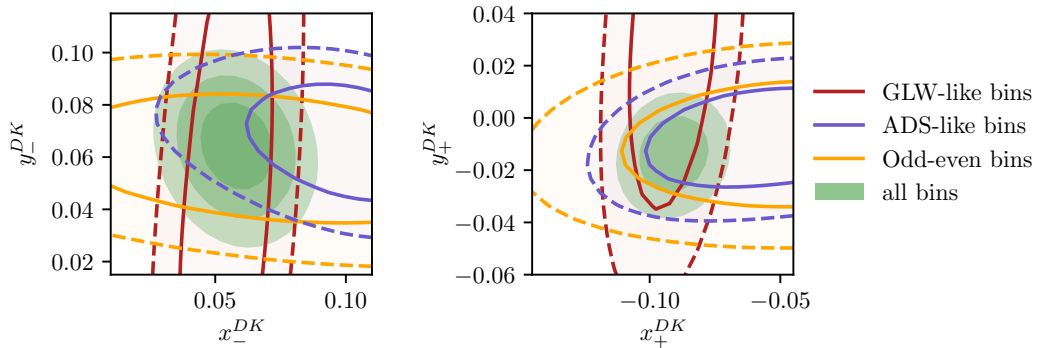


Figure 4.43: Caption here

as a kaon. The background mode is well described by the included shape component, and included in all relevant systematic studies. Nevertheless, an additional cross check is carried out to ensure that it is not having a significant effect on the fit: the analysis is repeated with PID requirement of $\text{PIDK} > 12$ required to place a candidate in the $B^\pm \rightarrow DK^\pm$ category, instead of $\text{PIDK} > 4$. With this requirement 99.7 % of $B^\pm \rightarrow D\pi^\pm$ decays are correctly identified, making the cross-feed component in the $B^\pm \rightarrow DK^\pm$ channels significantly smaller than in the default fit. This is clearly visible in Fig. 4.44, where the fit projections for the global fit of the $D \rightarrow K_S^0\pi^+\pi^-$ modes are shown. In return, the probability of correctly identifying a kaon companion drops to about 68–69 %, resulting in a smaller effective signal yield.

The measurement results are compared in Table 4.13, where the differences in central value are seen to be reasonably small. It is not trivial to determine whether the difference is statistically significant or not: the same candidates are analysed in both cases, the difference being that a number of candidates that are placed in the $B^\pm \rightarrow DK^\pm$ category in the nominal fit are placed in the $B^\pm \rightarrow D\pi^\pm$ category in the alternative fit. The uncertainty will not be 100 % correlated because signal events that move from the DK to $D\pi$ category are placed in a region with high background; however, this is somewhat compensated for by candidates that remain in the DK category gaining statistical power due to the increased purity. An estimate of the expected statistical fluctuation can be determined by taking the difference of the statistical uncertainties in quadrature. Using this estimate, the observed shifts are found to consistent with statistical fluctuation, and thus there is no sign of the background from $D\pi^\pm \rightarrow DK^\pm$ cross-feed causing issues.

2696 Compare results obtained with different strong-phase inputs

2697 It is interesting to compare the results obtained with different strong-phase inputs.
 2698 This is done in Fig. 4.45, where the default fit results are compared to those
 2699 obtained if the CP fit is done with the CLEO-only inputs [69], and with the model
 2700 predictions from the 2018 Belle model [51] and the 2008 BaBar model [57]. For the
 2701 measurements, only the strong-phase-related uncertainties are included in the plot,
 2702 since the statistical uncertainties are correlated. All results are found to agree well.

2703 4.6 Systematic uncertainties

2704 The following sections cover the suite of systematic uncertainties on the measurement
 2705 that has been considered. All uncertainties are summarised in Section 4.6.12.

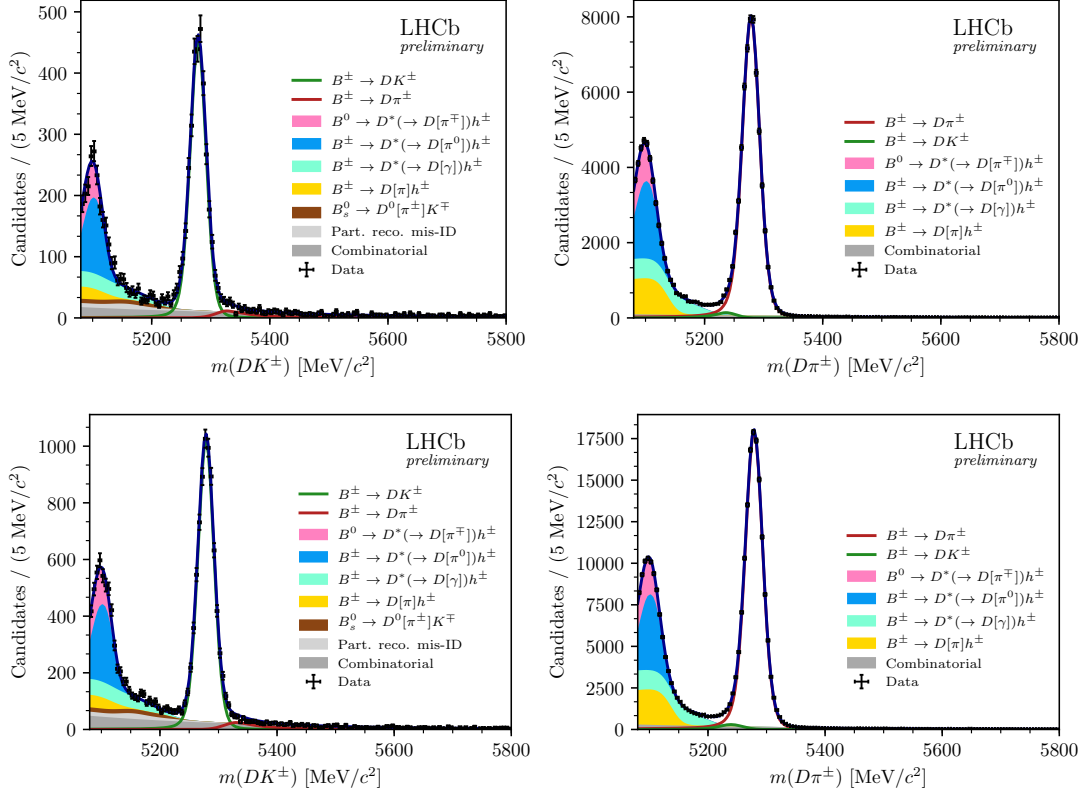


Figure 4.44: Fit projections for fits to the $D \rightarrow K_S^0 \pi^+ \pi^-$ candidates with a companion PIDK requirement at 12 instead of 4 used to split into (left) $B^\pm \rightarrow DK^\pm$ and (right) $B^\pm \rightarrow D\pi^\pm$ candidates, for the (top) LL and (bottom) DD categories.

Table 4.13: Results of running the measurement with the default PIDK cut at 4 used to separate $B^\pm \rightarrow DK^\pm$ and $B^\pm \rightarrow D\pi^\pm$ candidates, as well as with an alternative PIK cut at 12, resulting in much lower cross-feed from misidentified $B^\pm \rightarrow D\pi^\pm$ decays. We also show the pulls, defined as $\Delta x / \sqrt{|\sigma_{PIDK>12}^2 - \sigma_{PIDK>4}^2|}$ as described in the main text body. The comparison was made before the BESIII measurement of the $D \rightarrow K_S^0 K^+ K^-$ strong-phase inputs became available; therefore the fits use the CLEO-only results [69] for this mode, which explains why the results quoted for $PIDK > 4$ differ slightly from the nominal fit results.

Parameter	$PIDK > 4$	$PIDK > 12$	$\sigma = \sqrt{\sigma_{PIDK>12}^2 - \sigma_{PIDK>4}^2}$	Pull
x_-^{DK}	5.59 ± 0.96	5.82 ± 1.01	0.30	0.77
y_-^{DK}	6.45 ± 1.14	6.86 ± 1.19	0.36	1.13
x_+^{DK}	-9.21 ± 0.96	-8.94 ± 1.01	0.30	0.93
y_+^{DK}	-1.21 ± 1.20	-0.94 ± 1.26	0.37	0.71
$x_\xi^{D\pi}$	-5.30 ± 1.99	-5.13 ± 2.02	0.32	0.52
$y_\xi^{D\pi}$	1.03 ± 2.34	1.71 ± 2.33	0.28	2.40

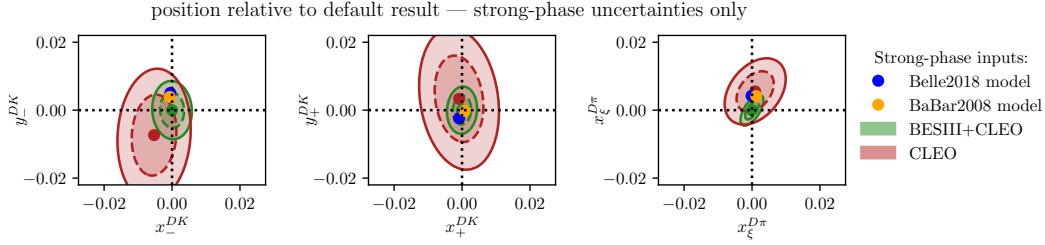


Figure 4.45: Fit results for (left) (x_-^{DK}, y_-^{DK}) , (centre) (x_+^{DK}, y_+^{DK}) , and (right) $(x_\xi^{D\pi}, y_\xi^{D\pi})$ depending on strong-phase inputs, shown relative to the default fit results. The included results are based on (green) the BESIII-CLEO combination, which is the default, (red) the CLEO-only results, (blue dot) the 2018 Belle model [51] and (orange dot) the 2008 BaBar model [57]. For the measurements, only strong-phase related uncertainties are included in the plotted confidence regions.

2706 4.6.1 Strong phase uncertainties

2707 The observables x_\pm^{DK} , y_\pm^{DK} , $x_\xi^{D\pi}$ and $y_\xi^{D\pi}$ are extracted using the central values
 2708 of c_i and s_i from the BESIII–CLEO combinations [69, 70, 73]. Subsequently, the
 2709 measurement uncertainty on these inputs is propagated to the observables by
 2710 performing a large set of fits to data, using alternative values of c_i and s_i . The
 2711 new c_i and s_i values are obtained by smearing the central values by their measured
 2712 statistical and systematic uncertainties while taking into account their correlations.
 2713 The use of different c_i and s_i values changes the extracted x_\pm^{DK} , y_\pm^{DK} , $x_\xi^{D\pi}$ and
 2714 $y_\xi^{D\pi}$ values. The width of the distributions of central values extracted from 1000
 2715 data fits are assigned as a systematic uncertainty. The distributions are shown
 2716 in Fig. 4.46 and the assigned uncertainties are summarised in Table 4.14. The
 2717 correlation matrix related to the strong-phase uncertainty can be obtained from the
 2718 correlations observed between observables in the fits, and is also given in the table.

2719 The set of (c_i, s_i) that was employed in this analysis will be used in a series
 2720 of future BPGGSZ measurements, both with additional B decay modes within
 2721 the LHCb collaboration and by the Belle II collaboration. This introduces some
 2722 correlation between the measurement results. In order to allow for an estimate
 2723 of the degree of correlation by future analysts, the 1000 samples (c_i, s_i) values
 2724 and the corresponding fit results for $(x_\pm^{DK}, y_\pm^{DK}, x_\xi^{D\pi}, y_\xi^{D\pi})$ have been made public
 2725 as supplementary material to Ref. [1].

2726 4.6.2 Efficiency-profile-related systematic uncertainties

2727 The non-trivial efficiency profile over the Dalitz plot can have a range of effects,
 2728 considered in the sections below.

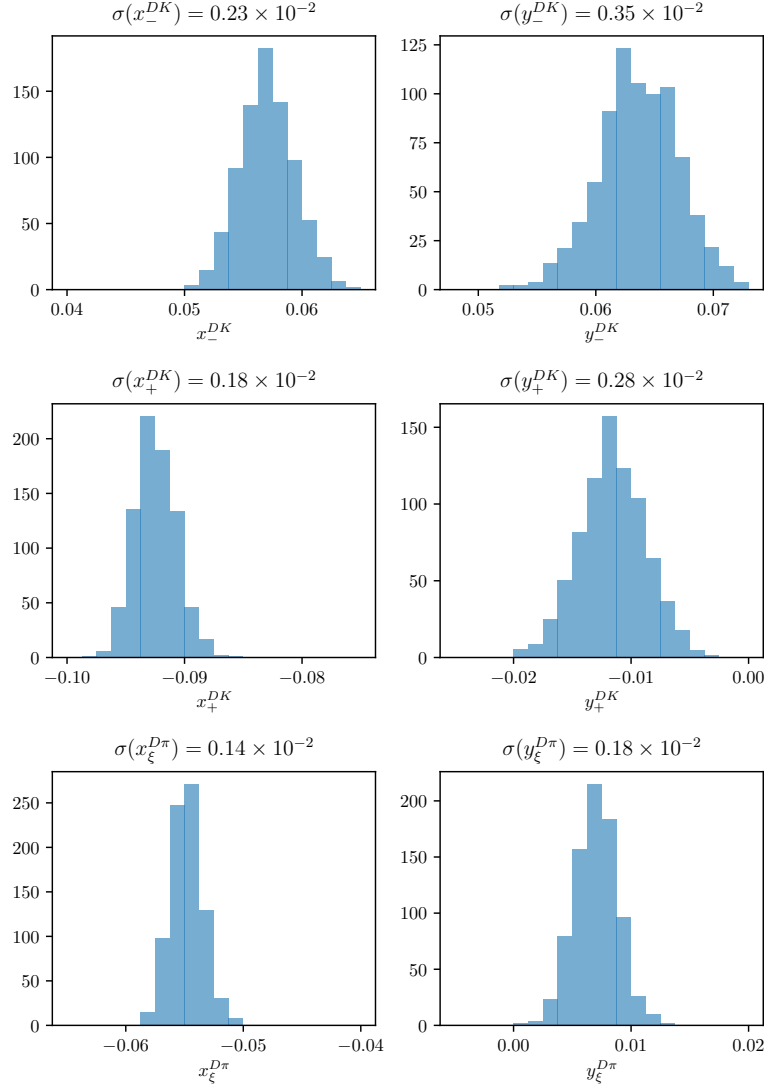


Figure 4.46: Spread of central values for the fitted observables when the input c_i and s_i from the BESIII+CLEO combination are varied according to their uncertainties and correlations.

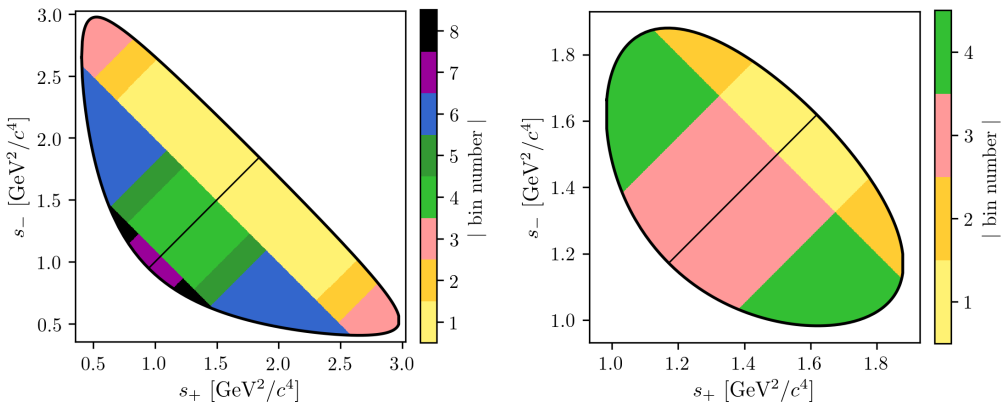
2729 **The assumption that** $\eta^{DK}(s_-, s_+) = \eta^{D\pi}(s_-, s_+)$

2730 The assumption that $\eta^{DK}(s_-, s_+) = \eta^{D\pi}(s_-, s_+)$ was examined in detail in Sec-
 2731 tion 4.2.2. It was found that with signal yields similar to those in the data set,
 2732 no statistically significant difference between the efficiency profiles $\eta^{DK}(s_-, s_+)$
 2733 and $\eta^{D\pi}(s_-, s_+)$ was discernible, and no additional uncertainty due to this as-
 2734 sumption is assigned.

Table 4.14: Systematic uncertainties and correlation matrix due to strong-phase inputs.

Uncertainty ($\times 10^{-2}$)						
	$x_-^{DK^\pm}$	$y_-^{DK^\pm}$	$x_+^{DK^\pm}$	$y_+^{DK^\pm}$	$x_\xi^{D\pi^\pm}$	$y_\xi^{D\pi^\pm}$
σ	0.23	0.35	0.18	0.28	0.14	0.18

Correlations						
	$x_-^{DK^\pm}$	$y_-^{DK^\pm}$	$x_+^{DK^\pm}$	$y_+^{DK^\pm}$	$x_\xi^{D\pi^\pm}$	$y_\xi^{D\pi^\pm}$
$x_-^{DK^\pm}$	1.000	-0.047	-0.490	0.322	0.189	0.144
$y_-^{DK^\pm}$		1.000	0.059	-0.237	-0.116	-0.117
$x_+^{DK^\pm}$			1.000	0.061	0.004	-0.139
$y_+^{DK^\pm}$				1.000	0.127	-0.199
$x_\xi^{D\pi^\pm}$					1.000	0.638
$y_\xi^{D\pi^\pm}$						1.000

**Figure 4.47:** The rectangular binning schemes used to group candidates in (left) the $D \rightarrow K_S^0 \pi^+ \pi^-$ and (right) the $D \rightarrow K_S^0 K^+ K^-$ categories in a number of systematic uncertainty studies.

2735 **The assumption that** $\eta(s_-, s_+) = \eta(s_+, s_-)$

2736 The measurement is sensitive to effects that break the assumption $\eta(s_-, s_+) =$
 2737 $\eta(s_+, s_-)$. Such a breakdown would mean that opposite points on the Dalitz plot
 2738 have different efficiencies and can only arise through a charge detection asymmetry
 2739 (e.g. that it is more likely to detect a K^+ in the detector rather than a K^-).⁶

2740 The potential size of such an asymmetry can be studied in simulation
 2741 where the D decay has a uniform distribution over the allowed phase space; in such

⁶Note that the measurement is insensitive to any asymmetry in the reconstruction of the companion track.

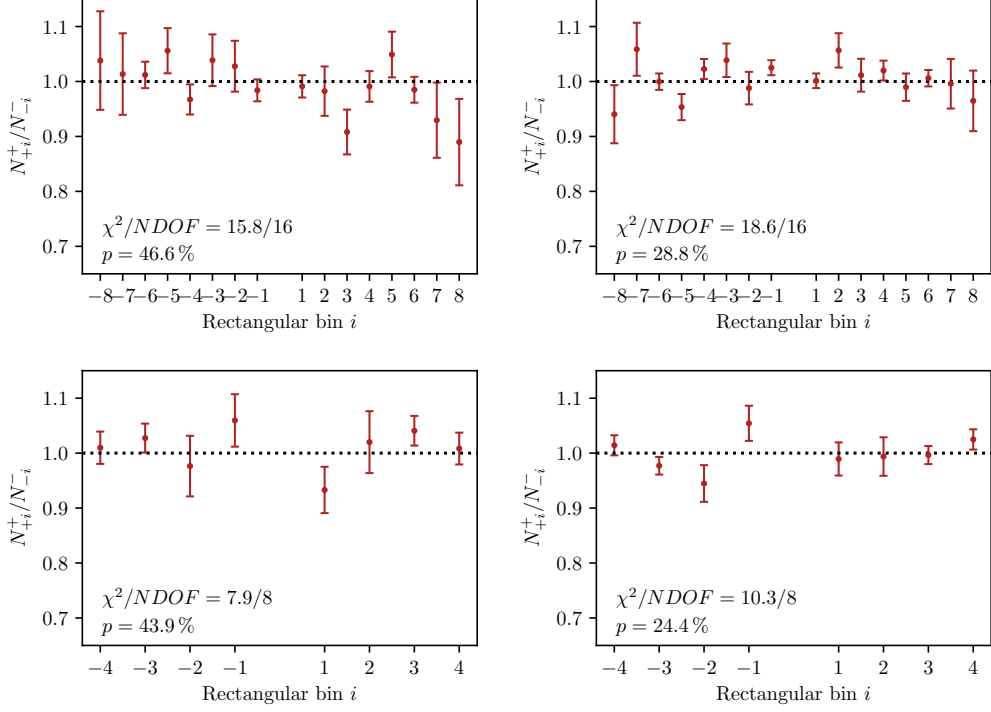


Figure 4.48: Comparison of the ratio of B^+ decays reconstructed in bin $+i$ to B^- decays reconstructed in bin $-i$ for simulated $B^\pm \rightarrow D\pi^\pm$ decays where (top) $D \rightarrow K_S^0 \pi^+ \pi^-$ and (bottom) $D \rightarrow K_S^0 K^+ K^-$, also split into (left) the LL and (right) the DD categories, using the rectangular binning schemes in Fig. 4.47. Calculated p values for the hypothesis that the ratio is flat are also shown, all of them being at least 20 %.

simulated samples, it would manifest itself as an observation different fractional yields of B^- decays in bin i and B^+ decays in bin $-i$. This effect has been looked for using the large samples of $B^\pm \rightarrow D\pi^\pm$ decays that were generated for the analysis of 2015 and 2016 data. The study is performed using the rectangular binning schemes shown in Fig. 4.47, because this scheme is most sensitive to effects that vary smoothly over phase space. The comparison plots are shown in Fig. 4.48, where it can be seen that the p values for the hypothesis that there is no asymmetry all take on reasonable values. Hence no further systematic uncertainty is considered.

2750 Effect of phase-space efficiency profile on c_i and s_i

As discussed in Section 1.4 there is a small bias, because the c_i and s_i values that are used correspond to the definition

$$c_i = \frac{\int_i ds^2 |A_S^D(s_{-+})| |A_S^D(s_{+-})| \cos[\Delta\delta_D(s_{-+})]}{\sqrt{\int_i ds^2 |A_S^D(s_{-+})|^2} \sqrt{\int_i ds^2 |A_S^D(s_{+-})|^2}}, \quad (\text{and equivalent for } s_i,) \quad (4.26)$$

2753 whereas the non-flat efficiency profile in LHCb, $\eta(s_-, s_+) \equiv \eta(s_{-+})$, means that the
 2754 appropriate c_i ' and s_i ' entering the exact yield expressions are

$$c_i^{\text{eff}} = \frac{\int_i ds^2 \eta(s_{-+}) |A_S^D(s_{-+})| |A_S^D(s_{+-})| \cos[\Delta\delta_D(s_{-+})]}{\sqrt{\int_i ds^2 |A_S^D(s_{-+})|^2} \sqrt{\int_i ds^2 |A_S^D(s_{+-})|^2}}, \quad (\text{and equivalent for } s_i^{\text{eff}}.) \quad (4.27)$$

2755 The shifts $\Delta c_i = c_i^{\text{eff}} - c_i$, $\Delta s_i = s_i^{\text{eff}} - s_i$ can be estimated using the efficiency
 2756 profile in simulation and the latest amplitude models: the 2018 Belle model [51]
 2757 for $D \rightarrow K_S^0 \pi^+ \pi^-$ and the 2010 BaBar model [58] for $D \rightarrow K_S^0 K^+ K^-$. The strong-
 2758 phase parameters are first calculated assuming a uniform reconstruction efficiency
 2759 over phase space according to Eq. (4.26), obtaining a set of values $\{c_i^{\text{model}}, s_i^{\text{model}}\}$.
 2760 Then, an alternative set is calculated, $\{c_i^{\text{eff}}, s_i^{\text{eff}}\}$, using the same model, and the
 2761 reconstruction efficiency profile found in full LHCb simulation. The results, as well
 2762 as their differences, are tabulated in Tables 4.15 and 4.16. The LHCb reconstruction
 2763 efficiency at a given point in phase-space is taken to be proportional to the yield
 2764 in simulation, as the simulated decays were generated with a uniform distribution
 2765 over phase space. The efficiency is averaged over the LL and DD categories
 2766 in the calculation.

2767 A systematic uncertainty due to employing the measured c_i and s_i directly
 2768 in the fit is assigned by generating a large number of toy data sets where the
 2769 signal yields are calculated using $(c_i^{\text{eff}}, s_i^{\text{eff}})$, and then fitting the data sets using
 2770 $(c_i^{\text{model}}, s_i^{\text{model}})$. The mean bias of each observable in these toys is assigned as the
 2771 systematic uncertainty, and is determined to be 0.1×10^{-2} or less for all observables.
 2772 The smallness of the effect is the reason no effort is made to correct the c_i and
 2773 s_i values in the nominal measurement.

2774 4.6.3 Mass shapes

2775 A number of uncertainties relate to the mass distributions that enter the fit model.
 2776 Each is described in detail the sections below.

2777 Determination of shape parameters

2778 The statistical uncertainties on the shape parameters that are obtained in fits
 2779 to simulated decays and in the first stage fit to data need to be propagated to
 2780 the uncertainty on the obtained parameters. This is done via a bootstrapping
 2781 procedure, repeating these steps many times:

Table 4.15: The c_i and s_i values for $D \rightarrow K_S^0 \pi^+ \pi^-$ decays calculated via the 2018 Belle model [51] in two cases: assuming a uniform reconstruction efficiency over phase space, denoted $(c/s)_i^{\text{model}}$, and including the LHCb efficiency profile as obtained in simulation, averaged for LL and DD, denoted $(c/s)_i^{\text{eff}}$. The change due to including the efficiency is also tabulated.

Bin	c_i^{model}	c_i^{eff}	Δc_i	s_i^{model}	s_i^{eff}	Δs_i
1	-0.027	-0.007	0.019	0.812	0.794	-0.018
2	0.837	0.859	0.022	0.164	0.152	-0.012
3	0.163	0.163	-0.000	0.872	0.880	0.008
4	-0.914	-0.915	-0.001	0.076	0.082	0.006
5	-0.149	-0.170	-0.021	-0.856	-0.854	0.002
6	0.373	0.362	-0.011	-0.782	-0.805	-0.023
7	0.863	0.862	-0.000	-0.203	-0.202	0.002
8	0.860	0.862	0.002	0.330	0.336	0.006

Table 4.16: The c_i and s_i values for $D \rightarrow K_S^0 K^+ K^-$ decays calculated via the 2010 BaBar model [58] in two cases: assuming a uniform reconstruction efficiency over phase space, denoted $(c/s)_i^{\text{model}}$, and including the LHCb efficiency profile as obtained in simulation, averaged for LL and DD, denoted $(c/s)_i^{\text{eff}}$. The change due to including the efficiency is also tabulated.

Bin	c_i^{model}	c_i^{eff}	Δc_i	s_i^{model}	s_i^{eff}	Δs_i
1	0.738	0.735	-0.002	0.266	0.263	-0.003
2	-0.697	-0.744	-0.046	0.332	0.329	-0.003

- 2782 • Each of the data sets used determine parameters of the signal, crossfeed, and
2783 lowmass shapes that are fixed in the first-stage fit to data of Section 4.4 are
2784 re-sampled with replacement, drawing a number of events equal to the original
2785 data-set size. These are from simulation for signal and lowmass shapes, and
2786 real data for the crossfeed shapes. All of the shapes are fit again, on the
2787 re-sampled data sets.
- 2788 • The real dataset is re-sampled with replacement, drawing a number of events
2789 equal to the original data-set size. Then, the first-stage fit of Section 4.4 is
2790 repeated with the shapes obtained as described above, obtaining values for
2791 the remaining shape parameters.
- 2792 • Finally, the CP fit is repeated using the shape parameters determined in the
2793 preceding steps, but *without* re-sampling the dataset (to avoid a statistical
2794 spread in the obtained central values that is independent of the shape
2795 parameters).

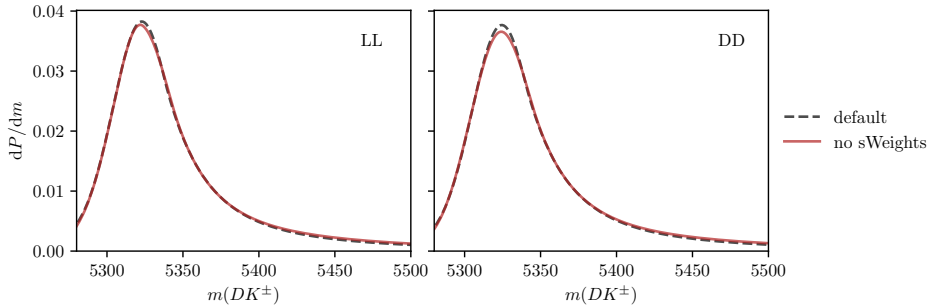


Figure 4.49: Comparison of the default and no-sWeights alternative shape for the $D\pi \rightarrow DK$ cross-feed component in the (left) LL and (right) DD categories where $D \rightarrow K_S^0 \pi^+ \pi^-$. The binned fit obtains essentially the same central values for the CP -violation observables, independently of which shape is used.

2796 The uncertainty on each observable is taken to be the standard deviation of the
 2797 set of central values obtained as described above. This procedure propagates
 2798 the statistical uncertainty on the fixed parameters to the observables, in a way
 2799 that takes correlations into account, and which does not rely on the uncertainty
 2800 estimates in the preliminary fits being accurate. The uncertainties are less than
 2801 0.1×10^{-2} for all DK^\pm observables, in line with earlier analyses, and less than
 2802 0.2×10^{-2} for all $D\pi^\pm$ observables.

2803 A potential bias arises due the use of sWeights when obtaining the mass
 2804 distribution of decays where a $\pi \leftrightarrow K$ misidentification has taken place. This
 2805 is because the $m_{\text{swap}}(Dh^\pm)$ mass that is calculated while assuming a swapped
 2806 companion hypothesis and the nominal $m_{\text{default}}(Dh^\pm)$ mass are correlated (it
 2807 is always the case that $m_{\text{swap}} > m_{\text{default}}$ for a $\pi \rightarrow K$ misidentification ,for
 2808 example). Thus, the assumptions of the sPlot method are not satisfied [135].
 2809 The correlation coefficient in the signal region is about 20 % for simulated signal
 2810 decays. In order to assess the potential impact, an alternative mass distribution
 2811 for $(B^\pm \rightarrow D\pi^\pm) \rightarrow (B^\pm \rightarrow DK^\pm)$ cross-feed is derived that does not rely on
 2812 sWeights. Instead of fitting $B^\pm \rightarrow D\pi^\pm$ sample in the whole fit range and assigning
 2813 sWeights before recalculating the B mass under the kaon companion hypothesis,
 2814 the shape is obtained using $B^\pm \rightarrow D\pi^\pm$ candidates in the signal region. This is
 2815 possible because the $B^\pm \rightarrow D\pi^\pm$ sample is very pure. The shapes are compared in
 2816 Fig. 4.49 and are seen to be almost identical. Thus the sWeights do successfully
 2817 subtract the contribution of combinatorial and partially reconstructed backgrounds
 2818 in the default setup. The impact on the obtained CP -violation observables of
 2819 using one or the other shape in the fits is negligible, and no further systematic
 2820 uncertainty is assigned due to this effect.

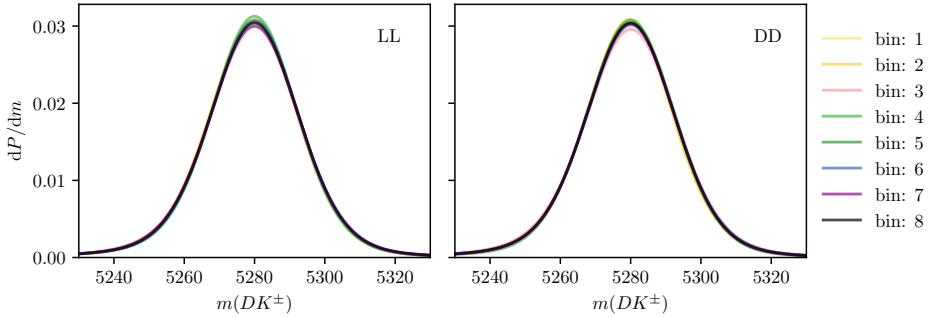


Figure 4.50: Signal shapes obtained in fits simulated $B^\pm \rightarrow D\pi^\pm$ decays for individual Dalitz bins in the optimal binning scheme, for (left) LL and (right) DD candidates in the $B^\pm \rightarrow D(\rightarrow K_S^0\pi^+\pi^-)\pi^\pm$ category.

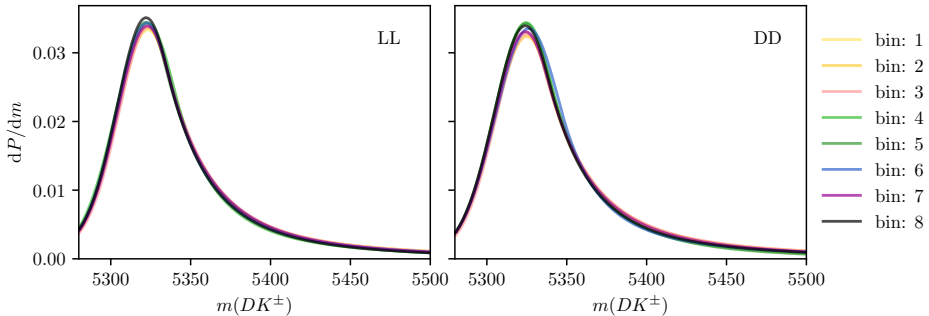


Figure 4.51: Mass shapes for $D\pi \rightarrow DK$ cross feed obtained for individual Dalitz bins in the optimal binning scheme, for (left) LL and (right) DD candidates in the $D \rightarrow K_S^0\pi^+\pi^-$ category.

2821 Using the same mass shapes in all Dalitz bins

2822 The mass shapes obtained the first-stage fit where all Dalitz bins are combined,
 2823 are used in each individual bin of the subsequent binned fit. However, there could
 2824 be some variation in the shape over the D -decay phase space, due to correlations
 2825 between the phase-space coordinates and particle kinematics. The potential effect is
 2826 investigated in pseudoexperiments, where toy data sets are generated with alternative
 2827 signal, crossfeed, and combinatorial-background shapes that are allowed to differ
 2828 between bins, and fitted with the default shapes. The partially reconstructed
 2829 background is treated in a separate study, because further physics effects contribute
 2830 to bin-by-bin variation, as described in the following section.

2831 The alternative signal and cross-feed mass shapes are fitted independently in
 2832 each bin, following identical procedures to those outlined in Sections 4.4.1 and 4.4.2.
 2833 Examples of the obtained shapes are compared in Figs. 4.50 and 4.51.

2834 The shape of the combinatorial background can also vary over the D decay
 2835 phase-space; for example will the relative amount of fake D candidates versus real

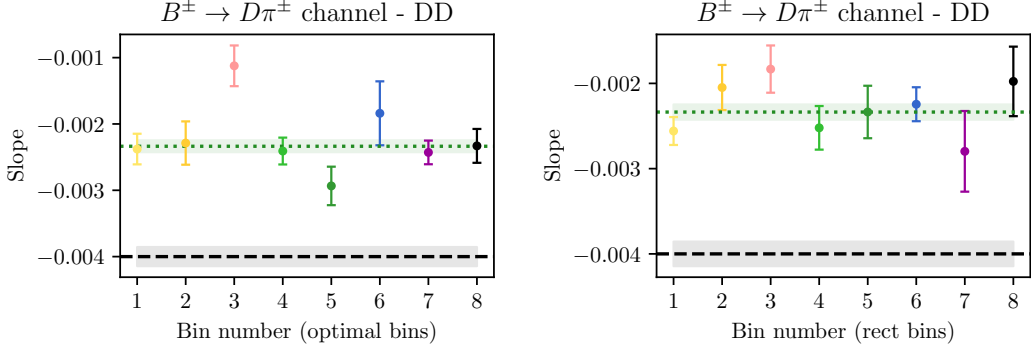


Figure 4.52: Plot of (dots) combinatorial slope in the high B mass background for each bin in the (left) the optimal binning scheme and (right) the rectangular binning scheme, for the DD $B^\pm \rightarrow D(\rightarrow K_S^0\pi^+\pi^-)\pi^\pm$ category. The slope when all bins are combined (green, dashed line) is also shown, and compared with (black dashed line) the slope in the default fit region.

2836 D decays paired with a random bachelor certainly depend on the real D decay
 2837 amplitude for a given phase-space region. The effect is investigated in the high
 2838 B -mass sideband $m_B \in [5600, 6500] \text{ MeV}/c^2$, in which the $m(Dh^\pm)$ distribution is
 2839 fitted with a single exponential distribution, in bins of the Dalitz plot. The fits
 2840 combine B^+ and B^- candidates and merge bins $+i$ and $-i$, and are carried out
 2841 for both the *optimal* binning scheme of Fig. 1.7 (on page 20) and a *rectangular*
 2842 binning scheme, shown in Fig. 4.47, which better captures continuous trends over
 2843 the Dalitz plot. The study is done for $D \rightarrow K_S^0\pi^+\pi^-$ only due to available statistics.
 2844 The DD category of $B^\pm \rightarrow D\pi^\pm$ decays has the largest statistics and shows the
 2845 largest variation, and the fitted slopes for this channel are shown in Fig. 4.52. Two
 2846 effects are visible: 1) there is some variation in the slope as a function of the Dalitz
 2847 bin, especially visible for the rectangular scheme, and 2) the exponential slope is
 2848 larger in general in the high B -mass sideband. The latter effect does not pose a
 2849 problem, since the employed exponential is found to provide an excellent fit in
 2850 the default fit region. It does however need to be taken into account when when
 2851 deriving alternative, bin-dependent combinatorial slopes relevant for the default
 2852 fit region. In order to do so, the alternative slope for bin i is defined

$$\alpha_{\text{default-range}}^i = \frac{\alpha_{\text{high-}m_B}^i}{\alpha_{\text{high-}m_B}^{\text{all-DP}}} \times \alpha_{\text{default-range}}^{\text{all-DP}}, \quad (4.28)$$

2853 and used when generating the combinatorial-background component of the toy
 2854 data sets for the study.

2855 The average bias obtained for each observable in the ensemble of pseudo-
 2856 experiments is assigned as a systematic uncertainty, found to be about 0.1×10^{-2}
 2857 for each observable.

2858 **Ignoring physics effects in the lowmass background**

2859 In the CP fit, the same relative fractions of partly reconstructed B^\pm and B^0
2860 backgrounds are used in each bin, as determined in the first-stage fit described
2861 in Section 4.4 (whereas the partly reconstructed $B_s^0 \rightarrow \bar{D}^0[\pi^+]K^-$ background is
2862 treated separately). However the distribution over the Dalitz plot depends on
2863 whether the partly reconstructed decays occur via an intermediate D^0 meson, a \bar{D}^0
2864 meson, or and admixture of both. Consider a decay reconstructed as $B^- \rightarrow DK^-$
2865 but which is actually a partially-reconstructed background. There are then four
2866 types of background that should be considered:

- 2867 • Decays in which the D -meson in the true decay is a D^0 -meson. An example of
2868 this is $B^- \rightarrow D^{*0}(D^0\pi^0)\pi^-$ for which the π^0 from the D^{*0} decay is missed and
2869 the π^- is misidentified as the companion K^- . These are denoted ' D^0 -like'.⁷
- 2870 • Decays in which the D -meson in the true decay is a \bar{D}^0 -meson. An example of
2871 this is $B_s^0 \rightarrow \bar{D}^0\pi^+K^-$ for which the π^+ is missed and the K^- is reconstructed
2872 as the companion K^- . These are denoted ' \bar{D}^0 -like'.
- 2873 • Decays in which the D meson in the true decay can be either flavour, and
2874 both D flavours contribute to the decay amplitude. An example of this is
2875 $B^- \rightarrow D^*K^-$ for which the total decay amplitude into a D final state has
2876 contributions from both D^{*0} (decaying to D^0) and \bar{D}^{*0} (decaying to \bar{D}^0). The
2877 relative amplitude magnitude and phase between the two possible B decays
2878 are denoted $r_B^{D^*}$ and $\delta_B^{D^*}$ respectively. These are denoted ' r_B -like'.
- 2879 • Decays that can be reconstructed as both D^0 - and \bar{D}^0 -like but where there is
2880 no quantum-mechanical interference. An example is $\bar{B}^0 \rightarrow D^0\pi^+\pi^-$ decays
2881 where either the π^+ or π^- can be reconstructed as the bachelor. These are
2882 denoted 50/50 D^0 -like and \bar{D}^0 -like.

2883 For $B^+ \rightarrow DK^+$ decays everything is CP conjugated. The Dalitz-plot distribution
2884 for each of these cases is:

- 2885 • D^0 decays (' D^0 -like')

$$\begin{aligned} N_{\pm i}(B^-) &\propto F_{\pm i} \\ N_{\pm i}(B^+) &\propto F_{\mp i} \end{aligned} \tag{4.29}$$

⁷The naming convention is defined in terms of the D present in candidates reconstructed as B^- decays. For the charge conjugate case this decay would of course happen via a \bar{D}^0 , but is still denoted D^0 -like.

2886 • \bar{D}^0 decays (' \bar{D}^0 -like'):

$$\begin{aligned} N_{\pm i}(B^-) &\propto F_{\mp i} \\ N_{\pm i}(B^+) &\propto F_{\pm i} \end{aligned} \quad (4.30)$$

2887 • Decays with a quantum-mechanical admixture of D^0 and \bar{D}^0 (' r_B -like'):

$$\begin{aligned} N_{\pm i}(B^-) &\propto F_{\pm i} + (r_B^*)^2 F_{\mp i} + 2\sqrt{F_{+i}F_{-i}}[x_-^*c_{\pm i} + y_-^*s_{\pm i}] \\ N_{\pm i}(B^+) &\propto F_{\mp i} + (r_B^*)^2 F_{\pm i} + 2\sqrt{F_{+i}F_{-i}}[x_+^*c_{\pm i} - y_+^*s_{\pm i}] \end{aligned} \quad (4.31)$$

2888 where (x_\pm^*, y_\pm^*) are defined analogously to the standard $B^\pm \rightarrow DK^\pm$ case.

2889 • 50/50 D^0 -like and \bar{D}^0 -like:

$$\begin{aligned} N_{\pm i}(B^-) &\propto F_{\pm i} + F_{\mp i} \\ N_{\pm i}(B^+) &\propto F_{\pm i} + F_{\mp i} \end{aligned} \quad (4.32)$$

2890 The use of a single background shape across all bins may therefore introduce biases
 2891 because, if an admixture of these backgrounds is present, such a shape has no
 2892 sensitivity to bin-to-bin variations.

2893 In the $D\pi$ channel, the dominant backgrounds are all D^0 -like ($\bar{B}^0 \rightarrow D^{*-}\pi^0$,
 2894 $B^- \rightarrow D^0\rho^-$, $B^- \rightarrow D^{*0}\pi^-$). There is a small contribution from $\bar{B}^0 \rightarrow D^0\rho(\rightarrow$
 2895 $\pi^+\pi^-)$ decays where either the π^+ or π^- from the ρ^0 decay can be assigned as the
 2896 bachelor, and thus this background is 50/50 D^0 -like and \bar{D}^0 -like. The background
 2897 only corresponds to about 0.5% of the total partially reconstructed background and
 2898 thus the impact is small. Nevertheless it is considered in the study described below.

2899 In the DK channel all categories of background appear. In the mass region
 2900 of the CP fit approximately 75.5% of backgrounds are D^0 -like ($\bar{B}^0 \rightarrow D^{*-}K^-$,
 2901 mis-identified $B^- \rightarrow D^{*0}\pi^-$, and mis-identified $B^- \rightarrow D^0\rho^-$), 7.5% are \bar{D}^0 -like
 2902 ($B_s^0 \rightarrow \bar{D}^0\pi^+K^-$), 1% is 50/50 D^0 - \bar{D}^0 -like (mis-identified $B^0 \rightarrow D\rho^0$), and 16% are
 2903 r_B -like ($B^- \rightarrow D^*K^-$, $B^0 \rightarrow DK^{*0}$, and $B^- \rightarrow DK^{*-}$).

2904 In order to estimate the bias due to ignoring this effect, a large number of toy
 2905 data sets are generated using the default low mass shapes and total yields from
 2906 the first-stage fit in Section 4.4, but distributing each of them individually over
 2907 the Dalitz-bins according to Eqs. (4.29)-(4.31). When calculating the distribution
 2908 of $B^+ \rightarrow D^{*0}K^+$ decays over the Dalitz plot, the values [128]

$$r_B^{D^*} = 0.191 \quad \delta_B^{D^*} = 331.6^\circ \quad (4.33)$$

2909 are used. When calculating the distribution of $B^+ \rightarrow D^0 K^{*+}$ decays over the
2910 Dalitz plot the values [128]

$$r_B^{K^*} = 0.092 \quad \delta_B^{K^*} = 40^\circ. \quad (4.34)$$

2911 are used. The toy data sets are then fit with the default set up, and the observed
2912 mean bias assigned as the corresponding uncertainty. The corresponding uncer-
2913 tainties were found to be about 0.1×10^{-2} for all uncertainties. The variation in
2914 the shapes is rather small in the mass range included in the fit, which explains
2915 the small impact.

2916 If the B_s^0 background is *not* treated separately in the default fit, but instead
2917 included in a single lowmass background shape along with the B^0 and B^\pm contribu-
2918 tions, the systematic uncertainty is an order of magnitude larger when evaluated
2919 as described above, and would be a dominating systematic. This motivates the
2920 separate treatment of the B_s^0 background.

2921 4.6.4 *CP* violation and material interaction of the K_S^0

2922 A systematic uncertainty due to *CP*-violation effects and material interaction of
2923 the K_S^0 is assigned using the results obtained in Section 3.3.7. In that section,
2924 the expected bias on all observables in a combined $B^\pm \rightarrow Dh^\pm$ measurement
2925 was evaluated for the detector geometry and particle kinematics of the LHCb
2926 experiment. The calculation was made for $(r_B^{DK^\pm/D\pi^\pm}, \delta_B^{DK^\pm/D\pi^\pm})$ values close to
2927 the world averages, and a number of γ values; the results were summarised in Fig. 3.8.
2928 The systematic uncertainty is taken to be the largest absolute bias observed for each
2929 parameter in the study. The largest uncertainty (on $y_\xi^{D\pi}$ where it is 0.46×10^{-2}) is
2930 still an order of magnitude smaller than the statistical uncertainty.

2931 4.6.5 Impact of D mixing

2932 The effect of D -mixing is not accounted for in the measurement, which leads to
2933 a small bias. Earlier studies have shown this to lead to a sub-degree bias on
2934 measurements of γ in $B^\pm \rightarrow DK^\pm$ decays, in the case where the F_i parameters
2935 are determined experimentally under the same experimental conditions as the γ
2936 measurement [144]. A number of pseudoexperiments are carried out to verify that
2937 this is also the case for the combined DK^\pm – $D\pi^\pm$ setup employed in the thesis. They
2938 are performed following the same procedure described in Section 4.6.4 for the case
2939 of K_S^0 *CP* violation. The yields are calculated while taking D mixing into account,
2940 using the mixing parameter values $x = (0.39_{-0.12}^{+0.11})\%$ and $y = (0.65_{-0.07}^{+0.06})\%$ [31],

and then fitted back assuming no D mixing. The biases are found to be small, as expected, all of them smaller than 0.05×10^{-2} . The largest relative biases are on the $B^\pm \rightarrow D\pi^\pm$ parameters, but even for those the relative effect is less than 2 %. In agreement with Ref. [144], it is found that the biases increase with an order of magnitude if the F_i parameters are fixed to the expected values with no D -mixing, instead of being determined as part of the fit.

4.6.6 PID efficiencies

The uncertainty related to PID efficiencies is assessed by repeating the full two-stage fit procedure a number of times, each time varying the PID efficiencies within the uncertainties. The used uncertainty includes both a statistical and systematic component, as described in detail in Section 4.1.3. The standard deviations of the central values obtained for each observable are assigned as the systematic uncertainty. The uncertainties come out below 0.1×10^{-2} for all observables.

4.6.7 Dalitz-coordinate resolution

There is a small systematic uncertainty related to Dalitz-plot-bin migration, where the non-perfect resolution on the momentum measurement means that a candidate is assigned to a different bin that it truly belongs to. This leads to non-negligible net migration between bins that share a border in a region of phase space where the amplitude varies rapidly. However, since the F_i are measured in the data set, all leading order effects of migration are inherently taken into account. The measurement is only sensitive to differences in migration between the DK^\pm and $D\pi^\pm$ channels and the effect is small.

The systematic uncertainty due to this effect is assigned using pseudoexperiments. The study is made for the $D \rightarrow K_S^0 \pi^+ \pi^-$ mode only, which is sufficient since it completely dominates the overall sensitivity.

1. Signal $B^\pm \rightarrow DK^\pm$ and $B^\pm \rightarrow D\pi^\pm$ decays are generated continuously over phase space, according to the expected distribution obtained with the latest amplitude model from the Belle collaboration [], assuming values of γ and $(r_B^{DK^\pm/D\pi^\pm}, \delta_B^{DK^\pm/D\pi^\pm})$ close to the current world averages.
2. The Dalitz coordinates of each candidate are then smeared using the experiment resolution obtained in simulation. This is described further below.
3. Finally, the generated candidates are binned and fitted back using the default setup.

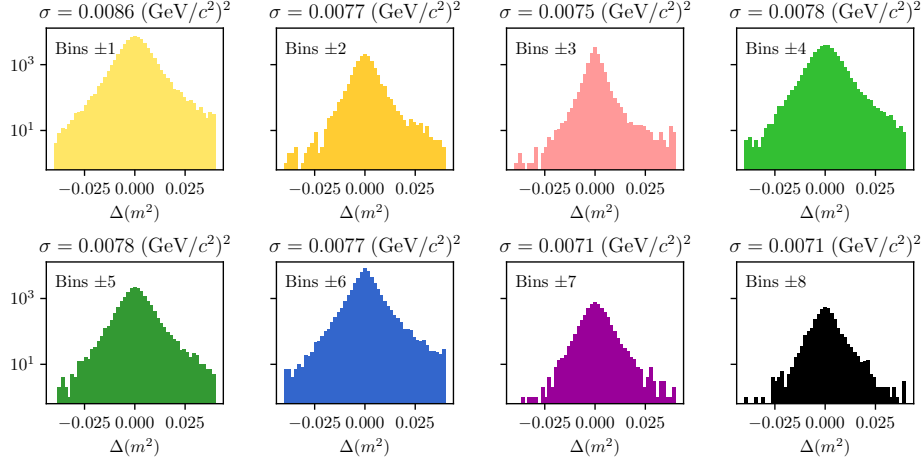


Figure 4.53: Distribution of the biases $\Delta(m^2) = m_{true}^2 - m_{reconstructed}^2$ in simulation for $m^2(K_S^0\pi^+)$ in bins of the rectangular binning scheme of Fig. 4.47.

The resolution is obtained via simulation, by comparing the reconstructed phase-space coordinates with those calculated from the true momenta in samples of simulated $D \rightarrow K_S^0\pi^+\pi^-$ decays. As can be seen in Fig. 4.53, the resolution is found to vary over phase space and the distribution of shifts has significant exponential tails. In order to take both effects into account, the smearing is done by shifting each generated decay with a realised coordinate shift in full simulation, for a simulated decay that took place at approximately the same place in the Dalitz plot. The shift is multiplied with 120 % to take into account that the resolution is generally better in simulation than data. If the shift results in Dalitz coordinates outside the kinematically allowed region, a different shift is applied randomly instead.

The average bias seen in the pseudoexperiments is assigned as the systematic uncertainty. The uncertainties come out at about $(0.1-0.2)\times 10^{-2}$ for all parameters. It is noted that for all four DK^\pm parameters the bias is towards a smaller value of r_B^{DK} ; this is to be expected, as bin migration washes out the asymmetries in different areas of the Dalitz plot.

4.6.8 The fixed yield fractions

A number of relative yields are fixed from efficiencies in simulation and branching fractions. In the DK^\pm modes, this is the case for all the relative yields of the partially reconstructed backgrounds, including partially reconstructed $B \rightarrow D\pi[X]$ decays where the pion is misidentified as a kaon, and the yield of the $B_s^0 \rightarrow DK\pi$ background relative to the $B \rightarrow D\pi$ yield. In the $B^\pm \rightarrow D\pi^\pm$ channel, the only fixed yield ratio is that of the partially reconstructed $B^\pm \rightarrow D^{*0}(\rightarrow D\pi^0)\pi^\pm$ and $B^0 \rightarrow$

Table 4.17: Summary of systematic uncertainties due to backgrounds that are potentially present with a small yield, but not included in the mass fit.

All uncertainties are quoted with implicit: $\times 10^{-2}$						
Mode	$\sigma(x_-^{DK^\pm})$	$\sigma(y_-^{DK^\pm})$	$\sigma(x_+^{DK^\pm})$	$\sigma(y_+^{DK^\pm})$	$\sigma(x_\xi^{D\pi^\pm})$	$\sigma(y_\xi^{D\pi^\pm})$
Λ_b^0 backgrounds	0.04	0.05	0.04	0.06	0.08	0.13
$B \rightarrow D\mu\nu X$	0.04	0.07	0.04	0.05	0.10	0.11
$B^\pm \rightarrow D(\rightarrow K_S^0\pi\mu\nu)h^\pm$	0.00	0.03	0.02	0.02	0.00	0.00
Swapped tracks	0.10	0.13	0.12	0.08	0.00	0.01
Total	0.11	0.16	0.13	0.12	0.08	0.13

2996 $D^{*\mp}(\rightarrow D\pi^\mp)\pi^\pm$ modes. The uncertainty on the observables due to uncertainties
 2997 on these fixed fractions is assessed by repeating the two-stage fit procedure many
 2998 times, each time shifting the yield ratios randomly within their uncertainties. The
 2999 uncertainty on each observable is taken to be the standard deviation of the set of
 3000 central values obtained in these fits. These are all smaller than 0.1×10^{-2} .

3001 **4.6.9 Systematic uncertainty due to backgrounds that are 3002 not modelled in fit**

3003 There are a number of backgrounds that are expected to be present at a small
 3004 level, but which are not modelled in the fits to data because their impact on the fit
 3005 results is minimal. Instead, a systematic uncertainty is assigned. Each contribution
 3006 is described in the following sections and the related systematic uncertainties
 3007 are summarised in Table 4.17.

3008 **Background from Λ_b decays**

3009 This section considers the possible impact of the two potential backgrounds from
 3010 Λ_b^0 decays described in Section 4.4.3: $\Lambda_b^0 \rightarrow D^0 p\pi^-$ decays where the pion is not
 3011 included in the candidate reconstruction and the proton assigned as the companion, and
 3012 $\Lambda_b^0 \rightarrow \Lambda_c^+(\rightarrow pK_S^0\pi^+\pi^-)\pi^-$ decays where a pion in the Λ_c^+ decay is not reconstructed
 3013 and the proton reconstructed as one of the D decay products. The impact of not
 3014 including these in the default fit is assessed by generating toy data sets where the
 3015 backgrounds are included in the generation step, which are then fitted back with
 3016 default model. The former background is distributed over the Dalitz plot as \bar{D}^0 -like,
 3017 cf. the terminology of Section 4.6.3, since a positive bachelor is produced along
 3018 with a D^0 meson. The latter is also distributed as \bar{D}^0 -like in the study; the exact
 3019 distribution is unknown, but a \bar{D}^0 -like background is likely to have the largest
 3020 effect and thus this is a conservative choice. The total yields are taken relative to

3021 the signal yields, using the yield ratios discussed in Section 4.4.3. The $m(Dh^\pm)$
 3022 distributions are obtained using simulated samples, produced with **RapidSim**. The
 3023 mean biases come out to be less than 0.1×10^{-2} for each CP -violation observable,
 3024 which is assigned as a systematic uncertainty.

3025 Semi-leptonic backgrounds

3026 The impact of remnant $B \rightarrow D\mu\nu_\mu$ decays after requiring `isMuon=0` on the bachelor
 3027 is assessed in pseudoexperiments. Toy datasets are generated where the background
 3028 is added in the generation step, which are then fitted with the default model. The
 3029 background yield relative to signal and the mass shape are obtained from a sample
 3030 of fully simulated decays for conditions corresponding to the run conditions in
 3031 2012. The obtained bias in the toys is assigned as the systematic uncertainties:
 3032 it is below 0.1×10^{-2} for all parameters.

3033 The systematic uncertainty relating to the presence of $D^0 \rightarrow K_S^0\pi^-\mu^+\nu_\mu$ is
 3034 estimated by repeating the bias studies of Section 4.3.3, but scaling the background
 3035 yields to 10% to take into account the lepton veto on the D decay products. All
 3036 biases are less than 0.05×10^{-2} in this case.

3037 Swapped tracks

3038 There is a peaking background present from $B^\pm \rightarrow D(\rightarrow K^\mp\pi^\pm)K_S^0\pi^\pm$ decays where
 3039 the kaon is reconstructed as the companion and the K_S^0 is assigned to the D decay.
 3040 The yield of this background is determined to be 0.5% of the signal yield in the
 3041 $B^\pm \rightarrow DK^\pm$ channel in Section 4.3.5. The potential impact from the presence
 3042 of the background is estimated by

- 3043 1. Calculating the expected $B^\pm \rightarrow D\pi^\pm$ and $B^\pm \rightarrow DK^\pm$ signal yields in each
 3044 bin for physics parameters similar to the world average values.
- 3045 2. Then calculating the background bin yields in each $B^\pm \rightarrow DK^\pm$ bin, using
 3046 a total yield equal to 0.5% of the signal yield, and the bin distribution
 3047 from simulated samples of $B^\pm \rightarrow D(\rightarrow K^\mp\pi^\pm)K_S^0\pi^\pm$ decays, produced via
 3048 **RapidSim**. The study is carried out for multiple simulated samples, including
 3049 decays where the $K_S^0\pi$ pair in the B decay originate in different K^* resonances
 3050 (generated with `EvtGen` and the proper resonance-spin models), as well as B
 3051 decays that are evenly distributed over the allowed phase space.
- 3052 3. For each sample, the signal and background yields are added, and the new
 3053 $B^\pm \rightarrow D\pi^\pm$ and $B^\pm \rightarrow DK^\pm$ yields are fitted back with the default signal-
 3054 yield expressions (including a fit of the F_i parameters).

Table 4.18: Biases observed with alternative input parameters and the systematic uncertainty assigned for the bias correction. All numbers are quoted with an implicit $\times 10^{-2}$.

Input ($\gamma, r_B^{DK^\pm}, \delta_B^{DK^\pm}, r_B^{D\pi^\pm}, \delta_B^{D\pi^\pm}$)	$x_-^{DK^\pm}$	$y_-^{DK^\pm}$	$x_+^{DK^\pm}$	$y_+^{DK^\pm}$	$x_\xi^{D\pi^\pm}$	$y_\xi^{D\pi^\pm}$
(72, 0.080, 117, 0.005, 288)	-0.02	-0.01	-0.02	-0.02	0.03	0.00
(75, 0.100, 130, 0.005, 300)	-0.03	-0.04	-0.00	0.02	0.01	-0.03
(82, 0.112, 144, 0.005, 330)	0.00	-0.01	0.00	0.03	-0.03	0.02
(71, 0.099, 129, 0.005, 300)	-0.02	-0.04	-0.00	-0.00	0.05	-0.00
Syst. uncertainty	0.04	0.03	0.02	0.04	0.09	0.05

3055 For each parameter, the most significant bias seen across the different RapidSim
 3056 samples is taken as the related systematic uncertainty. The uncertainty is below
 3057 0.15×10^{-2} for all parameters.

3058 4.6.10 Bias correction

3059 In the default sensitivity study, the bias was found to be compatible with zero.
 3060 However, the size of a potential bias can vary depending on the input para-
 3061 meters. The size of the bias has been investigated with alternate input values of
 3062 $(\gamma, r_B^{DK^\pm}, \delta_B^{DK^\pm}, r_B^{D\pi^\pm}, \delta_B^{D\pi^\pm})$, obtaining the results in Table 4.18. A systematic
 3063 uncertainty due to a potential, small bias is calculated as the difference between
 3064 the maximum and minimum bias for a given parameter. The uncertainty assigned
 3065 in this way is very small in general, and less than 0.1×10^{-2} for all parameters.

3066 4.6.11 Charmless backgrounds

3067 As discussed in Section 4.3.1, a small number of charmless background decays
 3068 survive the D flight distance cut. In this section the systematic uncertainty related
 3069 to those is assessed, in a series of pseudoexperiments. Toy datasets are generated,
 3070 where a charmless background component is included, using the yields and shapes
 3071 obtained in the studies of Section 4.3.1. The Dalitz-bin distribution is obtained
 3072 by repeating the fits of that section for each bin individually. These datasets are
 3073 subsequently fitted back using the default model, which does not include a charmless
 3074 component. No statistically significant bias is observed.

3075 The study described above does not allow for charge-asymmetries in the charmless
 3076 backgrounds, in terms of overall yields and phase-space distributions. These
 3077 asymmetries are likely to be present, due to large local CP -violation in regions
 3078 of phase space in B^\pm decays to hadrons []. The yields in the data-driven studies

Table 4.19: Overview of all sources of uncertainty on the measurement.

Source	All uncertainties are quoted with implicit: $\times 10^{-2}$					
	$\sigma(x_-^{DK^\pm})$	$\sigma(y_-^{DK^\pm})$	$\sigma(x_+^{DK^\pm})$	$\sigma(y_+^{DK^\pm})$	$\sigma(x_\xi^{D\pi^\pm})$	$\sigma(y_\xi^{D\pi^\pm})$
Statistical	0.96	1.14	0.96	1.20	1.99	2.34
Strong-Phase inputs	0.23	0.35	0.18	0.28	0.14	0.18
Efficiency correction of (c_i, s_i)	0.11	0.05	0.05	0.10	0.08	0.09
Mass-shape parameters	0.05	0.08	0.03	0.08	0.16	0.17
Mass-shape bin dependence	0.05	0.07	0.04	0.08	0.07	0.09
Lowmass physics effects	0.04	0.10	0.15	0.05	0.10	0.09
CP violation of K_S^0	0.03	0.04	0.08	0.08	0.09	0.46
D mixing	0.04	0.01	0.00	0.02	0.02	0.01
PID efficiencies	0.03	0.03	0.01	0.05	0.02	0.02
Fixed yield ratios	0.05	0.06	0.03	0.06	0.02	0.02
Dalitz-bin migration	0.04	0.08	0.08	0.11	0.18	0.10
Bias correction	0.04	0.03	0.02	0.04	0.09	0.05
Small backgrounds	0.11	0.16	0.13	0.12	0.08	0.13
Total LHCb systematic	0.20	0.25	0.24	0.26	0.32	0.54
Total systematic	0.31	0.43	0.30	0.38	0.35	0.57

of Section 4.3.1 are not large enough to assess asymmetries, let alone asymmetric bin distributions with any degree of statistical precision. Instead, an extreme-case scenario is investigated, where *all* the charmless background is added to either the B^+ or B^- data sample in generation. In both cases, no statistically significant biases are observed, and it is concluded that the impact of charmless background is negligible.

4.6.12 Summary of systematic uncertainties

The complete set of included systematic uncertainties are summarised in Table 4.19. It can be seen that the measurement is statistically limited. The correlation matrix pertaining to the LHCb related systematics is given in Table 4.20. For studies where the systematic uncertainty is obtained by repeating fits to data multiple times while varying some input, the correlation matrix from the correlations of the fitted central values. For studies that are based on generating a large number of toy datasets and determining the average bias, the correlation of a systematic on two observables is taken to be +100% if the biases are in the same direction, and -100% if they are in opposite directions. The total systematic correlation matrix, including both LHCb-related systematics and that of the strong-phase inputs, is given in Table 4.21.

The studies described in this section also allow for an estimate of the systematic uncertainties on the \mathcal{R}_i parameters of Eq. (4.23) or, equivalently the F_i parameters, in a completely analogous manner to how the uncertainty on the CP -violation observables was assigned. In all cases, however, the systematic uncertainty is found to be much small than the statistical uncertainties that were given in Table 4.10. The central values, statistical, and systematic uncertainties of the \mathcal{R}_i parameters

Table 4.20: Total LHCb-related systematic uncertainties and their correlation matrix.

Uncertainty ($\times 10^{-2}$)						
	$x_-^{DK\pm}$	$y_-^{DK\pm}$	$x_+^{DK\pm}$	$y_+^{DK\pm}$	$x_\xi^{D\pi\pm}$	$y_\xi^{D\pi\pm}$
σ	0.20	0.25	0.24	0.26	0.32	0.54

Correlations						
	$x_-^{DK\pm}$	$y_-^{DK\pm}$	$x_+^{DK\pm}$	$y_+^{DK\pm}$	$x_\xi^{D\pi\pm}$	$y_\xi^{D\pi\pm}$
$x_-^{DK\pm}$	1.000	0.864	0.734	0.897	0.349	0.318
$y_-^{DK\pm}$		1.000	0.874	0.903	0.408	0.362
$x_+^{DK\pm}$			1.000	0.771	0.563	0.447
$y_+^{DK\pm}$				1.000	0.507	0.451
$x_\xi^{D\pi\pm}$					1.000	0.484
$y_\xi^{D\pi\pm}$						1.000

Table 4.21: Total systematic uncertainties and their correlation matrix, including contributions due to strong-phase inputs as well as LHCb-related uncertainties.

Uncertainty ($\times 10^{-2}$)						
	$x_-^{DK\pm}$	$y_-^{DK\pm}$	$x_+^{DK\pm}$	$y_+^{DK\pm}$	$x_\xi^{D\pi\pm}$	$y_\xi^{D\pi\pm}$
σ	0.31	0.43	0.30	0.38	0.35	0.57

Correlations						
	$x_-^{DK\pm}$	$y_-^{DK\pm}$	$x_+^{DK\pm}$	$y_+^{DK\pm}$	$x_\xi^{D\pi\pm}$	$y_\xi^{D\pi\pm}$
$x_-^{DK\pm}$	1.000	0.301	0.156	0.576	0.265	0.231
$y_-^{DK\pm}$		1.000	0.437	0.218	0.183	0.170
$x_+^{DK\pm}$			1.000	0.445	0.414	0.310
$y_+^{DK\pm}$				1.000	0.353	0.243
$x_\xi^{D\pi\pm}$					1.000	0.502
$y_\xi^{D\pi\pm}$						1.000

³¹⁰¹ have been made public in Ref. [1] because they can be employed in future LHCb
³¹⁰² measurements, as discussed in Section 4.5.2.

³¹⁰³ 4.7 Obtained constraints on γ

³¹⁰⁴ The measured values of $(x_\pm^{DK}, y_\pm^{DK}, x_\xi^{D\pi}, y_\xi^{D\pi})$ can be used to put constraints on the
³¹⁰⁵ possible values of the CKM angle γ and the hadronic nuisance parameters $r_B^{DK\pm}$,
³¹⁰⁶ $\delta_B^{DK\pm}$, $r_B^{D\pi\pm}$, and $\delta_B^{D\pi\pm}$. This is handled using the `gammacombo` package, which is

3107 also used to combine all measurements of γ made by the LHCb collaboration [].

3108 4.7.1 Statistical approach

3109 The optimal central values determined in a maximum likelihood fit. The set of
3110 all observables for which a measurement has been made is denoted A , and the set
3111 of underlying physics parameters is denoted θ . The physics parameters of course
3112 determine the probability density function of measurement results of A , $f(A|\theta)$.
3113 Given a specific set of measurement results, A_{obs} , a likelihood function is defined

$$\mathcal{L}(\theta|A_{\text{obs}}) = f(A_{\text{obs}}|\theta) \quad (4.35)$$

3114 and the estimate of θ is the set of parameters that maximize the likelihood

$$\hat{\theta} = \arg \max_{\theta} \mathcal{L}(\theta|A_{\text{obs}}). \quad (4.36)$$

3115 In practice, a χ^2 function is defined

$$\chi^2(\theta|A_{\text{obs}}) = -2 \ln \mathcal{L}(\theta|A_{\text{obs}}) \quad (4.37)$$

3116 and minimized instead. In the specific case where the likelihood profile is Gaussian,
3117 it is given by the simple expression

$$\chi^2(\theta|A_{\text{obs}}) = (A_{\text{obs}} - A(\theta))^T \Sigma_{A_{\text{obs}}}^{-1} (A_{\text{obs}} - A(\theta)) + c, \quad (4.38)$$

3118 where $\Sigma_{A_{\text{obs}}}$ is the covariance matrix for the measured observables, $A(\theta)$ denotes the
3119 value of the observables expressed in terms of the underlying physics parameters,
3120 and c is a constant that is independent of θ . In the specific case considered here

$$\begin{aligned} A &= (x_-^{DK}, y_-^{DK}, x_+^{DK}, y_+^{DK}, x_\xi^{D\pi}, y_\xi^{D\pi}) \\ \theta &= (\gamma, r_B^{DK\pm}, \delta_B^{DK\pm}, r_B^{D\pi\pm}, \delta_B^{D\pi\pm}). \end{aligned} \quad (4.39)$$

3121 The likelihood scan presented in Section 4.5.2 proved that the Gaussian expression
3122 in Eq. (4.38) provides an excellent description of the likelihood profile of the
3123 measurement, when $\Sigma_{A_{\text{obs}}}$ is taken to be the covariance matrix obtained in that
3124 section. Thus, the χ^2 function defined in Eq. (4.38) is minimised to determine
3125 the best estimate of γ .

3126 Two different methods are employed to construct confidence regions for the
3127 observables of interest, known within the `gammacombo` framework as the PROB and
3128 PLUGIN methods. Both methods aim to construct confidence regions for some
3129 subset, ϕ , of the full parameter set θ . The remaining parameters, dubbed nuisance
3130 parameters below, are denoted $\eta = \theta \setminus \phi$. In practice, ϕ most often denotes a single

parameter, and of special interest is of course the case where $\phi = \gamma$. Both methods aim to solve the problem that due to the number of parameters in θ (six in the case considered here, but up to X in the latest LHCb combination []), it is not feasible to derive the confidence regions from a full-fledged Neumann construction []. Under assumptions discussed below, the methods achieve reasonable coverage nonetheless, ie. had the measurement been repeated many times, the confidence region is expected to cover the true parameter(s) with a probability at least at large as the quoted confidence level (CL), independently of the true parameter value. The presentation follows the `gammacombo` manual [].

The `PROB` method is a simple profile-likelihood method. The minimum value of the χ^2 function is denoted $\chi_{\min}^2 \equiv \chi^2(\hat{\theta}|A_{\text{obs}})$. To evaluate the CL for a specific value (set of values) of ϕ_0 , the χ^2 function is again minimised, this time under the constraint that $\phi = \phi_0$, resulting in a new minimum $\hat{\theta}' = (\phi_0, \hat{\eta}')$. In the approximation that all likelihoods are exactly Gaussian, the variable

$$\Delta\chi^2(\phi_0|A_{\text{obs}}) = \chi^2(\hat{\theta}'|A_{\text{obs}}) - \chi_{\min}^2 \quad (4.40)$$

follows a χ^2 distribution with n degrees of freedom, where n is the number of parameters in ϕ [31]. This can be used to evaluate CL at that point as

$$CL(\phi_0|A_{\text{obs}}) = F_n(\Delta\chi^2(\phi_0|A_{\text{obs}})) \quad (4.41)$$

where F_n is the cumulative distribution function of a χ^2 distribution with n degrees of freedom. The method takes its colloquial name from the fact that this function is named `Prob` in the `ROOT` package. Confidence regions can be defined by scanning the values of ϕ_0 over a region of interest. These confidence regions assume that the estimates $\hat{\theta}$ follow a Gaussian distribution centred on the true values, which is generally the case for maximum likelihood estimates in large samples []; in other cases they may not have good coverage properties. Given the Gaussian shape obtained in the likelihood scan of Section 4.5.2 the confidence regions are likely to be well behaved in the case considered here.

However, for the purpose of comparing to the combination of several LHCb measurements in Section 4.5.3 below, the `PLUGIN` method is necessary. It foregoes the assumption that $\Delta\chi^2$ follows a χ^2 distribution, and instead estimates the distribution in a bootstrapping scheme. The procedure is as follows: the values of $\hat{\theta}$, $\hat{\theta}'$, and $\Delta\chi^2(\phi_0|A_{\text{obs}})$ are determined as described above; then the following steps are carried out a number, N_{toys} , of times

- 3162 1. Generate a "toy" result, A_{toy}^i , following the distribution $f(A|\hat{\theta}')$

- 3163 2. Determine $\Delta\chi^2(\phi_0|A_{\text{toy}}^i)$ by minimising the χ^2 function for the results A_{toy}^i
 3164 twice, once where all parameters in θ are free, and once where $\phi = \phi_0$ is
 3165 enforced

3166 Then the CL is defined by

$$CL(\phi_0) = 1 - \frac{N(\Delta\chi^2(\phi_0|A_{\text{obs}}) < \Delta\chi^2(\phi_0|A_{\text{toy}}^i))}{N_{\text{toys}}}. \quad (4.42)$$

3167 The method is described in Ref. [145], based on the hybrid resampling method
 3168 presented in [146, 147]. While the coverage properties are not proven, evidence
 3169 is presented in terms of asymptotic results and simulation studies in those refer-
 3170 ences. The coverage properties have also been investigated in relation to LHCb
 3171 combinations, and the intervals were found to perform well in most cases [].

3172 4.7.2 Interpretation results

3173 The central values and confidence regions obtained for the physics parameters are

$$\begin{aligned} \gamma &= (68.7^{+5.2}_{-5.1})^\circ, \\ r_B^{DK^\pm} &= 0.0904^{+0.0077}_{-0.0075}, \\ \delta_B^{DK^\pm} &= (118.3^{+5.5}_{-5.6})^\circ, \\ r_B^{D\pi^\pm} &= 0.0050^{+0.0017}_{-0.0017}, \\ \delta_B^{D\pi^\pm} &= (291^{+24}_{-26})^\circ, \end{aligned} \quad (4.43)$$

3174 where the quoted uncertainties are obtained via the PLUGIN method. The one-
 3175 dimensional CL plots are shown in Fig. 4.54. It is also clear that the PROB and
 3176 PLUGIN confidence regions agree well; this is expected given the Gaussian likelihood.
 3177 A series of two-dimensional confidence regions are shown in Fig. 4.55, where it
 3178 can be seen that the observables define a single solution for γ as expected. It
 3179 is worth noticing that the uncertainty of this measurement alone is on par with
 3180 the current world average, due to the increased data sample, and the significant
 3181 reduction of systematic uncertainties due to the new measurement strategy and
 3182 updated inputs from BESIII.

3183 The contribution to the uncertainty on γ from each of the statistical, strong-
 3184 phase-related, and LHCb-related uncertainties in isolation can be estimated by
 3185 repeating the interpretation while only including subsets of the uncertainties on
 3186 the input parameters. Such studies have been performed using the PROB method.
 3187 Running with statistical uncertainties only yields an uncertainty on γ of 5.05° .
 3188 Including only the statistical and LHCb-related systematic uncertainties yields an

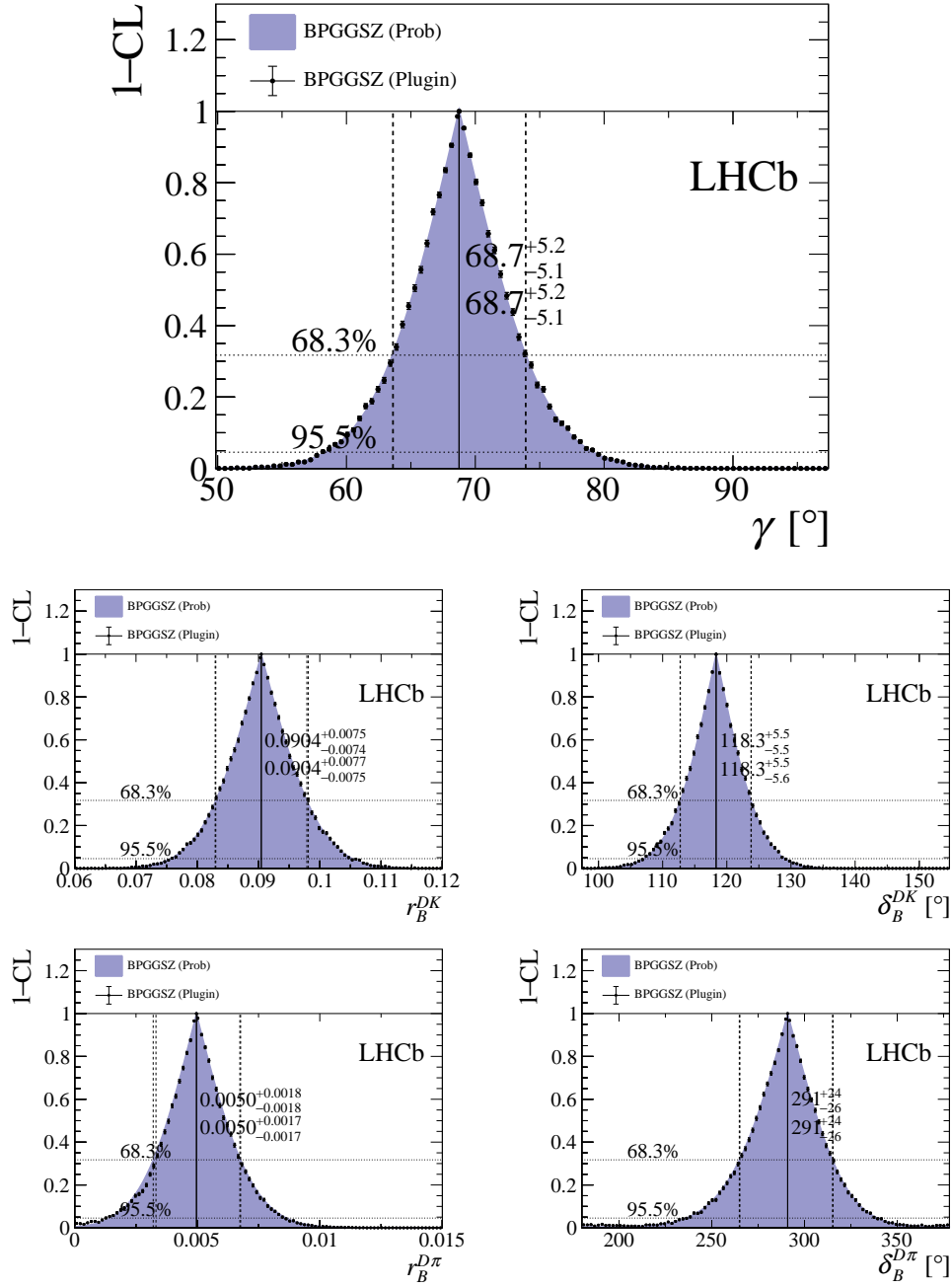


Figure 4.54: Confidence levels for the physics parameters of interest. The solutions are written on the plots, where the top number is given with PROB uncertainties and the bottom number with PLUGIN uncertainties.

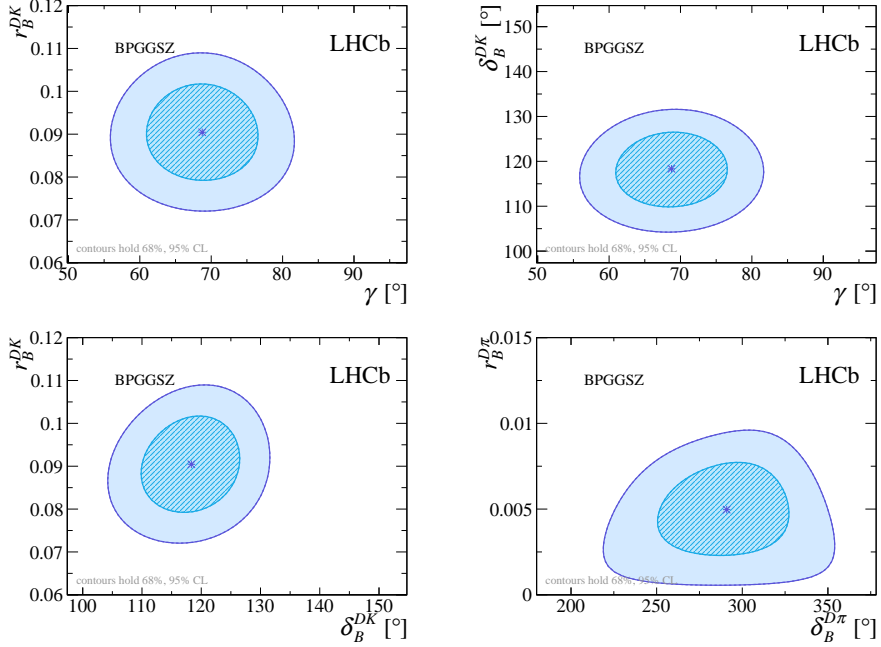


Figure 4.55: The 68 % and 95 % confidence regions for combinations of the physics parameters of interest, as obtained from the results of this measurement. The regions are calculated via the PROB method of `gammapcombo`.

uncertainty on γ of 5.08° , suggesting that the LHCb-related systematics contribute an uncertainty of 0.6° . This is a reduction compared to earlier analyses, where the contribution was about 2° . A significant contribution to the improvement is the efficiency-related systematic that has been avoided by promoting $B^\pm \rightarrow D\pi^\pm$ to a signal channel. Including only the statistical and the strong-phase-related uncertainties leads to an uncertainty on γ of 5.09° , showing the strong-phase-related uncertainty to be 0.6° , somewhat lower than the expectation of 1.2° presented in Ref. [70]. This is partly because the uncertainty estimate of that paper does not take into account the use of the $D \rightarrow K_S^0 K^+ K^-$ channel, and partly because the uncertainty estimate depends on the specific central values.

The obtained statistical uncertainty on γ is in excellent agreement with the expectation from pseudoexperiments. The interpretation procedure outlined above has been performed for each of the pseudoexperiments performed to establish the feasibility of the CP fit in Section 4.5.1 (including only statistical uncertainties on the observables) and the central 90 % interval of the obtained uncertainties is $[4.4^\circ, 6.0^\circ]$. Similar studies have been carried out where no background decays are included in the generated toy data sets. In this case, the precision on γ is improved by about 30 %.

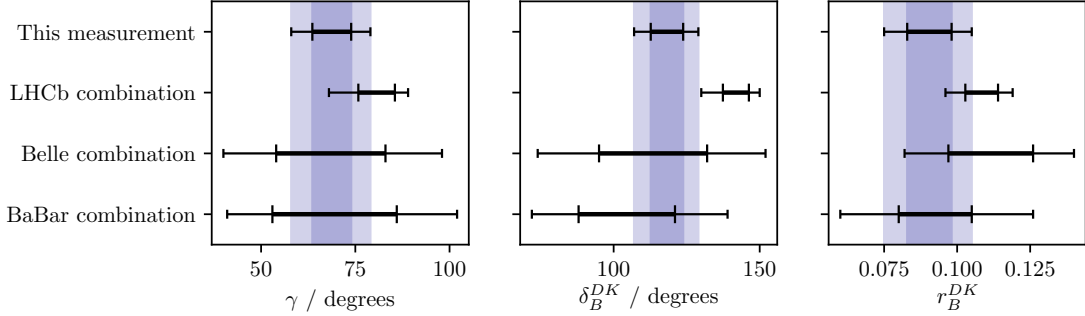


Figure 4.56: Comparison of the 1σ and 2σ confidence intervals obtained results for γ and the physics parameters relating to $B^\pm \rightarrow DK^\pm$ decays, with those from the combinations of γ measurements by the Belle [148] and BaBar [149] collaborations, and the 2018 combination of LHCb results [128] where the BPGGSZ measurements have been excluded.

3206 4.7.3 Compatibility with other measurements

3207 It is worth comparing the obtained constraints on the physics parameters with the
 3208 information available from other measurements, made at the B factories and by the
 3209 LHCb collaboration using other decay channels. This comparison is made for γ and
 3210 the hadronic parameters in the $B^\pm \rightarrow DK^\pm$ decay in Fig. 4.56, comparing to the
 3211 results of the combinations of γ measurements by the Belle [148] and BaBar [149]
 3212 collaborations presented in 2013, and the 2018 combination of LHCb results [128].
 3213 For this purpose, the LHCb combination is re-performed, removing the input from
 3214 earlier BPGGSZ measurements that use $B^\pm \rightarrow DK^\pm$ decays, because they were
 3215 made using data that is re-analysed in the present thesis; thus they need to be
 3216 excluded to make the results that are compared independent. The combination
 3217 employs the same statistical method outlined above, with the exception that
 3218 the likelihood now depends on observables measured in a number of different
 3219 analyses. The included measurements are summarised in Table 4.22. It can be
 3220 seen in Fig. 4.56 that the results obtained in this thesis agree well with the Belle
 3221 and BaBar results, but are in some tension with the 2018 LHCb combination,
 3222 especially for the δ_B^{DK} parameter.

3223 The level of compatibility can be quantified by calculating the three-dimensional
 3224 χ^2 of the BPGGSZ results and those of the LHCb combination (without the earlier
 3225 BPGGSZ measurements), with respect to the best fit values of $(\gamma, r_B^{DK\pm}, \delta_B^{DK\pm})$
 3226 when all measurements are combined. The two-dimensional confidence regions
 3227 obtained in these three cases are compared in Fig. 4.57, where some tension in $r_B^{DK\pm}$
 3228 and $\delta_B^{DK\pm}$ is visible again. The calculation is based on the PLUGIN uncertainties; for
 3229 the LHCb combination these uncertainty estimates are slightly larger than the ones

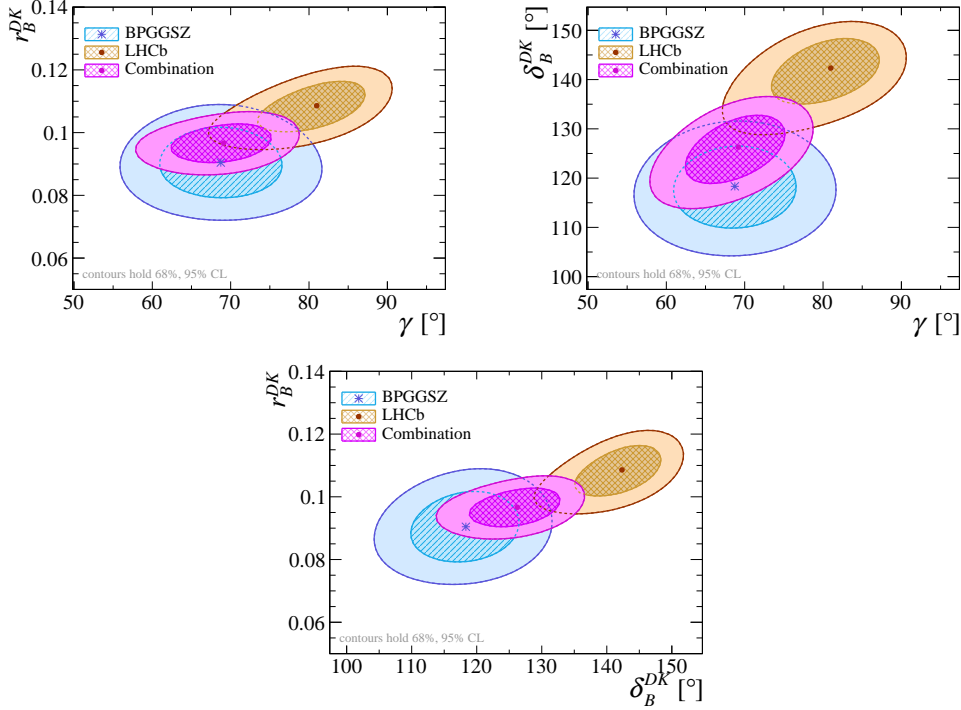


Figure 4.57: The 68 % and 95 % confidence regions for $(\gamma, r_B^{DK\pm})$, $(\gamma, \delta_B^{DK\pm})$, and $(\delta_B^{DK\pm}, r_B^{DK\pm})$ for this measurement, the 2018 LHCb combination [128] where the BPGGSZ results have been excluded, and the combination thereof, calculated via the PROB method of `gammacombo`.

obtained via the PROB method. One obtains $\chi^2 = \chi_{GGGSZ}^2 + \chi_{LHCb}^2 = 0.7 + 9.1 = 9.8$, which for 3 degrees of freedom correspond to a p -value of 2 %, or a 2.3σ deviation. However, this tension is expected to be reduced when other measurements in the LHCb combination are updated to include results based on the full Run 1 and 2 data set. The most important update is that of the two-body ADS/GLW measurement in $B^\pm \rightarrow DK^\pm$ decays because that measurement, and the BPGGSZ measurement presented in this thesis, have the largest impact in the combination.

The latest LHCb combination in which $B^\pm \rightarrow D\pi^\pm$ parameters were determined is from 2016 [127]. Two solutions existed for $(r_B^{D\pi^\pm}, \delta_B^{D\pi^\pm})$ which made the interpretation problematic. As can be seen in Fig. 4.58 the measurement presented in this thesis picks out one of these solutions, with which it is in excellent agreement. This solution agrees with the theoretically expected value of $r_B^{D\pi^\pm} \sim 0.005$ [47]. Thus, the inclusion of the results presented here are expected to lead to a much less problematic inclusion of the $B^\pm \rightarrow D\pi^\pm$ channel in future LHCb combinations.

Table 4.22: List of the LHCb measurements used in the combination that the results obtained in the present thesis is compared to. These correspond to the 2018 LHCb combination [128], except that the earlier BPGBS results made with $B^\pm \rightarrow DK^\pm$ decays have not been included in the comparison. In the method column, TD stands for "time-dependent".

B decay	D decay	Method	Ref.	Data set
$B^+ \rightarrow DK^+$	$D \rightarrow h^+h^-$	GLW	[141]	2011-16
$B^+ \rightarrow DK^+$	$D \rightarrow h^+h^-$	ADS	[150]	2011-12
$B^+ \rightarrow DK^+$	$D \rightarrow h^+\pi^-\pi^+\pi^-$	GLW/ADS	[150]	2011-12
$B^+ \rightarrow DK^+$	$D \rightarrow h^+h^-\pi^0$	GLW/ADS	[151]	2011-12
$B^+ \rightarrow DK^+$	$D \rightarrow K_S^0K^+\pi^-$	GLS	[152]	2011-12
$B^+ \rightarrow D^*K^+$	$D \rightarrow h^+h^-$	GLW	[141]	2011-16
$B^+ \rightarrow DK^{*+}$	$D \rightarrow h^+h^-$	GLW/ADS	[153]	2011-16
$B^+ \rightarrow DK^{*+}$	$D \rightarrow h^+\pi^-\pi^+\pi^-$	GLW/ADS	[153]	2011-16
$B^+ \rightarrow DK^+\pi^+\pi^-$	$D \rightarrow h^+h^-$	GLW/ADS	[154]	2011-12
$B^0 \rightarrow DK^{*0}$	$D \rightarrow K^+\pi^-$	ADS	[155]	2011-12
$B^0 \rightarrow DK^+\pi^-$	$D \rightarrow h^+h^-$	GLW-Dalitz	[140]	2011-12
$B^0 \rightarrow DK^{*0}$	$D \rightarrow K_S^0\pi^+\pi^-$	BPGBS	[63]	2011-12
$B_s^0 \rightarrow D_s^\mp K^\pm$	$D_s^+ \rightarrow h^+h^-\pi^+$	TD	[156]	2011-12
$B^0 \rightarrow D^\mp\pi^\pm$	$D^+ \rightarrow K^+\pi^-\pi^+$	TD	[157]	2011-12

Measurements included in Ref. [128] but not in the present comparison				
$B^+ \rightarrow DK^+$	$D \rightarrow K_S^0h^+h^-$	BPGBS	[74]	2011-12
$B^+ \rightarrow DK^+$	$D \rightarrow K_S^0h^+h^-$	BPGBS	[3]	2015-16

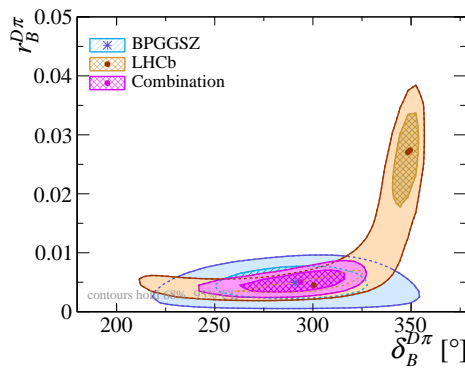


Figure 4.58: The 68 % and 95 % confidence regions for $(\delta_B^{D\pi^\pm}, r_B^{D\pi^\pm})$ obtained from the results of this measurement, in the 2016 LHCb combination [127], and the combination thereof, calculated via the PROB method of gammacombo.

Appendices

A

3245

3246

Projections of main fit to data

Bibliography

- [1] LHCb collaboration, R. Aaij *et al.*, *Measurement of the CKM angle γ in $B^\pm \rightarrow DK^\pm$ and $B^\pm \rightarrow D\pi^\pm$ decays with $K_S^0 h^\pm h^\mp$* , Submitted to JHEP (2020).
- [2] M. Bjørn and S. Malde, *CP violation and material interaction of neutral kaons in measurements of the CKM angle γ using $B^\pm \rightarrow DK^\pm$ decays where $D \rightarrow K_S^0 \pi^+ \pi^-$* , JHEP **19** (2019) 106, [arXiv:1904.01129](https://arxiv.org/abs/1904.01129).
- [3] LHCb collaboration, R. Aaij *et al.*, *Measurement of the CKM angle γ using $B^\pm \rightarrow DK^\pm$ with $D \rightarrow K_S^0 \pi^+ \pi^-$, $K_S^0 K^+ K^-$ decays*, JHEP **08** (2018) 176, Erratum ibid. **10** (2018) 107, [arXiv:1806.01202](https://arxiv.org/abs/1806.01202).
- [4] E. Noether, *Invariante Variationsprobleme*, Nachrichten von der Gesellschaft der Wissenschaften zu Göttingen, Mathematisch-Physikalische Klasse **1918** (1918) 235.
- [5] J. F. Donoghue, E. Golowich, and B. R. Holstein, *Dynamics of the Standard Model*, Cambridge University Press, Cambridge, 2014.
- [6] A. D. Sakarov, *Violation of CP Invariance, C Asymmetry, and Baryon Asymmetry of the Universe*, JETP Letters **5** (1966) 24.
- [7] G. Luders, *On the Equivalence of Invariance under Time Reversal and under Particle-Antiparticle Conjugation for Relativistic Field Theories*, Kong. Dan. Vid. Sel. Mat. Fys. Medd. **28N5** (1954) 1.
- [8] C. S. Wu *et al.*, *Experimental Test of Parity Conservation in Beta Decay*, Phys. Rev. **105** (1957) 1413.
- [9] T. D. Lee and C. N. Yang, *Question of Parity Conservation in Weak Interactions*, Phys. Rev. **104** (1956) 254.
- [10] J. H. Christenson, J. W. Cronin, V. L. Fitch, and R. Turlay, *Evidence for the 2π Decay of the K_2^0 Meson*, Phys. Rev. Lett. **13** (1964) 138.

- 3273 [11] BaBar collaboration, B. Aubert *et al.*, *Observation of CP Violation in the B^0*
 3274 *Meson System*, Phys. Rev. Lett. **87** (2001) 091801, [arXiv:hep-ex/0107013](#).
- 3275 [12] Belle collaboration, K. Abe *et al.*, *Observation of large CP violation*
 3276 *in the neutral B meson system*, Phys. Rev. Lett. **87** (2001) 091802,
 3277 [arXiv:hep-ex/0107061](#).
- 3278 [13] Belle collaboration, K. Abe *et al.*, *Study of $B^\pm \rightarrow D_{CP}K^\pm$ and $B^\pm \rightarrow D_{CP}^*K^\pm$*
 3279 *decays*, Phys. Rev. D **73** (2006) 051106, [arXiv:hep-ex/0601032](#).
- 3280 [14] Belle collaboration, Y. Horii *et al.*, *Evidence for the Suppressed Decay $B^- \rightarrow$*
 3281 *DK^- , $D \rightarrow K^+\pi^-$* , Phys. Rev. Lett. **106** (2011) 231803, [arXiv:1103.5951](#).
- 3282 [15] BaBar collaboration, P. del Amo Sanchez *et al.*, *Measurement of CP*
 3283 *observables in $B^\pm \rightarrow D_{CP}K^\pm$) decays and constraints on the CKM angle*
 3284 *gamma*, Phys. Rev. D **82** (2010) 072004, [arXiv:1007.0504](#).
- 3285 [16] BaBar collaboration, P. del Amo Sanchez *et al.*, *Search for $b \rightarrow u$ transitions*
 3286 *in $B^- \rightarrow DK^-$ and D^*K^- decays*, Phys. Rev. D **82** (2010) 072006,
 3287 [arXiv:1006.4241](#).
- 3288 [17] CDF collaboration, T. Aaltonen *et al.*, *Measurements of branching fraction*
 3289 *ratios and CP asymmetries in $B^\pm \rightarrow D_{CP}K^\pm$ decays in hadron collisions*,
 3290 Phys. Rev. D **81** (2010) 031105, [arXiv:0911.0425](#).
- 3291 [18] CDF collaboration, T. Aaltonen *et al.*, *Measurements of branching fraction*
 3292 *ratios and CP-asymmetries in suppressed $B^- \rightarrow D(\rightarrow K^+\pi^-)K^-$ and*
 3293 *$B^- \rightarrow D(- > K^+\pi^-)\pi^-$ decays*, Phys. Rev. D **84** (2011) 091504,
 3294 [arXiv:1108.5765](#).
- 3295 [19] LHCb collaboration, R. Aaij *et al.*, *Observation of CP violation in $B^\pm \rightarrow$*
 3296 *DK^\pm decays*, Phys. Lett. **B712** (2012) 203, Erratum ibid. **B713** (2012) 351,
 3297 [arXiv:1203.3662](#).
- 3298 [20] LHCb collaboration, R. Aaij *et al.*, *First observation of CP violation in the*
 3299 *decays of B_s^0 mesons*, Phys. Rev. Lett. **110** (2013) 221601, [arXiv:1304.6173](#).
- 3300 [21] LHCb collaboration, R. Aaij *et al.*, *Observation of CP violation in charm*
 3301 *decays*, Phys. Rev. Lett. **122** (2019) 211803, [arXiv:1903.08726](#).
- 3302 [22] T2K collaboration, K. Abe *et al.*, *Constraint on the matter–antimatter*
 3303 *symmetry-violating phase in neutrino oscillations*, Nature **580** (2020) 339,
 3304 [arXiv:1910.03887](#).

- [23] L. K. Gibbons *et al.*, *Measurement of the CP-violation parameter $\text{Re}(\varepsilon'/\varepsilon)$* , Phys. Rev. Lett. **70** (1993) 1203.
- [24] G. D. Barr *et al.*, *A new measurement of direct CP violation in the neutral kaon system*, Phys. Lett. **B317** (1993) 233.
- [25] NA48 collaboration, J. R. Batley *et al.*, *A precision measurement of direct CP violation in the decay of neutral kaons into two pions*, Phys. Lett. **B544** (2002) 97, [arXiv:hep-ex/0208009](https://arxiv.org/abs/hep-ex/0208009).
- [26] KTeV collaboration, A. Alavi-Harati *et al.*, *Measurements of direct CP violation, CPT symmetry, and other parameters in the neutral kaon system*, Phys. Rev. **D67** (2003) 012005, [arXiv:hep-ex/0208007](https://arxiv.org/abs/hep-ex/0208007).
- [27] HFLAV group, Y. S. Amhis *et al.*, *Averages of b-hadron, c-hadron, and τ -lepton properties as of 2018*, [arXiv:1909.12524](https://arxiv.org/abs/1909.12524), updated results and plots available at <https://hflav.web.cern.ch/>.
- [28] M. Kobayashi and T. Maskawa, *CP-Violation in the Renormalizable Theory of Weak Interaction*, Prog. Theor. Phys. **49** (1973) 652.
- [29] N. Cabibbo, *Unitary Symmetry and Leptonic Decays*, Physical Review Letters **10** (1963) 531.
- [30] L.-L. Chau and W.-Y. Keung, *Comments on the Parametrization of the Kobayashi-Maskawa Matrix*, Phys. Rev. Lett. **53** (1984) 1802.
- [31] Particle Data Group, P. A. Zyla *et al.*, *Review of particle physics*, Prog. Theor. Exp. Phys. **2020** (2020) 083C01.
- [32] L. Wolfenstein, *Parametrization of the Kobayashi-Maskawa Matrix*, Phys. Rev. Lett. **51** (1983) 1945.
- [33] Y. H. Ahn, H.-Y. Cheng, and S. Oh, *Wolfenstein parametrization at higher order: Seeming discrepancies and their resolution*, Phys. Lett. **B703** (2011) 571, [arXiv:1106.0935](https://arxiv.org/abs/1106.0935).
- [34] A. J. Buras, M. E. Lautenbacher, and G. Ostermaier, *Waiting for the Top Quark Mass, $K^+ \rightarrow \pi^+ \nu \bar{\nu}$, $B_s^0 - \bar{B}_s^0$ Mixing, and CP asymmetries in B decays*, Phys. Rev. **D50** (1994) 3433, [arXiv:hep-ph/9403384](https://arxiv.org/abs/hep-ph/9403384).
- [35] J. Charles *et al.*, *CP violation and the CKM matrix: Assessing the impact of the asymmetric B factories*, Eur. Phys. J. **C41** (2005) 1, [arXiv:hep-ph/0406184](https://arxiv.org/abs/hep-ph/0406184).

- 3336 [36] J. Brod and J. Zupan, *The ultimate theoretical error on γ from $B \rightarrow DK$*
 3337 *decays*, JHEP **2014** (2014) 51, arXiv:1308.5663.
- 3338 [37] M. Blanke and A. J. Buras, *Emerging ΔM_d -anomaly from tree-level de-*
 3339 *terminations of $|V_{cb}|$ and the angle γ* , Eur. Phys. J. **C79** (2019) 159,
 3340 arXiv:1812.06963.
- 3341 [38] CKMfitter group, J. Charles *et al.*, *Current status of the Standard*
 3342 *Model CKM fit and constraints on $\Delta F = 2$ new physics*, Phys. Rev. **D91**
 3343 (2015) 073007, arXiv:1501.05013, updated results and plots available at
 3344 <http://ckmfitter.in2p3.fr/>.
- 3345 [39] UTfit collaboration, M. Bona *et al.*, *The unitarity triangle fit in the*
 3346 *standard model and hadronic parameters from lattice QCD: A reap-*
 3347 *praisal after the measurements of Δm_s and $BR(B \rightarrow \tau\nu_\tau)$* , JHEP **10**
 3348 (2006) 081, arXiv:hep-ph/0606167, updated results and plots available at
 3349 <http://www.utfit.org/>.
- 3350 [40] Belle II collaboration, E. Kou *et al.*, *The Belle II Physics Book*, Prog. Theor.
 3351 Exp. Phys. **2019** (2019) 123C01, arXiv:1808.10567.
- 3352 [41] LHCb collaboration, I. Bediaga *et al.*, *Physics case for an LHCb Upgrade*
 3353 *II - Opportunities in flavour physics, and beyond, in the HL-LHC era*,
 3354 arXiv:1808.08865.
- 3355 [42] Y. Grossman and M. Savastio, *Effects of $K^0 - \bar{K}^0$ mixing on determining γ*
 3356 *from $B^\pm \rightarrow DK^\pm$* , JHEP **2014** (2014) 8, arXiv:1311.3575.
- 3357 [43] M. Gronau and D. Wyler, *On determining a weak phase from charged B decay*
 3358 *asymmetries*, Phys. Lett. **B265** (1991) 172.
- 3359 [44] M. Gronau and D. London, *How to determine all the angles of the unitarity*
 3360 *triangle from $B_d^0 \rightarrow DK_S^0$ and $B_s^0 \rightarrow D\phi$* , Phys. Lett. **B253** (1991) 483.
- 3361 [45] D. Atwood, I. Dunietz, and A. Soni, *Enhanced CP Violation with $B \rightarrow$*
 3362 *$K D^0 (\bar{D}^0)$ Modes and Extraction of the Cabibbo-Kobayashi-Maskawa Angle γ* ,
 3363 Phys. Rev. Lett. **78** (1997) 3257, arXiv:hep-ph/9612433.
- 3364 [46] D. Atwood, I. Dunietz, and A. Soni, *Improved methods for observing CP*
 3365 *violation in $B^\pm \rightarrow KD$ and measuring the CKM phase γ* , Phys. Rev. **D63**
 3366 (2001) 036005, arXiv:hep-ph/0008090.

- 3367 [47] M. Kenzie, M. Martinelli, and N. Tuning, *Estimating $r_B^{D\pi}$ as an input to*
 3368 *the determination of the CKM angle γ* , Phys. Rev. **D94** (2016) 054021,
 3369 arXiv:1606.09129.
- 3370 [48] T. Evans, J. Libby, S. Malde, and G. Wilkinson, *Improved sensitivity to the*
 3371 *CKM phase γ through binning phase space in $B^- \rightarrow DK^-$, $D \rightarrow K^+\pi^-\pi^-\pi^+$*
 3372 *decays*, Phys. Lett. **B802** (2020) 135188, arXiv:1909.10196.
- 3373 [49] S. Harnew *et al.*, *Model-independent determination of the strong phase*
 3374 *difference between D_0 and $\bar{D}_0 \rightarrow \pi^+\pi^-\pi^+\pi^-$ amplitudes*, JHEP **2018** (2018)
 3375 144, arXiv:1709.03467.
- 3376 [50] R. H. Dalitz, *CXII. On the analysis of τ -meson data and the nature of the*
 3377 *τ -meson*, The London, Edinburgh, and Dublin Philosophical Magazine and
 3378 Journal of Science **44** (1953) 1068.
- 3379 [51] BaBar and Belle collaborations, I. Adachi *et al.*, *Measurement of $\cos 2\beta$ in*
 3380 *$B^0 \rightarrow D^{(*)} h^0$ with $D \rightarrow K_S^0 \pi^+ \pi^-$ decays by a combined time-dependent*
 3381 *Dalitz plot analysis of BaBar and Belle data*, Phys. Rev. **D98** (2018) 112012,
 3382 arXiv:1804.06153.
- 3383 [52] S. U. Chung *et al.*, *Partial wave analysis in K -matrix formalism*, Annalen der
 3384 Physik **507** (1995) 404.
- 3385 [53] D. Aston *et al.*, *A study of $K^- \pi^+$ scattering in the reaction $K^- p \rightarrow \pi^+ n$ at*
 3386 *11 GeV/c*, Nucl. Phys. **B296** (1988) 493.
- 3387 [54] A. Bondar, *Proceedings of BINP special analysis meeting on Dalitz analysis,*
 3388 *24-26 Sep. 2002, unpublished*.
- 3389 [55] A. Giri, Y. Grossman, A. Soffer, and J. Zupan, *Determining γ using*
 3390 *$B^\pm \rightarrow DK^\pm$ with multibody D decays*, Phys. Rev. **D68** (2003) ,
 3391 arXiv:hep-ph/0303187.
- 3392 [56] BaBar collaboration, B. Aubert *et al.*, *Measurement of the Cabibbo-Kobayashi-*
 3393 *Maskawa angle γ in $B^\mp \rightarrow D^{(*)} K^\mp$ decays with a Dalitz analysis of $D \rightarrow$*
 3394 *$K_S^0 \pi^+ \pi^-$* , Phys. Rev. Lett. **95** (2005) 121802, arXiv:hep-ex/0504039.
- 3395 [57] BaBar collaboration, B. Aubert *et al.*, *Improved measurement of the CKM*
 3396 *angle γ in $B^\mp \rightarrow D^{(*)} K^{(*)\mp}$ decays with a Dalitz plot analysis of D decays to*
 3397 *$K_S^0 \pi^+ \pi^-$ and $K_S^0 K^+ K^-$* , Phys. Rev. **D78** (2008) 034023, arXiv:0804.2089.

- 3398 [58] BaBar collaboration, P. del Amo Sanchez *et al.*, *Evidence for direct CP*
 3399 *violation in the measurement of the Cabibbo-Kobayashi-Maskawa angle*
 3400 γ *with $B^\mp \rightarrow D^{(*)}K^{(*)\mp}$ decays*, Phys. Rev. Lett. **105** (2010) 121801,
 3401 [arXiv:1005.1096](https://arxiv.org/abs/1005.1096).
- 3402 [59] Belle collaboration, A. Poluektov *et al.*, *Measurement of ϕ_3 with Dalitz*
 3403 *plot analysis of $B^\pm \rightarrow D^{(*)}K^\pm$ decay*, Phys. Rev. **D70** (2004) 072003,
 3404 [arXiv:hep-ex/0406067](https://arxiv.org/abs/hep-ex/0406067).
- 3405 [60] Belle collaboration, A. Poluektov *et al.*, *Measurement of ϕ_3 with Dalitz*
 3406 *plot analysis of $B^+ \rightarrow D^{(*)}K^{(*)+}$ decay*, Phys. Rev. **D73** (2006) 112009,
 3407 [arXiv:hep-ex/0604054](https://arxiv.org/abs/hep-ex/0604054).
- 3408 [61] Belle collaboration, A. Poluektov *et al.*, *Evidence for direct CP violation in*
 3409 *the decay $B^\pm \rightarrow D^{(*)}K^\pm$, $D \rightarrow K_S^0\pi^+\pi^-$ and measurement of the CKM phase*
 3410 ϕ_3 , Phys. Rev. **D81** (2010) 112002, [arXiv:1003.3360](https://arxiv.org/abs/1003.3360).
- 3411 [62] LHCb collaboration, R. Aaij *et al.*, *Measurement of CP violation and*
 3412 *constraints on the CKM angle γ in $B^\pm \rightarrow DK^\pm$ with $D \rightarrow K_S^0\pi^+\pi^-$ decays*,
 3413 Nucl. Phys. **B888** (2014) 169, [arXiv:1407.6211](https://arxiv.org/abs/1407.6211).
- 3414 [63] LHCb collaboration, R. Aaij *et al.*, *Measurement of the CKM angle γ*
 3415 *using $B^0 \rightarrow DK^{*0}$ with $D \rightarrow K_S^0\pi^+\pi^-$ decays*, JHEP **08** (2016) 137,
 3416 [arXiv:1605.01082](https://arxiv.org/abs/1605.01082).
- 3417 [64] A. Bondar and A. Poluektov, *Feasibility study of model-independent approach*
 3418 *to ϕ_3 measurement using Dalitz plot analysis*, Eur. Phys. J. **C47** (2006) 347,
 3419 [arXiv:hep-ph/0510246](https://arxiv.org/abs/hep-ph/0510246).
- 3420 [65] A. Bondar and A. Poluektov, *The use of quantum-correlated D_0 decays for*
 3421 *ϕ_3 measurement*, Eur. Phys. J. **C55** (2008) 51, [arXiv:0801.0840](https://arxiv.org/abs/0801.0840).
- 3422 [66] Belle collaboration, H. Aihara *et al.*, *First measurement of ϕ_3 with a model-*
 3423 *independent Dalitz plot analysis of $B^\pm \rightarrow DK^\pm$, $D \rightarrow K_S^0\pi^+\pi^-$ decay*, Phys.
 3424 Rev. **D85** (2012) 112014, [arXiv:1204.6561](https://arxiv.org/abs/1204.6561).
- 3425 [67] LHCb collaboration, R. Aaij *et al.*, *A model-independent Dalitz plot analysis*
 3426 *of $B^\pm \rightarrow DK^\pm$ with $D \rightarrow K_S^0h^+h^-$ ($h = \pi, K$) decays and constraints on the*
 3427 *CKM angle γ* , Phys. Lett. **B718** (2012) 43, [arXiv:1209.5869](https://arxiv.org/abs/1209.5869).

- [68] A. Poluektov, *Unbinned model-independent measurements with coherent admixtures of multibody neutral D meson decays*, Eur. Phys. J. **C78** (2018) 121, [arXiv:1712.08326](#).
- [69] CLEO collaboration, J. Libby *et al.*, *Model-independent determination of the strong-phase difference between D^0 and $\bar{D}^0 \rightarrow K_{S,L}^0 h^+ h^-$ ($h = \pi, K$) and its impact on the measurement of the CKM angle γ/ϕ_3* , Phys. Rev. **D82** (2010) 112006, [arXiv:1010.2817](#).
- [70] BESIII collaboration, M. Ablikim *et al.*, *Model-independent determination of the relative strong-phase difference between D^0 and $\bar{D}^0 \rightarrow K_{S,L}^0 \pi^+ \pi^-$ and its impact on the measurement of the CKM angle γ/ϕ_3* , [arXiv:2003.00091](#).
- [71] LHCb collaboration, R. Aaij *et al.*, *Near-threshold $D\bar{D}$ spectroscopy and observation of a new charmonium state*, JHEP **07** (2019) 035, [arXiv:1903.12240](#).
- [72] C. Thomas and G. Wilkinson, *Model-independent $D^0 - \bar{D}^0$ mixing and CP violation studies with $D^0 \rightarrow K_S^0 \pi^+ \pi^-$ and $D^0 \rightarrow K_S^0 K^+ K^-$* , JHEP **2012** (2012) 185, [arXiv:1209.0172](#).
- [73] BESIII collaboration, M. Ablikim *et al.*, *Improved model-independent determination of the strong-phase difference between D^0 and $\bar{D}^0 \rightarrow K_{S,L}^0 K^+ K^-$ decays*, [arXiv:2007.07959](#).
- [74] LHCb collaboration, R. Aaij *et al.*, *Measurement of the CKM angle γ using $B^\pm \rightarrow D K^\pm$ with $D \rightarrow K_S^0 \pi^+ \pi^-$, $K_S^0 K^+ K^-$ decays*, JHEP **10** (2014) 097, [arXiv:1408.2748](#).
- [75] J. Garra Ticó, *A strategy for a simultaneous measurement of CP violation parameters related to the CKM angle γ in multiple B meson decay channels*, [arXiv:1804.05597](#).
- [76] C. De Melis, *The CERN accelerator complex. Complexe des accélérateurs du CERN*, <https://cds.cern.ch/record/2119882>, 2016.
- [77] ATLAS collaboration, *Luminosity determination in pp collisions at $\sqrt{s} = 13$ TeV using the ATLAS detector at the LHC*, ATLAS-CONF-2019-021, 2019.
- [78] LHCb collaboration, A. A. Alves *et al.*, *The LHCb Detector at the LHC*, J. Inst. **3** (2008) S08005.

- 3458 [79] LHCb collaboration, *LHCb reoptimized detector design and performance: 3459 Technical Design Report*, LHCb-TDR-9, 2003.
- 3460 [80] LHCb collaboration, C. Elsässer, $\bar{b}b$ production angle plots, 3461 https://lhcb.web.cern.ch/lhcb/speakersbureau/html/bb_ProductionAngles.html.
- 3462 [81] LHCb collaboration, P. R. Barbosa-Marinho *et al.*, *LHCb VELO (VErtex 3463 LOcator) - Technical Design Report*, LHCb-TDR-5, 2001.
- 3464 [82] LHCb VELO group, R. Aaij *et al.*, *Performance of the LHCb Vertex Locator,* 3465 *J. Inst.* **9** (2014) P09007, [arXiv:1405.7808](https://arxiv.org/abs/1405.7808).
- 3466 [83] LHCb Outer Tracker group, R. Arink *et al.*, *Performance of the LHCb Outer 3467 Tracker*, *J. Inst.* **9** (2014) P01002, [arXiv:1311.3893](https://arxiv.org/abs/1311.3893).
- 3468 [84] LHCb collaboration, R. Aaij *et al.*, *LHCb detector performance*, *Int. J. Mod.* 3469 *Phys* **A30** (2015) 1530022, [arXiv:1412.6352](https://arxiv.org/abs/1412.6352).
- 3470 [85] LHCb collaboration, S. Amato *et al.*, *LHCb RICH: Technical Design Report,* 3471 LHCb-TDR-3, 2000.
- 3472 [86] LHCb RICH collaboration, M. Adinolfi *et al.*, *Performance of the LHCb RICH 3473 detector at the LHC*, *Eur. Phys. J.* **C73** (2013) 2431, [arXiv:1211.6759](https://arxiv.org/abs/1211.6759).
- 3474 [87] LHCb RICH collaboration, A. Papanestis *et al.*, *Performance of the LHCb 3475 RICH detectors during the LHC Run II*, *Nucl. Instrum. Meth* **A876** (2017) 3476 221, [arXiv:1703.08152](https://arxiv.org/abs/1703.08152).
- 3477 [88] LHCb collaboration, S. Amato *et al.*, *LHCb calorimeters: Technical Design 3478 Report*, LHCb-TDR-2, 2000.
- 3479 [89] LHCb ECAL group, I. Machikhiliyan, *The LHCb electromagnetic calorimeter,* 3480 *J. Phys. : Conf. Ser.* **160** (2009) 012047.
- 3481 [90] D. Hutchcroft, *VELO Pattern Recognition*, LHCb-2007-013, 2007.
- 3482 [91] M. Needham and J. Van Tilburg, *Performance of the track matching*, LHCb- 3483 2007-020, 2007.
- 3484 [92] M. Needham, *Performance of the Track Matching*, LHCb-2007-129, 2007.
- 3485 [93] O. Callot, *Downstream Pattern Recognition*, LHCb-2007-026, 2007.

- 3486 [94] R. Frühwirth, *Application of Kalman filtering to track and vertex fitting*, Nucl.
3487 Instrum. Meth **A262** (1987) 444.
- 3488 [95] J. Van Tilburg, *Track simulation and reconstruction in LHCb*, CERN-
3489 THESIS-2005-040, 2005.
- 3490 [96] M. De Cian *et al.*, *Measurement of the track finding efficiency*, LHCb-PUB-
3491 2011-025, 2012.
- 3492 [97] LHCb collaboration, *PID performance plots*,
3493 <https://twiki.cern.ch/twiki/bin/view/LHCb/PIDConferencePlots>.
- 3494 [98] R. W. Forty and O. Schneider, *RICH pattern recognition*, LHCb-98-040, 1998.
- 3495 [99] J. R. T. De Mello-Neto and M. Gandelman, *Muon ID performance with the*
3496 *reoptimized LHCb detector*, LHCb-2003-089, 2003.
- 3497 [100] M. Gandelman and E. Polycarpo, *The Performance of the LHCb Muon*
3498 *Identification Procedure*, LHCb-2007-145, 2008.
- 3499 [101] H. Terrier and I. Belyaev, *Particle identification with LHCb calorimeters*,
3500 LHCb-2003-092, 2003.
- 3501 [102] LHCb collaboration, R. Aaij *et al.*, *Design and performance of the LHCb*
3502 *trigger and full real-time reconstruction in Run 2 of the LHC*, J. Inst. **14**
3503 (2019) P04013, [arXiv:1812.10790](https://arxiv.org/abs/1812.10790).
- 3504 [103] LHCb collaboration, R. Aaij *et al.*, *The LHCb trigger and its performance in*
3505 *2011*, J. Inst. **8** (2013) P04022, [arXiv:1211.3055](https://arxiv.org/abs/1211.3055).
- 3506 [104] I. Bird, *Computing for the Large Hadron Collider*, Annual Review of Nuclear
3507 and Particle Science **61** (2011) 99.
- 3508 [105] T. Sjöstrand, S. Mrenna, and P. Skands, *A brief introduction to PYTHIA 8.1*,
3509 Comput. Phys. Commun. **178** (2008) 852, [arXiv:0710.3820](https://arxiv.org/abs/0710.3820); T. Sjöstrand,
3510 S. Mrenna, and P. Skands, *PYTHIA 6.4 physics and manual*, JHEP **05** (2006)
3511 026, [arXiv:hep-ph/0603175](https://arxiv.org/abs/hep-ph/0603175).
- 3512 [106] I. Belyaev *et al.*, *Handling of the generation of primary events in Gauss, the*
3513 *LHCb simulation framework*, J. Phys. Conf. Ser. **331** (2011) 032047.
- 3514 [107] D. J. Lange, *The EvtGen particle decay simulation package*, Nucl. Instrum.
3515 Meth. **A462** (2001) 152.

- 3516 [108] P. Golonka and Z. Was, *PHOTOS Monte Carlo: A precision tool for*
3517 *QED corrections in Z and W decays*, Eur. Phys. J. **C45** (2006) 97,
3518 arXiv:hep-ph/0506026.
- 3519 [109] Geant4 collaboration, J. Allison *et al.*, *Geant4 developments and applications*,
3520 IEEE Trans. Nucl. Sci. **53** (2006) 270.
- 3521 [110] M. Clemencic *et al.*, *The LHCb simulation application, Gauss: Design,*
3522 *evolution and experience*, J. Phys. Conf. Ser. **331** (2011) 032023.
- 3523 [111] D. Müller, M. Clemencic, G. Corti, and M. Gersabeck, *ReDecay: A novel*
3524 *approach to speed up the simulation at LHCb*, Eur. Phys. J. **C78** (2018) 1009,
3525 arXiv:1810.10362.
- 3526 [112] G. A. Cowan, D. C. Craik, and M. D. Needham, *RapidSim: An application*
3527 *for the fast simulation of heavy-quark hadron decays*, Comput. Phys. Commun.
3528 **214** (2017) 239, arXiv:1612.07489.
- 3529 [113] A. Pais and O. Piccioni, *Note on the decay and absorption of the θ^0* , Phys.
3530 Rev. **100** (1955) 1487.
- 3531 [114] M. L. Good, *Relation between Scattering and Absorption in the Pais-Piccioni*
3532 *Phenomenon*, Physical Review **106** (1957) 591.
- 3533 [115] W. Petscher *et al.*, *Regeneration of arbitrary coherent neutral kaon states: A*
3534 *new method for measuring the $K^0 - \bar{K}^0$ forward scattering amplitude/forward*
3535 *scattering amplitude*, Z. Phys **C72** (1996) 543.
- 3536 [116] I. I. Bigi and H. Yamamoto, *Interference between Cabibbo allowed and doubly*
3537 *forbidden transitions in $D \rightarrow K_{S,L} + \pi$'s decays*, Phys. Lett. **B349** (1995) 363,
3538 arXiv:hep-ph/9502238.
- 3539 [117] CLEO collaboration, Q. He *et al.*, *Comparison of $D \rightarrow K_S^0 \pi$ and $D \rightarrow K_L^0 \pi$*
3540 *decay rates*, Phys. Rev. Lett. **100** (2008) 091801, arXiv:0711.1463.
- 3541 [118] Y. Grossman and Y. Nir, *CP violation in $\tau^\pm \rightarrow \pi^\pm K_S \nu$ and $D^\pm \rightarrow \pi^\pm K_S$: the*
3542 *importance of $K_S - K_L$ interference*, JHEP **2012** (2012) 2, arXiv:1110.3790.
- 3543 [119] J. Gassner, M. Needham, and O. Steinkamp, *Layout and Expected Performance*
3544 *of the LHCb TT Station*, LHCb-2003-140, 2004.

- [120] Belle collaboration, A. B. Kaliyar *et al.*, *Measurements of branching fraction and direct CP asymmetry in $B^\pm \rightarrow K_S^0 K_S^0 K^\pm$ and a search for $B^\pm \rightarrow K_S^0 K_S^0 \pi^\pm$* , Phys. Rev. **D99** (2019) 031102, [arXiv:1812.10221](https://arxiv.org/abs/1812.10221).
- [121] N. Hiroshi, *Search for new physics by a time-dependent CP violation analysis of the decay $B \rightarrow K_S^0$ eta gamma using the Belle detector*, PhD thesis, Tohoku University, Senday, 2015.
- [122] A. Gsponer *et al.*, *Precise Coherent K_S^0 Regeneration Amplitudes for C, Al, Cu, Sn, and Pb Nuclei from 20 to 140 GeV/c and Their Interpretation*, Phys. Rev. Lett. **22** (1979) 13.
- [123] R. A. Briere and B. Winstein, *Determining the Phase of a Strong Scattering Amplitude from Its Momentum Dependence to Better Than 1°: The Example of Kaon Regeneration*, Phys. Rev. Lett. **75** (1995) 402, [arXiv:1006.1938](https://arxiv.org/abs/1006.1938).
- [124] B. R. Ko, E. Won, B. Golob, and P. Pakhlov, *Effect of nuclear interactions of neutral kaons on CP asymmetry measurements*, Phys. Rev. **D84** (2011) 111501, [arXiv:1006.1938](https://arxiv.org/abs/1006.1938).
- [125] LHCb Collaboration, *LHCb VELO Upgrade Technical Design Report*, LHC-B-TDR-013, 2013.
- [126] LHCb Collaboration, *LHCb PID Upgrade Technical Design Report*, LHC-B-TDR-014, 2013.
- [127] LHCb collaboration, R. Aaij *et al.*, *Measurement of the CKM angle γ from a combination of LHCb results*, JHEP **12** (2016) 087, [arXiv:1611.03076](https://arxiv.org/abs/1611.03076).
- [128] LHCb collaboration, M. W. Kenzie and M. P. Whitehead, *Update of the LHCb combination of the CKM angle γ* , LHCb-CONF-2018-002, 2018.
- [129] P. K. Resmi, J. Libby, S. Malde, and G. Wilkinson, *Quantum-correlated measurements of $D \rightarrow K_S^0 \pi^+ \pi^- \pi^0$ decays and consequences for the determination of the CKM angle γ* , JHEP **01** (2018) 082, [arXiv:1710.10086](https://arxiv.org/abs/1710.10086).
- [130] W. D. Hulsbergen, *Decay chain fitting with a Kalman filter*, Nucl. Instrum. Meth. **A552** (2005) 566, [arXiv:physics/0503191](https://arxiv.org/abs/physics/0503191).
- [131] L. Breiman, J. H. Friedman, R. A. Olshen, and C. J. Stone, *Classification and regression trees*, Wadsworth international group, Belmont, California, USA, 1984.

- 3576 [132] H. Voss, A. Hoecker, J. Stelzer, and F. Tegenfeldt, *TMVA - Toolkit for*
 3577 *Multivariate Data Analysis with ROOT*, PoS **ACAT** (2007) 040.
- 3578 [133] A. Hoecker *et al.*, *TMVA 4 — Toolkit for Multivariate Data Analysis with*
 3579 *ROOT. Users Guide.*, arXiv:physics/0703039.
- 3580 [134] L. Anderlini *et al.*, *The PIDCalib package*, LHCb-PUB-2016-021, 2016.
- 3581 [135] M. Pivk and F. R. Le Diberder, *sPlot: A statistical tool to unfold data distri-*
 3582 *butions*, Nucl. Instrum. Meth. **A555** (2005) 356, arXiv:physics/0402083.
- 3583 [136] R. Barlow, *Extended maximum likelihood*, Nucl. Instrum. Meth. **A297** (1990)
 3584 496.
- 3585 [137] W. Verkerke and D. P. Kirkby, *The RooFit toolkit for data modeling*, eConf
 3586 **C0303241** (2003).
- 3587 [138] T. Skwarnicki, *A study of the radiative cascade transitions between the Upsilon-*
 3588 *prime and Upsilon resonances*, PhD thesis, Institute of Nuclear Physics,
 3589 Krakow, 1986, DESY-F31-86-02.
- 3590 [139] LHCb collaboration, R. Aaij *et al.*, *Dalitz plot analysis of $B^0 \rightarrow \bar{D}^0\pi^+\pi^-$*
 3591 *decays*, Phys. Rev. **D92** (2015) 032002, arXiv:1505.01710.
- 3592 [140] LHCb collaboration, R. Aaij *et al.*, *Constraints on the unitarity triangle angle*
 3593 *γ from Dalitz plot analysis of $B^0 \rightarrow DK^+\pi^-$ decays*, Phys. Rev. **D93** (2016)
 3594 112018, Erratum *ibid.* **D94** (2016) 079902, arXiv:1602.03455.
- 3595 [141] LHCb collaboration, R. Aaij *et al.*, *Measurement of CP observables in*
 3596 *$B^\pm \rightarrow D^{(*)}K^\pm$ and $B^\pm \rightarrow D^{(*)}\pi^\pm$ decays*, Phys. Lett. **B777** (2017) 16,
 3597 arXiv:1708.06370.
- 3598 [142] LHCb collaboration, R. Aaij *et al.*, *Dalitz plot analysis of $B_s^0 \rightarrow \bar{D}^0K^-\pi^+$*
 3599 *decays*, Phys. Rev. **D90** (2014) 072003, arXiv:1407.7712.
- 3600 [143] J. G. Ticó *et al.*, *A study of the sensitivity to CKM angle γ under simultaneous*
 3601 *determination from multiple B meson decay modes*, arXiv:1909.00600.
- 3602 [144] A. Bondar, A. Poluektov, and V. Vorobiev, *Charm mixing in a model-*
 3603 *independent analysis of correlated $D^0\bar{D}^0$ decays*, Phys. Rev. **D82** (2010)
 3604 034033, arXiv:1004.2350.

- 3605 [145] B. Sen, M. Walker, and M. Woodroffe, *On the Unified Method with Nuisance*
 3606 *Parameters*, Statistica Sinica **19** (2009) 301.
- 3607 [146] C.-S. Chuang and T. L. Lai, *Resampling Methods for Confidence Intervals in*
 3608 *Group Sequential Trials*, Biometrika **85** (1998) 317.
- 3609 [147] C.-S. Chuang and T. L. Lai, *Hybrid Resampling Methods for Confidence*
 3610 *Intervals*, Statistica Sinica **10** (2000) 1.
- 3611 [148] Belle collaboration, K. Trabelsi, *Study of direct CP in charmed B decays and*
 3612 *measurement of the CKM angle gamma at Belle*, arXiv:1301.2033.
- 3613 [149] BaBar collaboration, D. Derkach, *Combination of gamma measurements from*
 3614 *BaBar*, arXiv:1301.3283.
- 3615 [150] LHCb collaboration, R. Aaij *et al.*, *Measurement of CP observables in $B^\pm \rightarrow$*
 3616 *DK^\pm and $B^\pm \rightarrow D\pi^\pm$ with two- and four-body D decays*, Phys. Lett. **B760**
 3617 (2016) 117, arXiv:1603.08993.
- 3618 [151] LHCb collaboration, R. Aaij *et al.*, *A study of CP violation in $B^\mp \rightarrow Dh^\mp$*
 3619 *($h = K, \pi$) with the modes $D \rightarrow K^\mp\pi^\pm\pi^0$, $D \rightarrow \pi^+\pi^-\pi^0$ and $D \rightarrow K^+K^-\pi^0$* ,
 3620 *Phys. Rev. D91* (2015) 112014, arXiv:1504.05442.
- 3621 [152] LHCb collaboration, R. Aaij *et al.*, *A study of CP violation in $B^\pm \rightarrow DK^\pm$*
 3622 *and $B^\pm \rightarrow D\pi^\pm$ decays with $D \rightarrow K_S^0 K^\pm \pi^\mp$ final states*, Phys. Lett. **B733**
 3623 (2014) 36, arXiv:1402.2982.
- 3624 [153] LHCb collaboration, R. Aaij *et al.*, *Measurement of CP observables in $B^\pm \rightarrow$*
 3625 *$DK^{*\pm}$ decays using two- and four-body D-meson final states*, JHEP **11** (2017)
 3626 156, Erratum *ibid. D05* (2018) 067, arXiv:1709.05855.
- 3627 [154] LHCb collaboration, R. Aaij *et al.*, *Study of $B^- \rightarrow DK^-\pi^+\pi^-$ and $B^- \rightarrow$*
 3628 *$D\pi^-\pi^+\pi^-$ decays and determination of the CKM angle γ* , Phys. Rev. **D92**
 3629 (2015) 112005, arXiv:1505.07044.
- 3630 [155] LHCb collaboration, R. Aaij *et al.*, *Measurement of CP violation parameters*
 3631 *in $B^0 \rightarrow DK^{*0}$ decays*, Phys. Rev. **D90** (2014) 112002, arXiv:1407.8136.
- 3632 [156] LHCb collaboration, R. Aaij *et al.*, *Measurement of CP asymmetry in $B_s^0 \rightarrow$*
 3633 *$D_s^\mp K^\pm$ decays*, JHEP **03** (2018) 059, arXiv:1712.07428.
- 3634 [157] LHCb collaboration, R. Aaij *et al.*, *Measurement of CP violation in*
 3635 *$B^0 \rightarrow D^\pm\pi^\mp$ decays*, JHEP **06** (2018) 084, arXiv:1805.03448.